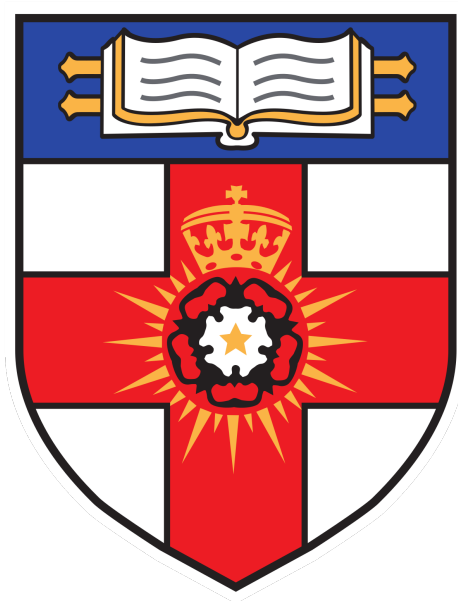


Detector Corrected Cross-Sections in Topologies Sensitive to Dark Matter Production with the ATLAS Experiment

Vasilis Konstantinides

Department of Physics and Astronomy
UCL



A thesis submitted to the University College London
for the degree of Doctor of Philosophy

Declaration

I declare that the work presented in this thesis is my own. Where the work of others has been consulted, this has been indicated in the thesis.

Vasilis Konstantinides
June 2020

Abstract

An analysis of events with large missing transverse momentum in association with jets is presented using 139.0 fb^{-1} of proton-proton collisions at a centre of mass energy of 13 TeV, delivered by the Large Hadron Collider and recorded by the ATLAS detector. The dominant Standard Model process contributing to this signature is the invisible decay of the Z boson as well as the leptonic decay of the W boson where the charged lepton is outside the detector acceptance. The similarities between these processes and the leptonic decays of the Z and W bosons are exploited in dedicated 1-lepton and 2-lepton regions where the in-acceptance leptons are treated as though they were invisible in order to constrain the modelling and minimise the experimental and theoretical uncertainties.

The analysis is performed in three jet phase-spaces that are sensitive to different mechanisms of dark matter production; the ≥ 1 jet, ≥ 2 jet and VBF phase-spaces. Fiducial cross-sections are presented single and double differentially as a function of missing transverse momentum and other jet kinematics, in events with zero leptons, one lepton and two leptons and in each of the jet phase-spaces. Ratios of cross-sections are also presented to facilitate comparisons between the regions. The data is corrected for detector effects via the iterative bayesian unfolding technique, making the measurements readily available for comparison to new physics models without the need of a detector simulation.

Impact Statement

Since the discovery of the Higgs boson in 2012, high energy physics has been one of the most exciting areas of research, drawing the interest of academic research institutes and captivating the imagination of the general public. Often referred to as particle physics, the discipline studies the most fundamental building blocks of matter and their interactions, offering glimpses into the fundamental nature of reality itself. The theory describing this subatomic world, known as the Standard Model of particle physics, is one of the most celebrated theories ever developed, successfully passing seemingly every experimental test thrown at it. Still, cosmological observations show that there are phenomena in the universe that the theory cannot explain - the existence of additional invisible matter particles, commonly referred to as dark matter.

The work presented in this thesis is part of the ongoing effort to test the Standard Model with extreme precision and search for evidence of dark matter production at the Large Hadron Collider. Data collected at the ATLAS detector are analysed using novel techniques, disentangling the measured data from current modelling methods and correcting them for detector effects, allowing for multiple models predicting new physical phenomena to be experimentally tested. The research carried out in this thesis - and by the wider particle physics community - pushes the frontiers of our understanding of the universe and of the subatomic world, while the technologies developed in the context of high energy physics have far and wide applications, with the development of new cancer treatment methods and the world wide web being only a few examples.

Acknowledgements

The work presented in this thesis would not have been possible without the academic and moral support of numerous people. First and foremost, I would like to thank my primary supervisor, Emily Nurse, for all her guidance and support throughout my studies. I am grateful for all our conversations and for all the feedback and encouragement you provided me with during my time at UCL. I would also like to thank Christian Gütschow, whose patience, tutoring and help with every aspect of my PhD has been invaluable. Thanks to the whole UCL HEP group and the amazing people of the $p_T^{\text{miss}} + \text{jets}$ analysis for creating a friendly and stimulating working environment. Thanks also to my fellow doctoral students for all their support and comradeship through the highs and lows of our PhDs.

Finally, I would like to thank my family, friends and partner for all their encouraging words and emotional support over the course of my studies. Special thanks to my mom, for her seemingly endless love and patience; to my dad, for driving me to the neighbouring city - three evenings per week during my high school years - so that I could have a proper chance at a physics education; to my brother and sister for being the most supporting and loving siblings I could have ever asked for.

Contents

Impact Statement	4
Acknowledgements	5
Introduction	10
I Theory And Experiment	13
1 Theoretical Framework	14
1.1 The Standard Model of particle physics	14
1.2 Phenomenology of proton-proton collisions	20
1.3 Physics beyond the Standard Model	21
2 Experimental Setup	29
2.1 The Large Hadron Collider	29
2.2 The ATLAS detector	33
2.3 Object reconstruction and identification	42
II Detector-corrected cross-sections in events with large missing transverse momentum in association with jets	51
3 The p_T^{miss} + jets analysis	52
3.1 Analysis strategy	52
3.2 Measured variables	58

3.3	Particle-level object and event selection	60
3.4	Detector-level object and event selection	64
3.5	Datasets and Monte Carlo simulation	69
3.6	Uncertainties	73
3.7	Detector-level results	77
4	Correcting for detector effects	93
4.1	Introduction	93
4.2	Optimising the number of unfolding iterations	96
4.3	Binning optimisation	98
4.4	Detector response	99
4.5	Uncertainties	100
4.6	Process composition variations	107
4.7	Signal injection tests	115
4.8	$Z \rightarrow \nu\bar{\nu} + \text{jets}$ slicing method bias	118
5	Results	120
5.1	Detector corrected differential cross-sections	120
5.2	Detector corrected R^{miss}	136
6	Conclusions	147
III Appendix		149
A Monte Carlo samples description		151
A.1	MC samples for SM processes	151
A.2	MC samples for BSM processes	153
B Top-enhanced control regions		155
B.1	$t\bar{t}$ contributions	155
B.2	Single top uncertainties	156

C	Detector response: migration matrices, reconstruction efficiencies, fiducial fractions and fiducial purity	163
D	Unfolded systematic uncertainties	183
E	Systematic uncertainties on R^{miss}	194
	Bibliography	202

Introduction

In 1897, while studying the properties of cathode rays, J.J Thomson made the first discovery of a subatomic particle. Though the term ‘Standard Model’ would not be coined until seven decades later, that discovery marked the beginning of one of the most ambitious research endeavours in physics, aiming to fully describe the behaviour of all fundamental particles in one single theory. The result of this research is the quantum field theory known as the Standard Model of particle physics. Since the discovery of the electron, an additional eleven fundamental building blocks of matter have been discovered, accompanied by five force-carrier particles mediating their interactions. The experimental research conducted in the last few decades has expanded our understanding of how the universe fundamentally works and has led to countless technological advancements, immensely affecting both the practical aspects of every-day life and our ideas about the nature of reality.

Though the Standard Model has been extremely successful in describing physical phenomena, it fails to provide an explanation for cosmological observations that point to the existence of a new type of gravitating matter. This new type of matter is known as *dark matter* since it does not interact electromagnetically or through the strong nuclear force, making it invisible to current detectors and telescopes. Still, dark matter could interact weakly with SM particles and different experimental setups around the world aim to detect and study these interactions. One such experiment is the ATLAS experiment, located at the Large Hadron Collider and collecting data from proton-proton collisions. Dark matter particles are not expected to interact with the detector’s apparatus which makes their detection non-trivial. Nevertheless, the production of dark matter particles would result in an energy imbalance in the transverse plane of the detector, assuming that they are produced in association with, and recoiling from, other detectable

SM particles. Such an energy imbalance can also be the result of Standard Model processes involving neutrinos, which are also invisible to the detector. Deviations from the Standard Model prediction for the rate of production of invisible particles could indicate the production of dark matter.

This thesis presents measurements of differential cross-sections in regions of phase-space that are largely populated by well-known SM process but are also expected to be sensitive to the production of dark matter particles or other beyond the Standard Model physics. A novel approach is taken in this analysis, with measurements defined in terms of final-state particles rather than in terms of a particular physical process. The measurements are also corrected for detector effects so that they are easily and directly comparable to new physics models without the need of a detector simulation, making them optimally useful long into the future and available for quick reinterpretation studies.

The thesis begins with Chapter 1, where an overview of the theoretical framework of the Standard Model is given. Evidence and possible models for dark matter are also briefly discussed here, along with an introduction to the physics of proton-proton collisions. Chapter 2 gives a brief description of the Large Hadron Collider and the ATLAS detector, followed by a description of the reconstruction and identification techniques for physics objects. The analysis strategy for the measurement of regions sensitive to dark matter production is discussed in detail in Chapter 3. Sources of theoretical and experimental systematic uncertainties are discussed here and the detector-level results of this analysis are presented. Chapter 4 describes the procedure used to correct the measurements for detector-effects and discusses additional systematic uncertainties and biases arising from this procedure. The detector-corrected differential cross-sections are finally presented and discussed in Chapter 5. A conclusion of the work presented in this thesis is given in Chapter 6.

Contributions

The work presented in this thesis was performed as part of the ATLAS Collaboration, in an analysis team with contributions from multiple international institutes. The bulk of the

author's contribution to this analysis is documented in this thesis and has benefited greatly from the work of others. Most notably, the theoretical systematic uncertainties used in this thesis were kindly provided by Christian Gütschow and Aidan Kelly. The QCD multijet background estimates were provided by Sebastian Weber. The software framework used for the full analysis chain was developed jointly by the author and Christian Gütschow.

Part I

Theory And Experiment

Chapter 1

Theoretical Framework

1.1 The Standard Model of particle physics

The Standard Model (SM) of particle physics is the theoretical framework describing the fundamental building blocks of nature and their interactions. It is a relativistic quantum field theory, with particles emerging as excitations of quantum fields defined at all points in space-time. Matter, as described in the SM, is comprised of two types of particles; particles that make up every-day structures, known as fermions, and particles that mediate the interactions between them, known as bosons. The SM bosons are the force-carriers of the three fundamental forces the theory describes: the electromagnetic (EM), weak and strong nuclear force. Figure 1.1 summarises the particle content of the SM and their properties. In the figure, the hypothetical graviton is also included, assumed to be the mediator of the fourth fundamental force, the gravitational force. In reality, the SM does not provide any description of gravity.

Fermions are governed by Fermi-Dirac statistics, obey the Pauli exclusion principle and have half-integer spin. Additionally, each fermion has its own antiparticle, with identical mass but opposite electric charge. The fermions can be arranged into three generations, with the first generation making up everyday matter. The fermions of the second and third generations have a higher mass than their equivalent first generation particle but otherwise have identical quantum properties. The fermionic content of the SM can be further divided into two groups;

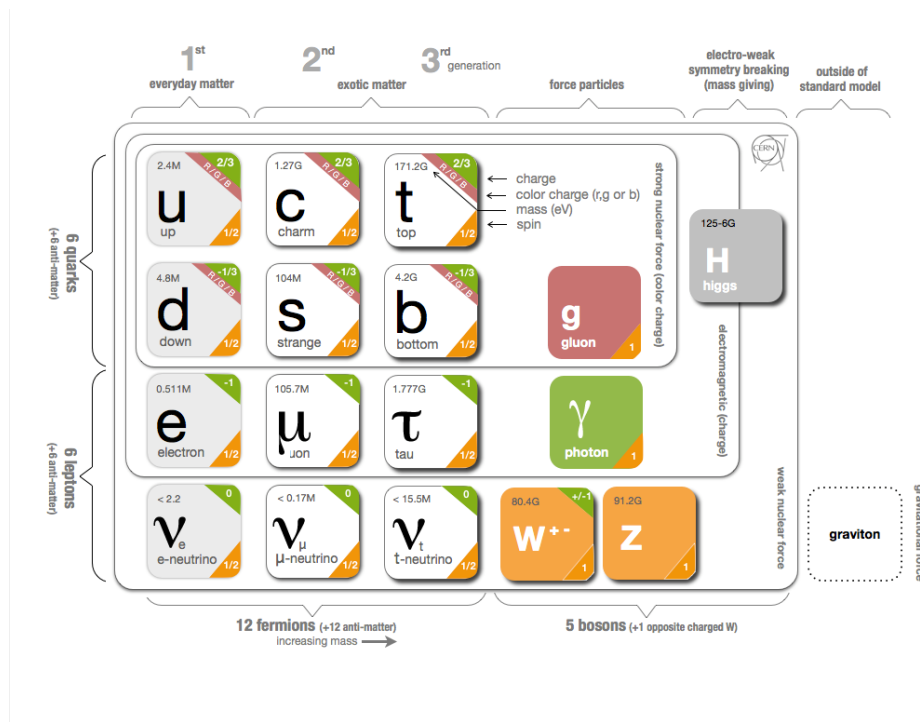


Figure 1.1 The particle content of the Standard Model. Particles can be arranged into groups depending on their quantum properties [1].

the quarks and the leptons. Quarks have an electric charge of $2/3$ or $-1/3$ and carry a color charge, allowing them to interact via all three fundamental forces. Leptons carry an electric charge of -1 (charged leptons) or 0 (neutrinos). Charged leptons are massive where neutrinos are predicted to be massless in the SM and neither of them carry a color charge. Hence, charged leptons interact through the EM and weak force and neutrinos interact only through the weak force.

The force-carrying bosons are also known as vector bosons because of their unit spin. The photon mediates the EM interaction by coupling to electrically charged particles and it is electrically neutral and massless. The W^\pm and Z^0 bosons mediate the weak interaction and are both massive, with the Z^0 boson being slightly heavier than the W^\pm . The W^\pm bosons carry a unit electric charge of ± 1 where the Z^0 boson is electrically neutral. The SM is completed by the Higgs boson which is a scalar boson with spin 0. The Higgs is massive and electrically neutral and provides mass to the W^\pm and Z^0 bosons by breaking the electroweak symmetry.

Requiring that the interactions between SM particles satisfy global symmetries guarantees that conservation laws are obeyed in the SM. Additionally, interactions in the SM are described by the *local* gauge symmetry group, $SU(3)_C \times SU(2)_L \times U(1)_Y$. Each one of the terms of the gauge group loosely represents one of the fundamental forces, with $SU(3)_C$ describing QCD interactions through the strong force [2], $SU(2)_L$ describing weak interactions [3] and $U(1)_Y$ replacing the $U(1)$ gauge symmetry of electromagnetism in the electroweak unification model. In order for the interactions to be invariant under the transformations of each Lie group, additional fields are introduced. These fields are interpreted as gauge bosons, mediating the interactions between particles.

Quantum Electrodynamics, electroweak unification and the Higgs mechanism

Quantum Electrodynamics is the quantum field theory described by the $U(1)$ unitary gauge group, initially developed to describe electromagnetic interactions. The interaction of a charged fermion ψ with the electromagnetic field can be summarised in the Lagrangian

$$\mathcal{L}_{\text{QED}} = \bar{\psi}(i\gamma^\mu D_\mu - m)\psi - \frac{1}{4}F_{\mu\nu}F^{\mu\nu} \quad (1.1)$$

where γ^μ are the Dirac matrices, m is the mass of the charged fermion, D_μ is the gauge invariant derivative given by

$$D_\mu = \partial_\mu + ieA_\mu \quad (1.2)$$

where e is the coupling constant equal to the electric charge of the fermion, A_μ is the electromagnetic field and $F_{\mu\nu}$ is the electromagnetic field tensor given by

$$F_{\mu\nu} = \partial_\mu A_\nu - \partial_\nu A_\mu \quad (1.3)$$

and representing the kinetic energy term of the excitation of the field.

The electromagnetic force is unified with the weak force in the electroweak model, forming a combined gauge theory represented by the $SU(2)_L \times U(1)_Y$ gauge symmetry group. In order

for the Lagrangian to be invariant under transformations of the $SU(2)$ symmetry group, three additional gauge fields must be introduced, W_μ^1, W_μ^2 and W_μ^3 , setting up the foundations of the gauge bosons of the weak interaction.

Though it is tempting to identify each of these gauge fields as the W^+, W^- and Z^0 bosons, experimental evidence shows that parity is violated in charged weak current interactions, meaning that only left handed particles interact with the charged W^\pm bosons, while both left and right handed particles couple to the Z boson through neutral current weak interactions. The left handedness of the weak force can be achieved by adding both a vector and an axial vector ($V - A$) component to weak interactions, modifying $SU(2)$ into an $SU(2)_L$ symmetry. The weak isospin charge, I_W , is introduced, with $I_W = \frac{1}{2}$ for left-handed fermion doublets and $I_W = 0$ for right-handed fermion singlets.

The coupling of the Z bosons to right handed particles is restored by unifying the $SU(2)_L$ and $U(1)$ symmetry groups into a combined $SU(2)_L \times U(1)_Y$ symmetry. In this unification, the original $U(1)$ symmetry which introduced the electromagnetic field A_μ is replaced with a new $U(1)_Y$ local gauge symmetry, which replaces A_μ with B_μ . $U(1)_Y$ also gives rise to a new quantum number, the weak hypercharge Y , which is defined as

$$Y = 2(Q - I_W^3) \quad (1.4)$$

where Q is the electric charge of the fermion and $I_W^3 = \pm \frac{1}{2}$ is the third component of the fermion's weak isospin. The W_μ^\pm, Z_μ and A_μ fields of the weak and electromagnetic force can then be expressed as combinations of the $W_1^\mu, W_2^\mu, W_3^\mu$ and B_μ gauge fields of the combined $SU(2)_L \times U(1)_Y$ symmetry, with

$$W_\mu^\pm = \frac{1}{\sqrt{2}}(W_\mu^1 \mp iW_\mu^2) \quad (1.5)$$

$$\begin{pmatrix} A_\mu \\ Z_\mu \end{pmatrix} = \begin{pmatrix} \cos \theta_W & \sin \theta_W \\ -\sin \theta_W & \cos \theta_W \end{pmatrix} \begin{pmatrix} B_\mu \\ W_\mu^3 \end{pmatrix} \quad (1.6)$$

where θ_W is the weak mixing angle. The weak mixing angle can be used to express the relation between the couplings of the photon (e), W (g_W) and Z (g_Z) bosons

$$e = g_W \sin \theta_W = g_Z \sin \theta_W \cos \theta_W \quad (1.7)$$

as well as the masses of the W and Z bosons,

$$m_W = m_Z \cos \theta_W. \quad (1.8)$$

The three gauge bosons of the weak force acquire their mass through the Higgs mechanism [4–6]. The mechanism introduces a complex scalar field ϕ into the Lagrangian, with a potential given by

$$V = -\frac{1}{2}\mu^2(\phi^*\phi) + \frac{1}{4}\lambda^2(\phi^*\phi)^2 \quad (1.9)$$

where μ and λ are scalar constants. For real solutions of Equation 1.9 the potential has non-zero vacuum expectation values which spontaneously breaks the $SU(2)_L \times U(1)_Y$ symmetry and introduces an additional massive particle, known as the Higgs boson. The interactions of the Higgs field with the Lagrangian of the $SU(2)_L \times U(1)_Y$ sector results in mass terms to appear for all bosons except the photon. The masses of the bosons can be related to the properties of the Higgs with

$$\begin{aligned} m_A &= 0 \\ m_Z &= \frac{1}{2}\sqrt{v(g_W^2 + g_B^2)} \\ m_W &= \frac{1}{2}g_W v \end{aligned} \quad (1.10)$$

where $v^2 = \frac{\mu^2}{\lambda}$. The mechanism described above results in the bosons of the electroweak symmetry acquiring mass. For SM fermions to also become massive, additional terms must be introduced into the Lagrangian known as Yukawa couplings, coupling the Higgs field to the fermion fields.

Quantum Chromodynamics

Quantum Chromodynamics is the quantum field theory based on the $SU(3)$ gauge symmetry describing the interactions of particles through the strong nuclear force. The generators of the group are related to the Gell-Mann 3×3 matrices, resulting in three additional degrees of freedom corresponding to the three colour charges of the strong interaction: red, blue and green. Local gauge transformations of the $SU(3)$ symmetry group are made invariant by introducing eight new boson fields, known as the gluons. In the SM only quarks and gluons carry a colour charge and can interact through the strong force. Because of the non-commutation of the $SU(3)$ generators gluons can also self interact.

The coupling strength of the strong interaction, α_s , depends on the energy scale of the interaction, Q , with approximately

$$\alpha_s(Q) \propto \frac{1}{\ln(Q/\Lambda)} \quad (1.11)$$

where Λ is the QCD scale. The running coupling of QCD results in a large coupling strength at low energies (or, equivalently, large distances) and a weaker coupling strength at high energies (or small distances). The large coupling strength at large distances leads to the phenomenon of confinement where free quarks and gluons are never observed free in nature but are always found in bound, colourless states. This results in the process of *hadronisation*, where in the presence of a pair of free propagating quarks, a quark anti-quark pair will be produced from the vacuum, each one bounding to one of the initial quarks and forming a hadron. Hadronisation is a low-energy process and so it cannot be described by perturbation theory. Instead, different effective theory models are used in simulations to form hadrons from free quarks produced in proton-proton collisions.

Conversely, the weak coupling strength of QCD at small distances leads to the phenomenon of asymptotic freedom, where the strong interactions between quarks and gluons at high energies become small and the particles become asymptotically free. At this energy scale, perturbation theory is able to approximate final states.

1.2 Phenomenology of proton-proton collisions

The energies at which the LHC is operating are large enough to resolve the internal structure of the proton which is composed of one down and two up quarks. Vacuum fluctuations can also add additional quarks (known as sea quarks) and gluons to the constituents of the proton. In reality, collisions at the LHC take place between these constituents, collectively known as partons. In such collisions, the process of interest is called the hard-scattering and it is the one where a large transfer of energy Q^2 between the two colliding partons occurs.

The probability of particle(s) X to be produced in a proton-proton collision is given by the cross-section of the process divided by the total proton-proton cross-section. The cross-section of $p_1 p_2 \rightarrow X$ is given by

$$\sigma_{p_1 p_2 \rightarrow X} = \sum_{n=0}^{\infty} \alpha_s^n(\mu_R^2) \int \int dx_1 dx_2 f_{a/p_1}(x_a, \mu_F^2) f_{b/p_2}(x_b, \mu_F^2) \sigma_{ab \rightarrow X} \quad (1.12)$$

where n denotes the order of the calculation, $\mu_R \equiv Q$ is the renormalisation scale at which α_s is evaluated and $\sigma_{ab \rightarrow X}$ is the cross section of the $ab \rightarrow X$ process. The functions $f_{a/p_1}(x_a, \mu_F^2)$ and $f_{b/p_2}(x_b, \mu_F^2)$ represent the parton distribution functions (PDFs) which give the probability of parton a/b carrying the momentum fraction $x_{a/b}$ of proton $p_{1/2}$, given the scale of the interaction μ_F^2 , also known as the factorisation scale. The factorisation scale can be interpreted as the energy scale at which the treatment of the interaction by the PDFs stops and perturbation theory can be used to calculate the matrix element (ME) of the cross-section. Both the renormalisation and factorisation scales are unphysical and their introduction into the cross-section calculation is accompanied by a theoretical uncertainty.

The matrix element of the hard-scattering is approximated at small distances, where α_s is small, using a perturbative expansion in α_s . Higher order terms of the expansion ($n \geq 1$) represent real and virtual corrections to the leading order (LO) calculation ($n = 0$). Real corrections at next-to-leading order (NLO) or higher materialise as parton emissions while virtual corrections are represented by parton loops. Higher order corrections often diverge when integrating over the full energy phase-space, causing the perturbative series to not converge.

Additional parton emissions usually diverge at small angles, also known as the *collinear limit*, while virtual loops can diverge at both small and large momenta, known as the *infrared limit* and the *ultraviolet catastrophe* respectively. Divergences in the collinear and infrared limit often cancel out and residual remainders can be treated using a method known as *resummation* where the most important terms in the expansion are summed up in a single factor. Ultraviolet catastrophe divergences are treated with a dimensional regularisation and the introduction of the renormalisation scale.

Initial and final state partons that participate in the interaction can radiate additional partons, referred to as initial and final state radiation (ISR and FSR). At high energies where α_s is small, the cascade of partons can be described by parton shower models [7, 8] as it evolves in time and the energy scale of the process decreases. Emissions of additional partons are often accounted for in the higher order corrections of the ME calculation. and multiple techniques exist so that the parton shower is matched and merged to the ME without double counting. Parton shower models break down at the energy scale of a few GeV where α_s is no longer small and perturbation theory no longer holds. Hadronisation models are then used to combine the free colour-charged partons into a final state of colourless hadrons, also known as a jets.

During the hard scattering process the proton breaks up and its colour-charged remnants are also evolved using parton shower and hadronisation models. This is known as the *underlying event* and it accounts for all particle production that is not associated with the hard-scattering. The underlying event also accounts for multiple parton interactions (MPI), where more than one hard interaction occurs in the same proton-proton collision.

1.3 Physics beyond the Standard Model

Even though the SM has been extremely successful at predicting phenomena observed in nature, it is still not a complete theory. Aspects of the theory itself seem suspicious, in the sense that parameters of the SM appear to be fine-tuned to values necessary for certain phenomena to arise. One such parameter is the relatively small mass of the Higgs boson, measured at $m_H \approx 125$ GeV

even though higher order corrections could result in it being orders of magnitudes larger. The large differences in the masses of other SM particles and differences in the coupling strengths of the EM, weak and strong forces also raise issues of fine-tuning, known as the hierarchy problem. The values of such parameters do not originate from theoretical reasoning but are rather assigned their values from experimental observations.

Additional problems arise from the experimental observation of neutrino oscillations, which require neutrinos to have both flavour and mass eigenstates. The SM itself does not predict massive neutrinos and additional parameters need to be added to the theory to accommodate for that. Even then, the masses of the neutrinos seem to be much smaller than the rest of the SM particles. Other caveats include the inability of the theory to incorporate a quantum field theory of gravity in its mechanisms and to fully explain the matter-antimatter asymmetry observed in the universe. Lastly, the SM has not been able to explain the existence of dark energy and, most relevant to this work, it has been unable to provide a possible particle candidate for dark matter.

Evidence for dark matter

Evidence for the existence of dark matter is found mainly in astrophysical observations. One of the first indications for the existence of unaccounted matter came from the measurement of the rotational curves of galaxies, showing the velocities at which gas and stars rotate around the centre of a galaxy. These rotational velocities were measured as a function of r , the distance of an object from the galactic centre, and were expected to decrease with $\propto \sqrt{1/r}$ given the distribution and amount of visible matter inside their orbit and following Newtonian mechanics. It was observed however that rotational velocities remain constant outside the central galactic region for increasing values of r , suggesting the existence of additional matter in a halo around the galaxy. This additional non-luminous matter was not visible to telescopes, suggesting that it does not interact electromagnetically and so it is referred to as dark matter.

Evidence for the existence of dark matter is also present in gravitational lensing measurements. Gravitational lensing occurs when the path of light from a distance light source is

bent as it travels towards an observer, because of the presence of a massive structure in its path bending space-time. The intensity of the lensing effect is proportional to the mass of the structure. Effects of gravitational lensing appear as distortions of far away objects around the lensing structure and can be used to measure its gravitational pull. Observations show that the gravitational pull of galaxy clusters far exceeds the one corresponding to their visible baryonic matter. A notable example of such a measurement is the *bullet cluster* case, where two galaxy clusters are in the process of separating after colliding. In the bullet cluster, visible matter slows down and remains close to the point of collision. Gravitational lensing however indicates that the largest fraction of gravitating matter has already moved away from the collision point in the form of dark matter.

Studies of the Cosmic Microwave Background (CMB) also provide strong evidence for the existence of dark matter particles. The CMB is the thermal black body radiation left over from the early stages of the expansion of the universe, after the cosmological era of recombination. Though it is almost completely isotropic at a temperature of ~ 2.7 K, small temperature differences can be observed, believed to be originating from gravitational and baryonic pressure differences in the early universe. The power spectrum of these anisotropies has been extensively measured and it can be used to constrain cosmological parameters of the Λ CDM model (also referred to as the Standard Model of cosmology) such as the curvature and the baryonic density of the universe. The Λ CDM has been very successful at describing the evolution of the universe but in order to match observations it requires the existence of cold dark matter and dark energy, where the former is predicted to be a non-relativistic, heavy particle and the latter is represented by the cosmological constant Λ . Possible candidates for cold dark matter are weakly interacting massive particles (WIMPs) which, as the name suggests, interact only through the gravitational and weak force. According to the Λ CDM model only $\sim 5\%$ of the energy density of the universe is attributed to visible matter. The rest is predicted to be $\sim 70\%$ due to dark energy and $\sim 25\%$ due to dark matter.

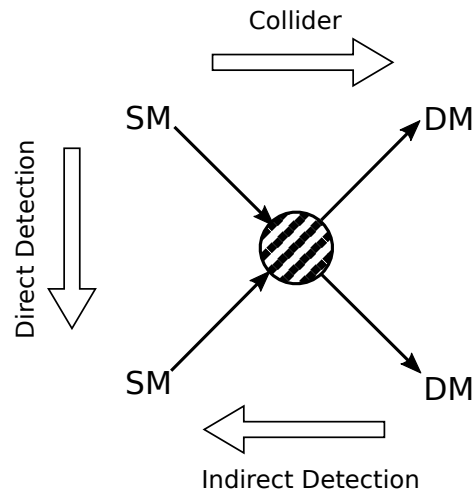


Figure 1.2 Feynman diagram showing three possible ways dark matter could be interacting with the SM. The arrows show the approach of different experiments [9].

1.3.1 Searches for dark matter

Experiments around the world exploit the fact that dark matter could be interacting with SM particles, albeit weakly. Three different approaches exist to search for such interactions: direct detection, indirect detection and collider searches. The type of interactions these approaches aim to detect are summarised in the feynman diagram of figure 1.2 [9].

A direct detection experiment aims to detect the recoil of a SM particle when a dark matter particle passes through the detector and scatters off it [10, 11]. Different noble gases are used as the active material of these detectors and the energy transfer of the interaction is measured from the recoil of the nucleus using ionisation or scintillation techniques. Such experiments need to be built deep underground to shield the apparatus from cosmic rays and both cosmic backgrounds and backgrounds coming from the material of the detector itself must be thoroughly understood in order to reach the required sensitivity.

Indirect detection experiments aim to detect the production of SM particles through the annihilation of dark matter particles. A possible signature for such experiments would be an excess of cosmic rays coming from inside or outside the solar system and so detectors are often placed in space. These type of experiments often suffer from large astrophysical backgrounds

that are hard to constrain. Another possible signature for indirect detection experiments are neutrinos produced from dark matter annihilation inside the sun. For these, earth based neutrino detectors search for an excess of neutrino fluxes above the expected backgrounds.

Collider searches look for the production of dark matter particle pairs through the collision of SM particles. Even though dark matter particles are not expected to interact with a detector's apparatus, they are expected to be produced in association with SM particles. The signature of such a production is an *imbalance* of energy in the transverse plane of the detector. Dark matter searches at the LHC look for SM particles recoiling off missing momentum in the transverse plane (p_T^{miss})¹ and are usually referred to as $p_T^{\text{miss}} + X$ searches, where X denotes the SM particle(s). Past searches at the LHC have searched for the production of p_T^{miss} in association with an electroweak boson (V) emitted from one of the incoming quarks [12–14]. The $p_T^{\text{miss}} + V$ signatures where the boson decays leptonically provide a clean signal with low backgrounds but suffer from poor statistics. Searches looking for the $p_T^{\text{miss}} + W$ signature where the W decays leptonically also face complications from the neutrino adding to the invisible energy of the event [15, 16]. A popular signature with much higher production cross-section is the $p_T^{\text{miss}} + \text{jets}$ one, where the dark matter particles recoil off an energetic jet [17]. Another popular signature to look for is the invisible decay of the Higgs boson, $H \rightarrow \chi\bar{\chi}$, with the Higgs decaying to dark matter particles [18].

1.3.2 Dark matter models

Multiple theories aiming to incorporate dark matter particles into the SM have been developed so far and efforts to do so are still ongoing. New physics models can be fully developed, self-consistent theories postulating the existence of a plethora of new particles and providing possible dark matter candidates. One such theory is the Minimal Supersymmetric Standard Model (SUSY). Other theories, such as effective field theories (EFTs), are model-independent and extend the SM by adding the minimum amount of particles required for interactions between the SM and the dark sector. EFTs are approximations of fully developed theories and

¹Missing transverse momentum is interchangeably referred to as MET or p_T^{miss} .

usually describe SM interactions with dark matter particles using contact operators instead of mediating bosons. Two more new physics model types relevant to this work are described below. In all cases new physics models are required to make as few assumptions as possible and to be consistent with the symmetries of the SM.

Simplified mediator models

Simplified mediator models are particularly popular in collider searches and predict dark matter particles that couple to the SM through mediators whose masses are within the energy limits of the LHC. Simplified models introduce as few parameters as possible into the SM Lagrangian and assume that additional particles of more fully developed theories do not affect SM-dark matter interactions and can be integrated out.

Simplified models usually extend the SM by postulating the existence of a dark matter particle, χ , and introducing a new U(1) gauge symmetry which is then spontaneously broken, giving rise to a new massive mediator, A_μ , that couples the dark matter particles to SM quarks, q . Popular models couple the two sectors through the s-channel, as shown in the feynman diagram of Figure 1.3a. Different models can have spin-1 mediators with vector or axial-vector couplings or spin-0 scalar or pseudo-scalar mediators. Here, a spin-1 axial-vector mediator is considered. The Lagrangian terms describing the interactions of such a mediator with quarks and dark matter particles are given by

$$\mathcal{L}_{\text{A-V}} \supset g_\chi A_\mu \bar{\chi} \gamma^\mu \gamma^5 \chi + \sum_q g_q A_\mu \bar{q} \gamma^\mu \gamma^5 q \quad (1.13)$$

where g_χ and g_q are the couplings the mediator to dark matter particles and quarks. In order for the limits that collider searches set on simplified models to be comparable, the couplings are usually set to $g_\chi = 1$ and $g_q = 0.25$. Constraints can then be set on the remaining two parameters of the model, the mass of the mediator, m_A , and the mass of the dark matter particle, m_χ . Exclusion limits are usually presented on the $m_A - m_\chi$ plane. Figure 1.4 shows the latest exclusion limits for such a model from multiple dark matter searches at the ATLAS experiment [19].

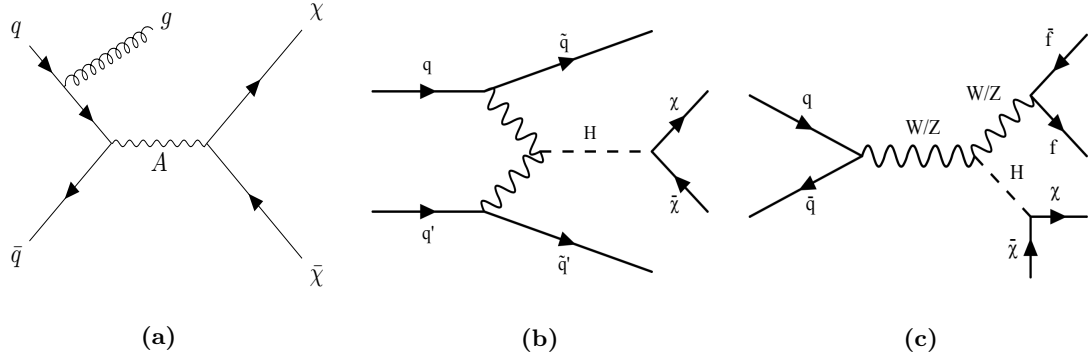


Figure 1.3 Feynman diagrams for the (a) production of a dark matter mediator, A , and dark matter particles, χ , through the s-channel, (b) production of dark matter particles through the decay of a VBF Higgs, (c) production of dark matter particles through VH associated production [20].

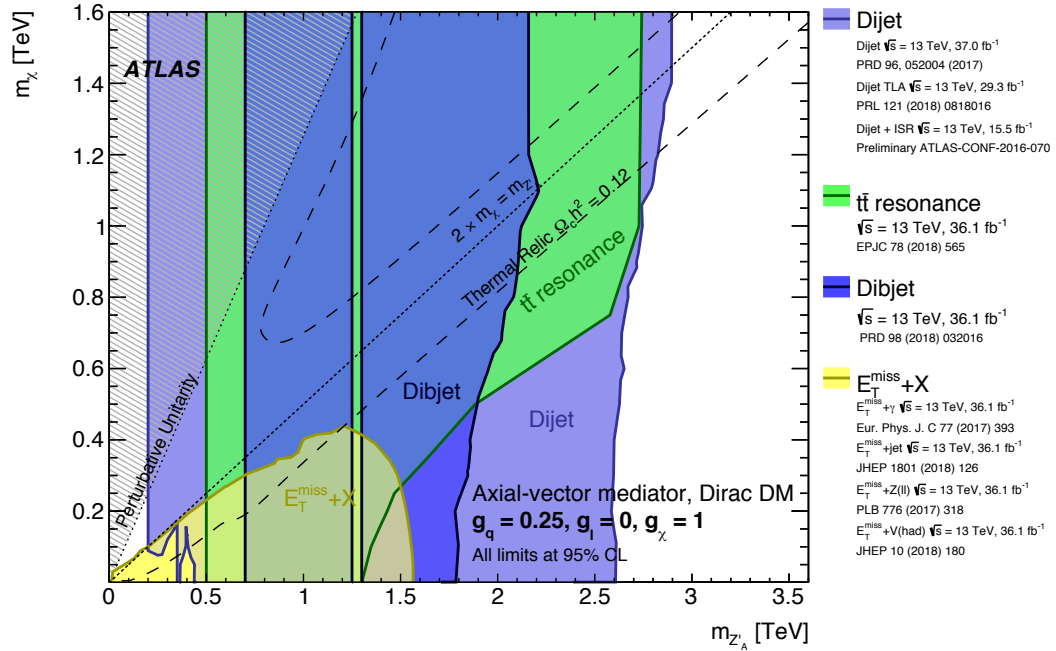


Figure 1.4 Regions in a mediator mass-dark matter mass plane excluded at 95% CL by visible and invisible searches at the ATLAS experiment, for an axial-vector mediator simplified model with couplings $g_\chi = 1$ and $g_q = 0.25$ [19].

Invisible Higgs decay models

Another scenario explored in collider searches is the one where the Higgs boson decays invisible to dark matter particles. In the SM the Higgs boson can decay invisibly only by first decaying to two Z bosons that subsequently decay to neutrinos. The branching fraction of $H \rightarrow ZZ \rightarrow \nu\bar{\nu}\nu\bar{\nu}$ is approximately $\sim 0.1\%$ which is too small for searches at the LHC to be sensitive to. The observation of a larger branching fraction than this would suggest that the Higgs couples to dark matter particles, acting as a portal between the SM and the dark sector.

The Lagrangian terms describing the mass term of a scalar dark matter particle and its coupling to the Higgs are given by

$$\mathcal{L}_{A-V} \supset \frac{1}{2}\mu^2\chi^2 + \frac{1}{2}g_{H-\chi}\chi^2|H|^2 \quad (1.14)$$

where $g_{H-\chi}$ is the coupling of the Higgs to the dark matter particle. Other models exist that predict the existence of fermionic dark matter particles which couple to a new scalar mediator mixing with the Higgs. The production mechanism most sensitive to the Higgs invisible decay is the one where the Higgs is produced through the vector boson fusion (VBF) mechanism due the distinctive signature of the VBF process. The associated vector boson-Higgs (VH) production mode is also explored in this work, where the Higgs decays to invisible particles and the vector boson decays to quarks. Feynman diagrams for both of these production mechanisms are shown in Figure 1.3.

Chapter 2

Experimental Setup

The data presented in this thesis were collected by the ATLAS detector which records and measures the properties of particles produced in high energy proton-proton collisions. This chapter describes the experimental apparatus and analysis techniques involved in obtaining these data and reconstructing the observed particles. Section 2.1 describes the experimental setup of the Large Hadron Collider which provides the proton-proton collisions. Section 2.2 discusses the ATLAS detector and its main components. The techniques and software algorithms involved in reconstructing various physics objects are discussed in Section 2.3.

2.1 The Large Hadron Collider

The Large Hadron Collider (LHC) [21] is the world's largest and most powerful particle accelerator. Located at the European Organization for Nuclear Research (CERN) in Geneva, Switzerland, it is a circular accelerator built in a tunnel 100 m underground, accelerating beams of protons in opposite directions in a 27 km circumference ring before colliding them at different interaction points. The LHC is designed to collide protons at a centre-of-mass energy of $\sqrt{s} = 14 \text{ TeV}^1$, though it has only been operating at energies of up to $\sqrt{s} = 13 \text{ TeV}$ so far. It

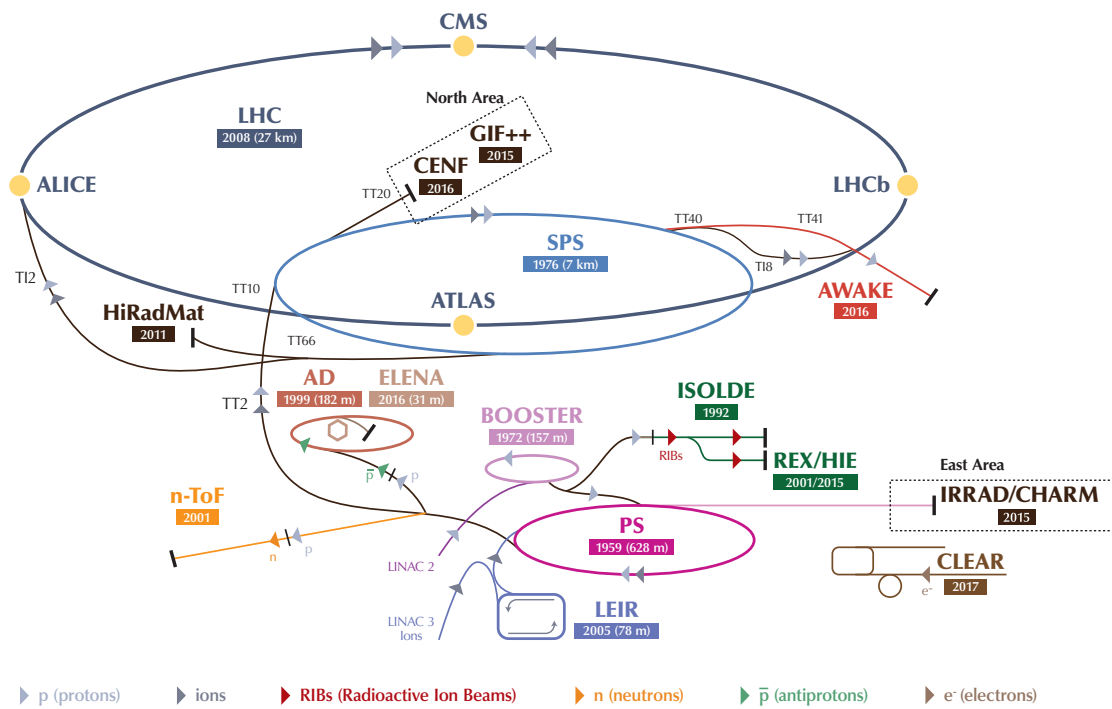
¹This thesis uses the natural units system where \hbar , the reduced Planck constant and c , the speed of light are both equal to unity. Energy, momentum and mass are all expressed in units of eV.

is currently in its second long shutdown, having completed Run-1 and Run-2, to allow for the accelerator complex to be upgraded, in preparations for Run-3.

The energy of the proton beam is increased incrementally using a system of sub-accelerators shown in Figure 2.1 [22], until it has the required energy of 450 GeV [23, 24] to enter the LHC ring. The procedure begins by ionising hydrogen atoms and stripping them of their electrons using an electric field, producing protons. The first accelerator in the chain, *LINAC 2*, accelerates these protons to 50 MeV. The protons are then accelerated to 1.4 GeV using the *Proton Synchrotron Booster* and further accelerated to 25 GeV by the *Proton Synchrotron*. At this point, the protons are already travelling at $\sim 99.9\%$ of the speed of light. The proton beam is then passed on to the 7 km long *Super Proton Synchrotron*, where its energy is increased still further to 450 GeV. At this stage, the proton beam is split into the two beam pipes of the LHC, with one part circulating clockwise and the other circulating anti-clockwise. The two beams spend ~ 20 minutes circulating the 27 km long LHC ring, reaching their final energy of 6.5 TeV ($\sim 99.999999\%$ of the speed of light). The beams are accelerated using a series of superconducting radiofrequency cavities and they are bent into their circular orbit by superconducting dipole magnets. Higher order multipole magnets are used to focus the beams.

The protons in the beams are grouped into bunches, with each beam containing up to 2808 bunches, and with each bunch containing up to 1.1×10^{11} protons. Bunch crossings occur every 25 ns at the interaction points.

There are four main independent physics experiments situated around the LHC ring; ATLAS (A Toroidal LHC ApparatuS) [25], CMS (Compact Muon Solenoid) [26], LHCb (LHC beauty) [27] and ALICE (A Large Ion Collider Experiment) [28]. ATLAS and CMS are general-purpose detectors with a varied physics program, conducting precision measurements of SM and searching for BSM physics. LHCb specialises in heavy flavour physics while ALICE investigates heavy-ion collisions.



LHC - Large Hadron Collider // SPS - Super Proton Synchrotron // PS - Proton Synchrotron // AD - Antiproton Decelerator // CLEAR - CERN Linear Electron Accelerator for Research // AWAKE - Advanced WAKEfield Experiment // ISOLDE - Isotope Separator OnLine // REX/HIE - Radioactive Experiment/High Intensity and Energy ISOLDE // LEIR - Low Energy Ion Ring // LINAC - LInear ACcelerator // n-ToF - Neutrons Time Of Flight // HiRadMat - High-Radiation to Materials // CHARM - Cern High energy AcceleRator Mixed field facility // IRRAD - proton IRRADIation facility // GIF++ - Gamma Irradiation Facility // CENF - CERN Neutrino platForm

Figure 2.1 The CERN accelerator complex in 2018 [22].

Luminosity

The instantaneous luminosity \mathcal{L} , is a measure of the rate at which the LHC delivers collisions and is given by

$$\mathcal{L} = n_b f_r \frac{n_1 n_2}{2\pi \Sigma_x \Sigma_y} \quad (2.1)$$

where n_b is the number of bunches, f_r is the LHC revolution frequency, n_1 and n_2 are the number of protons per bunch in each beam and Σ_x and Σ_y are the mean beam width in the x and y direction. To determine Σ_x and Σ_y dedicated beam-separation scans are conducted, also known as van der Meer scans [29]. \mathcal{L} is measured in units of inverse cross-section per time. The time integral of the instantaneous luminosity $L = \int \mathcal{L} dt$ over a data-taking period is known as the total integrated luminosity and is a measure of how much data has been collected. The number of delivered events can then be given by

$$N = \sigma L = \sigma \int \mathcal{L} dt \quad (2.2)$$

where σ is the total proton-proton inelastic cross-section.

For the Run-2 data-taking period between 2015 and 2018, the LHC has been colliding protons at a centre-of-mass energy of $\sqrt{s} = 13$ TeV, delivering 156 fb^{-1} of integrated luminosity. Figure 2.2 shows the luminosity delivered by the LHC and recorded by the ATLAS detector, as well as the fraction of the dataset that was certified by ATLAS as having good quality for physics analyses, over the whole Run-2 period. The difference in delivered, recorded and good for physics luminosity comes from inefficiencies of the data acquisition system, and from the detector only collecting data during high-quality beam conditions and only when all detector components are in good quality.

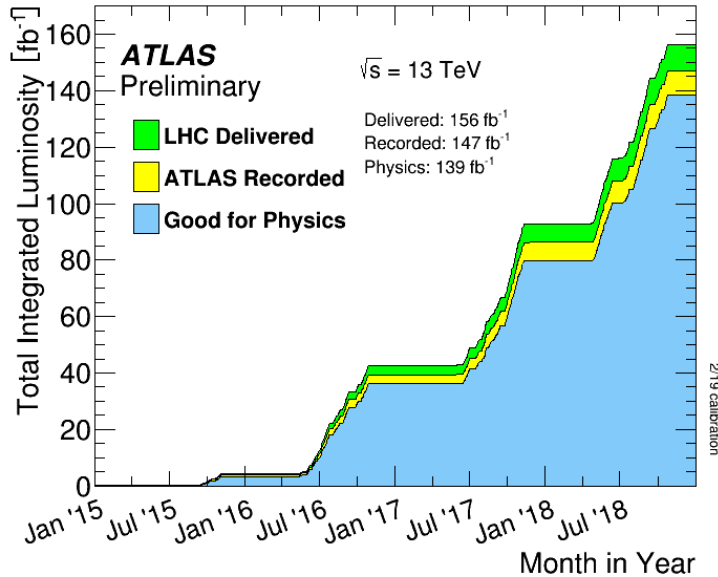


Figure 2.2 Delivered, recorded and good for physics integrated luminosity from the LHC and ATLAS [30].

2.2 The ATLAS detector

The ATLAS detector [25] is one of the main physics detectors at CERN, used by the ATLAS collaboration to collect data from the proton-proton collisions provided by the LHC. It has a cylindrical geometry, with the collisions taking place at the centre of the detector (also known as the interaction point). The detector is comprised of several components and subsystems, built symmetrically around the proton beampipe, as shown in Figure 2.3. The subsystems are designed to measure and identify properties of the outgoing particles and their combined information is used to reconstruct the full underlying physics event. A brief description of the detector’s coordinate system and of each subsystem is given below.

2.2.1 ATLAS coordinate system

The coordinate system used by ATLAS is a right-handed Cartesian system, with the origin at the interaction point at the centre of the detector. The z -axis is defined along the beampipe, the positive x -axis is defined as pointing from the origin to the centre of the LHC ring and the

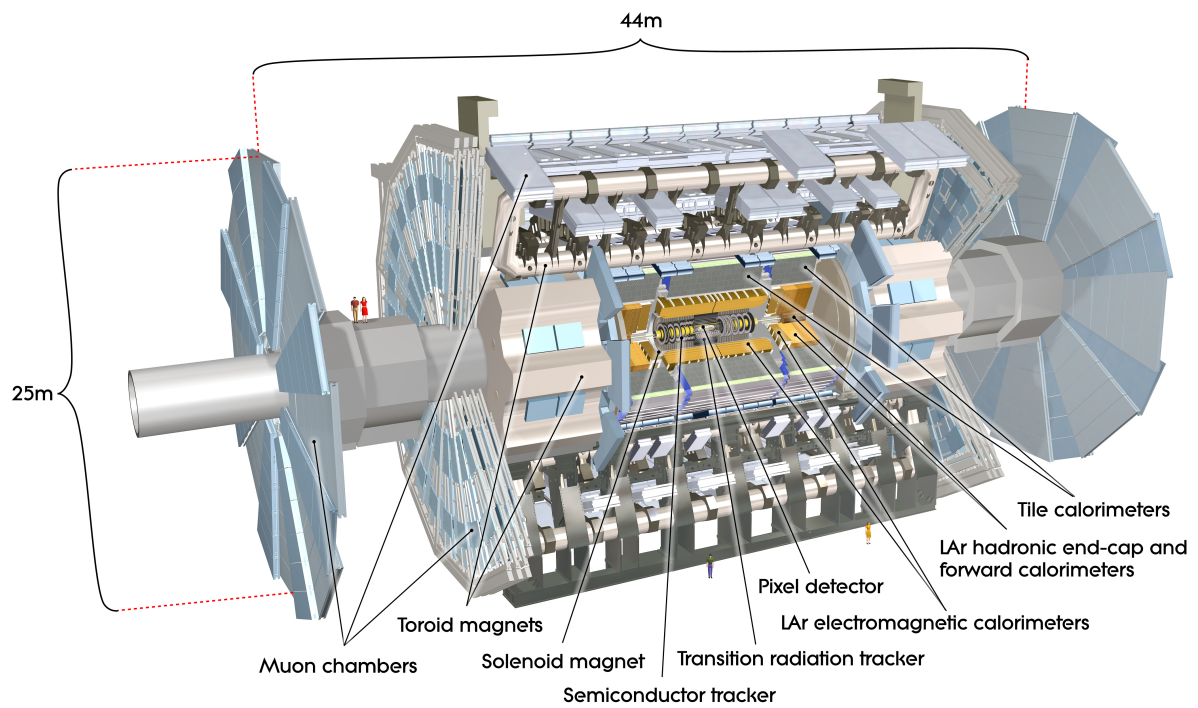


Figure 2.3 Schematic of the ATLAS detector highlighting major components within it [31].

positive y -axis is defined as pointing away from the the centre of the earth. The $x - y$ plane is referred to as the transverse plane and it is widely used in physics analyses. The azimuthal angle ϕ is defined in the transverse plane, starting from the x -axis and rotating around the beam pipe, while the polar angle θ is defined as the angle from the z -axis. A particle's energy is denoted by E and its invariant mass is denoted by m . An object's momentum is expressed as

$$\mathbf{p} = (p_x, p_y, p_z), \quad (2.3)$$

where p_x , p_y and p_z is the momentum in the x , y and z directions.

The pseudorapidity η is a useful transformation of the polar angle θ that is frequently used in particle physics and is defined as

$$\eta = -\log \left(\tan \left(\frac{\theta}{2} \right) \right). \quad (2.4)$$

In the relativistic particle limit where $m \approx 0$, the pseudorapidity is equivalent to the rapidity y , with

$$y = \frac{1}{2} \log \left(\frac{E + p_z}{E - p_z} \right). \quad (2.5)$$

As the form of Equation 2.4 shows, for a particle travelling along the beampipe the rapidity tends to infinity, $\eta \rightarrow \infty$, while for a particle travelling perpendicular to the beampipe $\eta = 0$. It is useful to define the projection of a particle's momentum and energy on the transverse plane, with the transverse momentum defined as $p_T = |\mathbf{p}| \sin(\theta)$ and the transverse energy defined as $E_T = E \sin(\theta)$. The $\phi - \eta$ space is used do define distances between objects in the detector, with

$$\Delta R = \sqrt{\Delta\phi^2 + \Delta\eta^2}. \quad (2.6)$$

2.2.2 Inner Detector

The Inner Detector (ID) is the innermost subsystem of the ATLAS detector and the one closest to the interaction point. It provides precise position and momentum measurements of charged particles by reconstructing their tracks using points, or “hits”, along their trajectories. The ID is immersed in a 2 T magnetic field parallel to the beampipe, provided by a solenoid magnet. The magnetic field bends the trajectories of charged particles, forcing them into curved paths. The momentum and charge of a particle is determined by measuring the curvature and bending direction of its path. The ID consists of three main subsections; the silicon pixel detector, the semiconductor tracker (SCT) and the gas based transition radiation tracker (TRT). These subsections are positioned symmetrically around the proton beampipe as shown schematically in Figure 2.4. A relatively new addition to the ID is the Insertable B-Layer (IBL), a silicon pixel layer, designed to improve the overall tracking performance of the ID [32]. Additional SCT and TRT end-cap parts are positioned in the plane perpendicular to the beampipe, with multiple discs on each side of the main barrel section of the ID, to allow for the reconstruction of particle tracks in the high- η space.

The silicon pixel detector provides a coverage of $|\eta| < 2.5$ and consists of three cylindrical pixel layers in the central barrel region and three end-cap discs on each side of the barrel. With 1744 sensor modules, each containing 47232 pixel sensors and each pixel covering $50 \times 400 \mu\text{m}^2$ of the $\phi \times z$ plane, the pixel detector provides a resolution of $10 \mu\text{m}$ in the ϕ direction and $115 \mu\text{m}$ in the z direction in the barrel.²

The SCT provides a coverage of $|\eta| < 2.5$ and contains 15912 silicon microstrip sensors. Surrounding the pixel detector, it is arranged into four layers of silicon microstrip pairs in the barrel region and nine double layers per side in the end-caps. A single measurement in the SCT is reconstructed by combining information from the front and back sides of a microstrip layer. The barrel region of the SCT provides a resolution of $17 \mu\text{m}$ and $580 \mu\text{m}$ in the ϕ and z directions respectively³.

²The dimensions of the pixels and the resolution of the pixel detector in the end-caps are identical, with the z replaced with the R direction.

³As in the pixel detector, the resolution of the SCT in the end-caps is identical to the one in the barrel region, with the z replaced with the R direction.

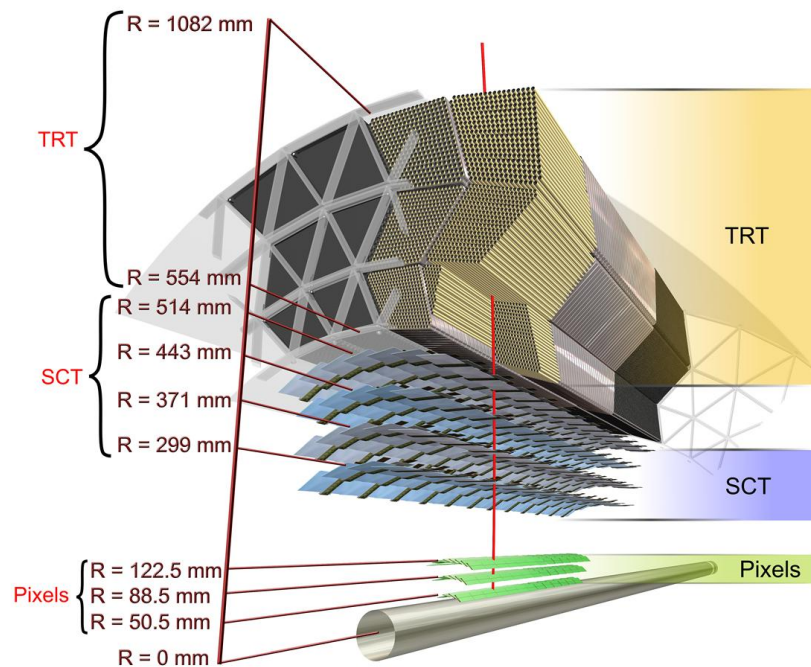


Figure 2.4 Schematic of the ATLAS Inner Detector highlighting major components within it [33].

The outermost subsystem of the ID, the TRT, provides a coverage of $|\eta| < 2.0$. It consists of 4 mm thick polyimide straw tubes, arranged parallel to the beampipe in the barrel and radially in the end-caps. The straw tubes are filled with a Xenon-based gas mixture, which is ionised as charged particles pass through the TRT. With the wall of the tubes kept at a negative voltage and a wire in the middle of each tube acting as central anode, ionised electrons are accelerated towards the anode, producing an electrical signal used for drift-time measurements. The space between the straws is filled with different polymer materials which cause the particles passing through to emit photons (transition radiation) which amplify the signal in the drift tubes. Relativistic particles such as electrons emit much more transition radiation than heavier hadrons when passing through the TRT and so this information is used to help differentiate between the two. The TRT provides a resolution of 130 μm in the ϕ direction, with an average of ~ 35 hits per track.

Information from the entirety of the ID is used to measure the momentum and charge of a particle. The target track momentum resolution σ_{p_T} of the ID, defined as a function of the particle's transverse momentum p_T , is given by

$$\frac{\sigma_{p_T}}{p_T} = 0.05\% \times p_T \oplus 1\% \quad (2.7)$$

2.2.3 Calorimeter system

A system of calorimeters surrounds the ID, providing up to $|\eta| < 4.9$ of coverage. The calorimeters stop particles, absorbing and measuring their energy in the process. The Electromagnetic calorimeter (ECAL) is designed to measure the energy of electrons and protons while the Hadronic calorimeter (HCAL) measures the energy of hadrons. Both of them are sampling calorimeters, meaning they measure only a fraction of a particle's energy and absorb the rest. The full energy is calculated using the measured fraction and a pre-determined calibration. The calorimeters consist of layers of active material and high-density metal (absorbing material). Incoming particles interact with the metal causing a "shower" of secondary charged particles that then ionise the active material, allowing the initial particle's energy to be measured.

The ECAL and HCAL are briefly discussed below, as well as the Forward calorimeter system (FCAL).

Electromagnetic calorimeter

The ECAL uses liquid argon (LAr) as the active material and lead as the absorbing material to measure the energy of photons and electrons⁴. With an accordion geometry, it provides complete coverage in ϕ . The barrel part provides a coverage of $|\eta| < 1.475$ while a pair of end-cap discs on each side of the detector extend the coverage to $1.375 < |\eta| < 2.5$ and $2.5 < |\eta| < 3.2$.

A calorimeter's size is often defined in terms of the absorbing material's radiation length X_0 , which is the distance over which an electron travelling in the material will deposit all but $1/e$ of its energy. The ECAL has a transverse length of more than $22X_0$ in the barrel and more than $24X_0$ in the end caps, enough to fully absorb the energy of a particle shower. The energy resolution of the ECAL is given by

$$\frac{\sigma_E}{E} = \frac{10\%}{\sqrt{E}} \oplus 0.7\% \quad (2.8)$$

Hadronic calorimeter

The HCAL consists of a central barrel with an extended barrel region around the ECAL barrel and two end-cap parts, one on each side of the ECAL end-caps. The central barrel uses steel absorbers and scintillator tiles as the active material while the end-caps use copper as the absorbing material and LAr technology for energy measurements. As in the ECAL, the HCAL's depth can be defined in terms of λ , which is the distance over which a hadron travelling in the HCAL will deposit all but $1/e$ of its energy. The central barrel region consists of three layers with depths of 1.5λ , 4.1λ and 1.8λ and a coverage of $|\eta| < 1.7$ ⁵. The end-cap discs extend the

⁴Muons interact with the calorimeter system minimally due to their larger mass which reduces the effect of bremsstrahlung.

⁵The three layers in the extended barrel region have depths 1.5λ , 2.6λ and 3.3λ .

coverage to $|\eta| < 3.2$, with a 12λ depth. The energy resolution of the HCAL is given by

$$\frac{\sigma_E}{E} = \frac{50\%}{\sqrt{E}} \oplus 3\% \quad (2.9)$$

Forward calorimeter

The FCAL is a combined electromagnetic and hadronic calorimeter system, using LAr as the active material. It has three layers of absorbing material; a copper layer for absorbing EM showers and two tungsten layers for hadronic showers. The FCAL has a depth of 10λ and extends the coverage of the calorimeter system to the range $3.1 < |\eta| < 4.9$. The energy resolution of the FCAL is given by

$$\frac{\sigma_E}{E} = \frac{100\%}{\sqrt{E}} \oplus 10\% \quad (2.10)$$

2.2.4 Muon spectrometer

The muon spectrometer (MS) is the outermost part of the ATLAS detector, designed to measure the paths of muons. It is immersed in a non-homogeneous magnetic field, ranging from 0.2 TeV to 3.5 TeV, produced by a series of toroidal magnets. A muon's momentum is calculated using the bending of its path as the muon travels through the magnetic field. The MS consists of a central barrel part and two end-cap regions, together covering $|\eta| < 2.7$. Monitored drift tubes are used for precision tracking over the full MS coverage with a position resolution of $35 \mu\text{m}$ in the axial plane. Cathode strip chambers are also used in the $2.0 < |\eta| < 2.7$ range with a resolution of $40 \mu\text{m}$ in the radial plane.

For the muon triggers system, resistive plate chambers are used in the range $|\eta| < 1.05$ and thin gap chambers in the end-caps are used in the region $1.05 < |\eta| < 2.4$. With a timing resolution of a few nano-seconds, the muon trigger system can also be used for bunch crossing association.

2.2.5 Trigger system

The LHC collides proton beams at the centre of the ATLAS detector every 25 ns. This is equivalent to a bunch crossing rate, or “event” rate, of about 40 MHz, too high for the ATLAS detector to record due to the detector’s readout capability and bandwidth and storage limitations⁶. A trigger system is thus used in ATLAS in order to identify and only record events of interest, bringing the event rate down to 1 kHz. These events of interest are usually events containing high- p_T leptons, photons and jets or events with large missing transverse momentum. The trigger system is split into two levels; the Level 1 trigger (L1), a hardware based trigger and the High Level Trigger (HLT), a software based trigger [34].

The L1 trigger uses information from the calorimeters and the muon spectrometer to identify Regions of Interest (RoIs) in the detector, where signatures of high- p_T objects have been detected. Only considering events satisfying these criteria reduces the event rate from 40 MHz to about 100 KHz. The RoIs are then passed on to the HLT for further processing.

The HLT uses software procedures to further identify events of interest, reducing the event rate to about 1 kHz, low enough for recording. With information from the RoIs, it applies online analysis techniques on only parts of the detector, reducing the amount of data transferred to the readout system. Offline algorithms are then used to fully reconstruct an event⁷.

Multiple triggers are in use in ATLAS, each one reflecting different physics goals and optimised to identify distinct final states of particles in the detector. This list of triggers defines the ATLAS “trigger menu”. Since the total rate of events available for readout is limited to below 1 kHz, triggers can be “prescaled”, meaning that only a fraction of events satisfying the trigger will be recorded. Taking into account detector and LHC conditions, triggers can be disabled or have the rate of events passing their selection reduced or increased. Primary triggers identifying events for physics analysis are usually kept unprescaled, allowing for all of the events satisfying them to be recorded, while support triggers used for detector monitoring and calibration are usually assigned a small prescaled bandwidth.

⁶Each recorded event requires ~1.5 MB of memory.

⁷Online algorithms refer to software used for triggering and data acquisition (DAQ). Offline algorithms refer to software used on the recorded data.

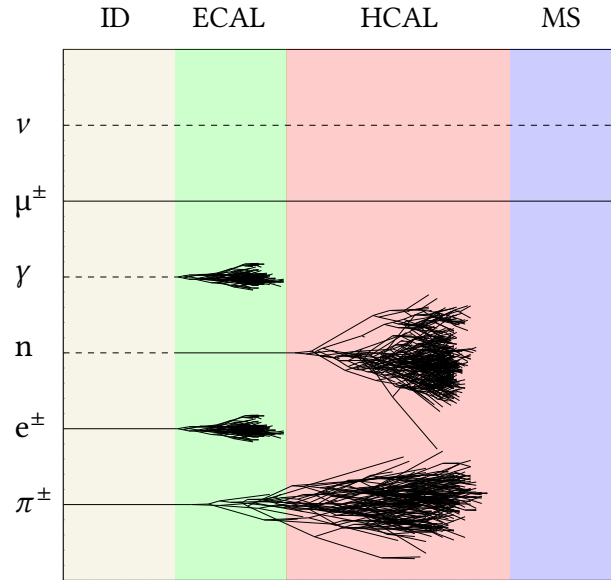


Figure 2.5 Signatures of different particles in the detector’s subsystems. Solid lines represent energy deposits while dashed lines represent no energy deposits [35].

2.3 Object reconstruction and identification

Objects in the detector, such as leptons, photons and hadronic jets, are reconstructed using and combining the signals recorded from each subsystem. Figure 2.5 [35] shows the signatures different particles leave in the sub-detectors. This section describes how each particle is reconstructed and identified using those signals.

2.3.1 Tracks

As a particle traverses through the detector, it deposits energy in multiple detector elements. The track of a particle can be reconstructed using information from all the energy deposits, or “hits”, mapping out in this way the path it followed in a 3D space [36].

Three-point hits in the pixel layer or SCT that are consistent with a single track form a track *seed*. Moving away from the interaction point, the track is extended by adding hits from

other subsystems that are compatible with the shape of the initial track seed. Particles can also be produced in secondary interactions, away from the interaction point. For these, track seeds are formed in the TRT and are backwards extended to the SCT and pixel layer using a back-track algorithm.

Ambiguities involving hits that can be associated with more than one track are resolved by ranking tracks based on their momentum, their constituent hits and on how well the hits can be associated to each other. Additional information is used by considering how many expected hits are missing (“holes”) from a track. Tracks are usually required to have a very small number of holes and tracks with less than 7 hits or $p_T < 400$ MeV are discarded.

2.3.2 Primary Vertex reconstruction

Multiple proton-proton collisions take place in each bunch crossing, resulting in tracks in the detector that originate from more than one interaction point or vertex. The reconstructed tracks are used to identify a possible vertex seed and tracks that are not associated with the seed are temporarily removed and the vertex position recalculated. The vertex position is fixed once it passes the required quality criteria. The procedure is repeated with the removed tracks to identify secondary interaction vertices. A vertex is characterised by $\sum_{\text{tracks}} p_T^2$, the sum of the squared transverse momentum of all associated tracks. The vertex with the highest sum is established as the primary vertex and is considered to be the vertex that the hard scattering has originated from.

2.3.3 Jets

Reconstruction and clustering

Jets are common objects resulting from the production of gluons and quarks in pp collisions and are widely used in physics analyses. They are formed by first clustering energy deposits in calorimeter cells to form topological clusters. Each cell is characterised by its energy significance,

σ_c , defined as

$$\sigma_c = \frac{\text{Energy deposited in cell}}{\text{Background noise level in cell}} \quad (2.11)$$

where the background noise level depends on different instrument and beam conditions sources⁸. A topological cluster starts as a cell seed, where the cell is required to have $\sigma_c > 4$. Neighbouring cells are added to the cluster if they satisfy $\sigma_c > 2$. The clustering stops when σ_c falls below 2, with the remaining neighbouring cells being added to the cluster if they satisfy $\sigma_c > 0$.

Jets are reconstructed from topological clusters using the anti- k_t jet clustering algorithm [37]. In the algorithm, the distance between two clusters, as well as the distance between a cluster and the beam, is gauged using the cluster’s transverse momentum, its position in the calorimeter and a jet-radius parameter R , related to the radius of a jet and typically set to $R = 0.4$. Topological clusters that are closer to each other than the beam are combined together and treated as a new cluster. A cluster that is closer to the beam than another cluster is defined as a “jet”. The procedure is repeated until all topological clusters are clustered into jets.

Calibration

The energy of a jet needs to be calibrated to correct for effects such as energy losses in the detector and pile-up. Additionally, the response of the calorimeters to electromagnetic showers is usually higher than their response to hadronic showers, an effect known as non-compensation which needs to be accounted for. Jet calibration is performed with the procedure outlined below [38].

The direction of the jet is corrected so that it points back to the primary vertex. A pile-up correction is then applied using an area-based subtraction process.

A jet energy scale (JES) correction derived from MC simulation is applied to correct the energy of the jet from the electromagnetic scale to the hadronic particle-level scale [39]. This is achieved by matching particle-level and reconstructed jets in simulated events and forming

⁸Electronic noise and pile-up are common background noise sources.

a ratio of the jet's energy at the two levels as a function of the particle-level energy of the jet and the jet's η value. Calibration factors derived from this ratio can then be applied on reconstructed jets in the data to correct their energy and η value back to the hadronic particle-level scale.

Additional corrections are applied to correct for differences in the jet energy response depending on the origin of the jet and the jet energy resolution (JER) [40]. Parton cascades originating from quarks are expected to include less, but more energetic, partons than ones originating from gluons. This results in narrower quark-jet shower shapes and wider gluon-jet shower shapes. The shape of the jet showers and the distribution of the jet's energy in the calorimeter are used in the global sequential calibration (GSC) procedure to identify the origin of a jet.

Finally, in-situ corrections are applied to correct for differences between the data and MC and to correct for differences in the detector response between different η regions [41]. These corrections are derived using Z +jets events for jets with p_T up to 500 GeV and γ +jets events for jets with p_T up to 950 GeV. In both cases, the jets recoil off the well understood decay systems of the γ or Z boson, making these processes ideal for jet calibration. Jets that have been already calibrated using these techniques are used to calibrate jets with $p_T > 950$ GeV in a jet balance technique.

Jet cleaning and pile-up

Jet cleaning refers to the process of rejecting jets that do not originate from the hard scattering. These jets can be traced back to non-collision background, such as cosmic-ray showers produced in the atmosphere, beam induced backgrounds or large scale noise in the calorimeters. Non-collision background jets, also known as fake jets, can be rejected using two sets of jet quality criteria, *LooseBad* and *TightBad* with efficiencies ranging from 99.5% to 99.9% and from 95% to 99.5% respectively, depending on the p_T of the jet [42]. Jets not associated with the hard scattering can also originate from secondary pp interactions (pile-up interactions). These can be rejected using the jet-vertex-tagger (JVT) algorithm [43], which uses the fraction of tracks

coming from the primary vertex and a two-dimensional likelihood to determine the origin of the jets. In the forward region with $|\eta| > 2.5$, the forward JVT (fJVT) algorithm is implemented, which uses timing, shape and topological information to reconstruct the origin of the jets.

2.3.4 Electrons

Similar to jets, electrons are reconstructed from energy clusters in the EM calorimeter with the additional requirement that a candidate electron cluster is associated with a track in the ID. The sliding window algorithm [44] is used to cluster calorimeter cells by combining cells within a window of 3×5 in units of $\Delta\eta \times \Delta\phi = 0.025 \times 0.0245$ ⁹. Clusters are required to have energy deposits in the transverse direction $E_T > 2.5$ GeV to be classified as seed clusters from which an electron will be reconstructed. If no tracks can be associated to a seed cluster, the cluster is discarded. If multiple tracks are matched to the seed cluster, the tracks are ranked based on their spacial separation from the cluster and their number of hits. The highest ranking track is considered to be the electron track.

The electron candidate is required to be prompt, meaning to be associated with the primary vertex. Their compatibility is quantified and ensured by requiring that

$$\frac{|d_0|}{\sigma_{d_0}} < 5 \quad \text{and} \quad |\Delta z_0 \sin \theta| < 0.5 \text{ mm} \quad (2.12)$$

where d_0 is the smallest distance between the primary vertex and the track, σ_{d_0} is the uncertainty on d_0 , Δz_0 is the distance between d_0 and the primary vertex in the z -direction and θ is the polar angle of the track.

Identification and isolation

Fake electrons originating from hadronic showers in the calorimeter mimicking an electron shower can be suppressed using identification algorithms. A likelihood based method uses information on the shape of the EM shower and on the quality of the track to discriminate

⁹This corresponds to the granularity of the second layer of the EM calorimeter.

between real and fake electrons. Three likelihood identification working points can be defined, with increasing fake rejection and decreasing real electron acceptance; *Loose*, *Medium* and *Tight*. All three working points are used for different purposes in this analysis and have an electron identification efficiency of 97%, 95% and 91% respectively and a fake rejection rate of 99.7%, 99.8% and 99.9%. Fake electrons can be further suppressed by requiring electron candidates to pass a list of isolation criteria. Isolation criteria can be based on the sum of the transverse momenta of tracks in a cone around the candidate electron track (track-based) or on the sum of the transverse momenta of EM clusters in a cone around the candidate electron cluster (calorimeter-based). The analysis presented here requires that electrons satisfy the *FCHighPtCaloOnly* isolation WP which requires that the sum of the p_T of energy clusters in the EM calorimeter within $\Delta R < 0.2$ of the candidate electron is less than 3.5 GeV. The WP provides a good background rejection in the high electron p_T region [45] with a fake rejection rate of 90% and a prompt electron selection efficiency of 95%.

2.3.5 Photons

Similar to electrons, photons are reconstructed from energy clusters in the EM calorimeter. As photons are neutral particles they leave no tracks in the ID, making them distinguishable from electrons. It is possible for electrons to produce photons through bremsstrahlung and for photons to convert to pairs of electrons. Information from the EM calorimeter and the tracks present in the ID is used to disentangle these processes and reconstruct the final state particles. A set of photon identification working points is defined based on the properties of the topo-clusters in the EM calorimeter, with varying efficiencies. In this analysis, energy deposits originating from photons are accounted for in the reconstruction of jets and no further photon selection is needed.

2.3.6 Muons

Muons are reconstructed using track information from the MS and the ID. Muon tracks are first reconstructed separately using hits in the MS and the ID. A combined muon track candidate is

is then formed by fitting to matching tracks in the MS and the ID [46]. Muons are required to be prompt by satisfying

$$\frac{|d_0|}{\sigma_{d_0}} < 3 \quad \text{and} \quad |\Delta z_0 \sin \theta| < 0.5 \text{ mm} . \quad (2.13)$$

Identification and isolation

Hadron decays, such as pion and kaon decays, can mimic the presence of a prompt muon. Real but non-prompt muons can also originate from semi-leptonic decays of heavy flavour hadrons or highly energetic hadrons that were not contained in the hadronic calorimeter and left tracks in the MS. Track quality criteria and variables based on the charge and momentum of the muon candidate are used to reject fake and real non-prompt muons. A list of muon identification working points is defined using the above information: *Loose*, *Medium*, *Tight* and *High- p_T* . Muons are further required to pass isolation criteria based on the sum of the transverse momenta of tracks in a cone around the candidate muon track (track-based) or on the sum of transverse momenta of topological clusters in a cone around the muon in the calorimeters. Similar to the isolation of electrons, a list of muon isolation working points can be defined using both track-based and calorimeter-based information, tailored to different physics analysis goals and offering varying rejection and acceptance efficiencies. The analysis presented here uses muons satisfying the *Loose* identification working point with a prompt muon selection efficiency of 98.1% and a non-prompt muon rejection efficiency of 99.2%. Muons are also required to satisfy the *Loose-Track* isolation working point, which uses a running cut on the sum of the p_T of tracks within a varying radius around the selected muon depending on its momentum, in order to ensure a prompt muon selection efficiency of 99%.

2.3.7 τ aus

The tau is the heaviest of the leptons and the only one heavy enough to decay into hadrons. τ aus decay into a W boson and a neutrino where the W boson can then decay leptonically or hadronically. Leptonically decaying taus are reconstructed as electrons or muons in this

analysis. Hadronically decaying taus usually decay into one or three hadrons, each mode known as one-prong and three-prong respectively. They are reconstructed using jets as seeds, which are reconstructed using the anti- k_t algorithm with $R = 0.4$ as described in Section 2.3.3. The tau jet seeds are required to have $p_T > 10$ GeV and $|\eta| < 2.5$ and are calibrated to the hadronic scale by having the Local Hadronic Cell Weighting (LCW) calibration applied on their constituent topo-clusters [47]. The visible energy of the tau lepton is defined by the total energy of the topo-clusters within a cone of $\Delta R < 0.2$. Hadronically decaying taus are distinguished from jets using Boosted Decision Tree (BDT) algorithms and taus that are matched to an electron within a cone of $\Delta R < 0.4$ and a large electron likelihood score are discarded. As with electrons and muons, three tau identification working points are defined (*Loose*, *Medium* and *Tight*), tailored to different analysis goals. The analysis presented here uses taus satisfying the *Loose* identification working point, with a selection efficiency of 85% for one-prong and 75% for three-prong taus.

2.3.8 Missing transverse momentum

The missing transverse momentum, p_T^{miss} , is defined as the vector momentum imbalance in the transverse plane. For the law of conservation of momentum to uphold, the vectorial sum of momenta in the transverse plane should sum to zero. An imbalance of transverse momentum is introduced when invisible particles are produced, such as neutrinos, or due to the limited acceptance of the detector, resulting in a non-zero p_T^{miss} . The p_T^{miss} reconstruction uses energy deposits from the calorimeter and muons reconstructed in the muon spectrometer. Tracks are used to recover momentum from low p_T charged particles which are missed in the calorimeters, and muons reconstructed from the inner detector are used to recover muons in regions not covered by the muon spectrometer. Calorimeter energy deposits are associated with a calibrated high- p_T parent object in a specific order: electrons (e), photons (γ), hadronically decaying τ -leptons (τ), jets and muons (μ). The components of p_T^{miss} in the x and y coordinates are calculated as

$$p_{x(y)}^{\text{miss}} = p_{x(y)}^{\text{miss}, e} + p_{x(y)}^{\text{miss}, \gamma} + p_{x(y)}^{\text{miss}, \tau} + p_{x(y)}^{\text{miss}, \text{jets}} + p_{x(y)}^{\text{miss}, \mu} + p_{x(y)}^{\text{miss}, \text{soft}} \quad (2.14)$$

where each component is defined as the negative vectorial sum of the momenta of the reconstructed objects. The soft term, $p_{x(y)}^{\text{miss, soft}}$, is defined as the vectorial sum of all remaining objects in the detector not passing the selection of the main physics objects¹⁰. The missing transverse momentum is given as a function of its x and y components by

$$p_{\text{T}}^{\text{miss}} = \sqrt{\left(p_x^{\text{miss}}\right)^2 + \left(p_y^{\text{miss}}\right)^2} . \quad (2.15)$$

¹⁰These include low momentum tracks in the ID or energy deposits in the calorimeter not matched to a hard object.

Part II

**Detector-corrected cross-sections in
events with large missing transverse
momentum in association with jets**

Chapter 3

The p_T^{miss} + jets analysis

The physics programme at ATLAS largely involves making measurements of Standard Model (SM) processes and searching for evidence of physics beyond the Standard Model (BSM), with analyses traditionally focusing on one of the two. The analysis presented in the next three chapters does both by performing a measurement of differential cross-sections in regions of phase-space that are largely populated by well-known SM processes but are also expected to be sensitive to BSM physics and more specifically to the production of dark matter particles. Section 3.1 outlines the analysis strategy and Section 3.2 describes and motivates the observables that are being measured. Section 3.3 and Section 3.4 discuss the physics object and event selections at the particle and detector-level respectively. Section 3.5 describes the datasets and MC simulation samples being used for the SM and BSM predictions. Section 3.6 discusses the experimental and theoretical systematic uncertainties and Section 3.7 presents the detector-level results.

3.1 Analysis strategy

Dark matter particles are not expected to interact with the detector's apparatus which makes their detection non-trivial. Instead of aiming to directly observe dark matter, searches at the LHC use p_T^{miss} , the missing transverse momentum in an event, as a proxy for evidence of the production of dark matter and other invisible particles. As discussed in Section 2.3.8, p_T^{miss} is

defined as the negative sum of the transverse momenta of all visible particles in the detector and, in a collision where all the final-state particles are visible, it is equal or close to zero since there is no initial momentum in the transverse plane. The production of invisible particles results in an energy *imbalance* in the transverse plane, assuming that the invisible particles are produced in association with, and recoiling from, other visible objects. Jets are the most common high- p_T objects produced at the LHC and so this analysis presents a measurement of the cross-section of events with large missing transverse momentum in association with jets ($p_T^{\text{miss}} + \text{jets}$). An example Feynman diagram involving the production of dark matter with a $p_T^{\text{miss}} + \text{jets}$ final state is shown in Figure 3.1a.

The production of invisible particles is not restricted to BSM processes and there exist SM processes with a $p_T^{\text{miss}} + \text{jets}$ final state. One such process is the production of a Z boson in association with jets, where the Z boson decays to a pair of neutrinos as seen in the Feynman diagram of Figure 3.1b. Background processes that result in final states indistinguishable from the one being measured are often referred to as “irreducible backgrounds”. A novel approach is taken in this analysis with measurements defined in terms of final-state particles rather than in terms of a particular physical process. Irreducible backgrounds that satisfy the selection requirements of a final state are then treated as part of the signal. In the case of the $p_T^{\text{miss}} + \text{jets}$ final state, in addition to the $Z(\rightarrow \nu\nu)+\text{jets}$ process, large contributions come from the production of a W boson in association with jets, where the W decays to a neutrino and a charged lepton (figure 3.1d). While the definition of the $p_T^{\text{miss}} + \text{jets}$ final state vetoes the presence of charged leptons, leptons can be produced in phase-spaces that are out-of-acceptance of the detector, resulting in a final state identical to the one being measured. Traditionally, such contributions would be treated as backgrounds and subtracted from the measured result. Following the final-state particle measurement definition approach, contributions from $Z(\rightarrow \nu\nu)+\text{jets}$ and out-of-acceptance $W+\text{jets}$ events are both considered part of the SM signal. The reason for treating irreducible backgrounds as part of the signal definition is that it disentangles the modelling of SM backgrounds, known to often be imprecise, from the data measurement. A measurement defined in terms of final-state particles, also known as a *fiducial* measurement, guarantees that the data remain uncontaminated from shortcomings

in current SM theoretical predictions and that future improvements and updates to these predictions can be considered and the published data reinterpreted. An additional *reducible* background originates from QCD multijet production where the mismeasurement of a jet's momentum can lead to a momentum imbalance in the transverse plane of the detector and fake a $p_T^{\text{miss}} + \text{jets}$ event. This background needs to be estimated using data-driven techniques since the MC has been shown to perform poorly in modelling multijet events.

In the absence of new physics, the cross-section of events in the $p_T^{\text{miss}} + \text{jets}$ region will correspond to the cross-section of SM events with a $p_T^{\text{miss}} + \text{jets}$ final state and the region will be mainly populated by events with invisibly decaying Z bosons and out-of-acceptance W bosons. This motivates the measurement of four regions containing charged leptons and targeting final states that have SM contributions similar to the ones in the $p_T^{\text{miss}} + \text{jets}$ region. The lepton regions are used to constrain the systematic uncertainties in the $p_T^{\text{miss}} + \text{jets}$ region coming from detector effects and from theoretical modelling. Additionally, the lepton regions can be used to search for, and place limits on, new physics models with final states involving leptons. The lepton regions are grouped based on the number of leptons they target and are listed below.

- **$2\mu + \text{jets}$ and $2e + \text{jets}$:** These predominantly contain $Z(\rightarrow \mu\mu)+\text{jets}$ and $Z(\rightarrow ee)+\text{jets}$ events respectively which are very similar to the dominant $Z(\rightarrow \nu\nu)+\text{jets}$ process in the $p_T^{\text{miss}} + \text{jets}$ final state, making them ideal for constraining theoretical uncertainties in this region. An example feynman diagram of this final state is presented in Figure 3.1c.
- **$1\mu + \text{jets}$ and $1e + \text{jets}$:** These predominantly contain $W(\rightarrow \mu\nu)+\text{jets}$ and $W(\rightarrow e\nu)+\text{jets}$ events and exploit the similarities of events containing W and Z bosons at the LHC to constrain the $Z(\rightarrow \nu\nu)+\text{jets}$ process in the $p_T^{\text{miss}} + \text{jets}$ region. An example feynman diagram of this final state is presented in Figure 3.1d. These lepton regions benefit from the relatively large cross-section of the $W+\text{jets}$ process (almost 10 times larger than that of $Z+\text{jets}$) leading to increased statistical precision. They also benefit from reduced systematic uncertainties associated with lepton efficiencies since the final state contains only one lepton. While the theoretical uncertainties between the $1\ell +$

jets and the $p_T^{\text{miss}} + \text{jets}$ final states are not as correlated as in the case of the $2\ell + \text{jets}$ final states, these lepton regions are still useful for constraining contributions from both $Z(\rightarrow \nu\nu)+\text{jets}$ and $W(\rightarrow \ell\nu)+\text{jets}$ events with out-of-acceptance leptons in the $p_T^{\text{miss}} + \text{jets}$ region.

The final state leptons in each lepton region are *marked invisible*, meaning that they are not included in the negative vector sum of the p_T^{miss} calculation set out in Equation 2.14. This results in a new observable known as “pseudo- p_T^{miss} ” which in the lepton regions acts as a proxy for the p_T of the boson producing the leptons, in the same way that real p_T^{miss} acts as a proxy for the p_T of the invisibly decaying boson in the $p_T^{\text{miss}} + \text{jets}$ region. All regions can then be easily compared to each other.

Three different phase-spaces are considered in this work. The phase-spaces aim to be sensitive to different dark matter production mechanisms and are defined by the jet kinematics of the event as described below. They are further discussed in Section 3.2 and Section 3.3.

1. **≥ 1 jet:** aims to be as inclusive as possible, requiring only the presence of at least one high- p_T jet. This is similar to the *monojet* signature, used by other popular dark matter searches, which requires the presence of a single energetic jet. An example Feynman diagram showing the production of dark matter in association with an initial state radiation gluon is shown in Figure 3.1a where the phase-space takes advantage of the strong coupling of the gluon to the initial state quark.
2. **≥ 2 jet:** requires the presence of at least two high- p_T jets so that two-jet variables can be measured. This phase-space is also sensitive to the associated vector boson-Higgs (VH) production, shown in the Feynman diagram of Figure 3.1f, where the Higgs decays invisibly and the vector boson decays hadronically.
3. **VBF:** requires the presence of at least two high- p_T jets and has additional selection requirements on the jet system aiming to enhance sensitivity to VBF processes. The phase-space aims to be sensitive to dark matter models where new mediator particles do not couple directly to quarks, as seen in the Feynman diagram of Figure 3.1e. It is also sensitive to the invisible decay of a VBF produced Higgs boson.

Each region is measured differentially and double-differentially with respect to a number of variables that are appropriate to the phase-space being considered. These variables are discussed in detail in Section 3.2. Measuring distributions differentially allows for the shape information of each variable to be exploited, increasing the sensitivity of the measurement to BSM physics. The differential distributions are then corrected for detector effects and the measurements are presented as particle-level differential cross-sections, in a process known as *unfolding*. Presenting a measurement in terms of particle-level objects allows it to be easily and directly comparable to particle-level predictions. The measurements can then be rapidly compared to BSM simulations without the need to simulate the ATLAS detector, making them optimally useful long into the future and available for quick reinterpretation studies. The unfolding technique used in this work is the *Iterative Bayesian Unfolding* method and it is discussed further in chapter 4.

This analysis extends the work done in [48], an analysis with similar goals and set-up that was performed using 3.2 fb^{-1} of 13 TeV data. In that analysis only the $2\mu + \text{jets}$ and $2e + \text{jets}$ lepton regions were considered, with both of the regions suffering from large statistical uncertainties. Furthermore, only single-differential distributions were measured and only of the ratio of the $p_T^{\text{miss}} + \text{jets}$ region and the lepton regions. The ratio is again measured here, in addition to measuring each region separately. The measurements of the individual cross-sections of each region are useful for constraining new physics models that contribute to the lepton regions as well as the $p_T^{\text{miss}} + \text{jets}$ region. In the absence of BSM physics, the individual measurements also allow mismodelling of the SM to be probed. The ratio of cross-sections is defined as

$$R^{\text{miss}} = \frac{\sigma_{\text{fid}}(p_T^{\text{miss}} + \text{jets})}{\sigma_{\text{fid}}(\text{X} + \text{jets})} \quad (3.1)$$

where the numerator is the fiducial cross-section of the $p_T^{\text{miss}} + \text{jets}$ final state and the denominator can be the fiducial cross-section of any of the lepton regions. This way the unobserved system that produces the p_T^{miss} in the numerator is replaced with a similarly produced observed one-lepton or two-lepton system in the denominator (with the leptons marked invisible in

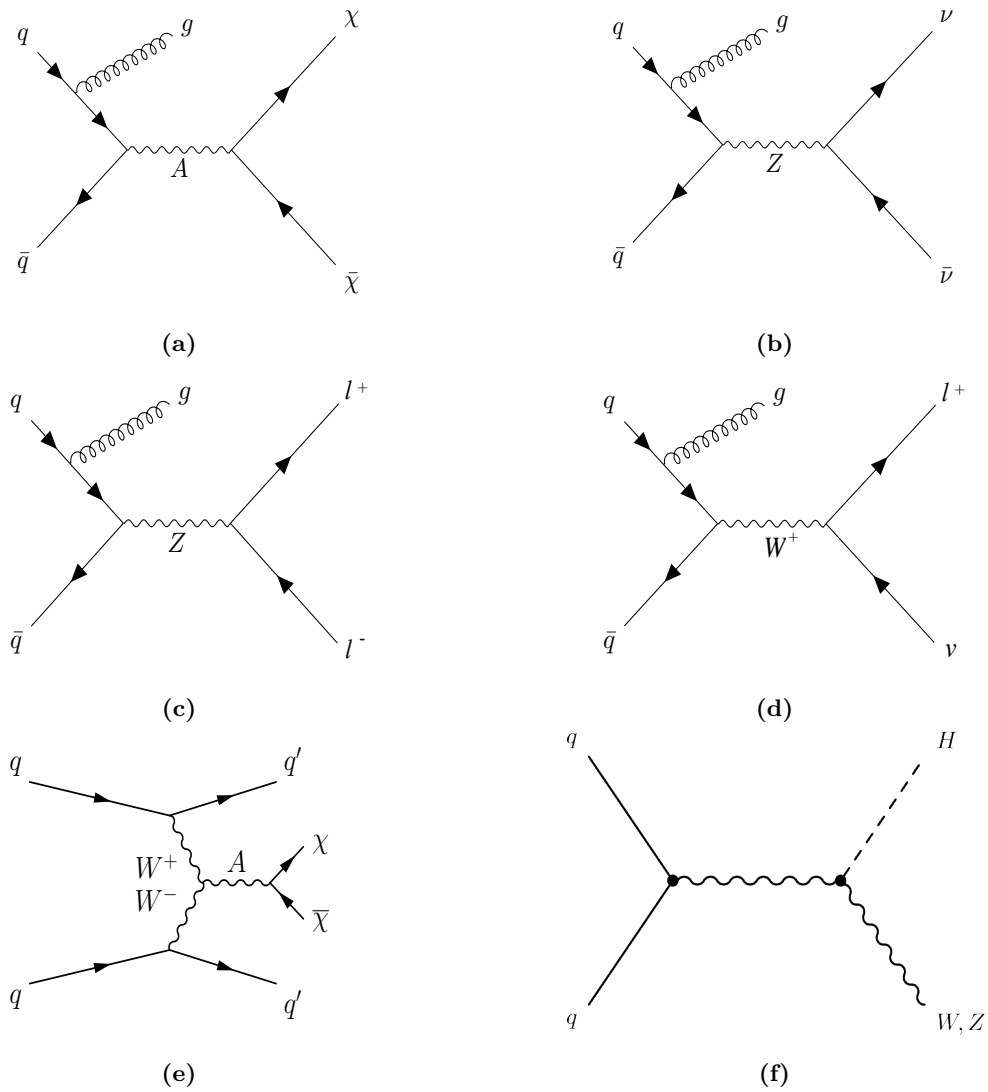


Figure 3.1 Feynman diagrams for the (a) production of a dark matter mediator, A , and dark matter particles, χ , with a monojet signature, (b) invisible decay of the Z boson, (c) leptonic decay of the Z boson, (d) leptonic decay of the W boson, (e) production of dark matter particles through the VBF process, (f) VH associated production.

the calculation of p_T^{miss} after being selected). The similarity of the two processes significantly reduces the theoretical uncertainties in the ratio measurement since any mismodelling of the physics processes will affect the numerator and denominators in a similar way. Furthermore, by requiring that the jet systems in both the numerator and denominators satisfy very similar selection criteria, the systematic uncertainties originating from various calibration procedures involving the jet system are also reduced. As with the individual cross-section measurements of each region, the ratio is measured differentially with respect to various particle-level observables¹ that are discussed in the next section. The presence of new physics in the numerator would lead to a discrepancy between the measured ratio and the one predicted by the SM.

3.2 Measured variables

Each region is measured differentially and double-differentially with respect to various observables. The choice of observables and phase-spaces together are designed to maximize the sensitivity of the measurement to differing dark matter production models. The variables chosen to be measured in each phase-space are listed and motivated below.

≥ 1 jet phase-space

The production of dark matter would lead to an excess of events with missing transverse momentum and so cross-sections in the ≥ 1 jet phase-space are measured as a function of p_T^{miss} (or pseudo- p_T^{miss} if in a lepton region). Many BSM models often involve higher energy scales and larger mediator masses than those in the SM, resulting in a harder p_T^{miss} spectrum. The p_T^{miss} distribution is then expected to have increased sensitivity to new physics in the higher p_T^{miss} range. In addition to the p_T^{miss} distribution, a double-differential measurement is also performed where the p_T^{miss} spectrum is measured as a function of the p_T of the leading jet of the event, $p_T^{j_1}$. The p_T^{miss} vs $p_T^{j_1}$ distribution would help differentiate between similar dark matter production models with different jet topologies, should a signal be observed. For example, in an event where a dark matter mediator is produced recoiling off a single jet then p_T^{miss} and $p_T^{j_1}$

¹When referring to the variables being measured, ‘variables’ and ‘observables’ will be used interchangeably.

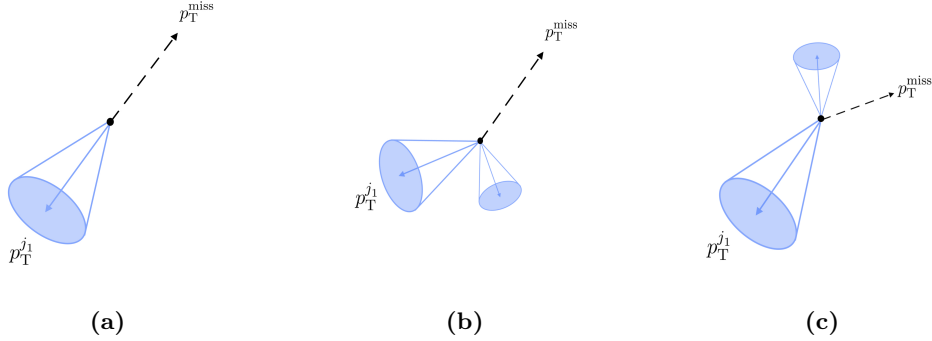


Figure 3.2 (a) Production of p_T^{miss} recoiling off a single jet, (b) production of p_T^{miss} with additional jets in the same direction as $p_T^{j_1}$, (c) production of p_T^{miss} with additional jets in the opposite direction as $p_T^{j_1}$.

will be similar, as seen in figure 3.2a. If, however, the mediator is produced with additional jets in the same direction as $p_T^{j_1}$, $p_T^{j_1}$ will be smaller than p_T^{miss} (figure 3.2b). In the same way, if a mediator is produced with additional jets in the opposite direction as $p_T^{j_1}$ then $p_T^{j_1}$ will be larger than p_T^{miss} (figure 3.2c). The p_T^{miss} vs $p_T^{j_1}$ distribution has the capability of discriminating between the two cases.

≥ 2 jet phase-space

For similar reasons to the ones outlined above, cross-sections in the ≥ 2 jet phase-space are measured again as a function of p_T^{miss} . By requiring the presence of at least two high- p_T jets, the ≥ 2 jet phase-space has the potential to probe hadronically decaying vector bosons in association with p_T^{miss} . One such process is the associated vector boson-Higgs (VH) production where the Higgs boson decays invisibly producing a large p_T^{miss} and the vector boson decays into two quark jets. The dijet system from the hadronic decay of the vector boson can be used to probe $V + p_T^{\text{miss}}$ events and so cross-sections in this phase-space are also measured as a function of the invariant dijet mass, m_{jj} , and the difference between the azimuthal angle of the two jets, $\Delta\phi_{jj}$. The m_{jj} distribution includes a dedicated bin centred on the midpoint of the W and Z boson mass resonance, specifically designed to probe the VH channel, and extends into higher m_{jj} values so that it can be sensitive to possible dark matter production models with a higher m_{jj} signature. The azimuthal correlation between the two leading jets often

depends on the spin of the dark matter mediator and so the $\Delta\phi_{jj}$ distribution can further be used to differentiate between new physics models if a signal is observed. In calculating $\Delta\phi_{jj}$, the two jets are first ordered in rapidity and the azimuthal angle of the least forward jet is subtracted from the most forward one². This allows the $\Delta\phi_{jj}$ observable to be additionally sensitive to CP-even and CP-odd models [49]. In events with large m_{jj} , $\Delta\phi_{jj}$ is also shown to be a powerful discriminant between spin-0 s -channel simplified dark matter models. To cover this wide range of possible new physics models, cross-sections in this phase-space are also measured double-differentially as a function of both $\Delta\phi_{jj}$ and m_{jj} , with the lower m_{jj} slices being sensitive to the VH process with the Higgs decaying invisibly and the higher m_{jj} slices sensitive to spin-0 s -channel simplified dark matter models.

VBF phase-space

As in the ≥ 2 jet phase-space, cross-sections in the VBF phase-space are measured differentially as a function of $p_{\text{T}}^{\text{miss}}$, m_{jj} and $\Delta\phi_{jj}$ and double-differentially as a function of $\Delta\phi_{jj}$ vs m_{jj} . The measured variables in this phase space have similar justifications as above but are here motivated by their sensitivity to VBF-like models and processes, such as the production and invisible decay of the Higgs boson through vector-boson fusion. VBF processes lead to a harder m_{jj} spectrum than processes involving the strong production of dijets or a vector boson decaying to two jets and so the tail region of the m_{jj} distribution is expected to be the most sensitive to BSM physics. The double-differential $\Delta\phi_{jj}$ vs m_{jj} distribution is also shown to offer increased sensitivity to the VBF Higgs production.

3.3 Particle-level object and event selection

The object definition and event selection at the particle-level define the fiducial space to which the ATLAS data are corrected. The kinematic criteria that define each of the three phase-spaces are also discussed in more detail in this section, as well as the definition of each region.

²This is often referred to as the *signed* $\Delta\phi$.

3.3.1 Particle-level object selection

Electrons and muons are required to be prompt, in that they do not originate from the decay of a hadron. Dressed leptons are used, meaning that the four-momenta of photons within a cone of $\Delta R < 0.1$ are added to the four-momentum of the lepton. Electrons are required to have $p_T > 7$ GeV and $|\eta| < 2.47$, excluding $1.37 < |\eta| < 1.52$ which corresponds to the crack region at the end of the ECAL barrel. Muons are required to have $p_T > 7$ GeV and $|\eta| < 2.5$.

Only hadronically decaying taus are considered since leptonic decays are included in the selection of electrons and muons. They are also required to be prompt and to have $p_T > 20$ GeV and $|\eta| < 2.47$, excluding again the crack region at $1.37 < |\eta| < 1.52$. Any jets that contain a hadron coming from the decay of a tau are classified as hadronically decaying taus.

Jets are reconstructed using the anti- k_t jet clustering algorithm with a radius parameter of 0.4, which clusters the four-momenta of particle-level objects. All stable final-state particles are used as input to the jet algorithm except neutrinos, other invisible particles and the dressed leptons. Jets are required to have $p_T > 30$ GeV and rapidity $|y| < 4.4$.

The particle-level p_T^{miss} is defined as the magnitude of a vector, which is the negative sum of the transverse components of the momentum of all visible final-state particles within $|\eta| < 4.9$. This excludes muons with $|\eta| > 2.5$ as these contribute only negligibly to the p_T^{miss} , since their contribution is only included via the momentum recorded in the ID. In the lepton regions, final-state leptons are treated as invisible and are not included in the negative vector sum of the p_T^{miss} calculation.

An overlap removal procedure is applied to the particle-level objects to match the one applied at the detector-level. The procedure is performed in five steps. First, jets that are within a cone of $\Delta R < 0.2$ around an electron are removed. Electrons are then removed if they are within a cone of $\Delta R < 0.4$ around a jet. Following that, jets are again removed if they are within a cone of $\Delta R < 0.2$ around a muon and then muons are similarly removed if they are within a cone of $\Delta R < 0.4$ around a jet. The last step removes jets that are within a cone of $\Delta R < 0.2$ around a tau lepton.

3.3.2 Particle-level event selection

As mentioned before, the analysis considers three different phase-spaces that are defined by the jet kinematics of the event and five different regions, defined in terms of the number, flavour and kinematics of the leptons. The selection and kinematic criteria required for jets and leptons in each phase-space and region are described in this section.

Phase-space event selection

Each phase-space provides different sensitivity to different BSM physics models, enhanced by the selection outlined below and summarised in table 3.1.

All three phase-spaces require that events have $p_T^{\text{miss}} > 200$ GeV, motivated by the large p_T^{miss} expected in dark matter production events, the efficiency of the trigger and the existence of large multijet backgrounds in events with p_T^{miss} below this cut. An angular separation between the four leading jets in p_T and the p_T^{miss} vector, $\Delta\phi(\text{jet}_i, p_T^{\text{miss}}) > 0.4$, is also required to match the one applied at the detector-level. The requirement aims to suppress contributions from multijet events, where mismeasured jets can result in fake p_T^{miss} aligned with one of the jets.

In events with at least one jet, the invisibly decaying Z boson or dark matter mediator producing the p_T^{miss} is expected to be largely balanced by the leading jet. This motivates the kinematic cuts defining the ≥ 1 jet phase-space where a high energy leading jet is required in the central $|\eta|$ region of the detector, with $p_T > 120$ GeV and $|\eta| < 2.4$.

The ≥ 2 jet phase-space enables the measurement of two-jet variables by requiring the presence of at least two jets, with $p_T > 110$ GeV for the leading jet and $p_T > 50$ GeV for the sub-leading jet. The asymmetry in the cuts comes from the requirement that at least one of the jets is high- p_T to help suppress contributions from QCD backgrounds. This phase-space has increased sensitivity to BSM models where a hadronically decaying vector boson is produced back-to-back with an invisibly decaying system, resulting in two or more jets balancing the p_T^{miss} .

The VBF phase-space targets events where two vector bosons, initially produced from two jets scattering off each other, fuse to produce a third, invisibly decaying, vector boson. As in the case of the ≥ 2 jet phase-space, the two leading jets balance the invisible system and are required to have $p_T > 80$ GeV and $p_T > 50$ GeV, with the asymmetry in the cuts required for the same reasons as above. The jets are also expected to be produced with a large angular separation which is enforced by the cut on the rapidity between the jets, $|y| > 1$. The cut on the invariant mass of the dijet system, $m_{jj} > 200$ GeV, ensures that the measurement is sensitive to regions of phase-space with high m_{jj} and suppresses contributions from diboson events where one of the bosons decays hadronically. Finally a veto on events with additional jets in the rapidity gap of the two leading jets is applied. It is possible for two incoming quark jets to radiate gluons, which are produced back-to-back with a vector boson through a QCD mechanism, resulting in a signature similar to the VBF one. The in-gap jet veto reduces the background coming from the QCD production of vector bosons and enhances the contributions coming from the colourless exchange involved in the VBF mechanism.

Region event selection

The analysis considers five different regions: the $p_T^{\text{miss}} + \text{jets}$ region and the $1e + \text{jets}$, $1\mu + \text{jets}$, $2e + \text{jets}$ and $2\mu + \text{jets}$ lepton regions. The lepton regions are used to constrain theoretical and systematic uncertainties originating from the detector in the $p_T^{\text{miss}} + \text{jets}$ region and can also serve as dedicated search regions for physics models predicting the production of BSM particles in association with leptons. Regions are also used together to construct R^{miss} . The selection and kinematic criteria for the lepton system in each region are outlined below and summarised in table 3.2.

The $p_T^{\text{miss}} + \text{jets}$ region requires that there are exactly zero leptons present in the final state of an event. Any events containing electrons or muons as defined in Section 3.3.1 are rejected. Events containing hadronically decaying tau leptons are also vetoed.

The $1e + \text{jets}$ and $1\mu + \text{jets}$ lepton regions require exactly one electron (e^+ or e^-) or exactly one muon (μ^+ or μ^-) respectively. Any events containing additional leptons or hadronically

decaying taus are rejected. In the $1e + \text{jets}$ lepton region, electrons are required to have $p_T > 25$ GeV and $|\eta| < 2.47$ (excluding the crack region). In the $1\mu + \text{jets}$ lepton region, muons are required to have $p_T > 7$ GeV and $|\eta| > 2.5$. The higher lepton p_T requirement in the $1e + \text{jets}$ region is due to the fact that trigger scale factors are only available for electrons with $p_T > 25$ GeV. Events containing muons are selected using p_T^{miss} triggers as muons are invisible to the HLT system. This allows for the lower lepton p_T requirement in the $1\mu + \text{jets}$ region and is further discussed in section 3.4.2. The $1e + \text{jets}$ region has an additional real- $p_T^{\text{miss}} > 45$ GeV requirement which is necessary to suppress contributions from multijet events³.

The $2e + \text{jets}$ and $2\mu + \text{jets}$ lepton regions require exactly one pair of opposite-charge, same-flavour leptons (e^+e^- or $\mu^+\mu^-$ respectively). Any events containing additional leptons or hadronically decaying taus are rejected. In both regions the leading lepton is required to have $p_T > 80$ GeV and the sub-leading lepton is required to have $p_T > 7$ GeV. The leading lepton p_T cut is motivated by the fact that the p_T of the lepton needs to be large enough to suppress backgrounds from top-pair events but still less than half of the targeted Z boson p_T (which is at least 200 GeV). Finally, the selected dilepton system is required to have an invariant mass of $66 < m_{\ell\ell} < 116$ GeV, which is a 50 GeV window around the mass of the Z boson. The $m_{\ell\ell}$ is designed to minimise contributions coming from $\gamma^* \rightarrow \ell^+\ell^-$ events and associated interference terms.

3.4 Detector-level object and event selection

The object definition and event selection at the detector-level are outlined in this section, following the object reconstruction, identification and calibration methods described in Section 2.3.

³The real- p_T^{miss} calculation treats leptons as *visible* particles and represents the p_T of actual invisible particles.

	≥ 1 jet	≥ 2 jet	VBF
(Modified) p_T^{miss}	> 200 GeV		
$\Delta\phi(\text{jet}_i, p_T^{\text{miss}})$	> 0.4 , where $i = 1, \dots, 4$ runs over the four highest p_T jets		
lead jet p_T	> 120 GeV	> 110 GeV	> 80 GeV
sub-lead jet p_T	—	> 50 GeV	> 50 GeV
lead jet $ \eta $	< 2.4	< 4.4	< 4.4
sub-lead jet $ y $	—	< 4.4	< 4.4
m_{jj}	—	—	> 200 GeV
$ \Delta y_{jj} $	—	—	> 1
In-gap jets	—	—	None with $p_T > 30$

Table 3.1 Selection cuts defining the ≥ 1 jet, ≥ 2 jet and VBF phase-spaces. These cuts apply to the $p_T^{\text{miss}} + \text{jets}$ and all lepton regions. The in-gap jet veto is applied to jets inbetween the rapidity region of the two-leading jets.

	$p_T^{\text{miss}} + \text{jets}$	$1\ell + \text{jets}$	$2\ell + \text{jets}$
Required leptons	Exactly none	Single e^+, e^-, μ^+ or μ^-	Pair of e^+e^- or $\mu^+\mu^-$
Additional muons	None with $p_T > 7, \eta < 2.5$		
Additional electrons	None with $p_T > 7, 0 < \eta < 1.37$ or $1.52 < \eta < 2.47$		
Hadronic taus	None with $p_T > 20, 0 < \eta < 1.37$ or $1.52 < \eta < 2.47$		
lepton $ \eta $ (muons)	—	$ \eta < 2.5$	
lepton $ \eta $ (electrons)	—	$0 < \eta < 1.37$ or $1.52 < \eta < 2.47$	
leading lepton p_T	—	> 25 GeV for $e, > 7$ GeV for μ	> 80 GeV
sub-leading lepton p_T	—	—	> 7 GeV
di-lepton mass	—	—	$66 < m_{\ell\ell} < 116$ GeV
real- p_T^{miss}	—	> 45 GeV for e only	—

Table 3.2 A summary of the lepton selection cuts defining the lepton-based signal and $p_T^{\text{miss}} + \text{jets}$ and lepton regions. These cuts apply to the ≥ 1 jet, ≥ 2 jet, and VBF regions.

3.4.1 Detector-level object selection

Objects at the detector-level are required to satisfy the same kinematic requirements as the ones at the particle-level outlined in Section 3.3, with some additional requirements described below.

Electrons are required to have *good object quality*, ensuring that all the instruments in the ECAL involved in the electron reconstruction were fully functional during data taking. In this analysis electrons can either be classified as “signal” electrons, meaning that they are selected to satisfy the lepton presence requirements of the $1e + \text{jets}$ or $2e + \text{jets}$ regions, or “base” electrons, meaning that their presence is used to veto the event in an appropriate region. Base electrons are required to satisfy the *Loose* likelihood working point for all regions. Signal electrons in the $2e + \text{jets}$ region are required to satisfy the *Medium* likelihood working point while signal electrons in the $1e + \text{jets}$ region are required to satisfy the *Tight* likelihood working point in order to reduce contributions from multijet events in this region. It is ensured that all electrons originate from the primary vertex by requiring that they satisfy the longitudinal impact parameter and transverse significance requirements outlined in equation 2.12. Finally, electrons are required to satisfy the *FCHighPtCaloOnly* isolation working point which is shown to perform better than other working points in reducing the multijet background in the $1e + \text{jets}$ lepton region. The selection and rejection efficiencies of each working point are given in section 2.3.4.

Muons are required to have type *Combined* or *Segment-tagged*. They must also satisfy the *Loose* identification working point, which offers the highest reconstruction efficiency, and pass a list of *track quality requirements* to suppress backgrounds from fake tracks and muons from hadron decays. Similar to the electron requirements, muons are required to have originated from the primary vertex by satisfying the longitudinal impact parameter and transverse significance requirements outlined in equation 2.13 of Section 2.3.6. Lastly, muons are required to be isolated by satisfying the *LooseTrackOnly* isolation working point. The selection and rejection efficiencies of each working point are given in section 2.3.6.

Hadronically decaying taus are required to have $p_{\text{T}} > 20$ GeV and $|\eta| < 2.47$, excluding the crack region of $1.37 < |\eta| < 1.52$. They must satisfy a set of *Loose* selection criteria, have 1 or 3 associated tracks corresponding to the one-prong and three-prong tau decay mode and have an absolute charge of one. Taus that are matched to an electron within a cone of $\Delta R < 0.4$ and a large electron likelihood score are discarded. Leptonically decaying taus are reconstructed by their electron or muon products and are included in the electron and muon reconstruction.

Jets are reconstructed from topological clusters of calorimeter cells using the anti- k_t algorithm, with a jet radius parameter of $R = 0.4$. They are required to have $p_{\text{T}} > 30$ GeV and $|y| < 4.4$ and are calibrated following the procedure described in Section 2.3.3. All jets are required to satisfy the *Medium* working point of the JVT algorithm, corresponding to a $\text{JVT} > 0.64$ cut. The *Medium* JVT working point is found to be 92% efficient at selecting jets originating from the primary vertex with a 2% fake rate from pile-up jets. Forward jets with $|\eta| > 2.5$ are also required to satisfy the *Tight* operating point of the fJVT algorithm, which selects jets originating from the primary vertex with an efficiency of 79.9% for jets with $20 < p_{\text{T}} < 30$ GeV and an efficiency of 94.6% for jets with $40 < p_{\text{T}} < 50$ GeV.

The missing transverse momentum, $p_{\text{T}}^{\text{miss}}$, is defined as the vector momentum imbalance in the transverse plane, obtained from the negative vector sum of the momenta of all visible particles. At the detector-level the $p_{\text{T}}^{\text{miss}}$ is calculated following the method described in Section 2.3.8, with objects that were reconstructed following the methods outlined in this section used as the input to Equation 2.14. In this analysis, photons are treated as jets in the $p_{\text{T}}^{\text{miss}}$ calculation. As in the particle-level $p_{\text{T}}^{\text{miss}}$, signal leptons in the lepton regions are treated as invisible and are excluded from the negative vector sum of the detector-level $p_{\text{T}}^{\text{miss}}$ calculation. Jets that overlap with a muon and have low track number and a low track p_{T} are assumed to originate from photon bremsstrahlung from the muons and are also marked invisible. This step is equivalent to using dressed leptons in the particle-level definition of $p_{\text{T}}^{\text{miss}}$ in Section 3.3.1.

An identical overlap removal procedure to the one performed at the particle-level and described in section 3.3.1 is also applied to the detector-level objects listed in this section.

3.4.2 Detector-level event selection

The jet and lepton kinematics that define the event selection at the particle-level also define the event selection at the detector-level. The two levels are designed to be as similar as possible to reduce the extrapolation to different topologies in the unfolding procedure. The lepton-based region event selection for events containing single leptons or lepton-pairs at the detector-level follows that given in table 3.2 at particle-level. The same applies for the detector-level definition

of the jet phase-spaces defined in table 3.1. Events are further required to satisfy the additional criteria discussed below.

Event and jet cleaning

Reconstructed events are required to have a primary vertex with at least two associated tracks. The associated tracks are also required to satisfy a list of quality requirements. Events must pass the *Good-Runs List* (GRL) requirement, meaning that only events that occurred during high-quality beam conditions are considered and only if the ATLAS detector was fully operational and in good quality. This ensures that corrupted luminosity blocks are rejected and that only good quality data are considered. If any errors are reported from the SCT or LAr and Tile calorimeters, it is assumed that the ATLAS detector was not in good quality and the events are discarded. Events that were partially reconstructed due to a TTC restart are also discarded.

Events containing any number of bad quality jets are rejected, in a process known as “jet cleaning”. These are jets that are suspected to have originated from non-collision backgrounds or calorimeter noise. The selection is enforced by requiring that all jets pass the *LooseBad* selection working point. Non-collision backgrounds are further reduced by requiring that the leading jet in each event also passes the *TightBad* selection working point which has more stringent criteria than the former one.

Trigger selection

Two types of triggers are used to select the events for this analysis. As the main feature of the $p_T^{\text{miss}} + \text{jets}$ final state is the large amount of missing transverse energy, events in this region are selected using the lowest unrescaled p_T^{miss} trigger in every run period of the years 2015, 2016, 2017 and 2018. The second level of the trigger system, the HLT, does not use information from the muon systems in the calculation of the trigger-level p_T^{miss} . Muons are therefore invisible to the trigger algorithm and events containing muons can be selected using the p_T^{miss} triggers. For this reason, events in the $1\mu + \text{jets}$ and $2\mu + \text{jets}$ regions are selected using the same triggers

as the ones in the $p_{\text{T}}^{\text{miss}} + \text{jets}$ region. Events in the $1e + \text{jets}$ and $2e + \text{jets}$ regions are selected using the lowest unrescaled single electron trigger in every run period of the whole Run-2 data taking period. The triggers used for each region in each year of data taking are summarised in table 3.3.

3.5 Datasets and Monte Carlo simulation

The datasets used in this analysis were collected by the ATLAS experiment during the Run-2 data taking period, in the years 2015, 2016, 2017 and 2018. The complete dataset corresponds to an integrated total luminosity of 139.0 fb^{-1} of proton-proton collisions at a centre-of-mass energy of $\sqrt{s} = 13 \text{ TeV}$ as shown in Figure 2.2 of Section 2.1. Only data that were collected during high quality beam and detector conditions are considered, following the requirements described in section 3.4.2. The uncertainty on the total integrated luminosity is derived from the calibration of the luminosity scale using x - y beam separation scans [29].

Standard Model processes contributing to the fiducial phase-space considered in this analysis are simulated using dedicated Monte Carlo chains known as the ATLAS simulation framework. The simulation chain begins with the event generation, where the matrix element (ME) of a scattering process is calculated at leading order (LO) or next to leading order (NLO) using a dedicated parton density function (PDF) set, which describes the distribution of partons inside the proton. The underlying event, describing low-energy processes resulting from the proton-proton collision additional to the hard scattering process, is also calculated. Secondary particle emissions are evolved in time using a parton shower model which describes both the initial and final state radiation of the event (ISR and FSR). Models of hadronization are then employed, combining free quarks and gluons to form colourless particles. Additional proton-proton collisions in the same bunch crossing (pileup) are overlaid. These additional proton-proton collisions are based on soft QCD processes simulated with PYTHIA 8.186 [50] using the NNPDF2.3LO PDF set [51] and the A3 set of tuned parameters [52] over the original hard-scattering event. Finally, the resulting event is passed through GEANT4 [53, 54] for a full

Region	Trigger requirement
p_T^{miss} + jets, 1μ + jets & 2μ + jets	2015: HLT $p_T^{\text{miss}} > 70$ GeV
	2016: HLT $p_T^{\text{miss}} > 90$ GeV
	2017: HLT $p_T^{\text{miss}} > 110$ GeV
	2018: HLT $p_T^{\text{miss}} > 110$ GeV
$1e$ + jets & $2e$ + jets	2015: <i>Loose</i> electron $p_T > 120$ GeV <i>Medium</i> electron $p_T > 24$ GeV
	2016: <i>Loose</i> electron $p_T > 140$ GeV <i>Medium</i> electron $p_T > 24$ GeV <i>Tight</i> electron $p_T > 24$ GeV
	2017: <i>Loose</i> electron $p_T > 140$ GeV <i>Medium</i> electron $p_T > 60$ GeV <i>Tight</i> electron $p_T > 26$ GeV
	2018: <i>Loose</i> electron $p_T > 140$ GeV <i>Medium</i> electron $p_T > 24$ GeV <i>Tight</i> electron $p_T > 24$ GeV

Table 3.3 A summary of the trigger requirements applied to the p_T^{miss} + jets region and the four lepton-based regions. The p_T^{miss} calculated by the HLT is used to trigger events in the p_T^{miss} + jets and the two muon regions. The p_T of single electrons is used to trigger events in the two electron regions. Different p_T cut-offs are used for electrons satisfying the *Loose*, *Medium* and *Tight* likelihood working points.

simulation of the ATLAS detector and is then reconstructed with the same analysis chain used for the data.

A detailed description of the Monte Carlo samples used in the analysis, along with information on the event generators, parton shower and hadronisation models used to produce them can be found in appendix [A](#).

Monte Carlo event reweighting

Simulated events are often reweighted to correct for various effects. For the simulations used in this analysis pathological large-weight events in the SHERPA samples that can lead to unphysical distributions are removed by setting the event weight to unity if the absolute value of the weight exceeds 100.

The central SHERPA 2.2.1 samples exhibit a difference in the boson p_T spectrum for the electron and muon channels at the level of 5–10%, with lepton universality being restored in the bugfix release 2.2.2. The muon channel is observed to be consistent between the two versions, while the electron channel is not. A reweighting function has been derived from the ratio of centrally produced $Z \rightarrow ee$ -to- $Z \rightarrow \mu\mu$ samples and is used to correct the central SHERPA $Z \rightarrow ee$ samples for this p_T dependence. A similar reweighting function needs to be applied to the central SHERPA $W \rightarrow e\nu$ samples but it is not included in this work. This leads to discrepancies between the $1e + \text{jets}$ and $1\mu + \text{jets}$ regions which are discussed in Section [5.2](#).

The SHERPA $V + \text{jets}$ samples have also been reweighted to approximately account for higher-order electroweak effects. The electroweak corrections are based on a fixed-order calculation at next-to-leading order accuracy in the electroweak coupling, performed in [\[55\]](#). The numerical values from the paper have been made publicly available by the authors and are used in this analysis to reweight the SHERPA $V + \text{jets}$ samples as a function of the inclusive boson transverse momentum.

All events are reweighted using multiple scale factors per lepton, to account for known efficiency differences between data and simulation. The scale factors correct for effects such as lepton identification, reconstruction, isolation and track-to-vertex-association.

The level of pileup in each event is quantified by the average number of inelastic interactions per bunch crossing, $\langle\mu\rangle$. It can be estimated by using the instantaneous luminosity, the inelastic pp cross-section and the corresponding beam parameters for the relevant luminosity blocks. The MC events are weighted to reproduce the distribution of the average number of interactions per bunch crossing observed in the data, referred to as ‘‘pile-up reweighting’’. In this procedure, the $\langle\mu\rangle$ value from the data is divided by a factor of 1.03 ± 0.04 , a rescaling which makes the number of reconstructed primary vertices agree better between data and simulation and reproduces the visible cross section of inelastic pp collisions as measured in the data.

Slicing of SM samples

The SHERPA $V + \text{jets}$ samples are generated in slices which need to be combined according to their relative cross-sections. This ensures sufficient statistics in the tails of kinematic distributions. For W and Z bosons decaying into charged leptons, the slicing is done based on the maximum of the boson p_T and the H_T in the event. For the $Z \rightarrow \nu\nu$ samples the slicing is based on a combination of the Z boson p_T and the dijet invariant mass in events with at least two jets. These different slicing choices lead to differences in the actual predictions when the slices are merged and has the potential to affect the unfolded data through the unfolding procedure. This is further studied in Section 4.8.

Single-top Wt associated production

Two samples for the single-top Wt associated production process are provided, differing in the subtraction scheme they use to account for interference terms between top-pair and Wt associated production. These are the Diagram Subtraction (DS) and Diagram Removal (DR) schemes [56]. Studies on top-enhanced control regions in appendix B.2 show that the DS subtraction scheme provides better modelling of the top contributions in all of the regions

considered in this analysis. The MC sample using the DS subtraction scheme is therefore chosen as the default one to use. The effect of using the alternative DR sample to simulate this process in the unfolding procedure is studied in Section 4.6.

3.6 Uncertainties

Experimental systematic uncertainties

Each of the methods described in Section 2.3, involving the calibration, energy scale and energy resolution of physics objects, has an associated experimental systematic uncertainty. To propagate such uncertainties to the final measurement, each calibration method is assigned a list of nuisance parameters. Each nuisance parameter is varied by one standard deviation around its nominal value, corresponding to the uncertainty of the calibration method. The effect of each uncertainty on the detector-level result is calculated by varying one nuisance parameter at a time, recalibrating all physics objects and repeating the simulated measurement. The resulting relative shift of the final distribution compared to the nominal one is taken as the systematic uncertainty associated with the calibration method being varied.

The dominant systematic uncertainties arising from the jet calibration procedure come from the in-situ corrections used to correct for differences between the data and the MC and the modelling of the events used in the calibration. Together with systematic uncertainties coming from the jet flavour composition, the jet energy scale calibration and the treatment of pile-up jets, they are grouped into the JES systematic uncertainty. Additional systematic uncertainties come from the jet energy resolution (JER) calibration, the contribution of soft terms to the calculation of p_T^{miss} and the reweighting of recorded events to account for pile-up effects.

Additional experimental systematic uncertainties arise from the reconstruction and treatment of leptons, and the differences between the performance of these methods in data and in simulation. These differences are accounted for by applying a scale factor on the event weight for each lepton being selected and processed. The scale factors are provided by dedicated ATLAS performance groups and are estimated in measurements of well-known SM processes.

As before, each scale factor is varied by one standard deviation around its nominal value and the uncertainty associated with it is propagated to the final result. The analysis presented here considers experimental systematics arising from the electron and muon energy scale and resolution, and the electron and muon identification, isolation, reconstruction and trigger efficiencies. Additional systematic uncertainties arising from the muon track resolution and muon track-to-vertex-association efficiency are also considered in the muon regions.

A breakdown of how each group of systematic uncertainties affects the MC prediction for the p_T^{miss} distributions of all regions in the ≥ 1 jet phase-space is shown in Figure 3.3. The dominant systematic in all regions is the one coming from jet calibration techniques. This uncertainty is expected to be considerably reduced in the construction of R^{miss} since it is highly correlated between processes. In regions containing leptons, the second most dominant systematic is the one associated with the lepton efficiencies.

3.6.1 Theoretical systematic uncertainties

Uncertainties on the top-pair, diboson and triboson samples come from PDFs and the renormalisation and factorisation scale choices, the latter of which accounts for missing higher-order QCD effects. In each case the PDF uncertainty was estimated by taking the standard deviation of the 100 Monte Carlo replicas of the default NNPDF3.0NNLO set, as well as by reweighting to the alternative CT14 NNLO [57] and MMHT [58] PDF sets, and taking the envelope of these contributions as a combined PDF uncertainty. In case of top-pair production, the NLO versions of the PDF sets are used to match the PDF choice used for the nominal. In addition, upwards and downwards variations in the strong coupling constant, α_S , are evaluated and added in quadrature with the combined PDF uncertainty.

The scale uncertainties were estimated using seven sets of values for the renormalisation and factorisation scales obtained by independently varying each to either one half, one, or two times the nominal value (using the multiweights available in the MC samples). The envelope of these variations is taken as the uncertainty. For top-pair production, the factorisation scale in

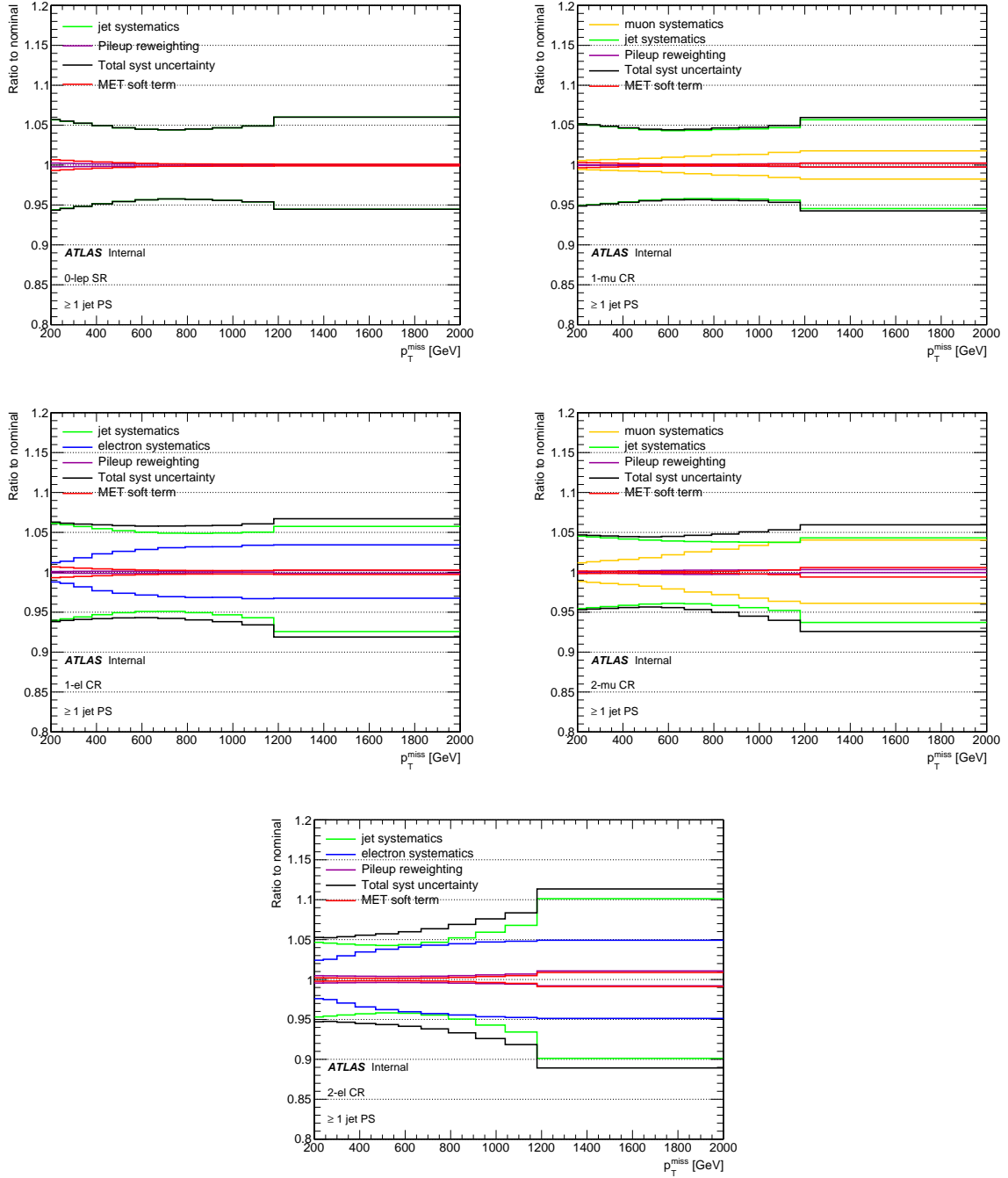


Figure 3.3 Systematic breakdown for p_T^{miss} in the ≥ 1 jet phase-space for all regions (grouped by source of systematic).

the parton shower is varied up and down by a factor of two for ISR and FSR separately. These two uncertainties are added in quadrature with the other uncertainties.

An additional uncertainty on the top samples comes from the choice of treatment of the overlap between top-pair and Wt single-top associated production events. This is estimated by using the recommended alternative prescription to remove the overlap (Diagram Removal rather than nominal Diagram Subtraction).

For the dominant $V+\text{jets}$ samples, a more sophisticated uncertainty model is used, based on the recommendations in [55]. This includes the PDF uncertainty and the standard seven-point scale variations, including those in the parton shower. In addition to this, a shape uncertainty (versus the p_T of the boson) due to the scale variations is given. As recommended in this reference, the scale variations are assumed to be fully correlated between the different processes. The contribution to the scale uncertainty that is uncorrelated between W s and Z s is estimated from the difference in the NLO K -factors⁴ with respect to the average of the K -factors in the various channels. The impact of parton showering on the jet-balancing cuts as well as the central-jet veto in the VBF region is estimated by varying the resummation scale by factors of two and one half. For the m_{jj} distribution an additional shape uncertainty is estimated by taking the difference in the prediction using the nominal METS scale setter in SHERPA, compared to the prediction using m_{jj} as the central scale choice. The logic here is that there are actually two hard scales in the event coming from the p_T of the boson and m_{jj} . While the latter is found to give a reasonable modelling of the m_{jj} distribution, this particular scale choice can only be constructed for events with at least two additional parton emissions in the matrix element, which makes it difficult to reweight the nominal prediction.

Theoretical uncertainties mostly affect the particle-level predictions to which the unfolded data is compared to. There are also small contributions of theory uncertainties to the systematic uncertainty applied on the unfolded data due to their effect on the unfolding procedure. This effect is further studied in Section 4.6 for the theory uncertainties arising from the modelling of

⁴The NLO K -factor of a process is defined as the ratio of cross-sections at NLO and LO for that process.

$V + \text{jets}$ and top-pair production and the treatment of the overlap between top-pair and Wt single-top associated production events.

3.7 Detector-level results

In this section comparisons between detector-level data and the SM prediction are shown for the $p_T^{\text{miss}} + \text{jets}$, $1e + \text{jets}$, $1\mu + \text{jets}$, $2e + \text{jets}$ and $2\mu + \text{jets}$ regions. Each of the contributions to the SM prediction are shown as stacked histograms. Backgrounds from QCD multijet events are included in the SM histograms for the $p_T^{\text{miss}} + \text{jets}$ region and only for the one-dimensional distributions. These backgrounds contribute mainly to the low- p_T^{miss} and high- $\Delta\phi_{jj}$ bins and only at the level of 1-2%. The estimation of these backgrounds in the lepton regions is still in progress at the time of writing and so these backgrounds are not included in the following comparisons. They are expected to contribute mainly to the high- p_T^{miss} region of the $1e + \text{jets}$ region with negligible contributions in the rest of the lepton regions. In the bottom panel of each Figure a ratio of detector-level data to MC is shown where the statistical uncertainties are shown as error bars. Systematic uncertainties added in quadrature to the statistical uncertainties are only shown in the ratio panel as a band with hatched lines. The band includes the experimental systematic uncertainties discussed in Section 3.6. Theoretical systematic uncertainties on the particle-level SM predictions are shown as a pink band. Large statistical contributions to the calculation of these uncertainties lead to shape differences in the theory uncertainty band between regions. These fluctuations are expected to reduce with a more precise calculation of the theory uncertainties, which is currently in progress. Since this is an ongoing analysis, the $p_T^{\text{miss}} + \text{jets}$ region is blinded to the 2017 and 2018 datasets to avoid biases in the analysis' strategy and methodology. Comparisons between data and MC in the $p_T^{\text{miss}} + \text{jets}$ region are instead shown only using the 2015 and 2016 datasets and the corresponding MC campaign.

Figures 3.4, 3.5 and 3.6 show comparisons between data and MC for p_T^{miss} and p_T^{miss} vs p_T^j , in the ≥ 1 jet phase-space for all regions. A 10% to 20% discrepancy in the agreement between data and MC in the p_T^{miss} distribution is seen in all regions. However, the shape of the distribution is reasonably well modelled and deviations from the MC prediction observed in the

data are covered by the theoretical systematic uncertainties. A slightly larger disagreement between data and MC is observed for low values of p_T^{miss} in the $2e + \text{jets}$ lepton region compared to the $2\mu + \text{jets}$ lepton region. The absence of a QCD background estimate in the $1e + \text{jets}$ region leads to an increase in the ratio between data and MC in the tails of the distribution. For the p_T^{miss} versus $p_T^{j_1}$ distributions the ratio between data and MC decreases with increasing values of $p_T^{j_1}$ for all regions. This is again covered by the band of theoretical systematic uncertainties, which are estimated using the uncertainty versus p_T^{miss} in each region.

Figures 3.7, 3.8 and 3.9 show comparisons between detector-level data and MC for p_T^{miss} , m_{jj} , and $\Delta\phi_{jj}$ for all regions in the ≥ 2 jet phase-space. Figures 3.10 and 3.11 show comparisons for m_{jj} vs $\Delta\phi_{jj}$ for all regions in the ≥ 2 jet phase-space. Overall shifts in normalisation and shape discrepancies in the p_T^{miss} distribution are similar to those seen in the ≥ 1 jet region. The m_{jj} distribution is badly modelled by the MC in all the regions with the MC exhibiting a much harder m_{jj} distribution than the data. This can also be seen in Figures 3.10 and 3.11 where the ratio between data and MC decreases for slices with larger m_{jj} values. The theoretical uncertainties on these Figures are estimated using the uncertainty versus m_{jj} in each region and cover most of the discrepancies. The fact that this mismodelling is similar for all regions indicates that using the lepton regions to constrain experimental and theoretical uncertainties in the $p_T^{\text{miss}} + \text{jets}$ region will be effective. The $\Delta\phi_{jj}$ distribution is peaked towards small values, for jets produced close to each other, with a dip at very low values as the jets cannot be exactly on top of each other. The data has a slightly more peaked structure than the MC in all regions. The discrepancy in the shape becomes more pronounced at larger m_{jj} values, as seen in Figures 3.10 and 3.11.

Figures 3.12, 3.13 and 3.14 show comparisons between detector-level data and MC for p_T^{miss} , m_{jj} , and $\Delta\phi_{jj}$ for all regions in the VBF phase-space. Figures 3.15 and 3.16 show comparisons for m_{jj} vs $\Delta\phi_{jj}$ for all regions in the VBF phase-space. The agreement between data and MC in the p_T^{miss} distributions exhibits a similar pattern to those in the ≥ 1 jet and ≥ 2 jet phase-spaces. The m_{jj} is badly modelled in a similar way as in the ≥ 2 jet phase-space, although a better agreement is observed in this phase-space. In the VBF phase-space there is a much larger contribution from the EWK production of $V + \text{dijets}$ events compared to the ≥ 2 jet

phase-space, which appears to be better modelled. The $\Delta\phi_{jj}$ distribution has a larger dip at low values, compared to the same distribution in the ≥ 2 jet phase-space, due to the additional $m_{jj} > 200$ GeV requirement in this phase-space. The discrepancies between data and MC are similar to those seen in the ≥ 2 jet phase-space. The agreement in the m_{jj} vs $\Delta\phi_{jj}$ distribution of Figure 3.15 also exhibits similar patterns as the one in the ≥ 2 jet phase-space.

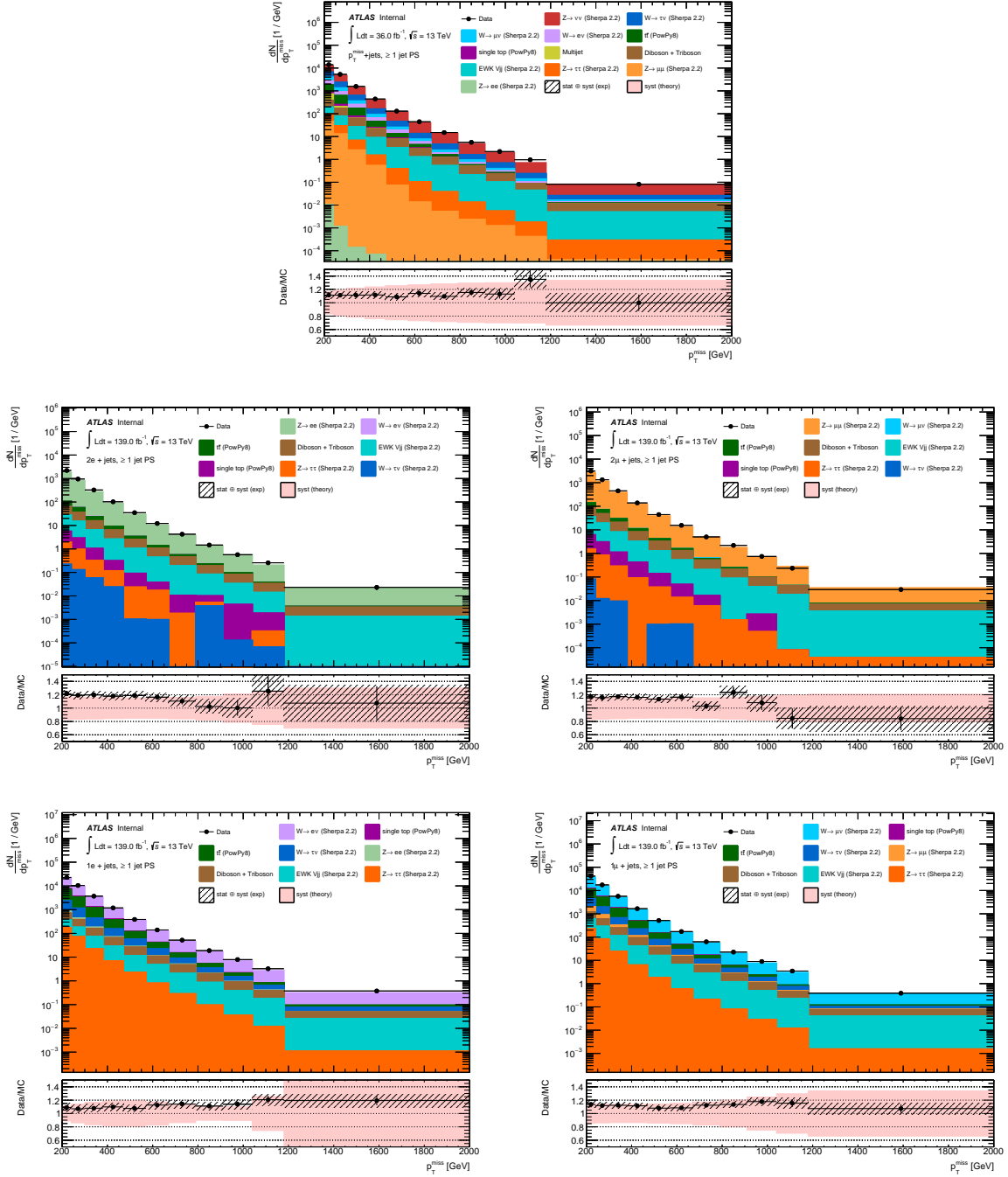


Figure 3.4 Detector-level data/MC comparisons for p_T^{miss} in the ≥ 1 jet phase-space. The hatched lines show the combination of statistical and systematic uncertainties. The pink band shows the theoretical uncertainties on the particle-level SM prediction. The dominant contributions to the $p_T^{\text{miss}} + \text{jets}$ region at low p_T^{miss} come from the $Z \rightarrow \nu\nu$ ($\sim 49\%$), $W \rightarrow \ell\nu$ ($\sim 38\%$) and $t\bar{t}$ ($\sim 8\%$) processes.

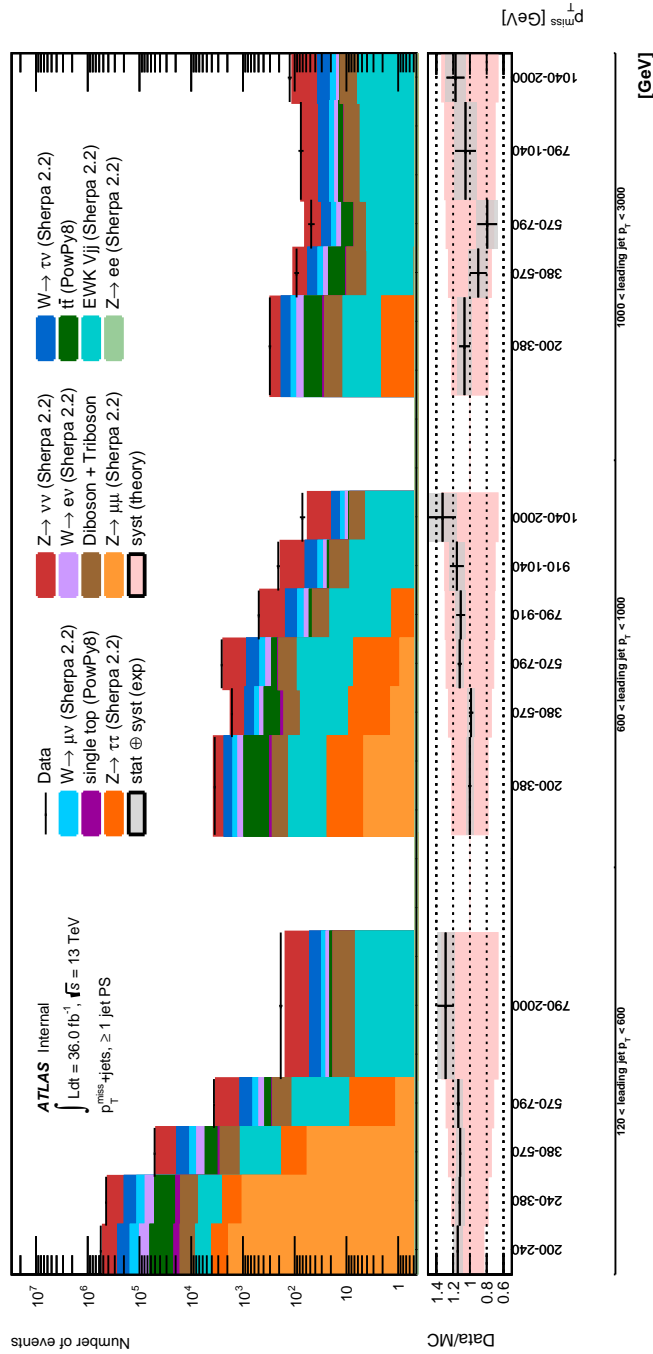


Figure 3.5 Detector-level data/MC comparisons for p_T^{miss} vs p_T^{j1} in the ≥ 1 jet phase-space for the $p_T^{\text{miss}} + \text{jets}$ region. The grey band shows the combination of statistical and systematic uncertainties. The pink band shows the theoretical uncertainties on the particle-level SM prediction.

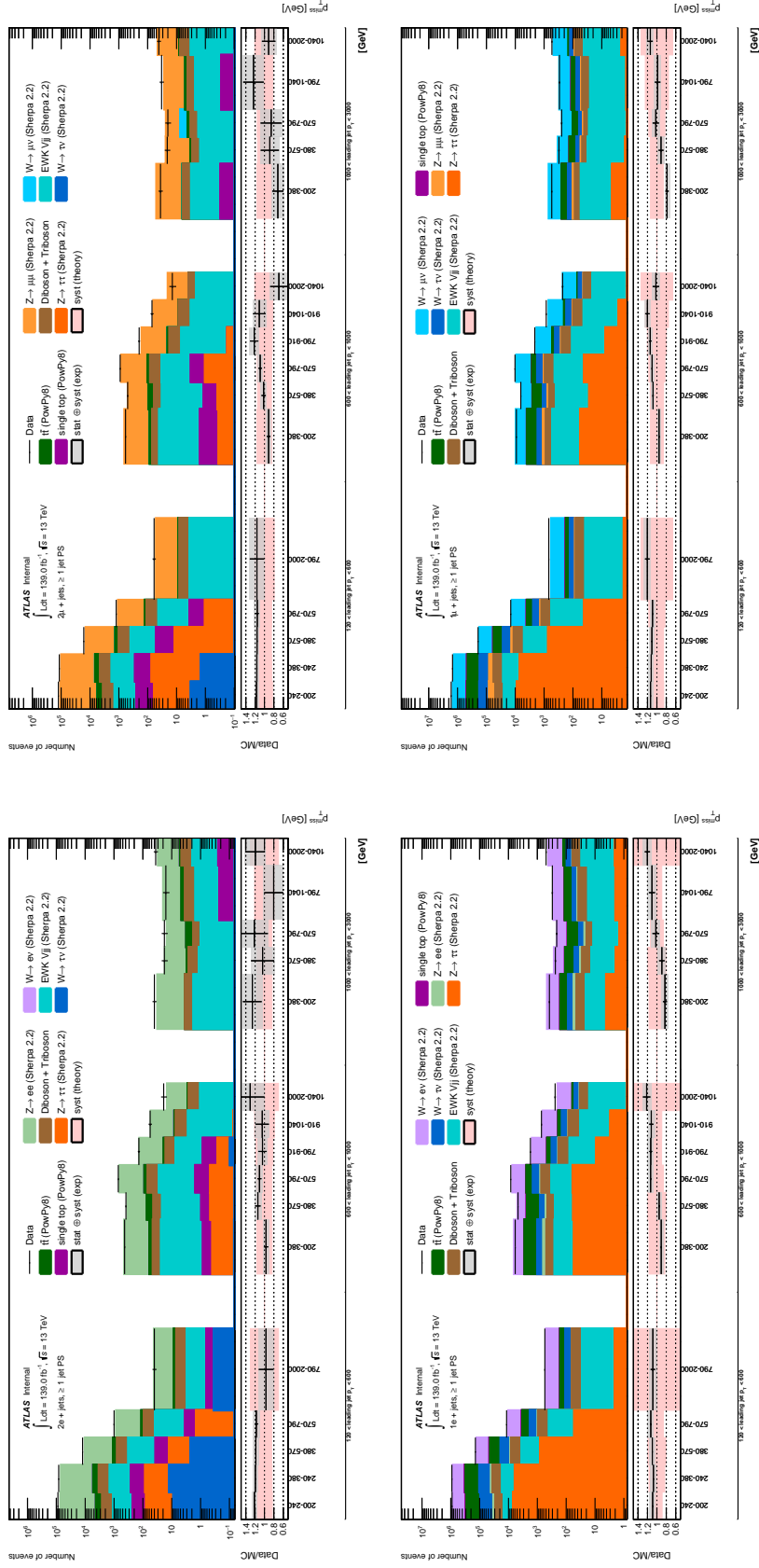


Figure 3.6 Detector-level data/MC comparisons for p_T^{miss} vs $p_T^{j_1}$ in the ≥ 1 jet phase-space for the $1\ell + \text{jets}$ and $2\ell + \text{jets}$ regions. The grey band shows the combination of statistical and systematic uncertainties. The pink band shows the theoretical uncertainties on the particle-level SM prediction.

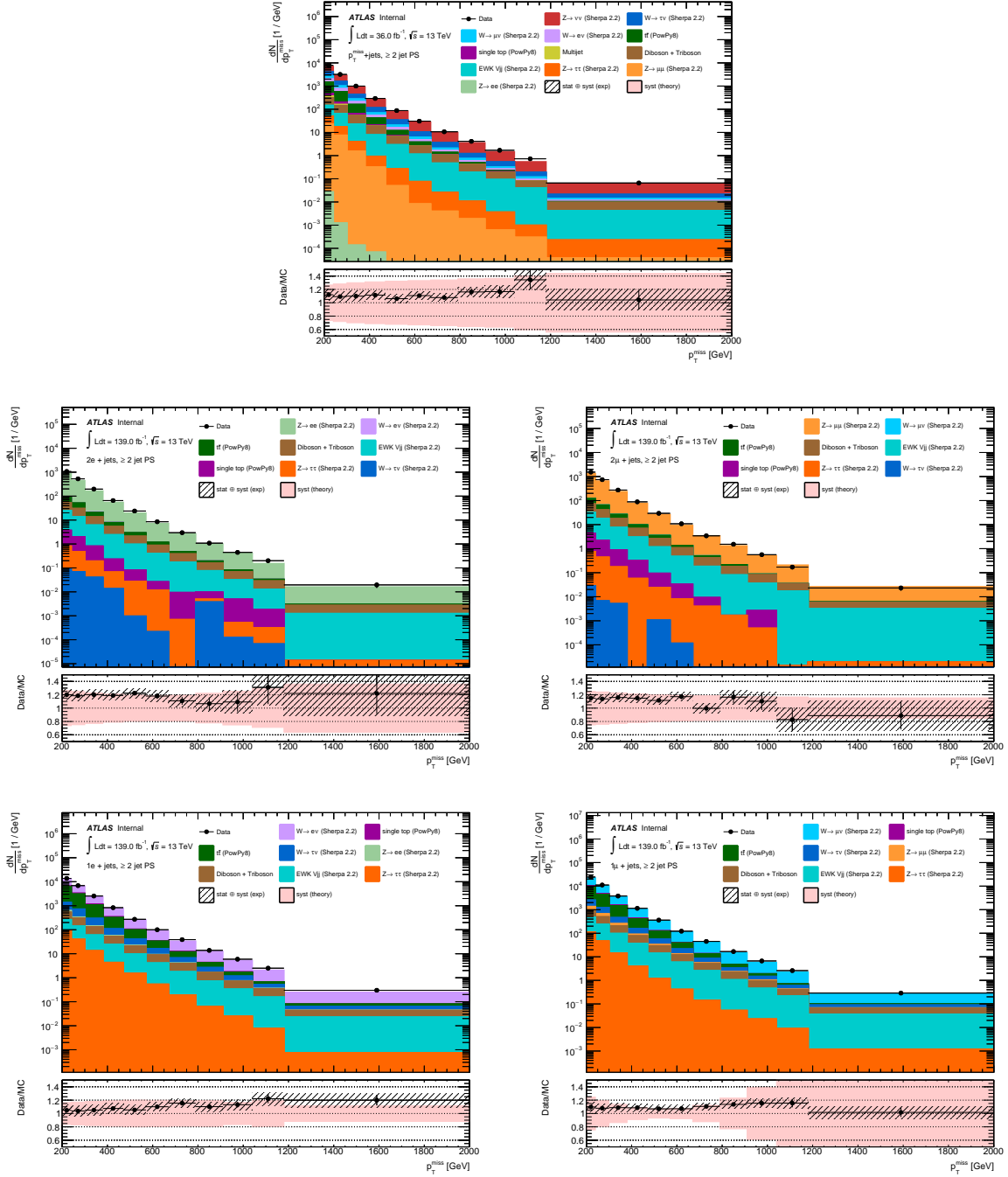


Figure 3.7 Detector-level data/MC comparisons for p_T^{miss} in the ≥ 2 jet phase-space. The hatched lines show the combination of statistical and systematic uncertainties. The pink band shows the theoretical uncertainties on the particle-level SM prediction. The dominant contributions to the p_T^{miss} + jets region at low p_T^{miss} come from the $Z \rightarrow \nu\nu$ ($\sim 43\%$), $W \rightarrow \ell\nu$ ($\sim 37\%$) and $t\bar{t}$ ($\sim 15\%$) processes.

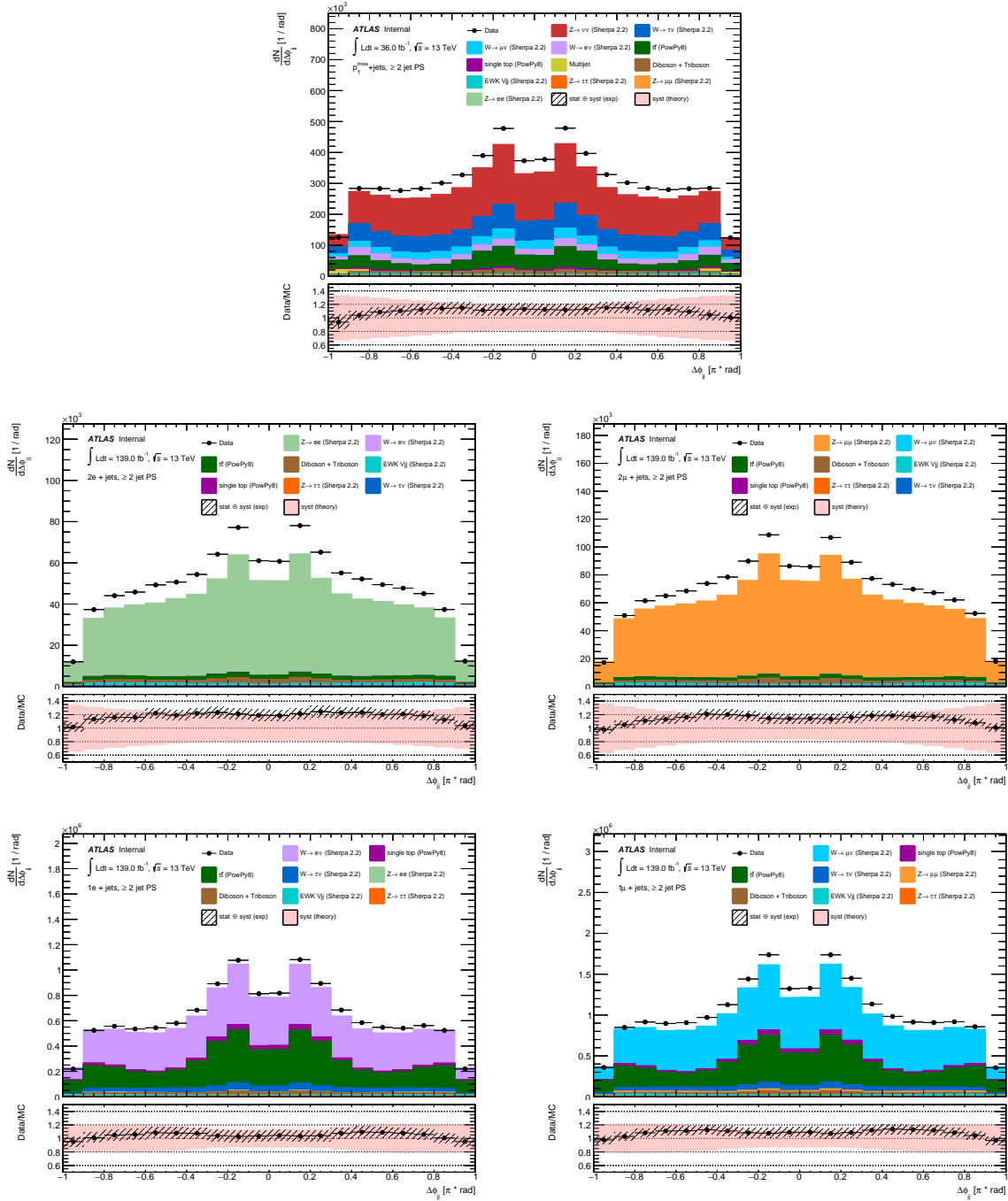


Figure 3.9 Detector-level data/MC comparisons for $\Delta\phi_{jj}$ in the ≥ 2 jet phase-space. The hatched lines show the combination of statistical and systematic uncertainties. The pink band shows the theoretical uncertainties on the particle-level SM prediction.

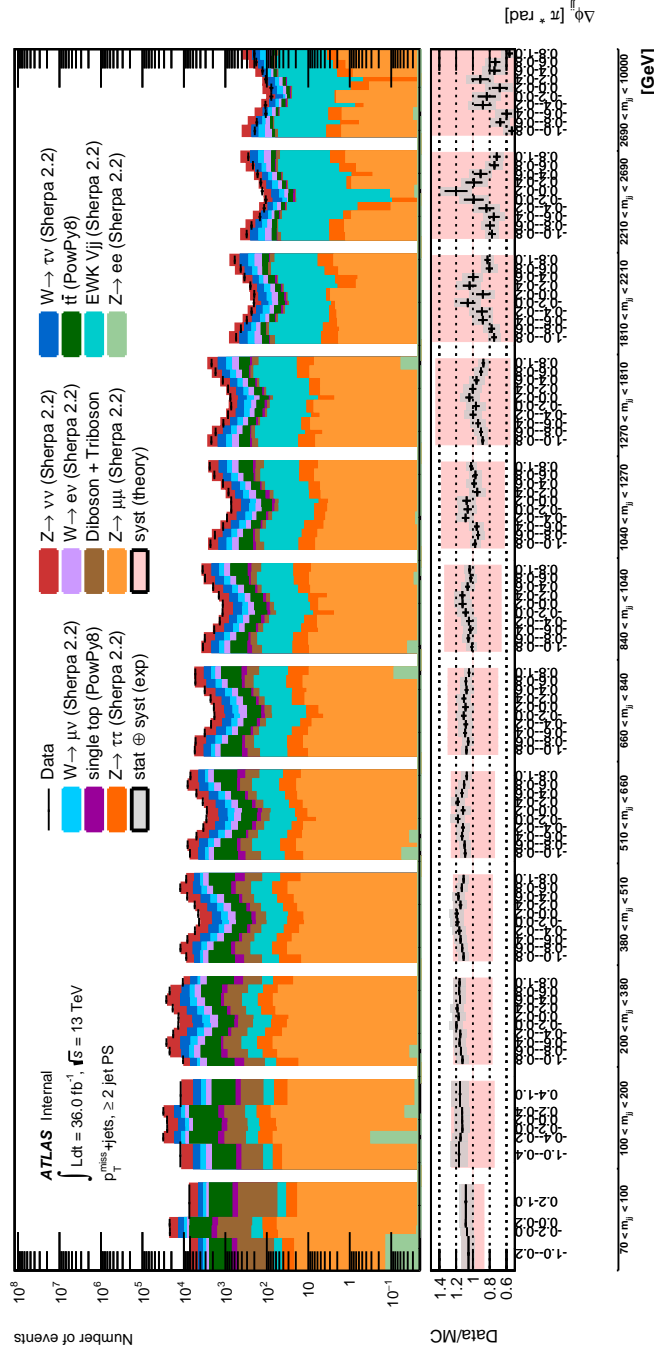


Figure 3.10 Detector-level data/MC comparisons for m_{jj} versus $\Delta\phi_{jj}$ in the ≥ 2 jet phase-space for the $p_T^{\text{miss}} + \text{jets}$ region. The grey band shows the combination of statistical and systematic uncertainties. The pink band shows the theoretical uncertainties on the particle-level SM prediction.

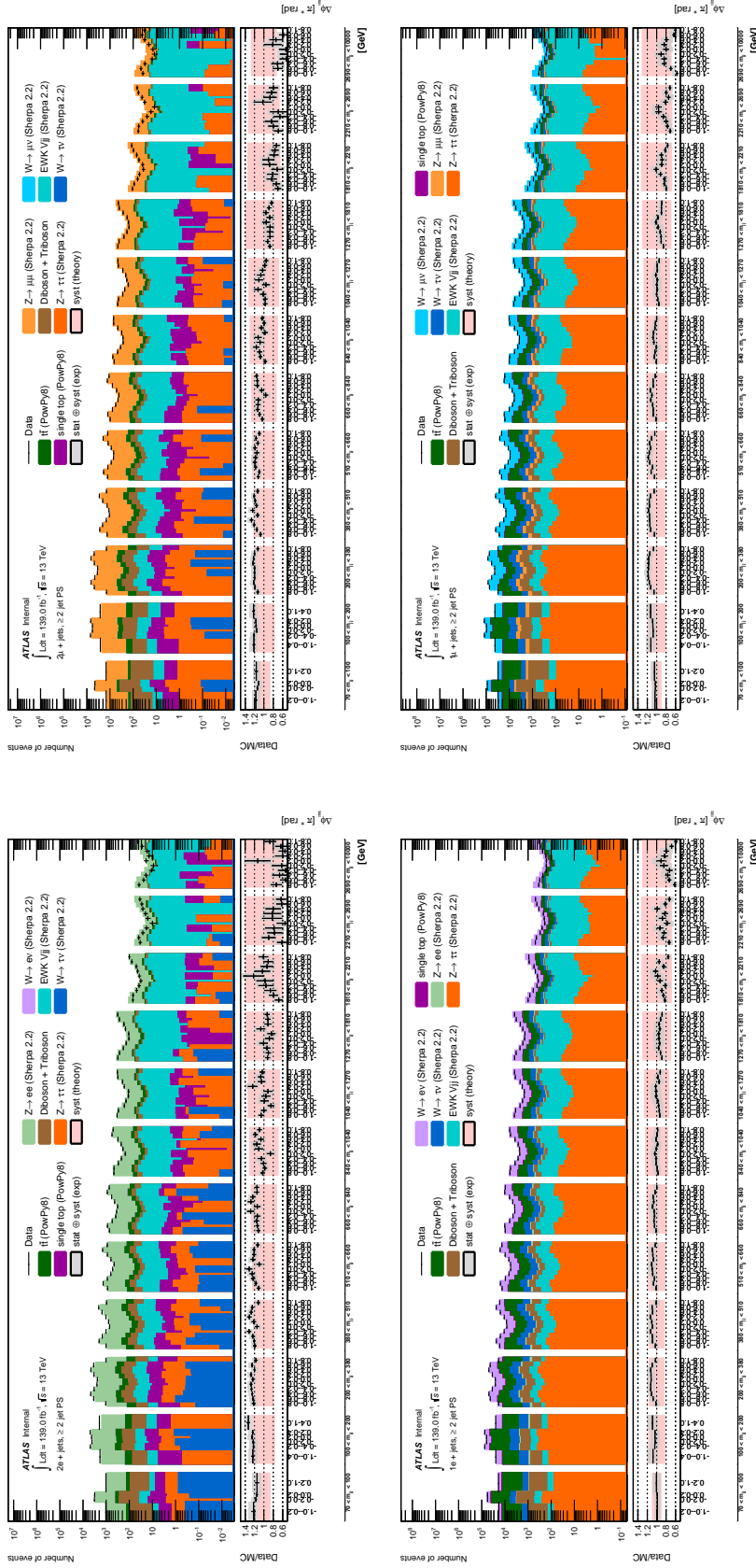


Figure 3.1.1 Detector-level data/MC comparisons for m_{jj} versus $\Delta\phi_{jj}$ in the ≥ 2 jet phase-space for the $1\ell + \text{jets}$ and $2\ell + \text{jets}$ regions. The grey band shows the combination of statistical and systematic uncertainties. The pink band shows the theoretical uncertainties on the particle-level SM prediction.

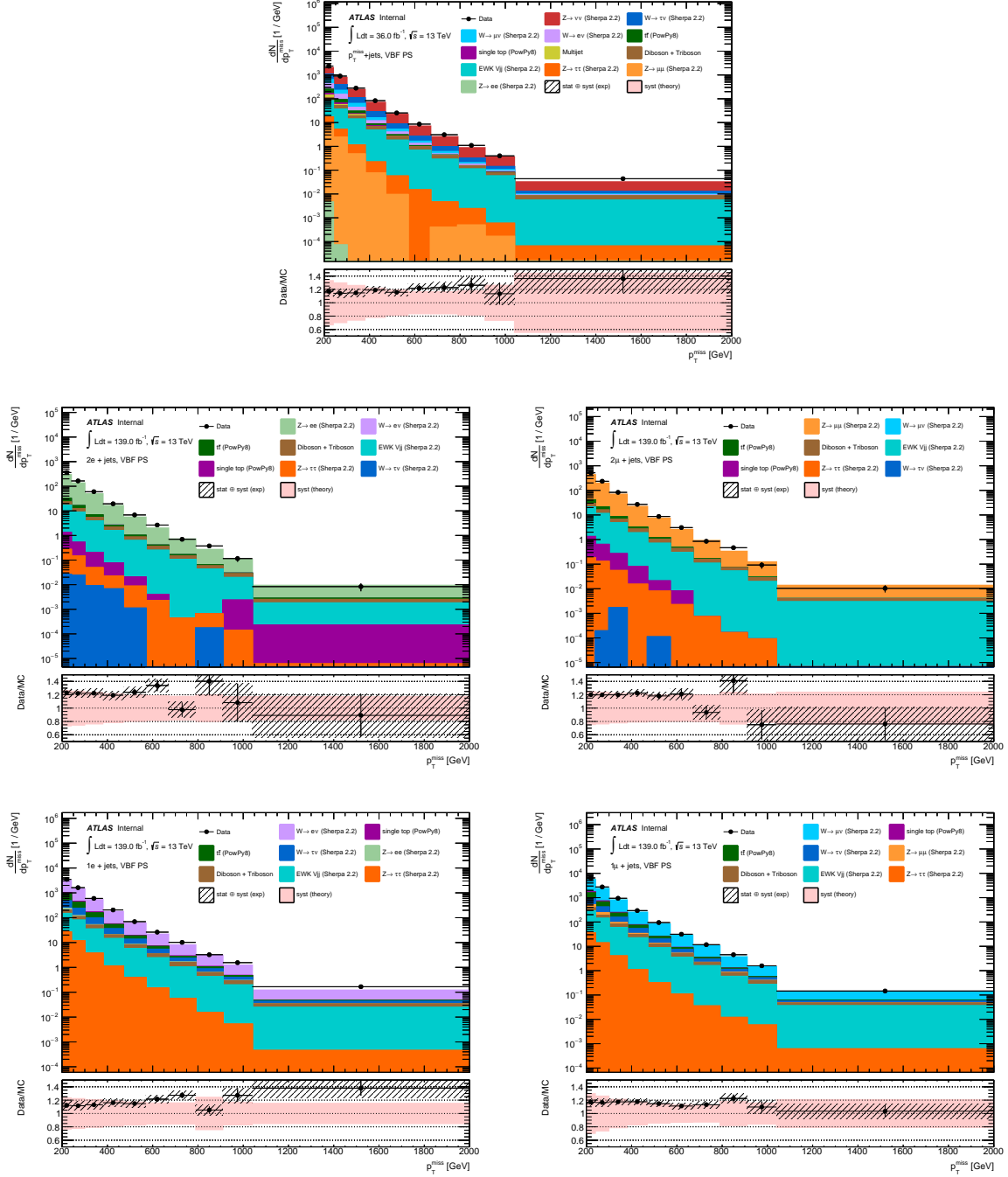


Figure 3.12 Detector-level data/MC comparisons for p_T^{miss} in the VBF phase-space. The hatched lines show the combination of statistical and systematic uncertainties. The pink band shows the theoretical uncertainties on the particle-level SM prediction. The dominant contributions to the p_T^{miss} + jets region at low p_T^{miss} come from the $Z \rightarrow \nu\nu$ (~48%), $W \rightarrow \ell\nu$ (~40%) and $t\bar{t}$ (~4%) processes.

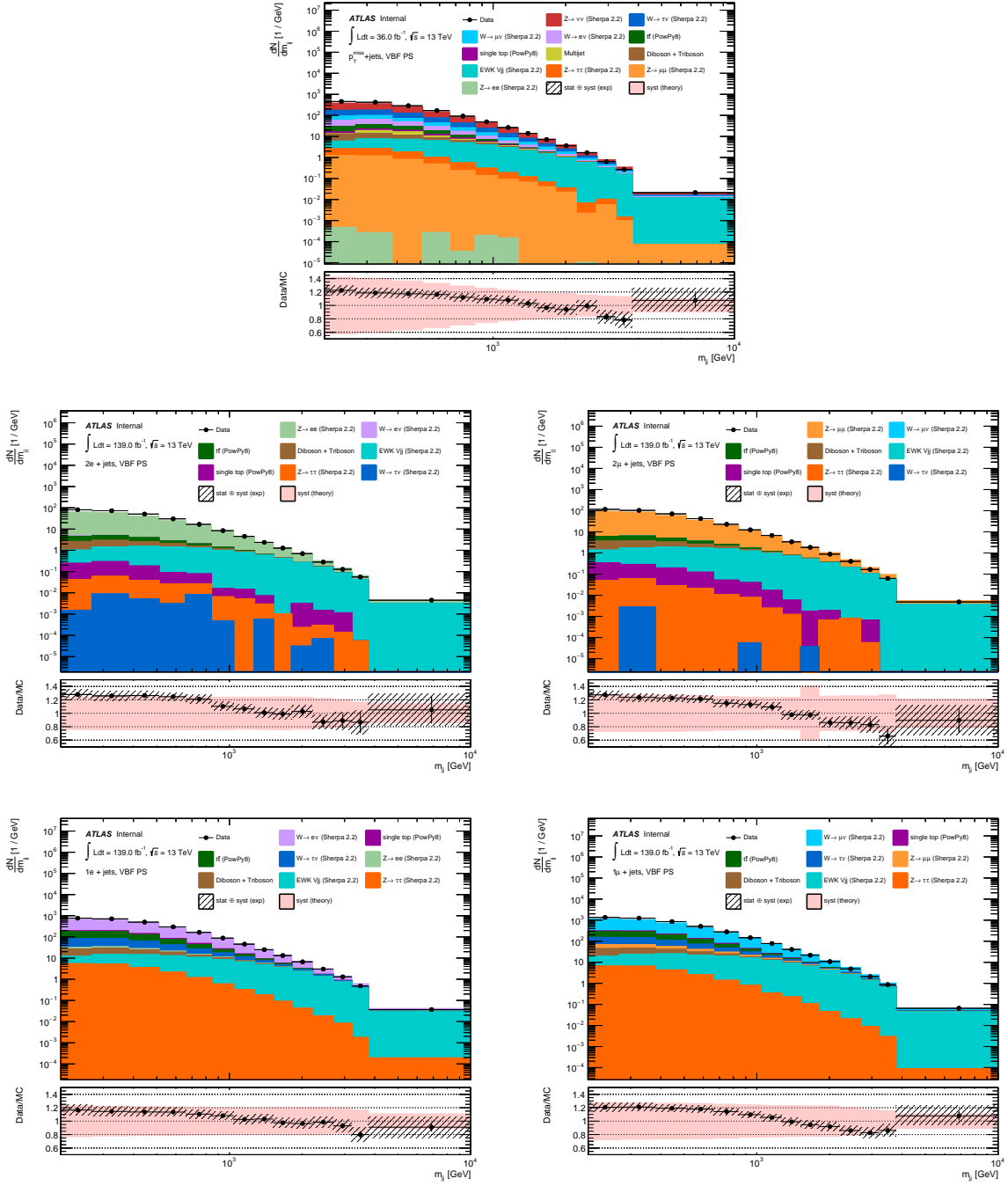


Figure 3.13 Detector-level data/MC comparisons for m_{jj} in the VBF phase-space. The hatched lines show the combination of statistical and systematic uncertainties. The pink band shows the theoretical uncertainties on the particle-level SM prediction.

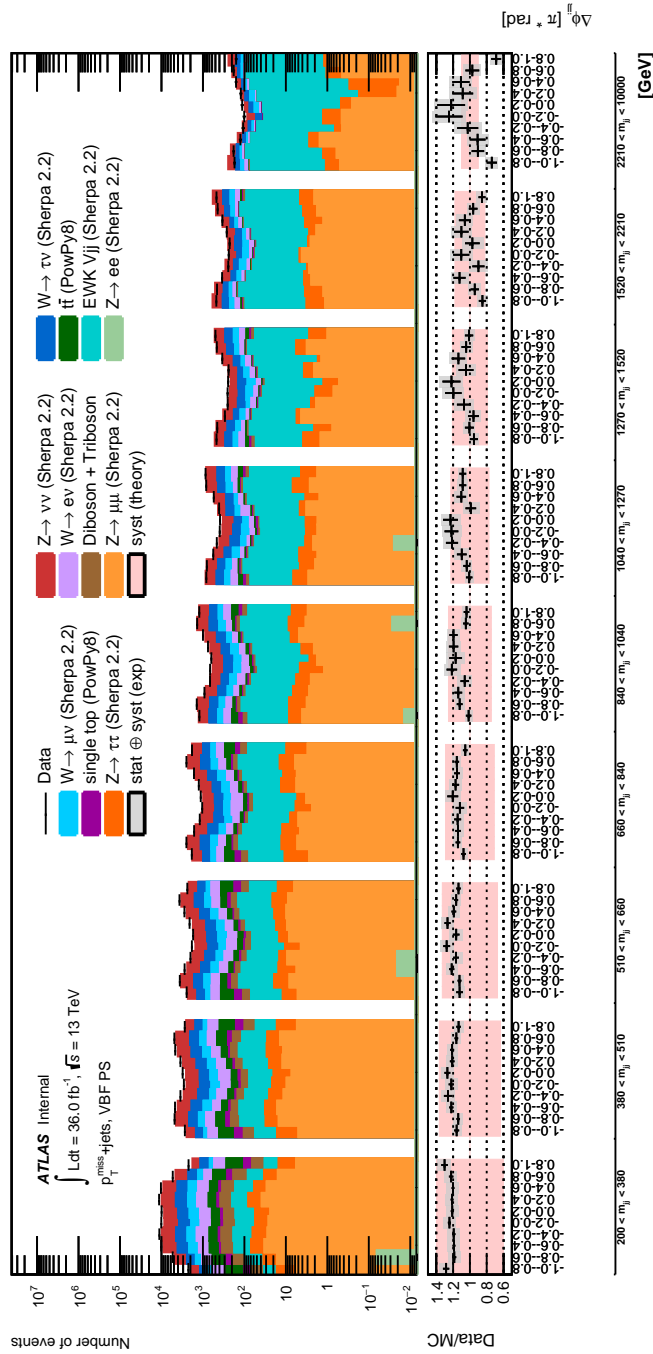


Figure 3.15 Detector-level data/MC comparisons for m_{jj} versus $\Delta\phi_{jj}$ in the VBF phase-space for the $p_T^{\text{miss}} + \text{jets}$ region. The grey band shows the combination of statistical and systematic uncertainties. The pink band shows the theoretical uncertainties on the particle-level SM prediction.

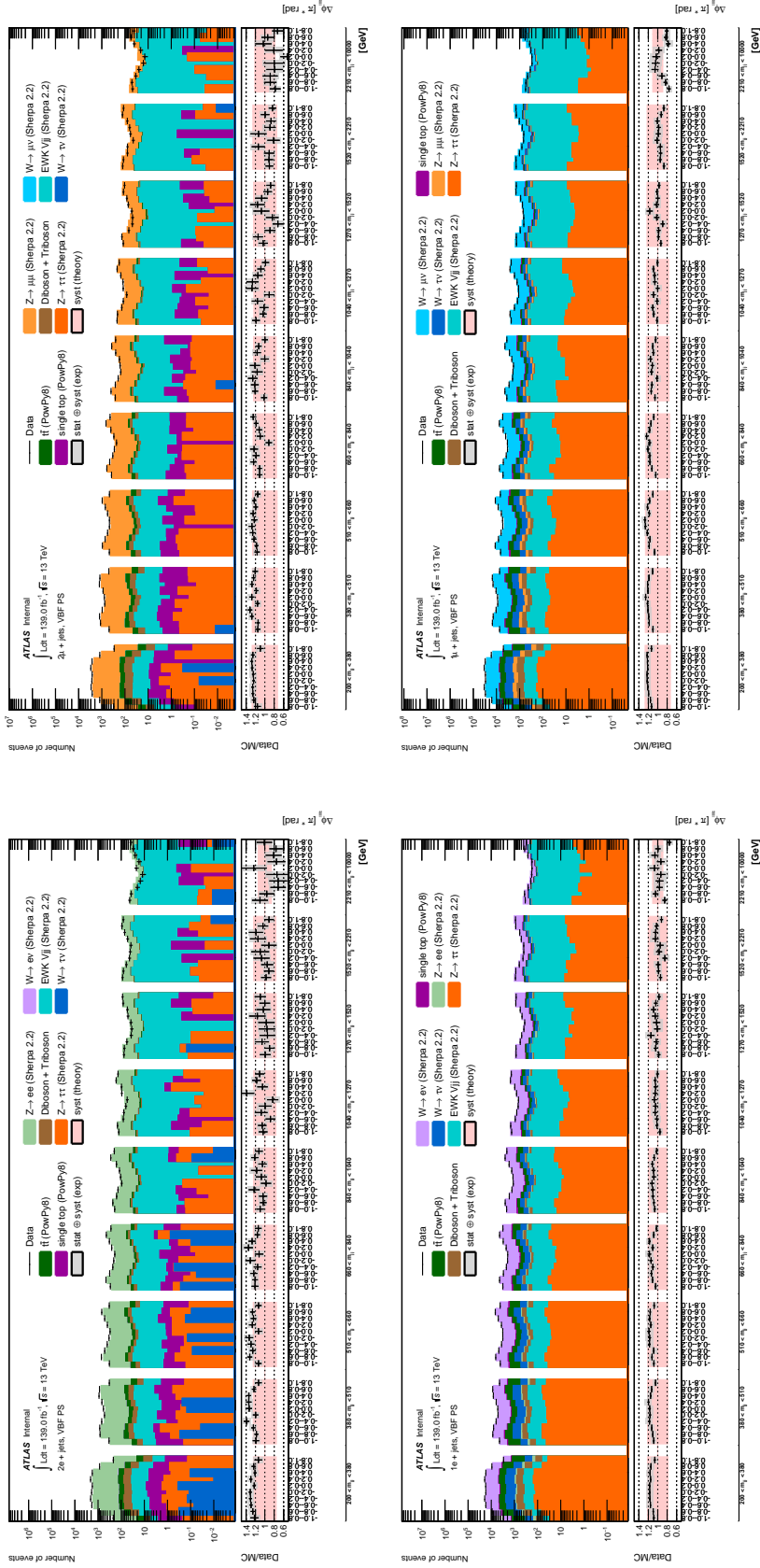


Figure 3.16 Detector-level data/MC comparisons for m_{jj} versus $\Delta\phi_{jj}$ in the VBF phase-space for the $1\ell + \text{jets}$ and $2\ell + \text{jets}$ regions. The grey band shows the combination of statistical and systematic uncertainties on the particle-level SM prediction.

Chapter 4

Correcting for detector effects

4.1 Introduction

Measurements can be presented in terms of particle-level objects so that they are easily and directly comparable to particle-level predictions. These can also be rapidly compared to BSM simulations without the need to simulate the ATLAS detector, making them optimally useful long into the future and for quick reinterpretation studies. Any improvements to precision predictions of SM background processes can also be included and the data can be re-interpreted taking those into consideration. Measurements at the particle-level are usually presented as differential cross-sections and are determined by correcting the reconstructed differential distributions of events for detector effects, in a process known as “unfolding”. These effects include the acceptance, efficiency, resolution and calibration of the detector. Some useful terminology involved in the unfolding procedure is defined below:

- **Reconstruction efficiency** Due to the efficiency and acceptance of the detector, only a fraction of particle-level events will be reconstructed and included in the measured distribution. The reconstruction efficiency (ϵ) accounts for this and is defined as the ratio of simulated events which pass both the particle and detector-level selections to all events passing the particle-level selection, as a function of the particle-level value of the variable being unfolded.

- **Fiducial fraction** Due to the resolution of the detector, events which do not pass the particle-level selection can still pass the detector-level selection and be included in the measured distribution. The fiducial fraction (ϕ) accounts for these “fake” events and is defined as the ratio of simulated events passing both the particle and detector-level selections to those which pass only the detector-level selection, as a function of the detector-level value of the variable being unfolded.
- **Migration matrix** Events in a specific bin in a particle-level distribution can migrate to a different, neighbouring bin in the measured distribution. This is due to the variable of interest being reconstructed with a higher or lower value than its true value, resulting in the event filling a different bin. The migration matrix (M) maps the particle-level distribution on to the detector-level distribution by keeping track of the final bins of events passing both the particle-level and detector-level selections. The elements of the migration matrix give the probability that an event in a particle-level bin j will be reconstructed at detector-level in bin i .
- **Fiducial purity** This is equivalent to the diagonal of the migration matrix. The fiducial purity (p) gives the probability that an event will be found in the same bin at the particle and detector-level.

The information above can be used to define the **response matrix** (R),

$$R_{ij} = M_{ij}\epsilon_j\phi_i \quad (4.1)$$

which, together with the detector-level distribution of the reducible background (b), relates the detector-level measured distribution r to the particle-level distribution t ,

$$r_i = R_{ij}t_j + b_i \quad (4.2)$$

where i and j indicate the bin indices at the detector and at the particle-level respectively. In a similar way, an unfolded distribution u can be related to the detector-level measured distribution by inverting the same response matrix and using the background-subtracted

measured distribution,

$$u_j = R_{ji}^{-1}(r_i - b_i) \quad (4.3)$$

At this step, unfolding by matrix inversion becomes non-trivial. Even if the response matrix is invertible, solutions to the above equation can be unstable due to the nature of the measured values r_i , which are random variables following Poisson distributions. Statistical fluctuations in the measured distribution can lead to large statistical uncertainties in the unfolded particle-level distribution when the fiducial purity is low and the off-diagonal elements of the response matrix are large. This can be dealt with by adding a regularisation process in the unfolding procedure.

In this analysis, the *Iterative Bayesian Unfolding* method is used along with Bayes' theorem to invert the response matrix and add this regularisation step. Extracting the reconstruction efficiency and fiducial fraction out of the response matrix, equation 4.3 can be re-written as

$$u_j = \frac{1}{\epsilon_j \phi_i} \sum_i P(\text{in true bin } j \mid \text{in reconstructed bin } i)(r_i - b_i) \quad (4.4a)$$

$$= \frac{1}{\epsilon_j \phi_i} \sum_i \frac{P(\text{in reconstructed bin } i \mid \text{in true bin } j)P(\text{in true bin } j)}{P(\text{in reconstructed bin } i)}(r_i - b_i) \quad (4.4b)$$

which introduces a *prior* particle-level distribution $t^{(0)}$. The above equation can be more compactly expressed as

$$u_j^{(1)} = \frac{1}{\epsilon_j \phi_i} \sum_i \frac{R_{ij} t_j^{(0)}}{\sum_q R_{iq} t_q^{(0)}}(r_i - b_i) \quad (4.5)$$

The particle-level distributions $t^{(k)}$ and the unfolded distributions $u^{(k)}$ are identical, with the only difference being that $u^{(0)}$ is nonsensical since a *prior* unfolded distribution does not exist. Contrarily, $t^{(0)}$ can be modelled using MC simulations. Using $u^{(1)}$ as the prior, a second solution $u^{(2)}$ can be computed and so on, with every iteration using the previous unfolded result as the

prior and $t^{(0)}$ as $u^{(0)}$. Equation 4.5 then becomes

$$u_j^{(k)} = \frac{1}{\epsilon_j \phi_i} \sum_i \frac{R_{ij} u_j^{(k-1)}}{\sum_q R_{iq} u_q^{(k-1)}} (r_i - b_i) \quad (4.6)$$

where the number of iterations k is the regularisation parameter.

The regularisation bias, which is introduced when using the MC-calculated prior truth distribution $t^{(0)}$, is reduced with every iteration as the shape of the detector-level data distribution is used to calculate the next prior. Increasing the number of iterations decreases the regularisation bias and the dependence of the result on $t^{(0)}$ but comes with the drawback that as k increases so do the statistical uncertainties on the unfolded result. In practice, two or three iterations are usually enough for the regularisation bias to be negligible.

4.2 Optimising the number of unfolding iterations

Optimising the regularisation parameter k reduces to finding the minimum number of iterations for which the regularisation bias converges, preferably to a negligible value. A non-negligible regularisation bias is treated as a systematic uncertainty and is propagated to the final unfolded result. The regularisation bias can be quantified and estimated using the data-driven method described in detail in [59] and summarised below.

First, a smooth polynomial function is obtained by fitting the agreement between the measured data and the detector-level MC. Events that pass both the particle and detector-level selections are then identified and reweighted at the particle-level using the smooth polynomial, such that the resulting reweighted detector-level distribution matches the measured data. This reweighted detector-level distribution is then unfolded using the nominal response matrix from the un-reweighted MC, keeping the efficiency and fiducial fraction at unity so as not to introduce any additional effects coming from the migration of events in and out of the phase-space. The regularisation bias is defined as the ratio between the unfolded reweighted MC and the reweighted prior particle-level distribution.

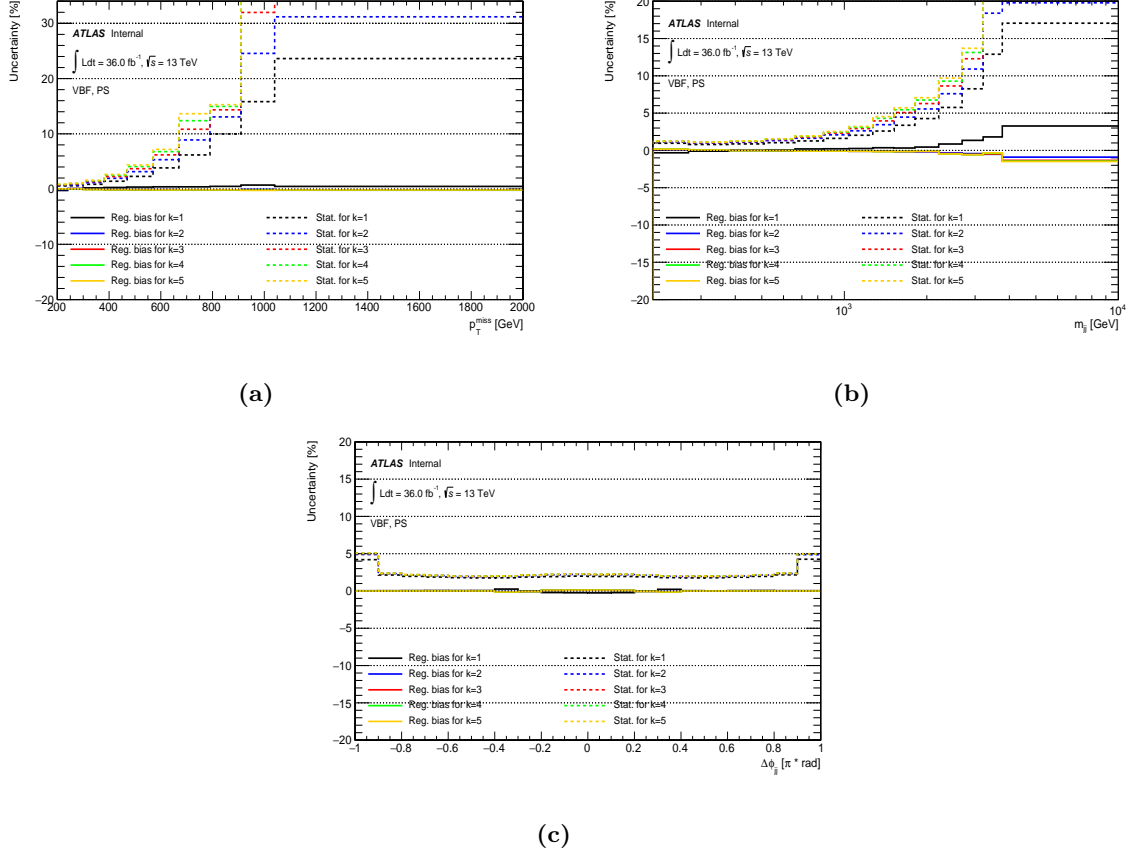


Figure 4.1 Statistical and regularisation bias systematic uncertainties for multiple values of k for (a) p_T^{miss} , (b) m_{jj} and (c) $\Delta\phi_{jj}$ in the VBF phase-space in the $2\mu + \text{jets}$ region. The regularisation bias converges to a minimum for $k = 2$.

The statistical and the regularisation bias systematic uncertainty for multiple values of k are shown in Figure 4.1 for three different observables in the $2\mu + \text{jets}$ region. The setting $k = 1$ represents the first iteration of Equation 4.6, where the particle-level distribution $t^{(0)}$ is taken as the prior. From the figures it can be concluded that 2 iterations are enough for the bias to converge to a minimum. The same applies to the rest of the observables considered in this analysis.

4.3 Binning optimisation

The binning of a distribution is usually preferred to be kept as fine as possible so that the features of the shape of a distribution are resolved. This is not always possible since extremely fine binning can lead to large migrations of events between neighbouring bins. This would result in a low fiducial purity and large off-diagonal elements in the response matrix which, as discussed in Section 4.1, lead to large statistical uncertainties in the unfolded result. Bins must also be wide enough so that they are well populated. The binning of both the one-dimensional and the two-dimensional distributions measured in this analysis is optimised by requiring the following criteria:

- The fiducial purity of each bin must be at least 60 %.
- Each bin must have at least 20 expected events so that the expected statistical uncertainty is always $\lesssim 25$ %.

This is achieved by initially binning the p_T^{miss} and m_{jj} distributions with 10 GeV width bins and then sequentially merging bins until the purity and the expected number of events satisfy the above criteria. The p_T^{miss} and m_{jj} observables are expected to have steeply falling distributions due to the limited number of events involving very energetic invisible systems. This results in a finer binning at low values of the observables and a wider one in the tails of the distributions. The shape of the $\Delta\phi_{jj}$ distribution is expected to be relatively flat and so a binning with 20 equal width bins is chosen, spanning from $-\pi$ to $+\pi$. The $\Delta\phi_{jj}$ binning satisfies the criteria set out above, with wider bins than what the minimum requirements allow. Nevertheless, the chosen binning is expected to be fine enough to differentiate between possible new physics models and be sensitive to CP-even and CP-odd models, while keeping computational memory consumption at a minimum.

Requiring that the binning of the two-dimensional distributions satisfies both of the above requirements leads to having to choose slightly different binning between the slices of the secondary observable. For the p_T^{miss} vs $p_T^{j_1}$ distribution, different pairs of p_T^{miss} bins have to be merged in each slice of $p_T^{j_1}$ so that the fiducial purity is at least 60 % in every bin. For the $\Delta\phi_{jj}$

vs m_{jj} distribution, bins of $\Delta\phi_{jj}$ have to be merged in the first two slices of m_{jj} in the ≥ 2 jet phase-space so that all bins are populated with at least 20 events.

4.4 Detector response

As seen in Equation 4.6, three different pieces of information are needed to perform the unfolding and obtain a particle-level measurement from a detector-level one: the migration matrix, the reconstruction efficiency and the fiducial fraction of the region in consideration, as a function of the observable being unfolded. These are all obtained from simulation as described in the introduction and together they define the detector response.

Migration matrices for p_T^{miss} in the ≥ 1 jet phase-space are shown for all regions in Figure 4.2. Identical binning is used at the detector and particle-level to keep the extrapolation to different topologies at a minimum during the unfolding process, resulting in square-shaped migration matrices. The reconstruction efficiency, fiducial fraction and fiducial purity as a function of p_T^{miss} are shown in Figure 4.3 for all regions. Corresponding figures and migration matrices for all other observables and phase-spaces can be found in appendix C.

The efficiency is lowest for the $2e + \text{jets}$ region due to the inefficiency of reconstructing both electrons. The efficiency in this region decreases further in bins with large values of p_T^{miss} . This is because in events with large p_T^{miss} (and hence large Z boson p_T) electrons are produced close to each other causing calorimeter based isolation criteria to fail. The highest efficiency is seen in the $p_T^{\text{miss}} + \text{jets}$ region which has no leptons to reconstruct. This pattern is seen in the efficiency plots of all observables. The fiducial fraction is lowest in the $p_T^{\text{miss}} + \text{jets}$ region due to the presence of W events with in-acceptance leptons. These events are considered as part of the signal and are included in the $p_T^{\text{miss}} + \text{jets}$ region at the detector-level when the detector-level lepton is not reconstructed due to inefficiencies of the detector. However, since the lepton is in-acceptance, these events are not included in the $p_T^{\text{miss}} + \text{jets}$ region at the particle-level, causing the region to have a lower fiducial fraction. The $1e + \text{jets}$ fiducial fraction is also lower than the other regions, which could be due to migrations in the real p_T^{miss} cut that is applied

only in this region. The migration matrices and purity plots are similar between all regions as migrations between neighbouring p_T^{miss} bins are very similar between all regions. The same patterns are seen for the rest of the observables in the ≥ 2 jet and VBF phase-space.

4.5 Uncertainties

The statistical uncertainty on the unfolded data is evaluated using the bootstrap method [60, 61] where a detector-level data distribution is poisson fluctuated, producing 2000 replicas. Each replica is then unfolded using the nominal detector response, resulting in 2000 unfolded distributions. The root-mean-square (RMS) of the results per bin is taken as the statistical uncertainty in that bin. The bootstrap method allows for statistical correlations between bins, introduced in the iterative part of the unfolding, to be properly propagated to the unfolded result.

Two groups of systematic uncertainties must be accounted for and applied to the unfolded data. The first group consists of experimental systematic uncertainties that affect the detector-level measurement and have to be propagated to the unfolded measurement. These are discussed in subsection 4.5.1. The second group consists of systematic uncertainties that are associated with the unfolding method itself. These are discussed in subsections 4.5.2 and 4.5.3. Theory systematic uncertainties affect the particle-level predictions used in data and MC comparisons but can also affect the unfolded data through the modelling of the detector response. These effects are studied in sections 4.6 and 4.8.

4.5.1 Experimental systematic uncertainties

The systematic uncertainties that affect the detector-level measurement are discussed in section 3.6 and listed in tables ?? and ?. The effect of each systematic uncertainty on the unfolded measurement is determined by using the systematically varied MC to construct the detector response and repeating the unfolding procedure with the varied detector response as input to Equation 4.6. This effectively produces one unfolded result for each systematic

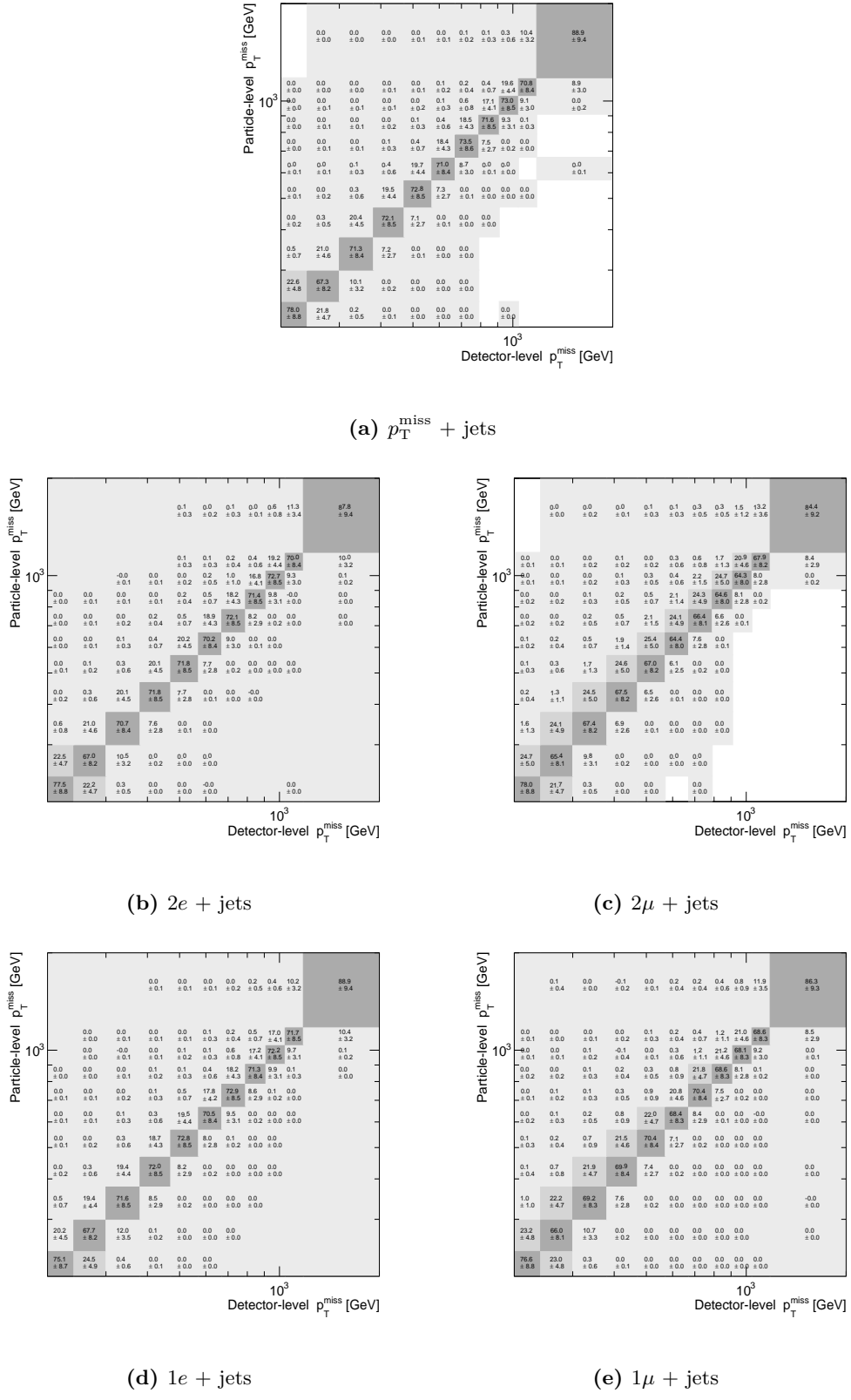


Figure 4.2 Migration matrices for p_T^{miss} in the ≥ 1 jet phase-space for (a) $p_T^{\text{miss}} + \text{jets}$, (b) $2e + \text{jets}$, (c) $2\mu + \text{jets}$, (d) $1e + \text{jets}$ and (e) $1\mu + \text{jets}$ regions.

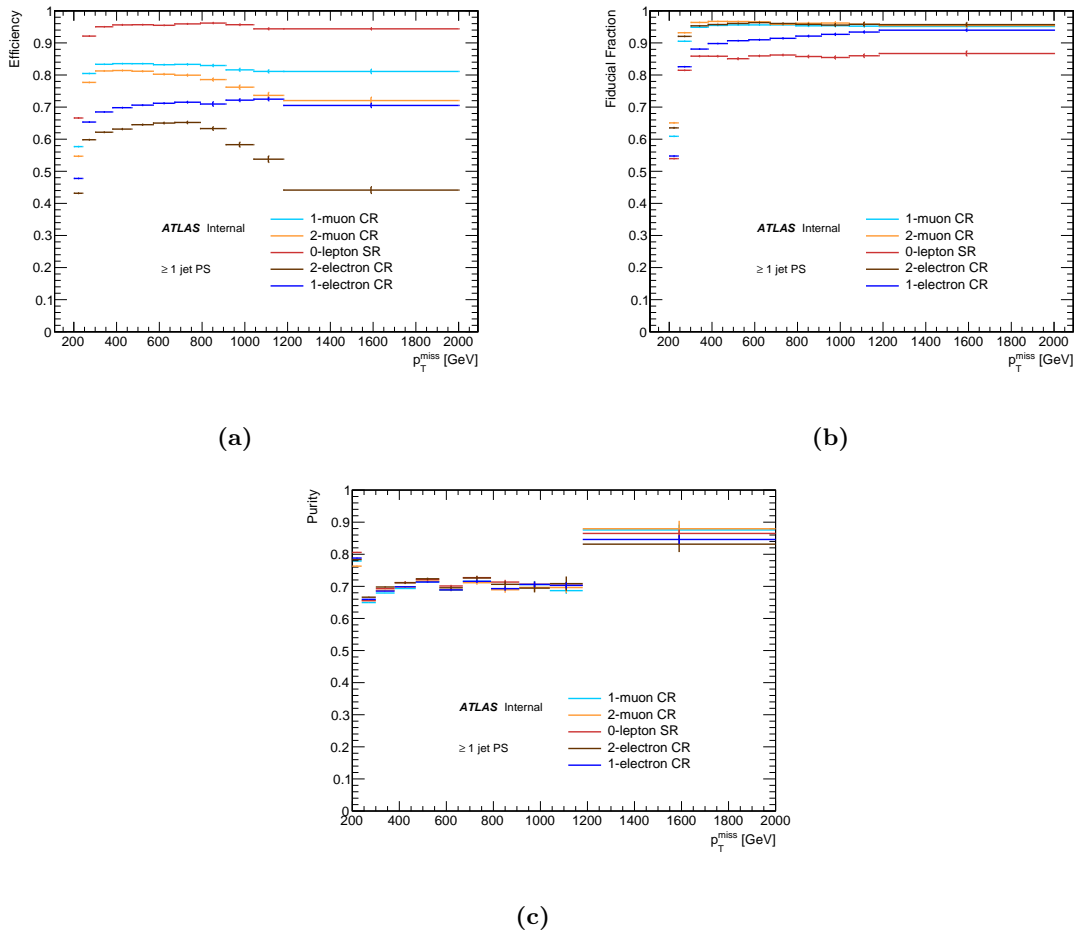


Figure 4.3 (a) Reconstruction efficiency, (b) fiducial fraction and (c) fiducial purity of the p_T^{miss} distribution in the ≥ 1 jet phase-space for all regions.

variation. The relative shift of the unfolded result produced with the varied detector response compared to the one produced with the nominal detector response is taken as the unfolded systematic uncertainty. A breakdown of how each group of systematic uncertainties affects the unfolded measurement is shown in figure 4.4 for the p_T^{miss} distributions of all regions in the ≥ 1 jet phase-space. The effect of each systematic group on the unfolded data follows the same trend as the one seen on the detector-level results, with the dominant systematic in all regions coming from the jet calibration techniques. In regions containing leptons, the second most dominant systematic is the one associated with the lepton efficiencies. Similar figures showing how each group of experimental systematic uncertainties affects the rest of the observables can be found in appendix D.

4.5.2 Hidden observables systematic

The regularisation step of the Iterative Bayesian Unfolding method requires a prior particle-level distribution which is taken from simulation. This introduces a dependence of the unfolded result on the modelling of the variable being unfolded which is quantified in the regularisation bias systematic and minimised in the iterative part of the method as discussed in Section 4.2. However, the unfolded result is also indirectly dependent on the modelling of variables different than the one being unfolded, often referred to as “hidden observables”. This can be quantified in a hidden observable systematic by following the same procedure outlined in Section 4.2 but this time reweighting events at particle-level so that the detector-level MC distribution of the hidden observable matches the one measured in the data. Figure 4.5 shows the hidden observable systematic coming from the modelling of the leading jet p_T in the $2e + \text{jets}$ region for three observables of interest. For the chosen number of iterations, $k = 2$, the systematic is at the sub-percent level for all observables.

4.5.3 Systematic for event migrations into the fiducial space

The particle and detector-level phase-spaces are defined using a number of selection requirements, based on different kinematic observables of an event. Due to resolution and acceptance effects,

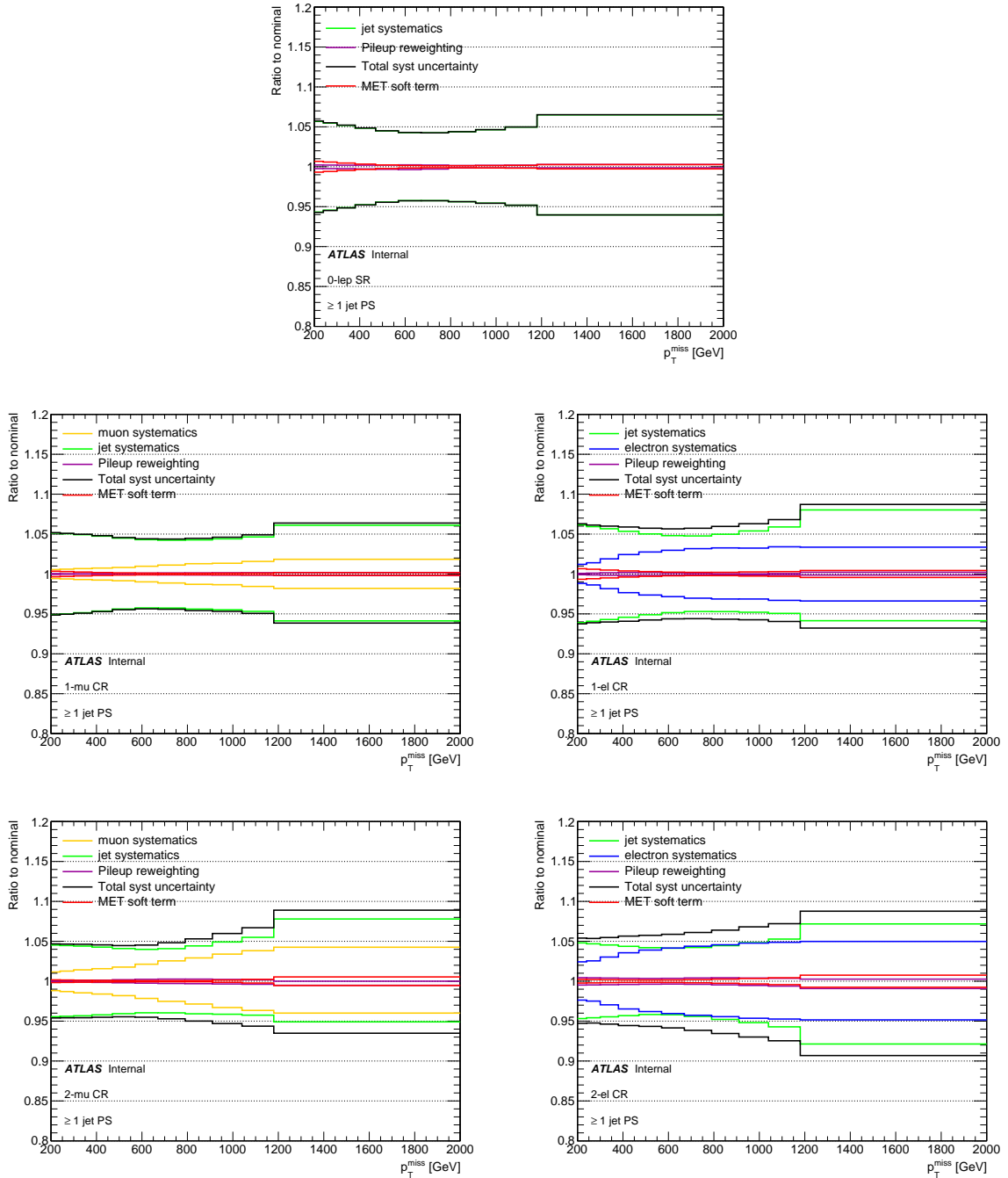


Figure 4.4 Systematic breakdown for p_T^{miss} in the ≥ 1 jet phase-space for all regions.

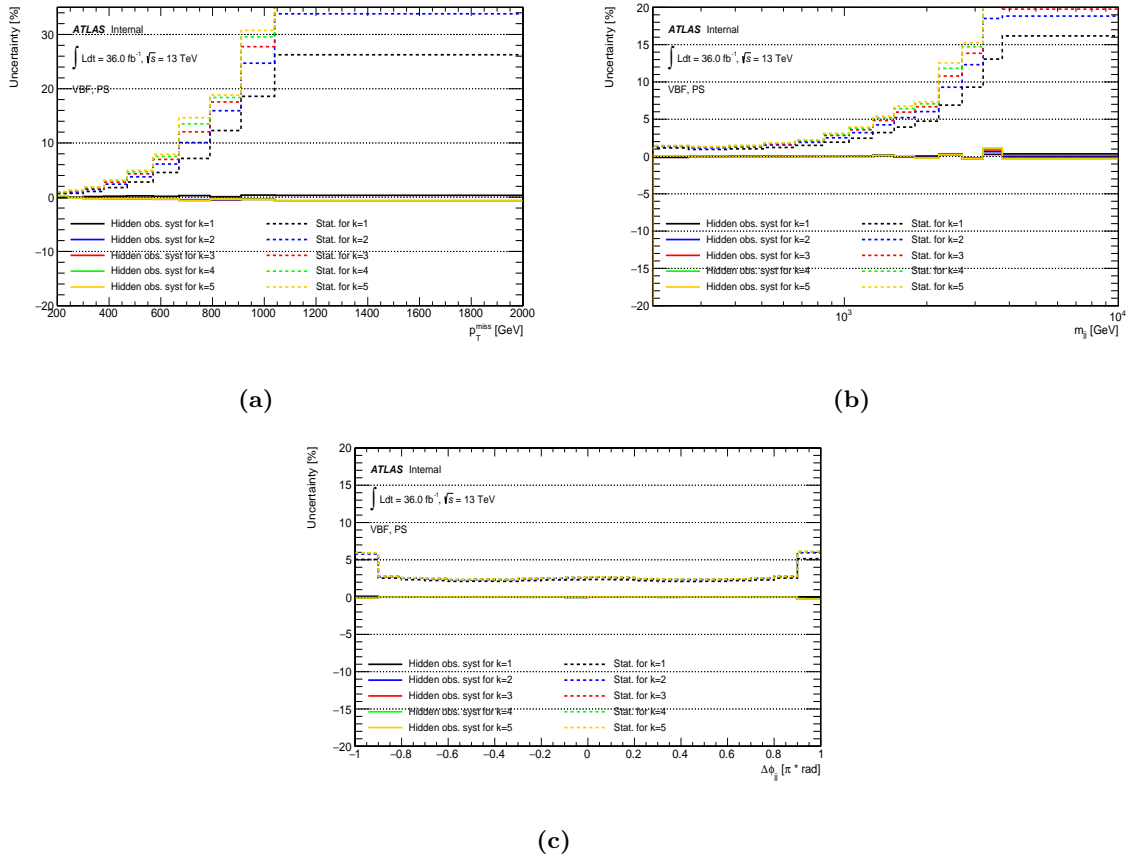


Figure 4.5 Hidden observable systematic coming from the modelling of the leading jet p_T in the $2e +$ jets for different values of the regularisation parameter k , for (a) p_T^{miss} , (b) m_{jj} and (c) $\Delta\phi_{jj}$ in the VBF phase-space. Statistical uncertainties are also shown as a function of k .

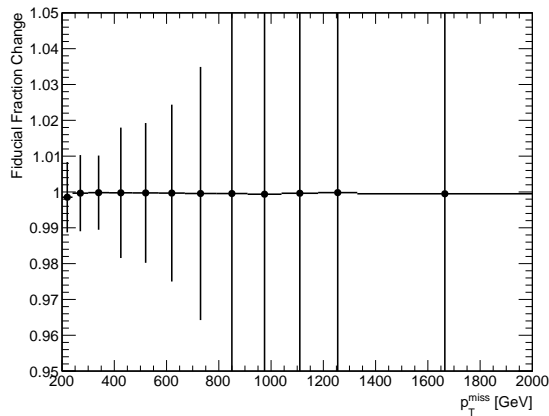


Figure 4.6 The fiducial fraction after reweighting is divided by the fiducial fraction before reweighting for p_T^{miss} in the ≥ 1 jet phase-space for the $2e + \text{jets}$ regions. Events were reweighted so that the detector-level distribution of p_T^{miss} matched the one measured in the data, with the requirement relaxed from $p_T^{\text{miss}} > 200$ GeV to $p_T^{\text{miss}} > 150$ GeV. The systematic is found to be negligible.

events that pass these criteria at the detector-level are not identical to those that pass the selection at the particle-level. If the underlying distribution, for an observable that is used to define a selection requirement, is not well modelled by the MC, then migrations in and out of the phase-space will not be properly modelled. In order to account for this effect, each requirement can be relaxed so that the agreement between the data and the detector-level MC prediction of an observable can be studied outside the measurement’s phase-space. A reweighting function can then be obtained and applied to MC events that pass the detector-level selection criteria so that the detector-level distribution of the observable in question matches the one measured in the data (with the selection requirement based on the observable relaxed). The effect is quantified by comparing the fiducial fraction of the main observable being unfolded, before and after reweighting. Figure 4.6 shows this comparison for p_T^{miss} in the ≥ 1 jet phase-space in the $2e + \text{jets}$ region, where events were reweighted so that the detector-level distribution of the p_T^{miss} observable matched the one measured in the data, with the requirement relaxed from $p_T^{\text{miss}} > 200$ GeV to $p_T^{\text{miss}} > 150$ GeV. The systematic is found to be completely negligible.

4.6 Process composition variations

Since the SM MC used to unfold the data consists of various different SM process contributions in each region, the unfolding is dependent on the modelling of the process composition. In particular, in the $p_T^{\text{miss}} + \text{jets}$ region, contributions from W processes and top processes will have different detector corrections than those from $Z \rightarrow \nu\nu$.

The relative contributions of different SM processes are only known to a certain accuracy. A systematic uncertainty from the knowledge of the relative contributions is found by varying each contribution in the detector response and determining the resulting effect on the unfolded results. MC pseudo-data is formed from the nominal composition and then unfolded using the varied detector response. A closure test is performed where the unfolded pseudo-data from the nominal composition sample is compared to the truth distribution from the nominal composition sample. Any residual difference is taken as a systematic uncertainty. Three process composition variations are investigated below.

W +jets contributions

The $W \rightarrow e\nu$, $W \rightarrow \mu\nu$ and $W \rightarrow \tau\nu$ contributions to the $p_T^{\text{miss}} + \text{jets}$ region are varied with a variation determined using a data driven technique that is sensitive to any differences between data and MC, regarding the number and kinematics of leptons used to veto events in the $p_T^{\text{miss}} + \text{jets}$ region [62, 63]. This is in turn sensitive to the relative contribution of W +jets events with out-of-acceptance leptons in the $p_T^{\text{miss}} + \text{jets}$ region. This study concludes that the best agreement between data and MC is achieved if the $W \rightarrow e\nu$ contribution is scaled by a factor of 0.9, the $W \rightarrow \mu\nu$ contribution is unscaled and the $W \rightarrow \tau\nu$ contribution is scaled by a factor of 1.2. For $W \rightarrow e\nu$ and $W \rightarrow \tau\nu$ these scaling factors are much larger than the uncorrelated theoretical uncertainties between the different V +jets processes that contribute to this region. Figure 4.7 shows a comparison between the nominal detector-level MC and the composition varied MC at the detector-level to show how the distributions differ. This is shown for p_T^{miss} in the ≥ 1 jet and VBF phase-spaces. The resulting bias in the unfolded distributions is shown in

Figure 4.8. It amounts to a negligible change for the $W \rightarrow e\nu$ variation and a 1% effect for the $W \rightarrow \tau\nu$ variation. The latter is included as a systematic uncertainty.

$t\bar{t}$ contributions

The $t\bar{t}$ process contribution in all five regions is varied with a variation obtained by combining the theoretical uncertainties on the top production modelling, as described in Section 3.6.1. The maximum variation in the cross-section is 25% or less for all regions. As a very conservative approach the top contribution is varied by 25%. Studies in appendix B.1 show that this variation is also large enough to account for the differences observed between data and MC in top-enhanced control regions. Figures 4.9, 4.11, 4.13 show a comparison between the nominal detector-level MC and the composition varied MC at the detector-level to show how the distributions differ. This is shown for p_T^{miss} , m_{jj} and $\Delta\phi_{jj}$ in the VBF phase-space. Figures 4.10, 4.12, 4.14 show the comparison between unfolded and particle-level nominal composition MC to demonstrate the size of the bias from this effect. For all variations and all distributions the effect is negligible, demonstrating that the unfolding is robust against exact knowledge of the process composition. No uncertainty is thus assigned to this variation.

Single-top Wt associated production contributions

An additional uncertainty depending on the subtraction scheme used to account for interference terms in different top processes (Diagram Subtraction (DS) or Diagram Removal (DR)) is studied by using either MC sample to simulate the Wt associated production contributions in the detector response. The effect of this on the unfolded results is shown in figures 4.15, 4.16, 4.17 for p_T^{miss} , m_{jj} and $\Delta\phi_{jj}$ in the VBF phase-space for the $p_T^{\text{miss}} + \text{jets}$, $1e + \text{jets}$ and $1\mu + \text{jets}$ regions. The effect is negligible for all distributions and well within the theory uncertainties on the top production modelling in these regions.

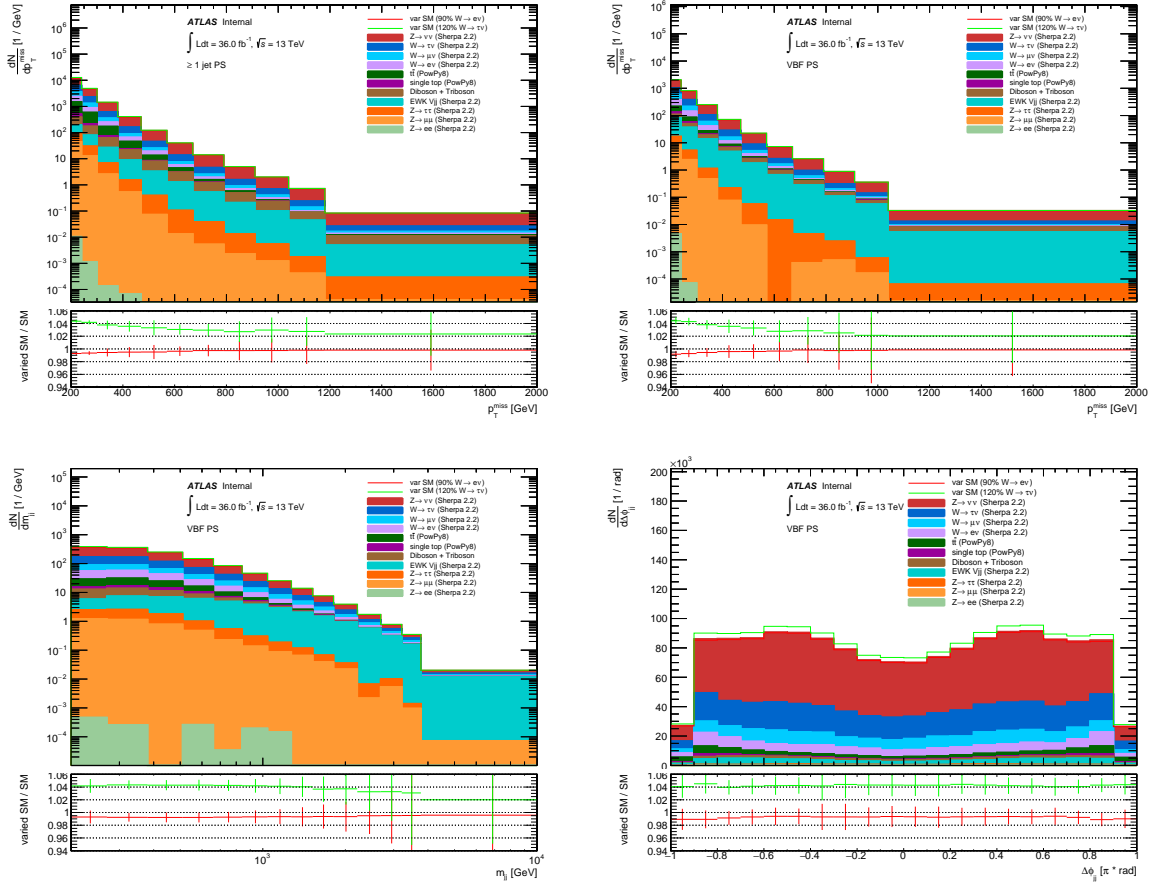


Figure 4.7 Nominal detector-level MC compared to process composition varied detector-level MC for p_T^{miss} in the $p_T^{\text{miss}} + \text{jets}$ region for the ≥ 1 jet and VBF phase-spaces. The $W \rightarrow e\nu$ cross-section is scaled by a factor of 0.9 and the $W \rightarrow \tau\nu$ cross-section is scaled by a factor of 1.2.

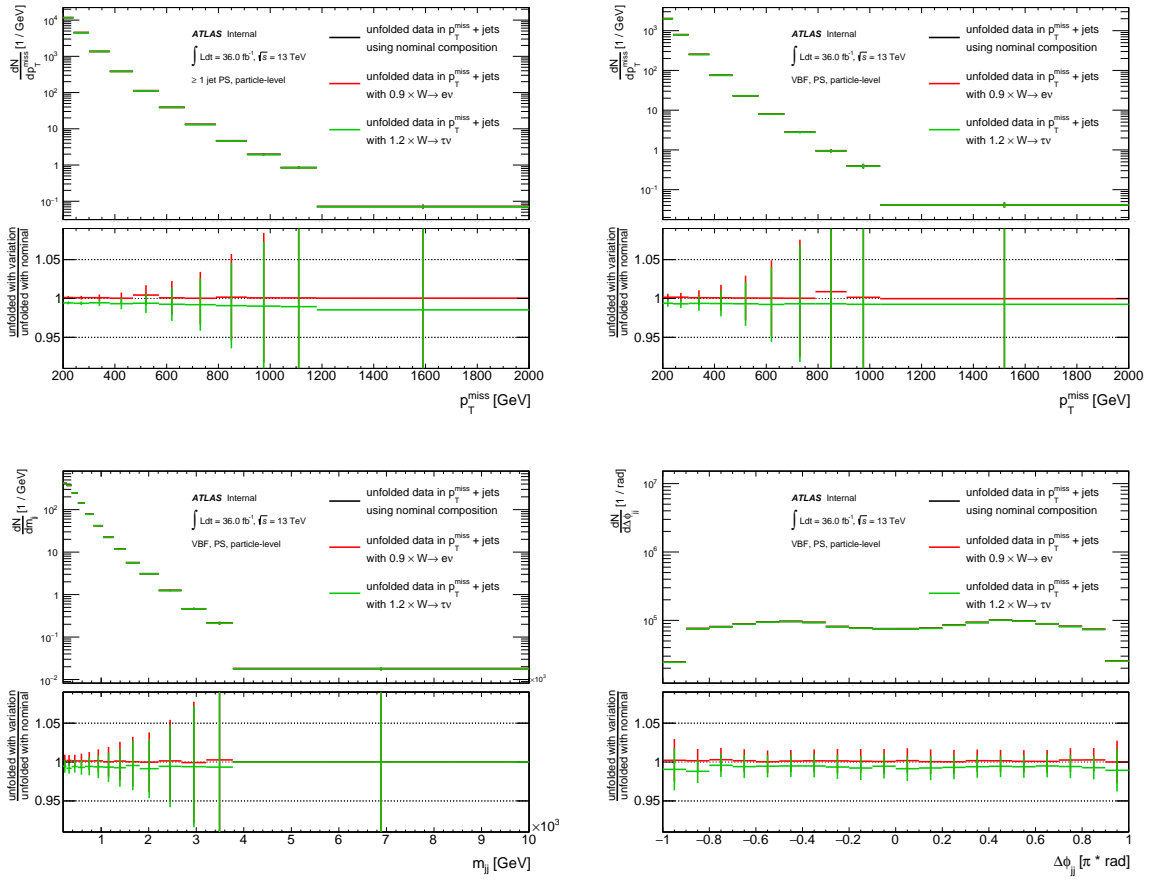


Figure 4.8 Resulting bias in the unfolded distribution following variations of the $W \rightarrow e\nu$, $W \rightarrow \mu\nu$ and $W \rightarrow \tau\nu$ cross-sections, for p_T^{miss} in the ≥ 1 jet phase-space, p_T^{miss} , m_{jj} and $\Delta\phi_{jj}$ in the VBF phase-space.

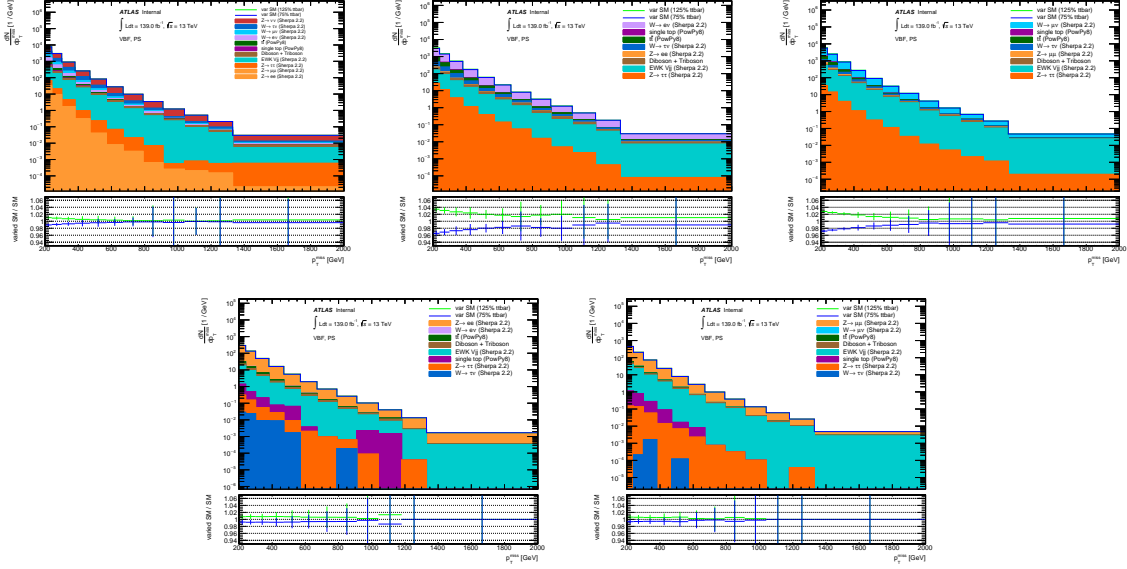


Figure 4.9 Nominal detector-level MC compared to process composition varied detector-level MC for p_T^{miss} in all regions for the VBF phase-space. The top cross-sections are varied by $\pm 25\%$.

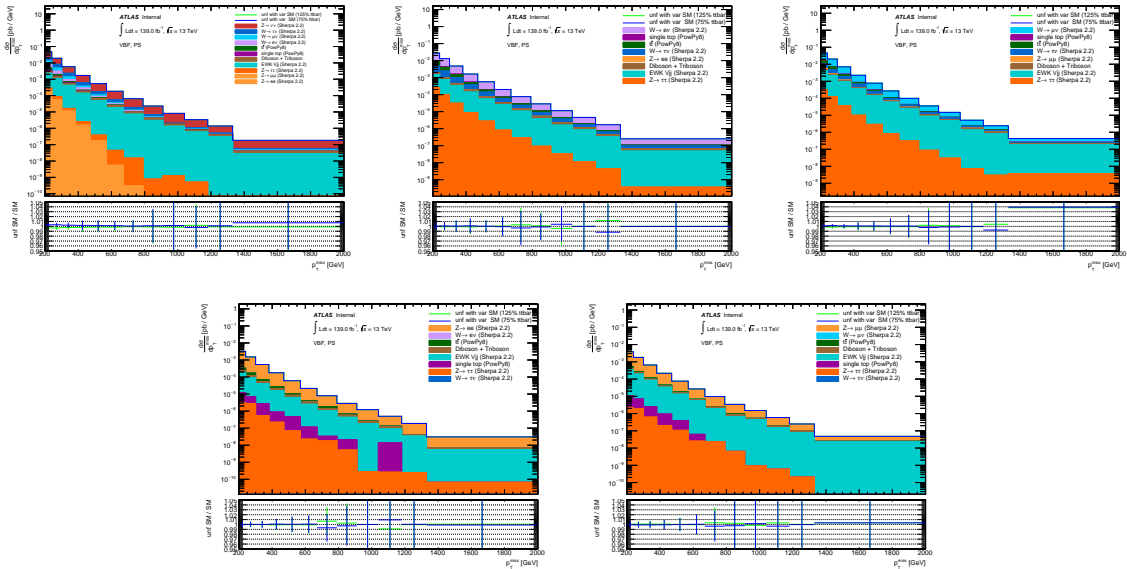


Figure 4.10 Unfolded nominal MC compared to nominal particle-level MC for p_T^{miss} in all regions for the VBF phase-space. The unfolding is done with the top cross-sections varied by $\pm 25\%$ in the detector response.

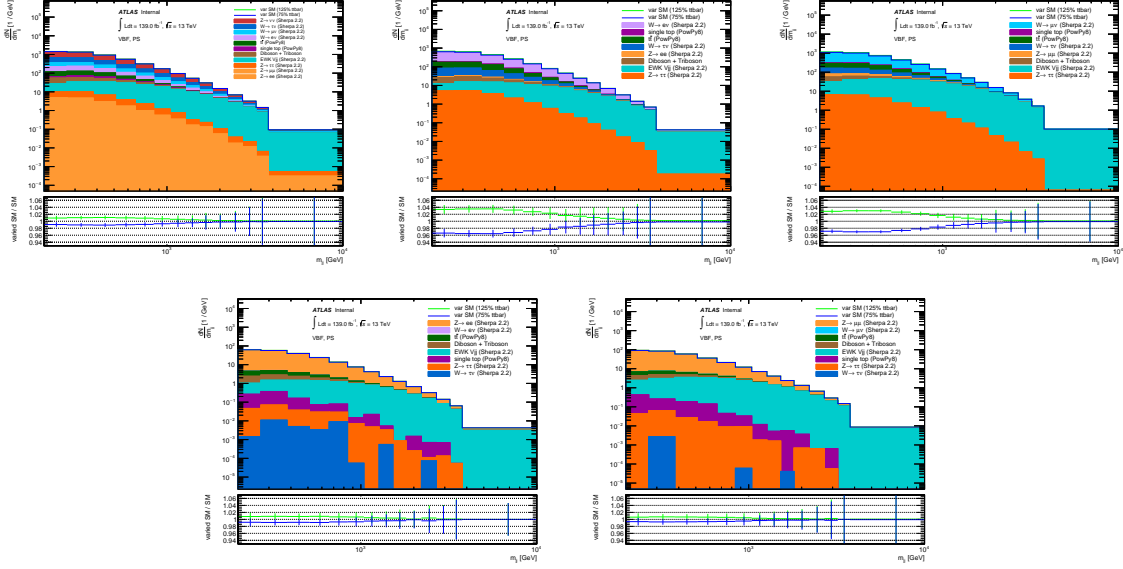


Figure 4.11 Nominal detector-level MC compared to process composition varied detector-level MC for m_{jj} in all regions for the VBF phase-space. The top cross-sections are varied by $\pm 25\%$.

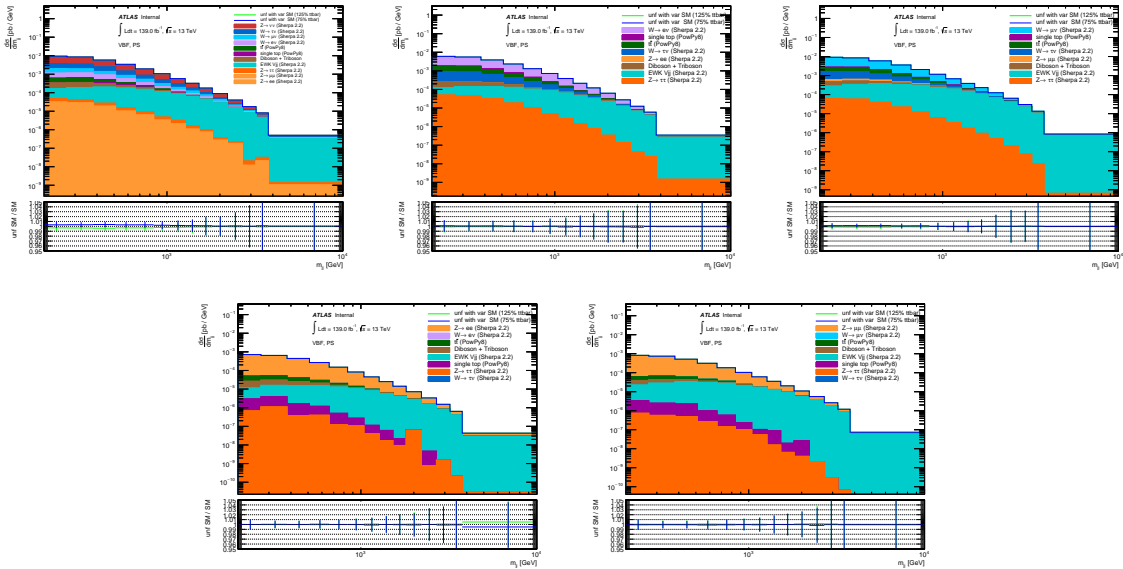


Figure 4.12 Unfolded nominal MC compared to nominal particle-level MC for m_{jj} in all regions for the VBF phase-space. The unfolding is done with the top cross-sections varied by $\pm 25\%$ in the detector response.

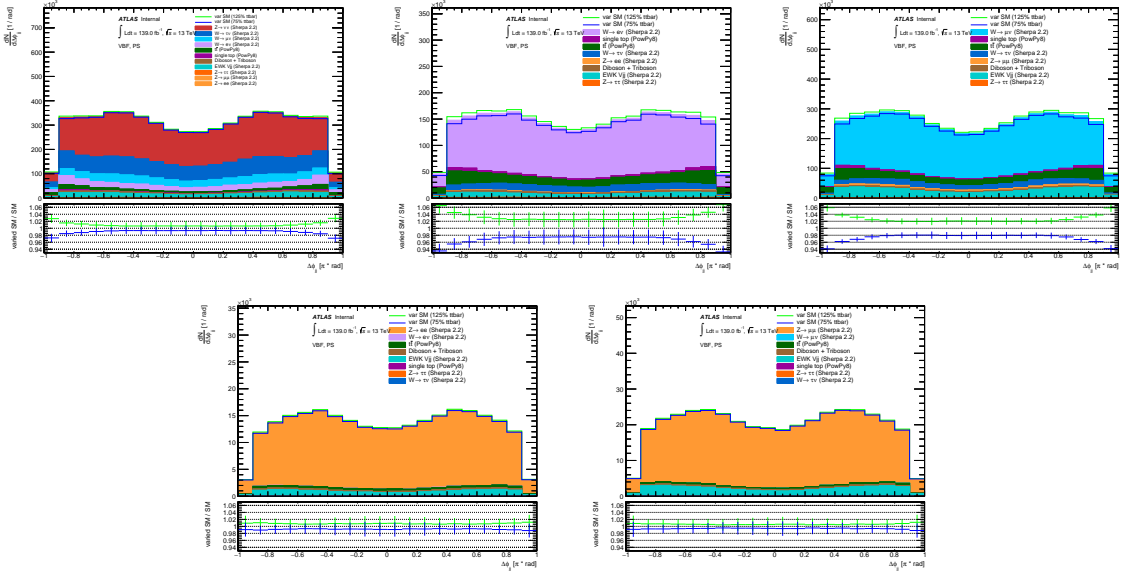


Figure 4.13 Nominal detector-level MC compared to process composition varied detector-level MC for $\Delta\phi_{jj}$ in all regions for the VBF phase-space. The top cross-sections are varied by $\pm 25\%$.

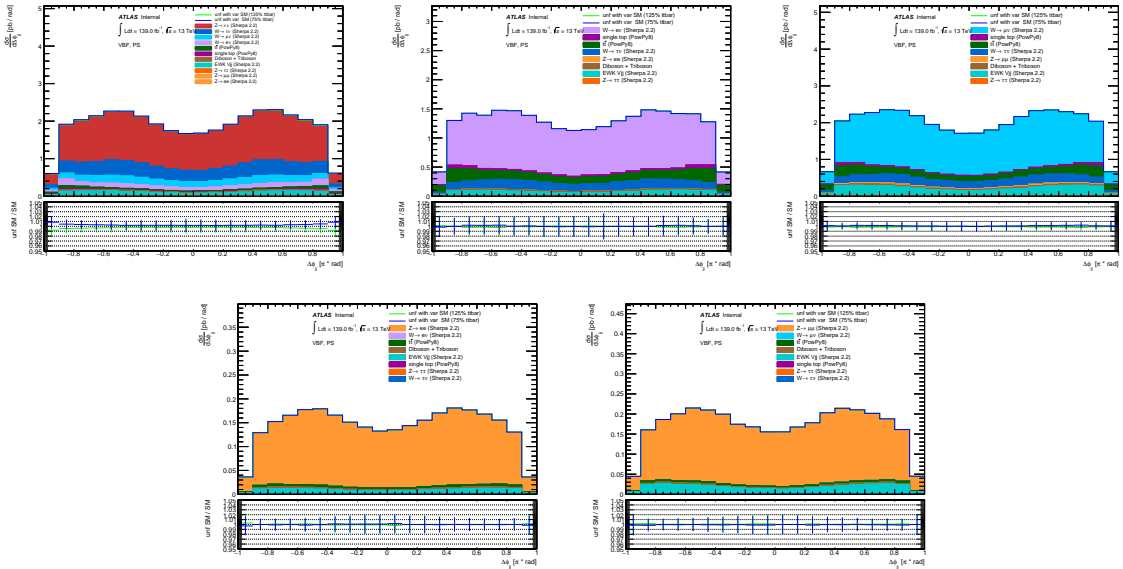


Figure 4.14 Unfolded nominal MC compared to nominal particle-level MC for $\Delta\phi_{jj}$ in all regions for the VBF phase-space. The unfolding is done with the top cross-sections varied by $\pm 25\%$ in the detector response.

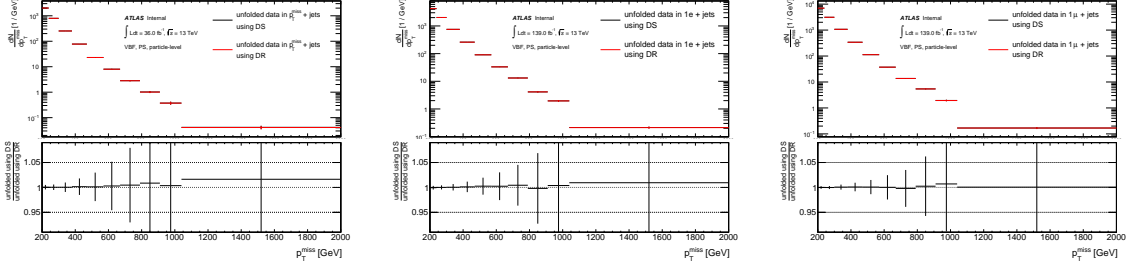


Figure 4.15 Comparisons between unfolded data distributions in the $p_T^{\text{miss}} + \text{jets}$ (left), $1e + \text{jets}$ (middle) and $1\mu + \text{jets}$ (right) region using either the DR or DS single-top subtraction scheme for p_T^{miss} in the VBF phase-space.

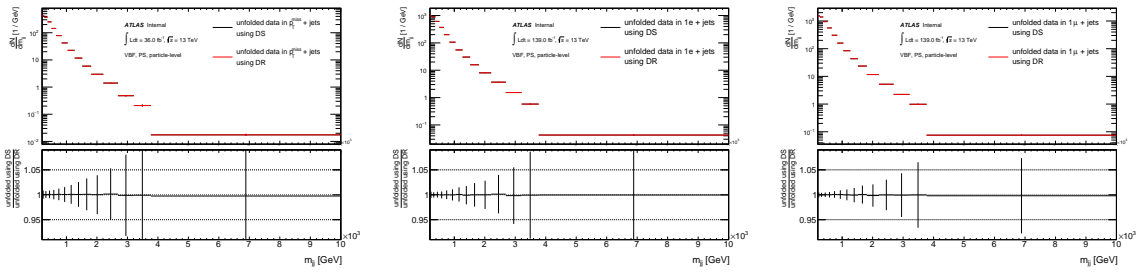


Figure 4.16 Comparisons between unfolded data distributions in the $p_T^{\text{miss}} + \text{jets}$ (left), $1e + \text{jets}$ (middle) and $1\mu + \text{jets}$ (right) region using either the DR or DS single-top subtraction scheme for m_{jj} in the VBF phase-space.

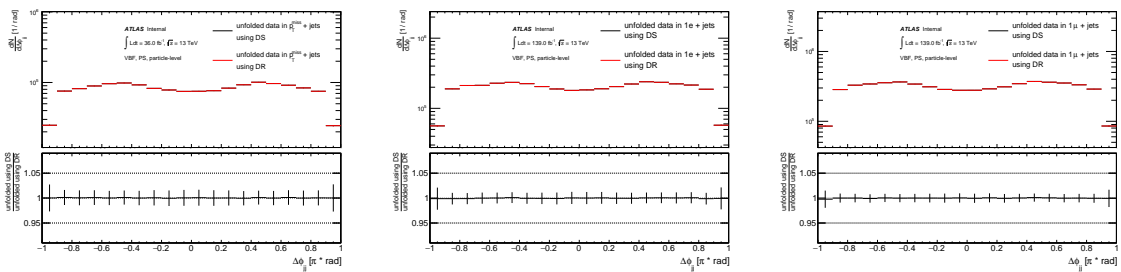


Figure 4.17 Comparisons between unfolded data distributions in the $p_T^{\text{miss}} + \text{jets}$ (left), $1e + \text{jets}$ (middle) and $1\mu + \text{jets}$ (right) region using either the DR or DS single-top subtraction scheme for m_{jj} in the VBF phase-space.

4.7 Signal injection tests

If the data contains BSM physics then the SM MC used to construct the detector response in the unfolding will not be representative of the data. In order to test if the unfolding is biased by possible BSM signal in the data, various BSM processes are injected into the SM MC, which is then treated as pseudo-data and unfolded with a detector response constructed from the nominal SM MC. In the following plots two samples of VBF produced Higgs events decaying invisibly (to four neutrinos via two Z bosons) with the branching fraction of the Higgs to this decay channel set to 100%, are used, testing a very extreme Higgs to invisible particles scenario. The two samples correspond to two different Higgs masses: 125 GeV and 750 GeV. Figure 4.18 shows comparisons between detector-level SM+BSM and SM only MC for m_{jj} and $\Delta\phi_{jj}$ in the VBF phase-space in the $p_T^{\text{miss}} + \text{jets}$ region. A clear enhancement is seen at large m_{jj} and small $\Delta\phi_{jj}$ values. Figure 4.19 shows the unfolded SM+BSM MC compared to truth SM+BSM MC for the same distributions. The bias in the unfolded results is negligible for all but the high m_{jj} bins, where it reaches up to 10%.

The test is repeated for p_T^{miss} in the ≥ 1 jet phase-space, where four BSM samples are used. Figure 4.20 shows comparisons between detector-level SM+BSM and SM only MC using the following s-channel DM models:

- DM model with a spin-1 axial-vector mediator with $m_\chi = 1$ GeV and $m_A = 50$ GeV.
- DM model with a spin-1 axial-vector mediator with $m_\chi = 1$ GeV and $m_A = 700$ GeV.
- DM model with a spin-1 axial-vector mediator with $m_\chi = 355$ GeV and $m_A = 700$ GeV.
- DM model with a spin-0 pseudo-scalar mediator with $m_\chi = 1$ GeV and $m_A = 50$ GeV.

A large enhancement is seen for the two axial-vector mediator models with $m_\chi = 1$ GeV. Figure 4.21 shows the unfolded SM+BSM MC compared to truth SM+BSM MC. A small bias of up to about 10% is seen at large p_T^{miss} for the two models mentioned above.

The effects on the unfolded distributions are likely to come from the differences in fiducial fraction and efficiency depending on the processes contributing to $p_T^{\text{miss}} + \text{jets}$ region. When

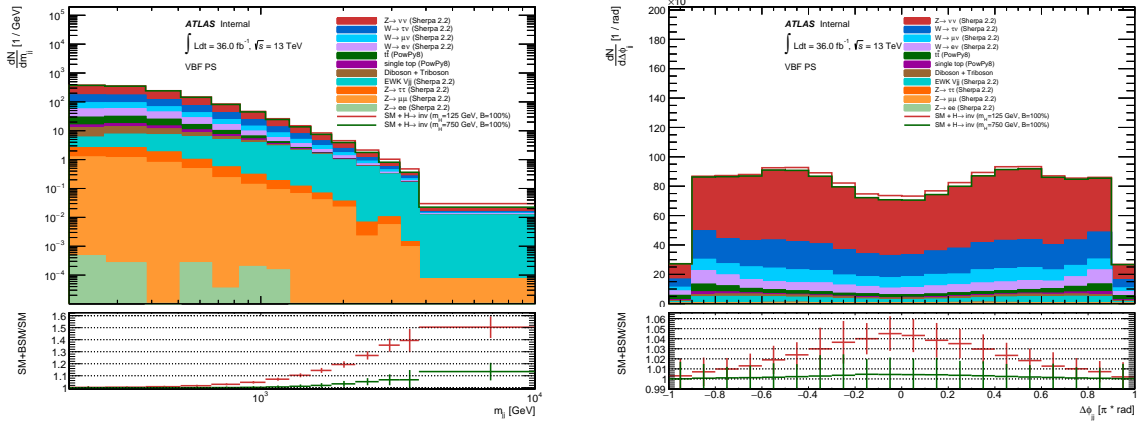


Figure 4.18 detector-level SM+BSM MC compared to nominal MC for m_{jj} (left) and $\Delta\phi_{jj}$ (right) in the $p_T^{\text{miss}} + \text{jets}$ regions for the VBF phase-space.

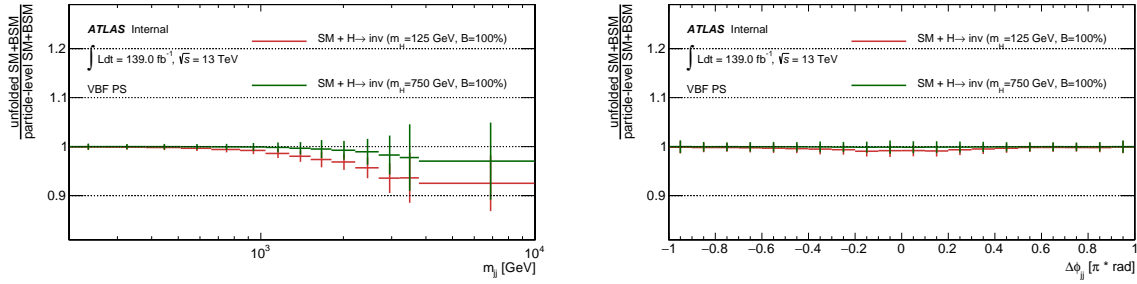


Figure 4.19 Unfolded SM+BSM MC compared to truth SM+BSM MC for m_{jj} (left) and $\Delta\phi_{jj}$ (right) in the $p_T^{\text{miss}} + \text{jets}$ regions for the VBF phase-space. The unfolding is done with SM only MC.

BSM models with no leptons in the final state are injected into the MC process composition, there is a larger fraction of $Z \rightarrow \nu\nu$ -like events and hence the overall fiducial fraction increases. When unfolded with SM-only MC, this leads to a decrease in the unfolded event yield. All of the above models describe extreme BSM scenarios and in order to have any non-negligible effects on the unfolding procedure, a BSM signal would need to be completely inconsistent with the data.

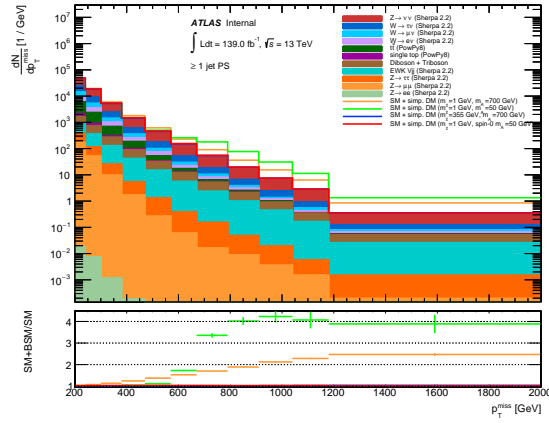


Figure 4.20 detector-level SM+BSM MC compared to nominal MC for p_T^{miss} in the $p_T^{\text{miss}} + \text{jets}$ region for the ≥ 1 jet phase-space.

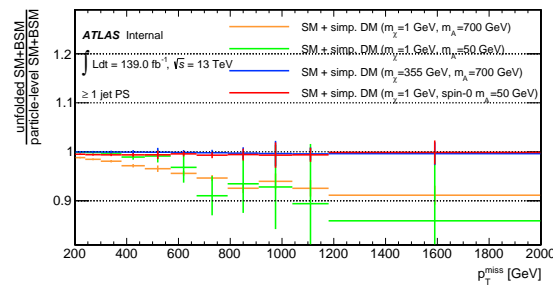


Figure 4.21 Unfolded SM+BSM MC compared to truth SM+BSM MC for p_T^{miss} in the $p_T^{\text{miss}} + \text{jets}$ regions for the ≥ 1 jet phase-space. The unfolding is done with SM only MC.

4.8 $Z \rightarrow \nu\bar{\nu} + \text{jets}$ slicing method bias

The effect the two different slicing schemes for $Z \rightarrow \nu\bar{\nu} + \text{jets}$ mentioned in Section 3.5 have on the unfolded result is investigated by using either of the schemes to construct the detector response used in the unfolding procedure. Figure 4.22 shows comparisons for the contributions of the $Z \rightarrow \nu\bar{\nu} + \text{jets}$ samples in the $p_{\text{T}}^{\text{miss}} + \text{jets}$ region at the detector-level using either of the two schemes. The comparisons are shown for $p_{\text{T}}^{\text{miss}}$ and m_{jj} in the VBF phase-space. Large differences between the two schemes are observed for large m_{jj} values. Figure 4.23 shows comparisons between unfolded data distributions using either of the two slicing schemes in the detector response. No significant bias on the unfolded result is observed.

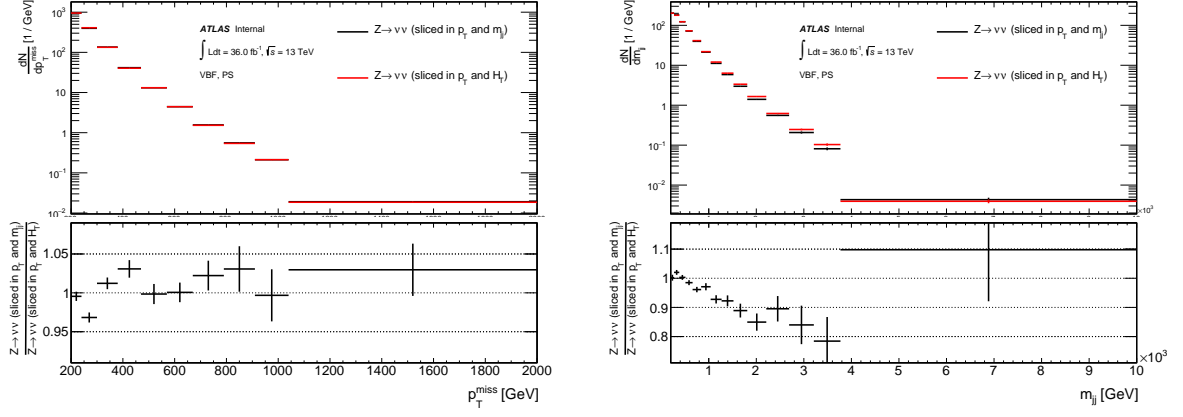


Figure 4.22 Comparisons for the contributions of the $Z \rightarrow \nu\bar{\nu} + \text{jets}$ samples in the $p_T^{\text{miss}} + \text{jets}$ region at the detector level, with the slicing based on the maximum of the boson p_T and the H_T in the event or based on a combination of the Z boson p_T and m_{jj} in events with at least two jets. The comparisons are shown for for p_T^{miss} (left) and m_{jj} (right) in the VBF phase-space.

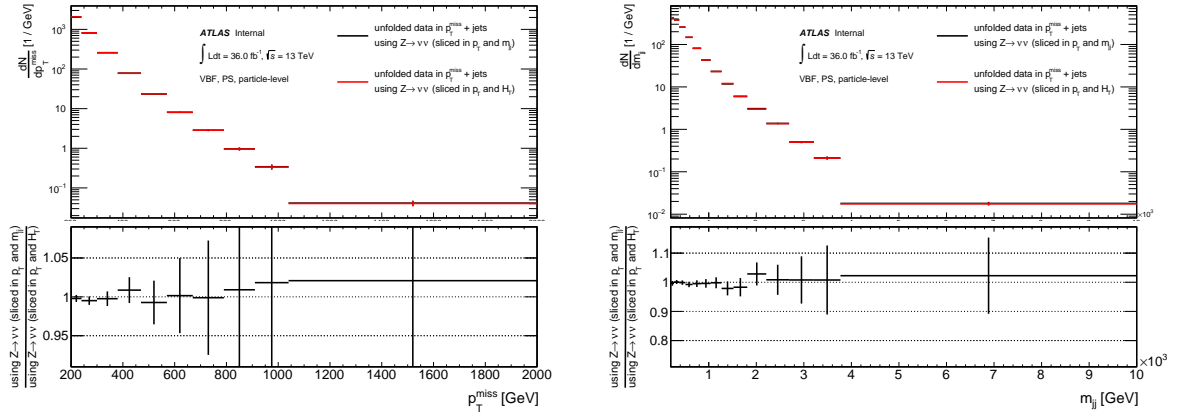


Figure 4.23 Comparisons between unfolded data distributions in the $p_T^{\text{miss}} + \text{jets}$ region, with a detector response constructed using the slicing based on the maximum of the boson p_T and the H_T in the event or based the Z boson p_T and m_{jj} in events with at least two jets. The comparisons are shown for for p_T^{miss} (left) and m_{jj} (right) in the VBF phase-space.

Chapter 5

Results

5.1 Detector corrected differential cross-sections

This chapter presents the results of the analysis discussed in this thesis. Detector corrected differential cross-sections measured in the data are compared to particle-level SM predictions. In the $p_T^{\text{miss}} + \text{jets}$ region, these are also compared to predictions assuming the presence of additional BSM models. Backgrounds from QCD multijet events in the $p_T^{\text{miss}} + \text{jets}$ region are subtracted from the data prior to the unfolding. Contributions to the SM prediction are shown as stacked histograms. In the bottom panel of each Figure a ratio of unfolded data to MC is shown where the statistical uncertainties are shown as error bars. Systematic uncertainties added in quadrature to the statistical uncertainties are only shown in the ratio panel as a band with hatched lines. The band includes the experimental systematic uncertainties discussed in Section 4.5 as well as the effect of the theoretical systematic uncertainties on the unfolded data discussed in section 4.6. Theoretical systematic uncertainties on the particle-level SM predictions are shown as a pink band. As observed in the detector-level results, large statistical contributions to the calculation of these uncertainties lead to shape differences in the theory uncertainty band between regions. These fluctuations are expected to reduce with a more precise calculation of the theory uncertainties, which is currently in progress. Since this is an ongoing analysis, the $p_T^{\text{miss}} + \text{jets}$ region is blinded to the 2017 and 2018 datasets to avoid biases in the analysis' strategy and methodology. Comparisons between data and MC in the

$p_T^{\text{miss}} + \text{jets}$ region are instead shown using only the unfolded 2015 and 2016 datasets and the corresponding MC campaign.

Figures 5.1, 5.2 and 5.3 show comparisons between unfolded data and particle-level SM predictions for p_T^{miss} and p_T^{miss} vs $p_T^{j_1}$ respectively, in the ≥ 1 jet phase-space for all regions. The unfolded data in the p_T^{miss} distribution are also compared to three simplified models of WIMP production with an s -channel exchange of an axial-vector mediator coupling to quarks and WIMPs. Three combinations for the mass of the WIMPs (m_χ) and the mass of the mediator (m_A) are considered: $m_\chi = 1$ GeV and $m_A = 700$ GeV; $m_\chi = 1$ GeV and $m_A = 50$ GeV; $m_\chi = 355$ GeV and $m_A = 700$ GeV. Similarly to the detector-level distributions, a 10% to 20% discrepancy is observed between the unfolded data and MC in the p_T^{miss} distribution in all regions. However, the shape of the distribution is reasonably well modeled and deviations from the MC prediction observed in the data are covered by the theoretical systematic uncertainties. A slightly larger disagreement between unfolded data and MC is observed for low values of p_T^{miss} in the $2e + \text{jets}$ lepton region compared to the $2\mu + \text{jets}$ lepton region. For the p_T^{miss} vs $p_T^{j_1}$ distributions the ratio between unfolded data and MC decreases with increasing values of $p_T^{j_1}$ for all regions. This is again covered by the band of theoretical systematic uncertainties, which are estimated using the uncertainty versus p_T^{miss} in each region.

Figures 5.4, 5.5 and 5.6 show comparisons between unfolded data and particle-level SM predictions for p_T^{miss} , m_{jj} , and $\Delta\phi_{jj}$ for all regions in the ≥ 2 jet phase-space. The unfolded data are also compared to three BSM models representing the Higgs boson decaying to invisible particles with 100% branching fraction, where the Higgs is produced in association with a vector boson: W^- , W^+ and Z . Figures 5.7 and 5.8 show comparisons for m_{jj} vs $\Delta\phi_{jj}$ for all regions in the ≥ 2 jet phase-space. Overall shifts in normalisation and shape discrepancies in the p_T^{miss} distribution are similar to those seen in the ≥ 1 jet region. The m_{jj} distribution is badly modeled by the MC in all regions with the MC exhibiting a much harder m_{jj} distribution than the unfolded data. These discrepancies are again covered by the theoretical systematic uncertainties. This can also be seen in the m_{jj} vs $\Delta\phi_{jj}$ distributions of Figures 5.7 and 5.8 where the ratio between data and MC decreases for slices with larger m_{jj} values. The theoretical uncertainties on this Figures are estimated using the uncertainty versus m_{jj} in each region

and cover most of the discrepancies. The $\Delta\phi_{jj}$ distribution is peaked towards small values, for close together jets, with a dip at very low values as the jets cannot be exactly on top of each other. The unfolded data has a slightly more peaked structure than the MC in all regions. The discrepancy in the shape becomes more pronounced at larger m_{jj} values, as seen in Figure 5.7.

Figures 5.9, 5.10 and 5.11 show comparisons between unfolded data and particle-level SM predictions for p_T^{miss} , m_{jj} , and $\Delta\phi_{jj}$ for all regions in the VBF phase-space. The unfolded data are also compared to two BSM models representing the Higgs boson decaying to invisible particles with 100% branching fraction, where the Higgs is produced with a mass of $m_H = 75$ GeV and $m_H = 750$ GeV respectively. Figures 5.12 and 5.13 shows comparisons for m_{jj} vs $\Delta\phi_{jj}$ for all regions in the VBF phase-space. The agreement between data and MC in the p_T^{miss} distributions exhibits a similar pattern as the one observed in the ≥ 1 jet and ≥ 2 jet phase-spaces. The m_{jj} is badly modeled in a similar way as in the ≥ 2 jet phase-space and as in the detector-level distributions. It is observed that the contributions from the EWK production of V +dijets events at the particle-level are larger in the VBF phase-space compared to the ≥ 2 jet phase-space. The $\Delta\phi_{jj}$ distribution has a larger dip at low values, compared to the same distribution in the ≥ 2 jet phase-space, due to the particle-level m_{jj} cut in this region. The discrepancies between data and MC are similar to those seen in the ≥ 2 jet phase-space and are largely covered by the theoretical systematic uncertainties. The agreement in the m_{jj} vs $\Delta\phi_{jj}$ distributions of Figures 5.12 and 5.13 also exhibits a similar pattern as the ones in the ≥ 2 jet phase-space.

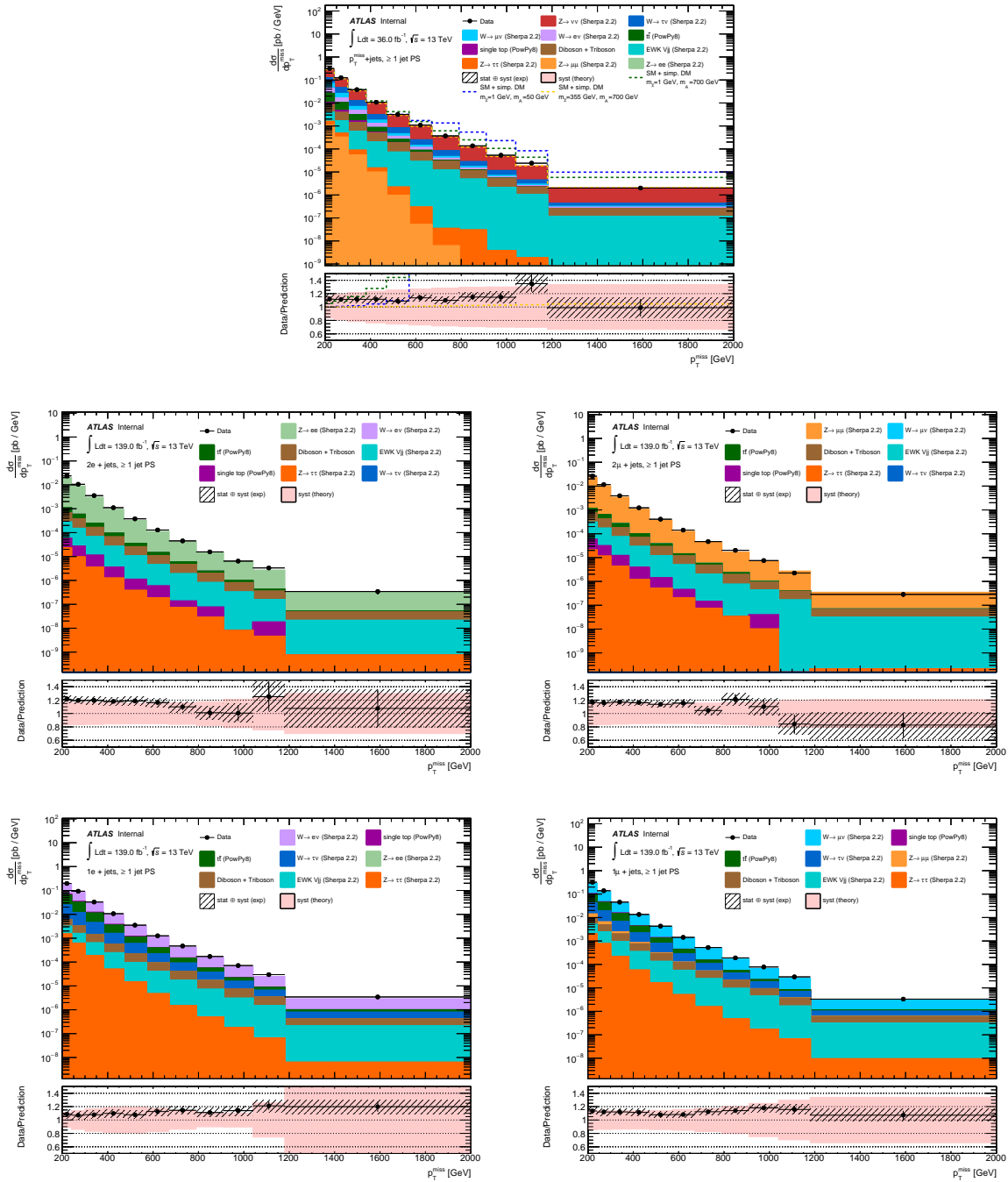


Figure 5.1 Particle-level data/MC comparisons for p_T^{miss} in the ≥ 1 jet phase-space. The hatched lines show the combination of statistical and systematic uncertainties. The pink band shows the theoretical uncertainties on the particle-level SM prediction.

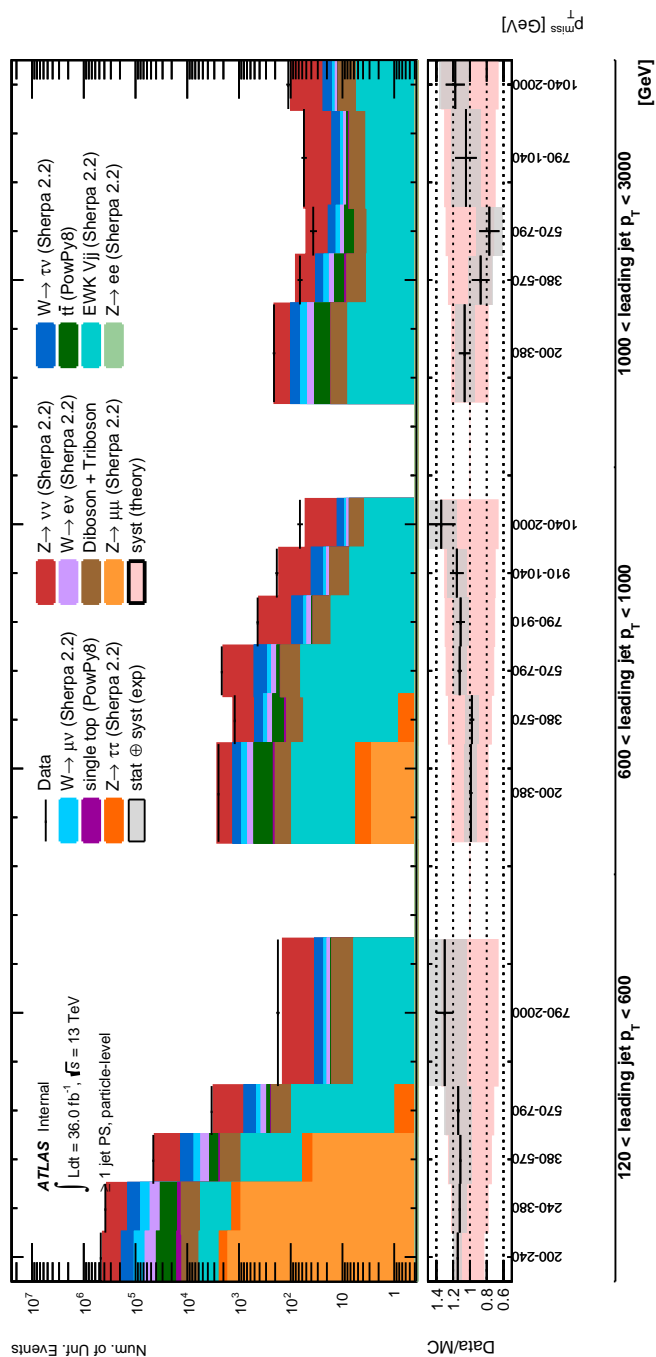


Figure 5.2 Particle-level data/MC comparisons for $p_{\text{T}}^{\text{miss}}$ vs p_{T}^1 in the ≥ 1 jet phase-space for the $p_{\text{T}}^{\text{miss}} + \text{jets}$ region. The grey band shows the combination of statistical and systematic uncertainties. The pink band shows the theoretical uncertainties on the particle-level SM prediction.

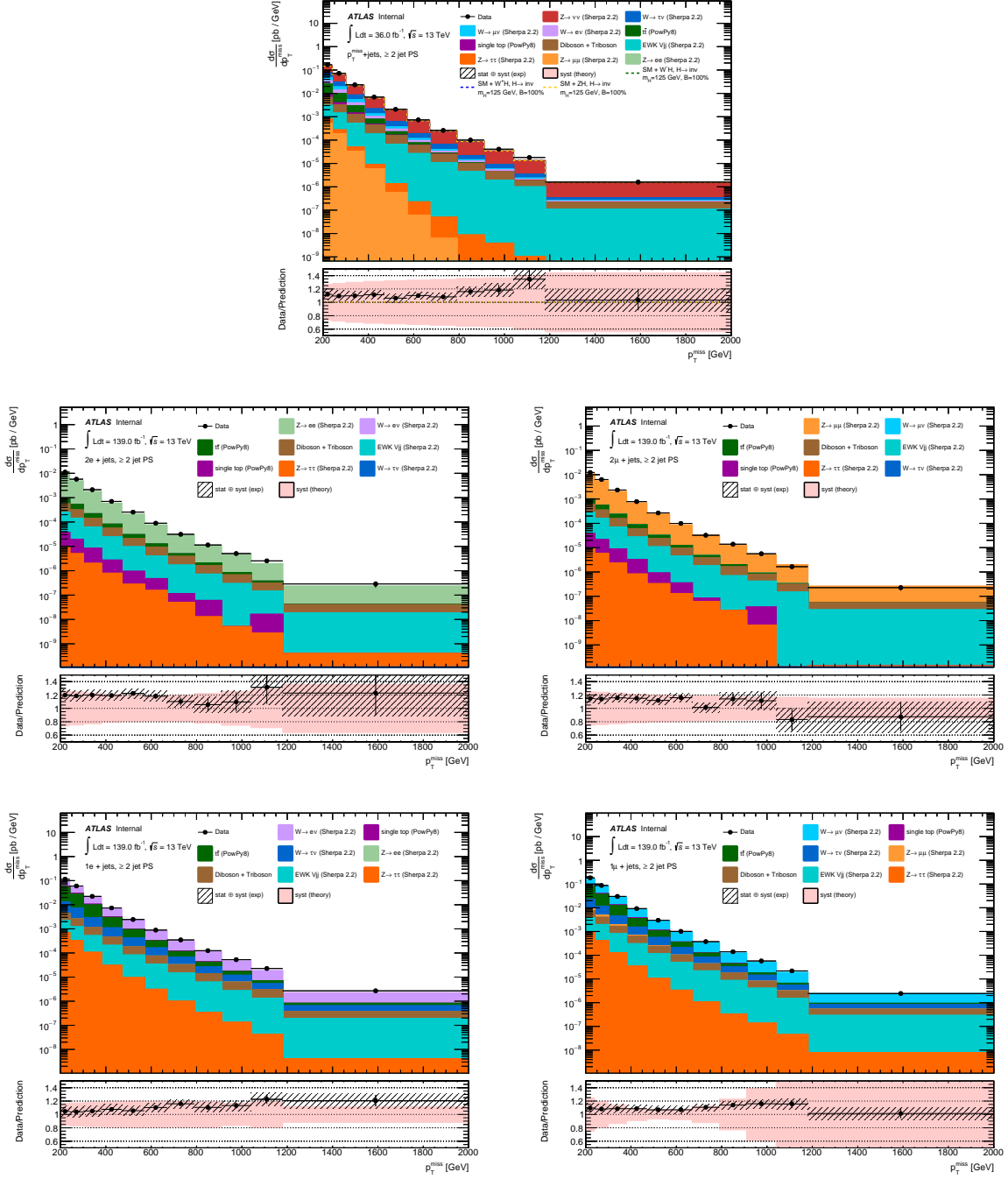


Figure 5.4 Particle-level data/MC comparisons for p_T^{miss} in the ≥ 2 jet phase-space. The hatched lines show the combination of statistical and systematic uncertainties. The pink band shows the theoretical uncertainties on the particle-level SM prediction.

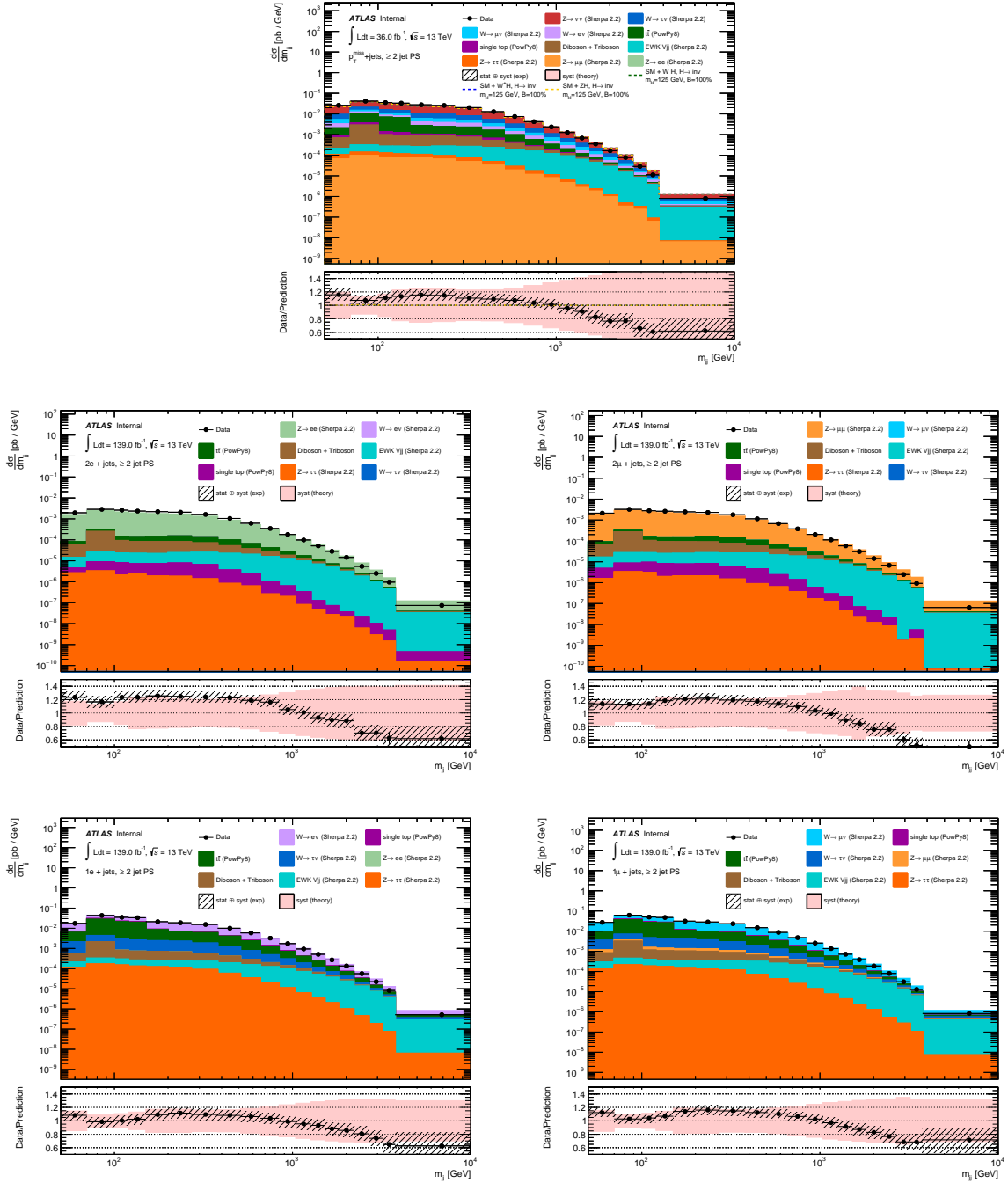


Figure 5.5 Particle-level data/MC comparisons for m_{jj} in the ≥ 2 jet phase-space. The hatched lines show the combination of statistical and systematic uncertainties. The pink band shows the theoretical uncertainties on the particle-level SM prediction.

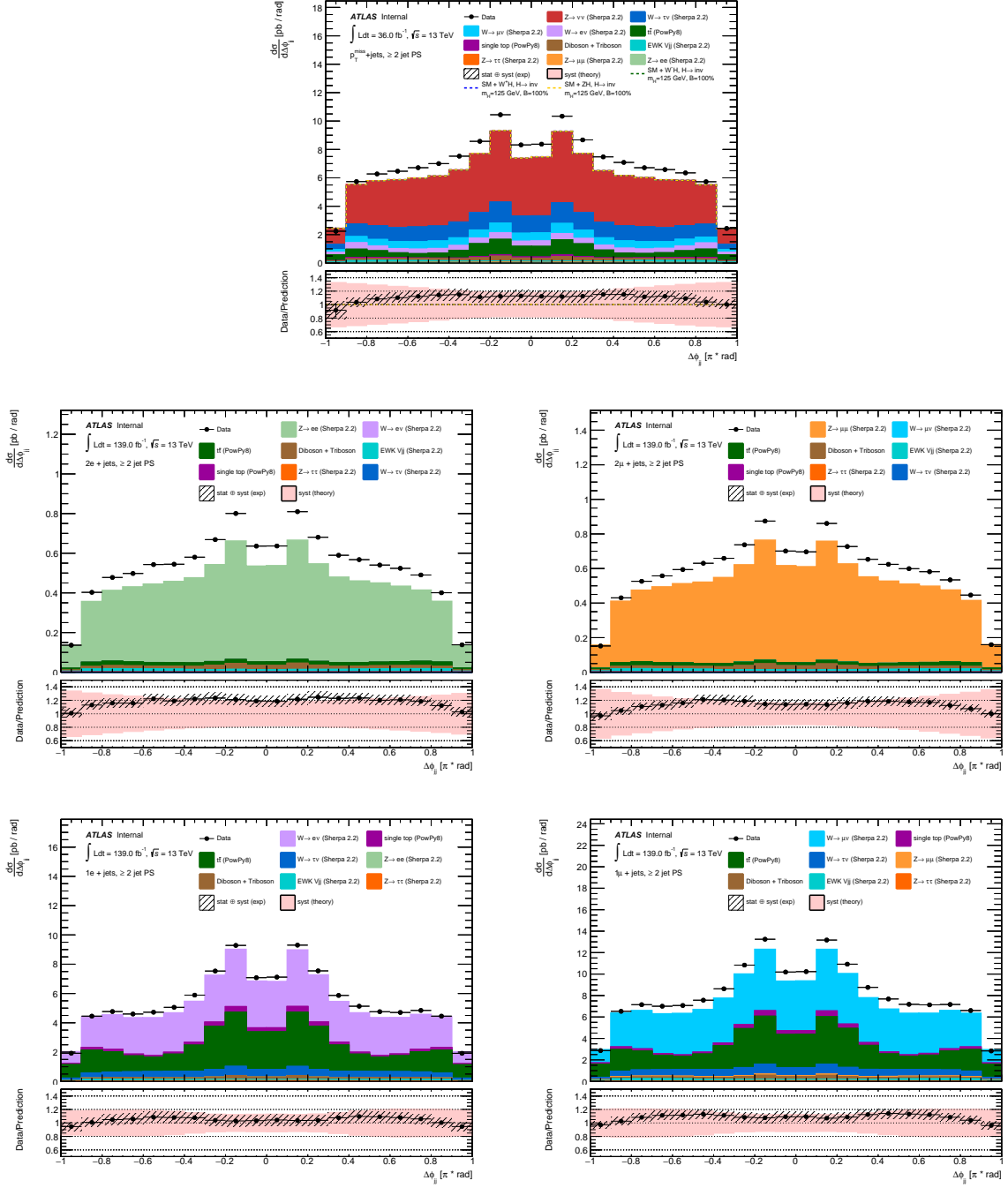


Figure 5.6 Particle-level data/MC comparisons for $\Delta\phi_{jj}$ in the ≥ 2 jet phase-space. The hatched lines show the combination of statistical and systematic uncertainties. The pink band shows the theoretical uncertainties on the particle-level SM prediction.

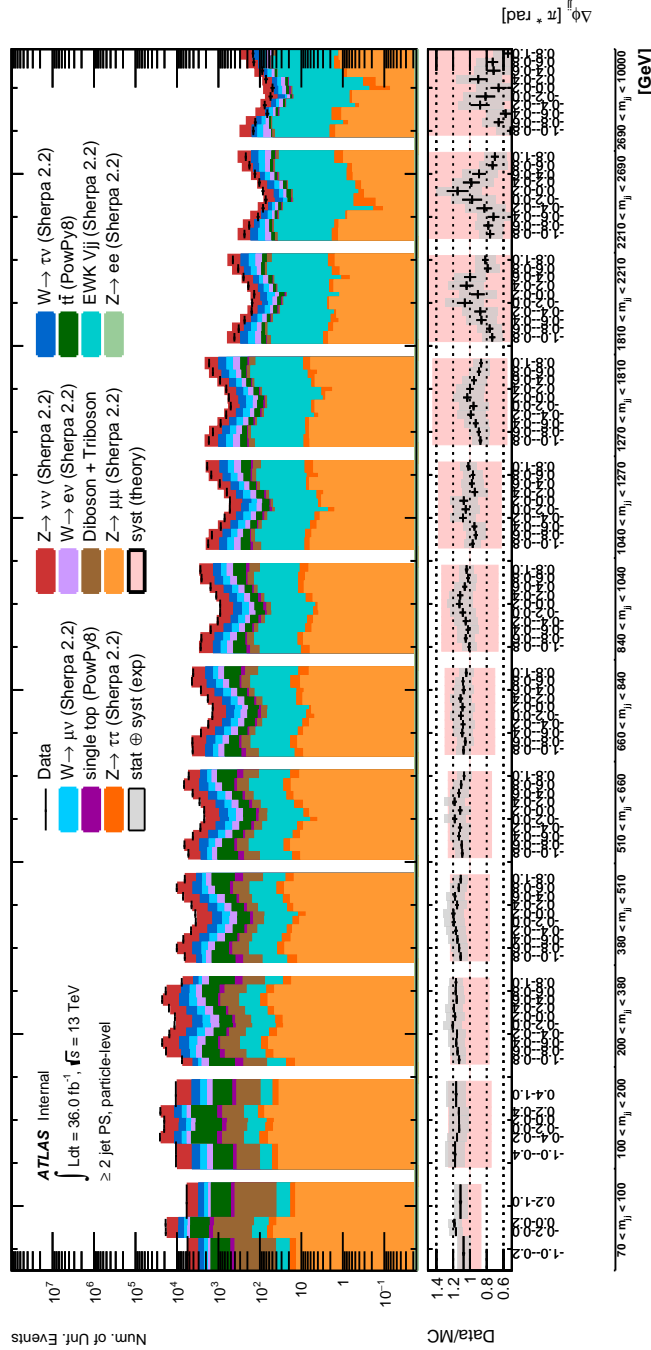


Figure 5.7 Particle-level data/MC comparisons for m_{jj} vs $\Delta\phi_{jj}$ in the ≥ 2 jet phase-space for the $p_T^{\text{miss}} + \text{jets}$ region. The grey band shows the combination of statistical and systematic uncertainties. The pink band shows the theoretical uncertainties on the particle-level SM prediction.

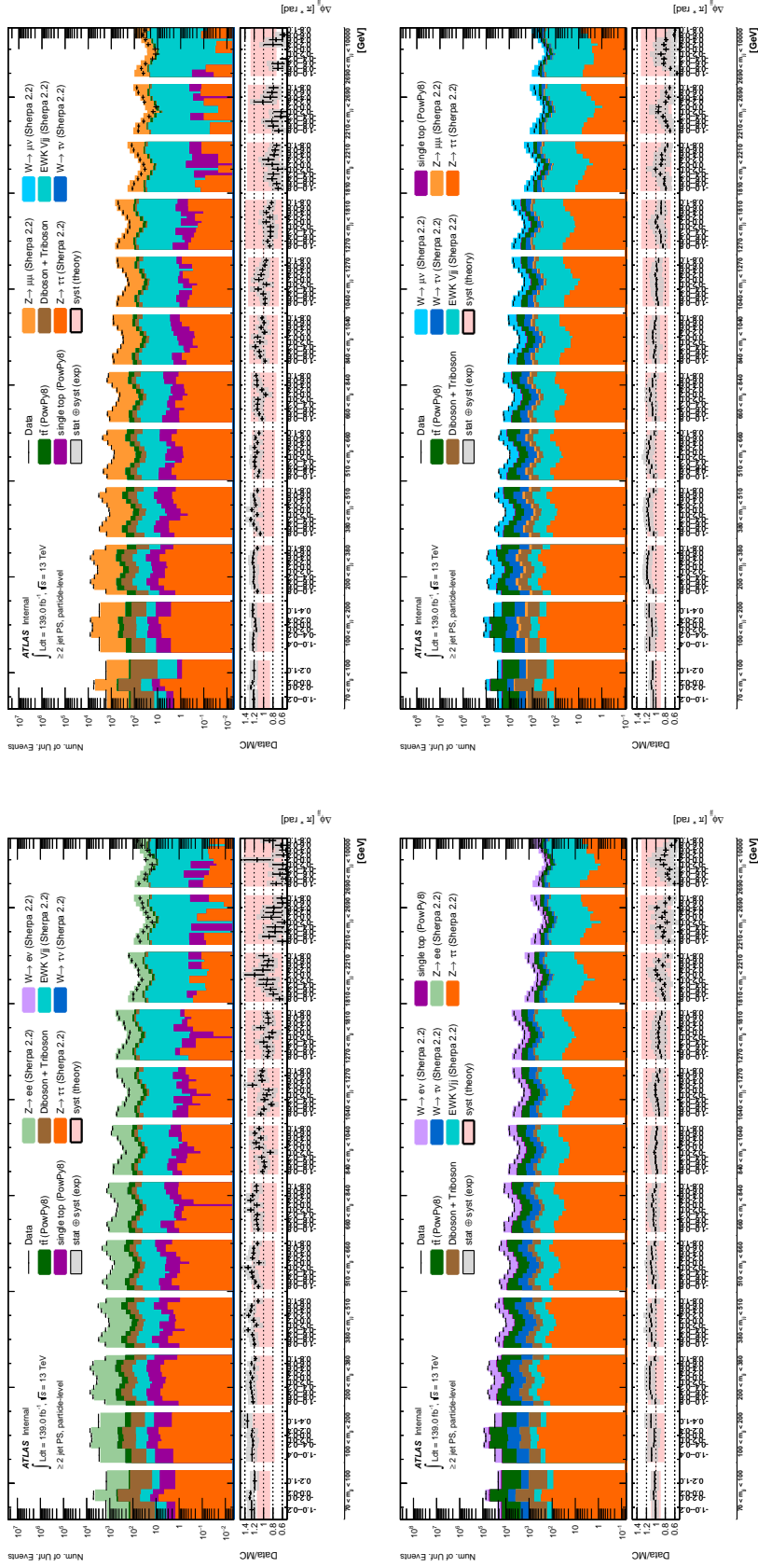


Figure 5.8 Particle-level data/MC comparisons for m_{jj} vs $\Delta\phi_{jj}$ in the ≥ 2 jet phase-space for the $1\ell + \text{jets}$ and $2\ell + \text{jets}$ regions. The grey band shows the combination of statistical and systematic uncertainties. The pink band shows the theoretical uncertainties on the particle-level SM prediction.

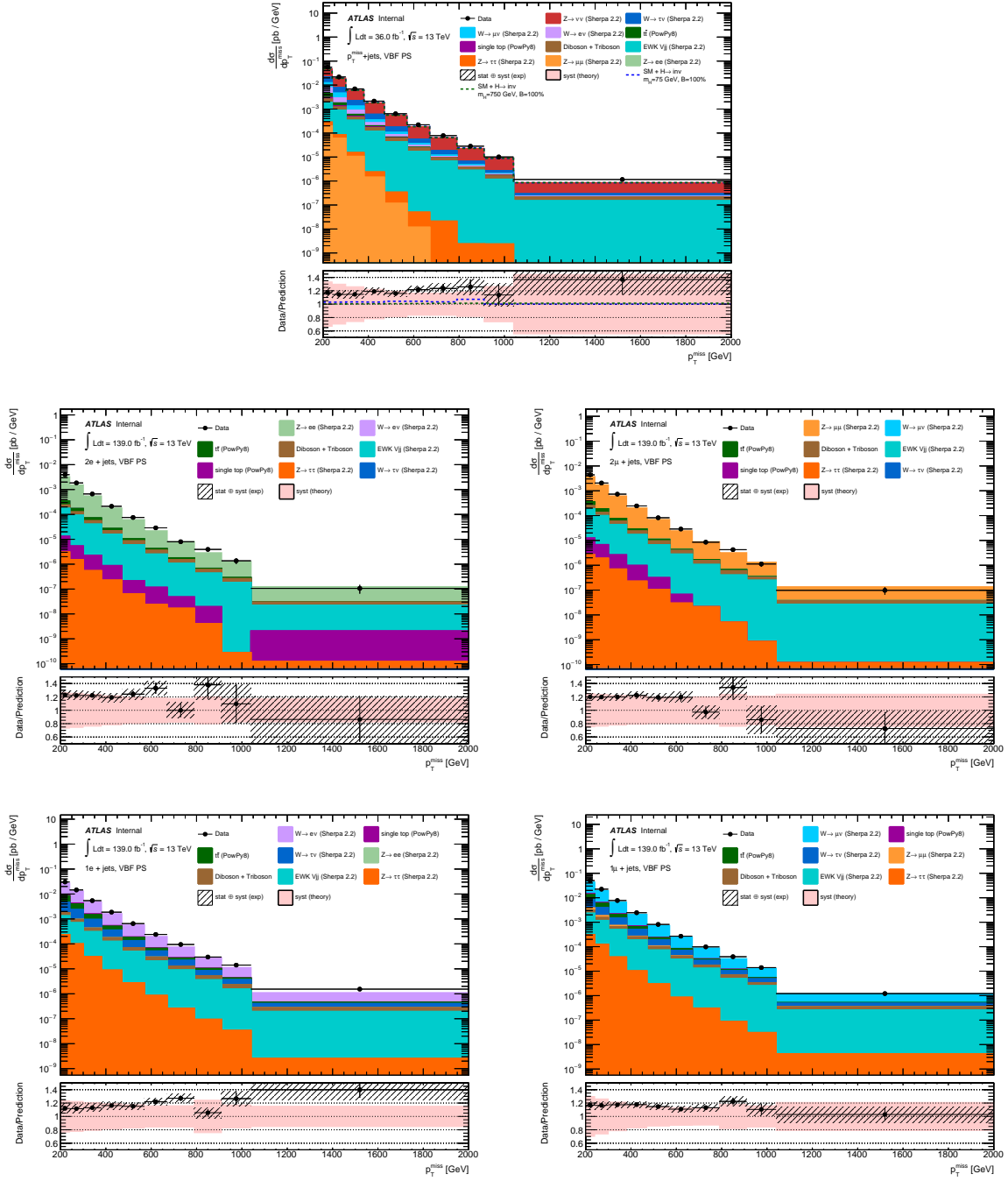


Figure 5.9 Particle-level data/MC comparisons for p_T^{miss} in the VBF phase-space. The hatched lines show the combination of statistical and systematic uncertainties. The pink band shows the theoretical uncertainties on the particle-level SM prediction.

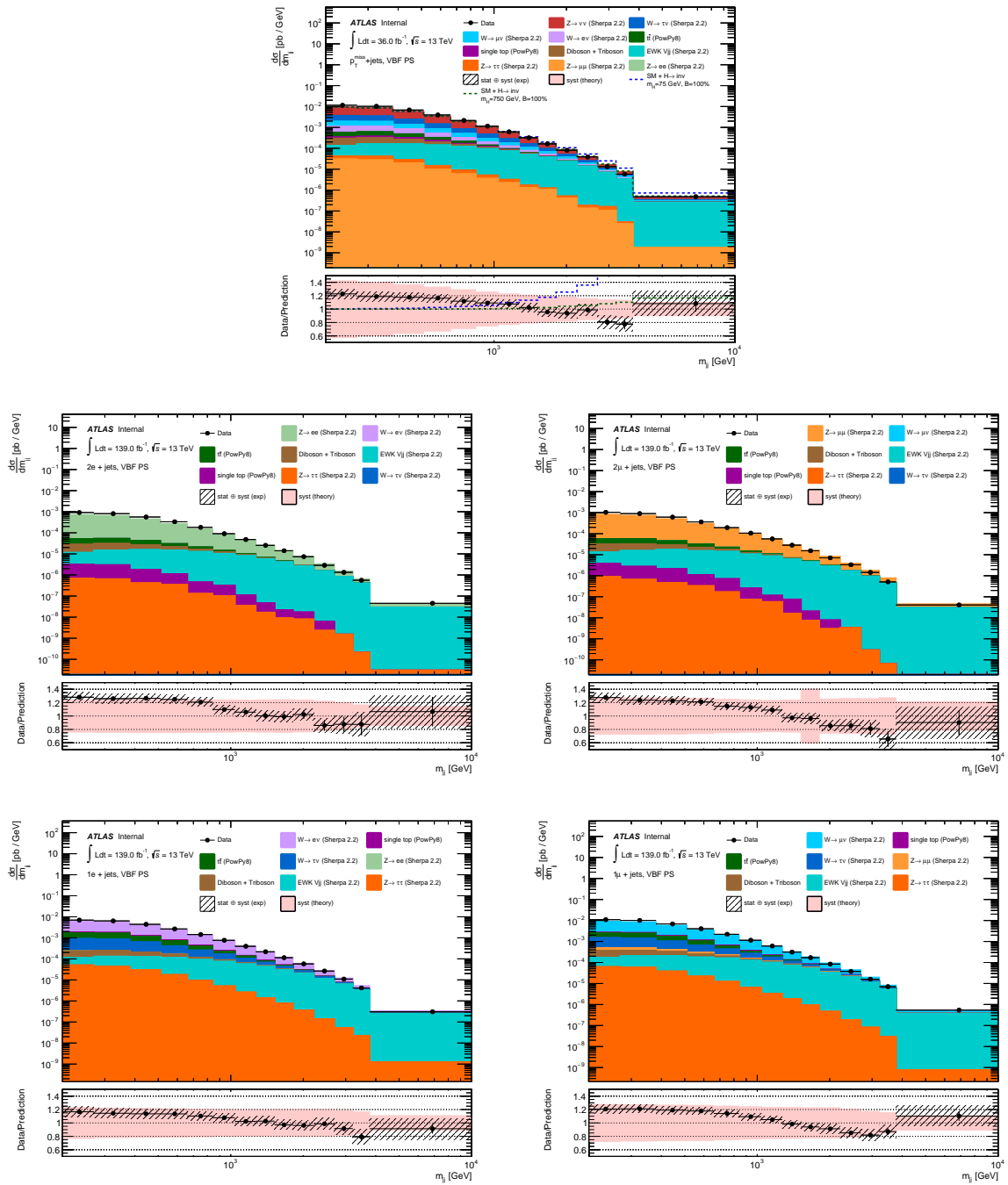


Figure 5.10 Particle-level data/MC comparisons for m_{jj} in the VBF phase-space. The hatched lines show the combination of statistical and systematic uncertainties. The pink band shows the theoretical uncertainties on the particle-level SM prediction.

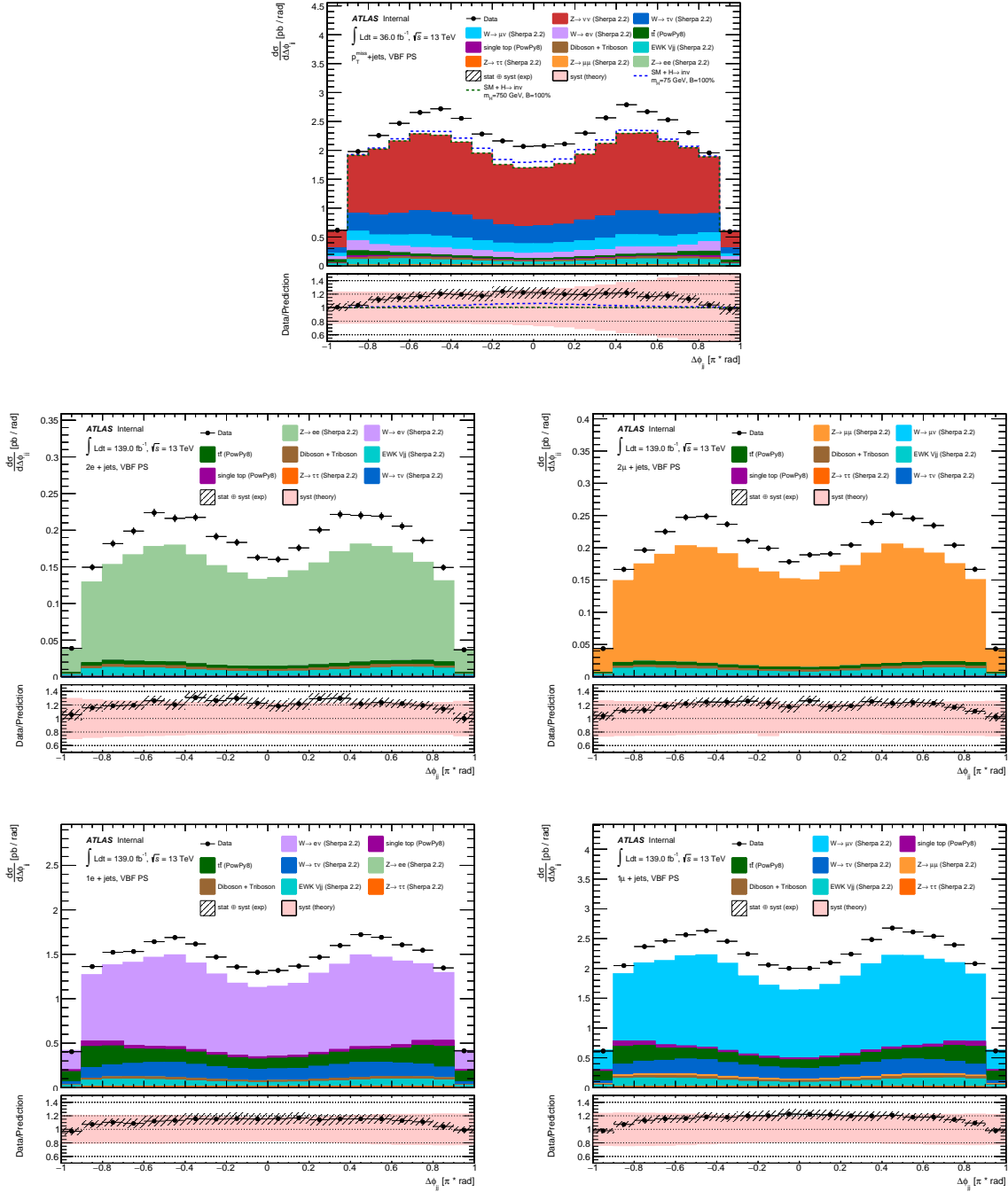


Figure 5.11 Particle-level data/MC comparisons for $\Delta\phi_{jj}$ in the VBF phase-space. The hatched lines show the combination of statistical and systematic uncertainties. The pink band shows the theoretical uncertainties on the particle-level SM prediction.

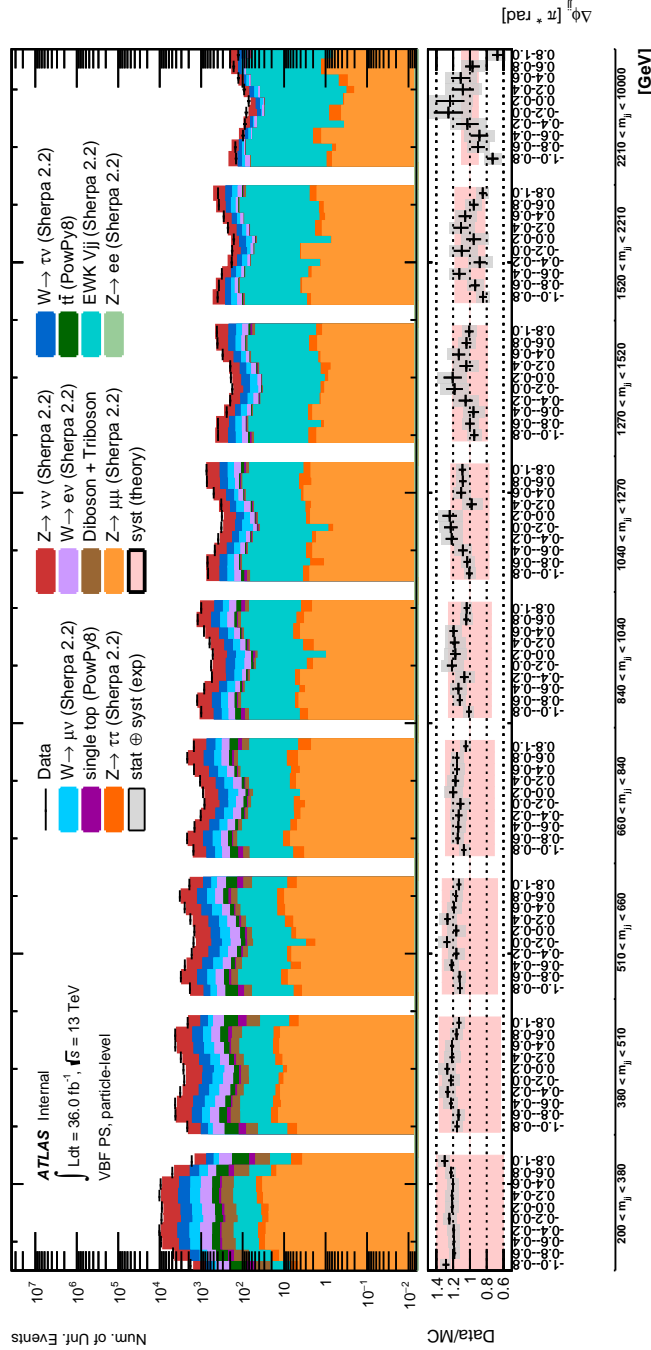


Figure 5.12 Particle-level data/MC comparisons for m_{jj} vs $\Delta\phi_{jj}$ in the VBF phase-space for the $p_T^{\text{miss}} + \text{jets}$ region. The grey band shows the combination of statistical and systematic uncertainties. The pink band shows the theoretical uncertainties on the particle-level SM prediction.

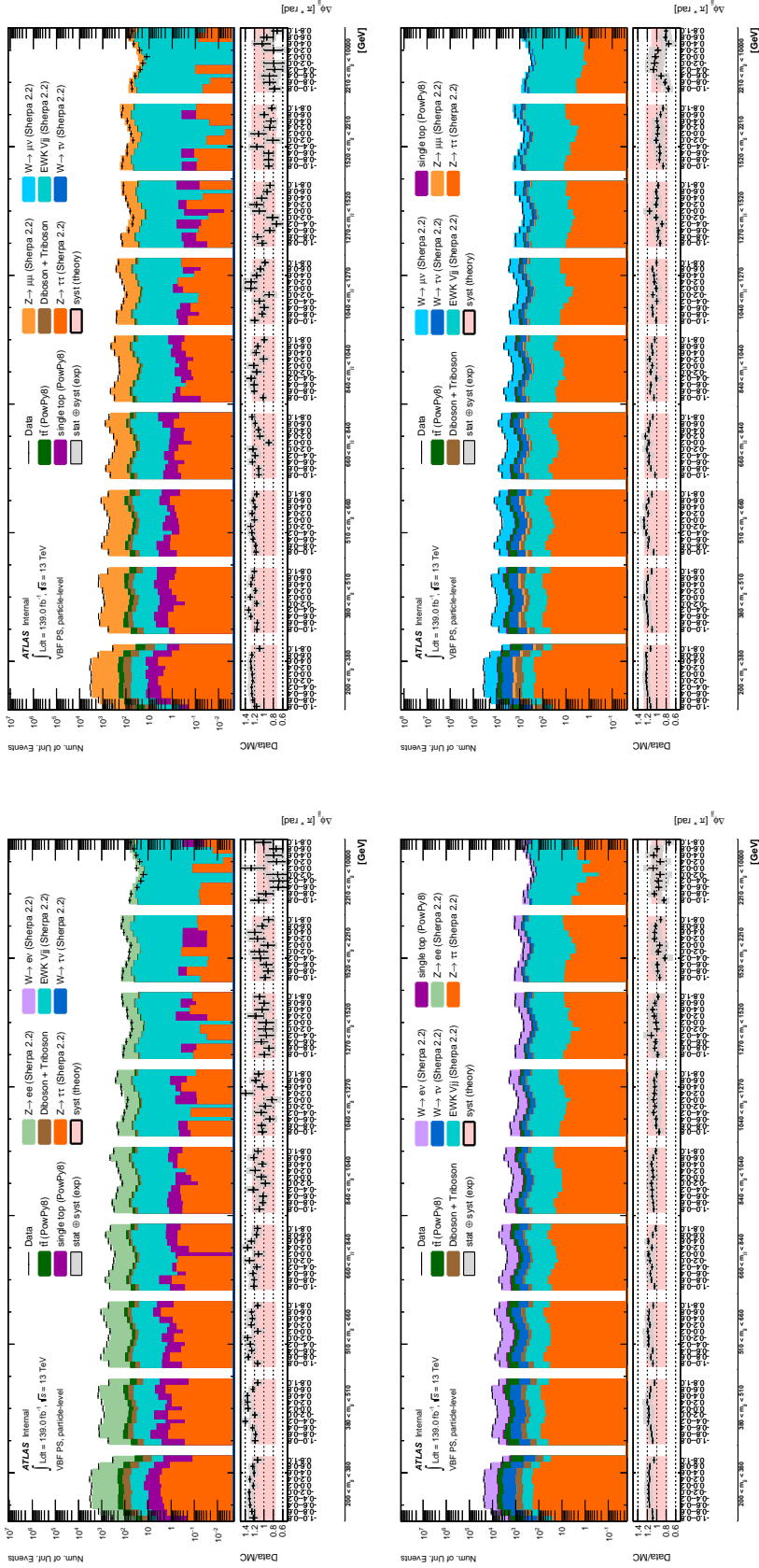


Figure 5.13 Particle-level data/MC comparisons for m_{jj} vs $\Delta\phi_{jj}$ in the VBF phase-space for the $1\ell + \text{jets}$ and $2\ell + \text{jets}$ regions. The grey band shows the combination of statistical and systematic uncertainties. The pink band shows the theoretical uncertainties on the particle-level SM prediction.

5.2 Detector corrected R^{miss}

The detector corrected differential cross-sections of the previous section are used here to construct the R^{miss} ratio. R^{miss} , as introduced in Section 3.1, is defined as the fiducial cross-section for $p_{\text{T}}^{\text{miss}} + \text{jets}$ events divided by the fiducial cross-section for events in any of the $1e + \text{jets}$, $1\mu + \text{jets}$, $2e + \text{jets}$ and $2\mu + \text{jets}$ regions. In the following figures, R^{miss} is presented as a function of $p_{\text{T}}^{\text{miss}}$, m_{jj} and $\Delta\phi_{jj}$ in each region and each phase-space, to demonstrate the strength of the method. The results are also compared to predictions of R^{miss} , assuming the presence of the BSM models introduced in the previous section. In the bottom panel of each figure, the agreement between R^{miss} as measured in the data and R^{miss} as predicted by the SM is shown. Statistical uncertainties are shown as error bars. Systematic uncertainties added in quadrature to the statistical uncertainties are shown as a band with hatched lines. Experimental systematic uncertainties originating from the jet calibration procedure are significantly reduced in the ratio due to the similarity of the jet systems in the $p_{\text{T}}^{\text{miss}} + \text{jets}$ region in the numerator and the lepton regions in the denominator. The lepton efficiency systematics only affect the lepton regions in the denominator and are the dominant experimental systematic uncertainties on the R^{miss} ratio. The effect of each group of systematic uncertainties is shown in appendix E where the cancellation of experimental systematic uncertainties arising from the treatment of jets is clearly demonstrated.

Theoretical systematic uncertainties on the particle-level SM predictions are shown as a pink band. These are also significantly reduced in the ratio because of the similarity of the processes in the numerator and the denominator. A slightly weaker cancellation of theoretical uncertainties is observed here compared to the previous measurement of R^{miss} , published in [48]. This is expected since all regions in this thesis are defined in terms of final-state particles instead of a particular process, resulting in the $p_{\text{T}}^{\text{miss}} + \text{jets}$ region being populated by both $Z + \text{jets}$ and $W + \text{jets}$ events. Both of these processes introduce theoretical uncertainties that have uncorrelated components between the $p_{\text{T}}^{\text{miss}} + \text{jets}$ region and the $2\ell + \text{jets}$ (mainly populated by $Z + \text{jets}$ events) or $1\ell + \text{jets}$ (mainly populated by $W + \text{jets}$ events) regions. Statistical contributions to the shape of the theory uncertainties also lead to an overestimation of these

uncertainties in poorly populated regions of phase space. This is most evident in the tails of the $p_{\text{T}}^{\text{miss}}$ and m_{jj} distributions in all phase-spaces. In reality, theoretical uncertainties on R^{miss} are expected to be at the level of a few percent in all bins, as demonstrated in the studies of [55]. A more precise calculation of the theoretical uncertainties on R^{miss} is currently in progress.

Figure 5.14 shows comparisons between R^{miss} as measured in the data and as predicted by the MC, using either of the lepton regions in the denominator, as a function of $p_{\text{T}}^{\text{miss}}$ in the ≥ 1 jet phase-space. Figures 5.14a and 5.14b show R^{miss} using the $2e + \text{jets}$ and $2\mu + \text{jets}$ lepton regions in the denominator. The SM prediction shows a large R^{miss} at low $p_{\text{T}}^{\text{miss}}$ for both, at approximately 14.5 and 12.5 respectively, which decreases for bins with higher $p_{\text{T}}^{\text{miss}}$ to approximately 6.5 and 6, approaching the SM ratio of branching fractions between the $Z \rightarrow \nu\nu$ and $Z \rightarrow \ell\ell$ processes of 5.9. The higher value of R^{miss} is mainly due to the effect of $W + \text{jets}$ contributions to the $p_{\text{T}}^{\text{miss}} + \text{jets}$ region, which are much larger at low $p_{\text{T}}^{\text{miss}}$. The shape is also affected by the fiducial requirements on the charged leptons in the denominator. At higher $p_{\text{T}}^{\text{miss}}$, the leptons have larger p_{T} and are more central, making them more likely to pass the selection criteria of the $2\ell + \text{jets}$ regions, thus increasing the fiducial cross-sections of the denominators. The shape of R^{miss} as measured in the data is reasonably well modeled by the MC, however a discrepancy between the data and MC of up to 10% is observed when using the $2e + \text{jets}$ region in the denominator, with the MC overestimating the value of R^{miss} at low $p_{\text{T}}^{\text{miss}}$. This discrepancy is not covered by the theoretical systematic uncertainties in the first two bins. A similar discrepancy of up to 5% is observed with the $2\mu + \text{jets}$ region in the denominator, though that is covered by the theoretical uncertainties.

Figures 5.14c and 5.14d show R^{miss} using the $1e + \text{jets}$ or $1\mu + \text{jets}$ lepton regions in the denominator, for the same observable as above. The SM prediction shows a higher R^{miss} at low $p_{\text{T}}^{\text{miss}}$ for both at approximately 1.6 and 1.0 respectively, which decreases for bins with higher $p_{\text{T}}^{\text{miss}}$ to approximately 0.7 and 0.65, approaching the SM ratio of branching fractions between the $Z \rightarrow \nu\nu$ and $W \rightarrow \ell\nu$ processes of 0.6. The shape of R^{miss} in both cases is the result of the effects discussed above. QCD multijet events are not subtracted from the data in the lepton regions prior to unfolding. These are expected to contribute mainly to the tails of the $p_{\text{T}}^{\text{miss}}$ distribution in the $1e + \text{jets}$, which leads to a decrease in the bottom panel ratio of Figure 5.14c.

A flat agreement is expected when those backgrounds are taken into account. The ratio is also shown to be higher when using the $1e + \text{jets}$ region in the denominator. This is because of the additional real- $p_{\text{T}}^{\text{miss}} > 45$ GeV requirement in the $1e + \text{jets}$ region, which results in a smaller cross-section for this region. Differences between the two ratios also originate from differences observed in the central SHERPA 2.2.1 $V + \text{jets}$ samples, used in the particle-level SM prediction here. The samples exhibit a difference in the boson p_{T} spectrum for the electron and muon channels and while a reweighting function was used to correct the central SHERPA $Z \rightarrow ee$ samples for this difference, a reweighting function for the central SHERPA $W \rightarrow e\nu$ samples has not been derived yet. At the time of writing, these were the most up-to-date samples available and new samples restoring the lepton universality in the $V + \text{jets}$ process are being produced. The two ratios are expected to be in agreement with each other when a more updated set of SM predictions is used to construct R^{miss} . As shown in Section 4.6, the unfolding method is robust against the exact knowledge of the process composition of a region and so the discrepancies observed in the central SHERPA $V + \text{jets}$ samples do not affect the unfolded data. The shape of R^{miss} as measured in the data is again reasonably well modeled by the MC and small discrepancies are covered by the theoretical uncertainties.

An increased sensitivity to the three BSM models is evident in the bottom panel of each figure, compared to what is observed in figure 5.1 of the previous section, demonstrating the strength of the R^{miss} ratio. The advantage of using R^{miss} rather than using differential cross-sections for setting limits on BSM models will be even more apparent with the use of a more realistic theoretical uncertainty on the particle-level SM predictions in the future.

Figure 5.15 shows comparisons between R^{miss} as measured in the data and as predicted by the MC, using either of the lepton regions in the denominator, as a function of $p_{\text{T}}^{\text{miss}}$ in the ≥ 2 jet phase-space. The shape of R^{miss} is similar to the one seen in the ≥ 1 jet phase-space. Overall shifts in normalisation and shape discrepancies in the agreement between data and MC are also similar to those seen in the ≥ 1 jet phase-space.

Figure 5.16 shows comparisons between R^{miss} as measured in the data and as predicted by the MC, using either of the lepton regions in the denominator, as a function of m_{jj} in the

≥ 2 jet phase-space. The mismodelling observed in the m_{jj} distributions of Figure 5.5 in the previous section largely cancels out in the construction of R^{miss} . The SM prediction shows a relatively flat R^{miss} with a bump (dip) in the ratio at around 100 GeV when using one of the $2\ell + \text{jets}$ ($1\ell + \text{jets}$) regions in the denominator. In the top two figures, this is because of an increase in contributions from top-pair events to the $p_{\text{T}}^{\text{miss}} + \text{jets}$ region. In the bottom two figures, this is because of an even larger increase in contributions from top-pair events to the $1e + \text{jets}$ and $1\mu + \text{jets}$ regions. A divergence from a flat ratio is also observed in the tails of the distributions, possibly because of the different slicing method used in the $Z + \text{jets}$ MC samples compared to the rest of the $V + \text{jets}$ samples.

Figure 5.17 shows comparisons between R^{miss} as measured in the data and as predicted by the MC, using either of the lepton regions in the denominator, as a function of $\Delta\phi_{jj}$ in the ≥ 2 jet phase-space. Figures 5.17a and 5.17b show R^{miss} using the $2e + \text{jets}$ or $2\mu + \text{jets}$ lepton regions in the denominator. The SM prediction shows a flat R^{miss} in the central region which increases for large positive and negative $\Delta\phi_{jj}$ values. This is because the removal of jets overlapping with charged leptons described in Section 3.3.1 mostly affects $Z \rightarrow \ell\ell$ events with large $\Delta\phi_{jj}$, where a hard jet balances the Z boson and a softer one overlaps with one of the leptons from the Z decay. Removal of jets in such a topology leads to events failing the selection criteria of the $2\ell + \text{jets}$ regions and a reduced cross-section in the denominator. Figures 5.17c and 5.17d show R^{miss} using the $1e + \text{jets}$ or $1\mu + \text{jets}$ lepton regions in the denominator. A decrease in R^{miss} is seen for large positive and negative values of $\Delta\phi_{jj}$ as well as in the central region. Large contributions from top-pair events can be seen in these topologies of the $1\ell + \text{jets}$ regions in figure 5.6 of the previous section, resulting in an increased cross-section in the denominator of R^{miss} and a smaller overall ratio. The MC models these effects well, resulting in a flat agreement between the data and MC in all regions. A slightly more peaked structure is observed in the data in figure 5.17c where R^{miss} using the $1e + \text{jets}$ region in the denominator is shown. This leads to a discrepancy between data and MC of up to 10%, which is not covered by the theoretical systematic uncertainties.

Figures 5.18, 5.19 and 5.20 show comparisons between R^{miss} as measured in the data and as predicted by the MC, using either of the lepton regions in the denominator, as a function

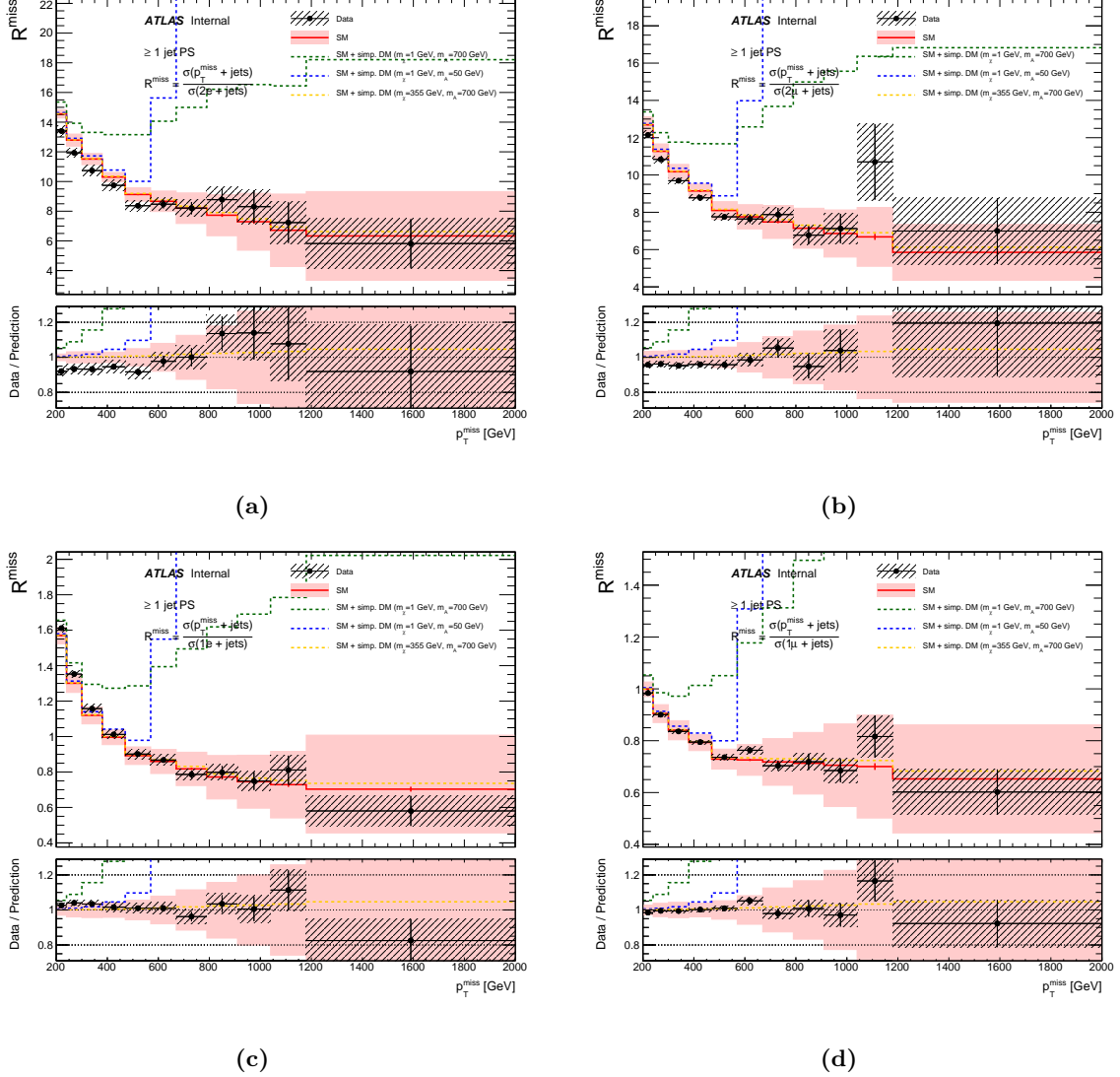


Figure 5.14 Particle-level data/MC comparisons for R^{miss} as a function of p_T^{miss} in the ≥ 1 jet phase-space. Statistical uncertainties are shown as error bars and the total statistical and experimental systematic uncertainty is shown as hatched lines. Theoretical systematic uncertainties are shown as a pink shaded band.

of p_T^{miss} , m_{jj} and $\Delta\phi_{jj}$ in the VBF phase-space. Overall shifts in normalisation and shape discrepancies are similar to the ones observed in the ≥ 1 jet and ≥ 2 jet phase-spaces. The data is found to be in agreement with the SM prediction within uncertainties. An increased sensitivity to the two BSM models is again observed here.

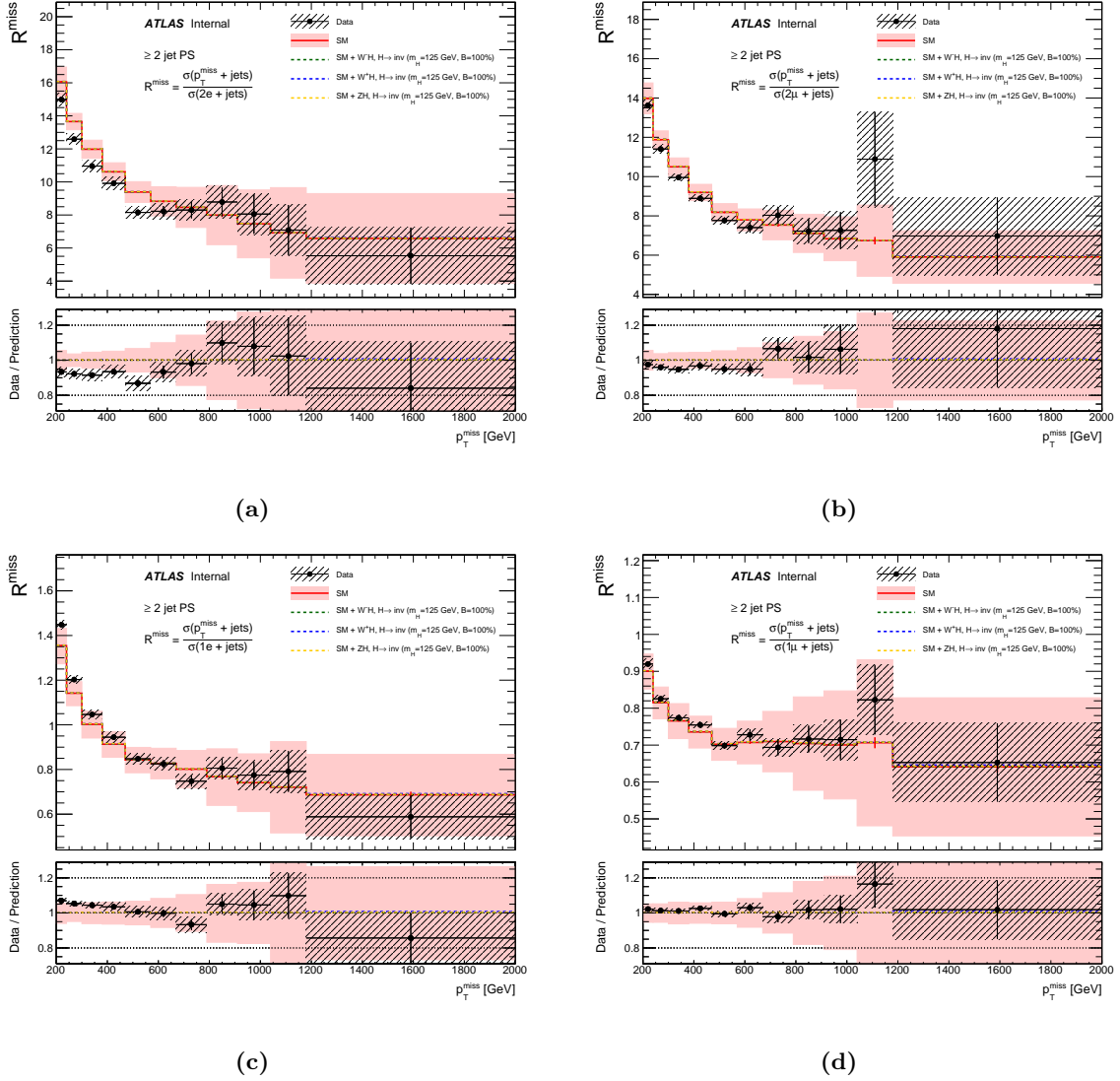


Figure 5.15 Particle-level data/MC comparisons for R^{miss} as a function of p_T^{miss} in the ≥ 2 jet phase-space. Statistical uncertainties are shown as error bars and the total statistical and experimental systematic uncertainty is shown as hatched lines. Theoretical systematic uncertainties are shown as a pink shaded band.

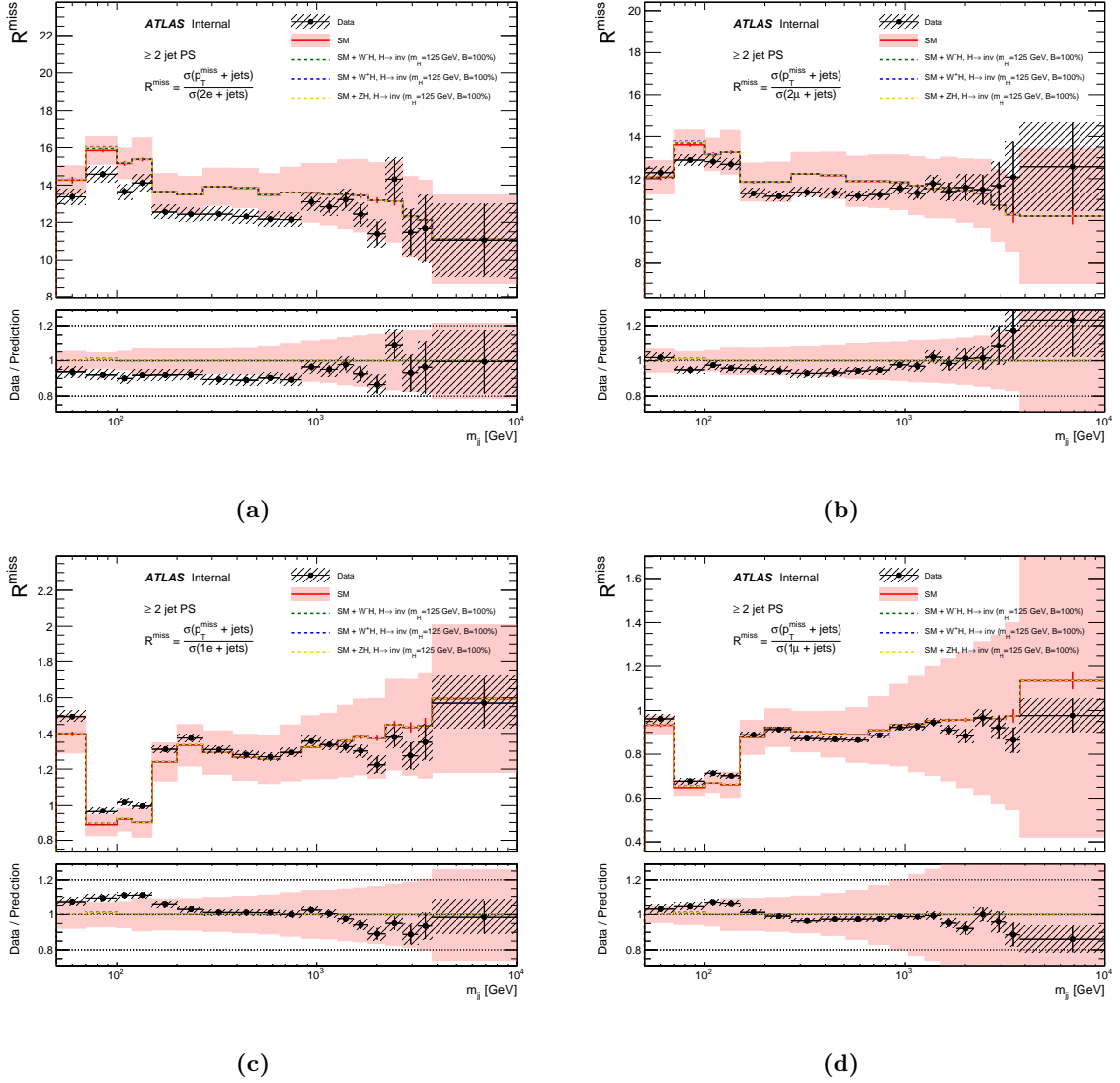


Figure 5.16 Particle-level data/MC comparisons for R^{miss} as a function of m_{jj} in the ≥ 2 jet phase-space. Statistical uncertainties are shown as error bars and the total statistical and experimental systematic uncertainty is shown as hatched lines. Theoretical systematic uncertainties are shown as a pink shaded band.

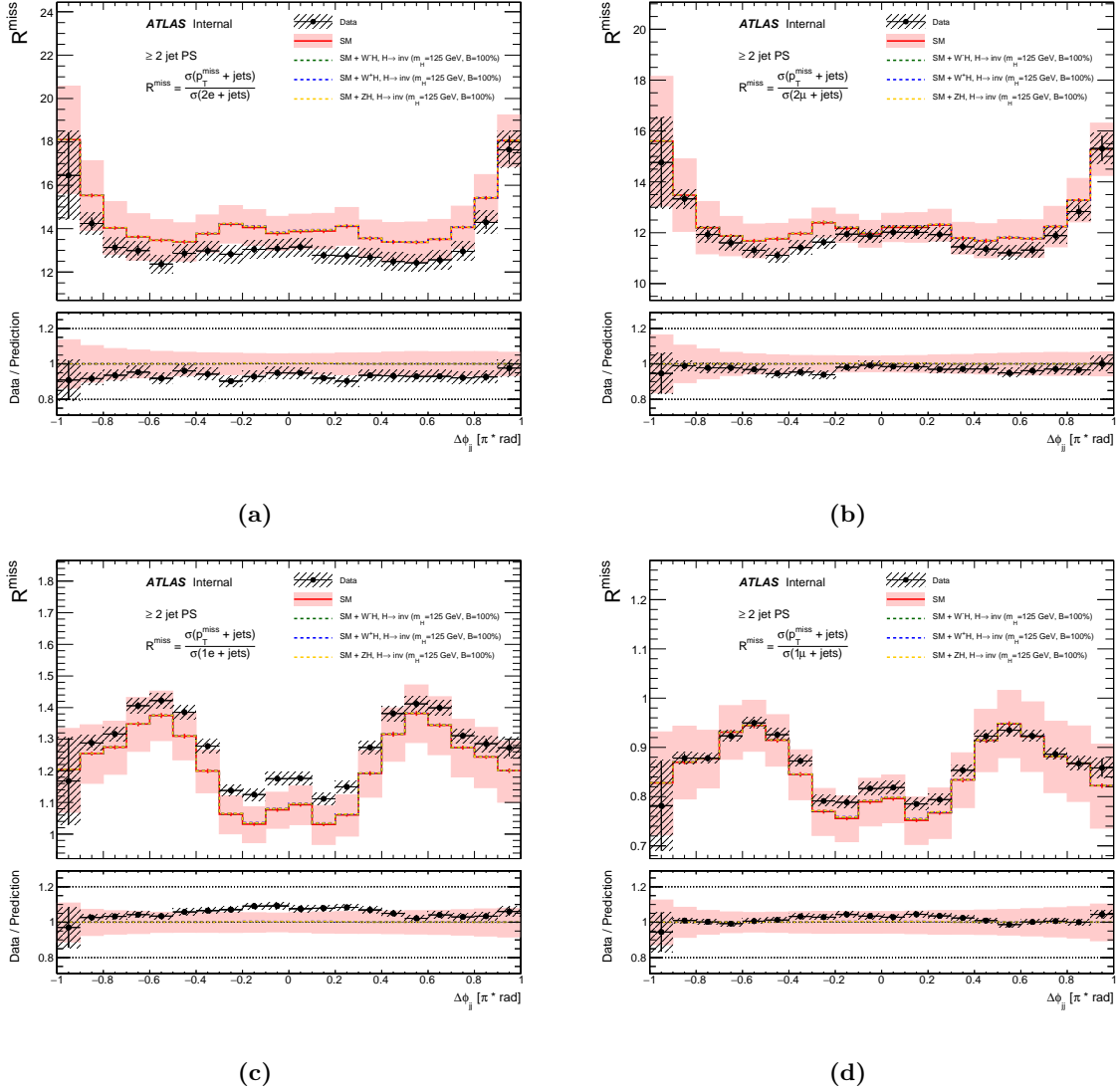


Figure 5.17 Particle-level data/MC comparisons for R^{miss} as a function of $\Delta\phi_{jj}$ in the ≥ 2 jet phase-space. Statistical uncertainties are shown as error bars and the total statistical and experimental systematic uncertainty is shown as hatched lines. Theoretical systematic uncertainties are shown as a pink shaded band.

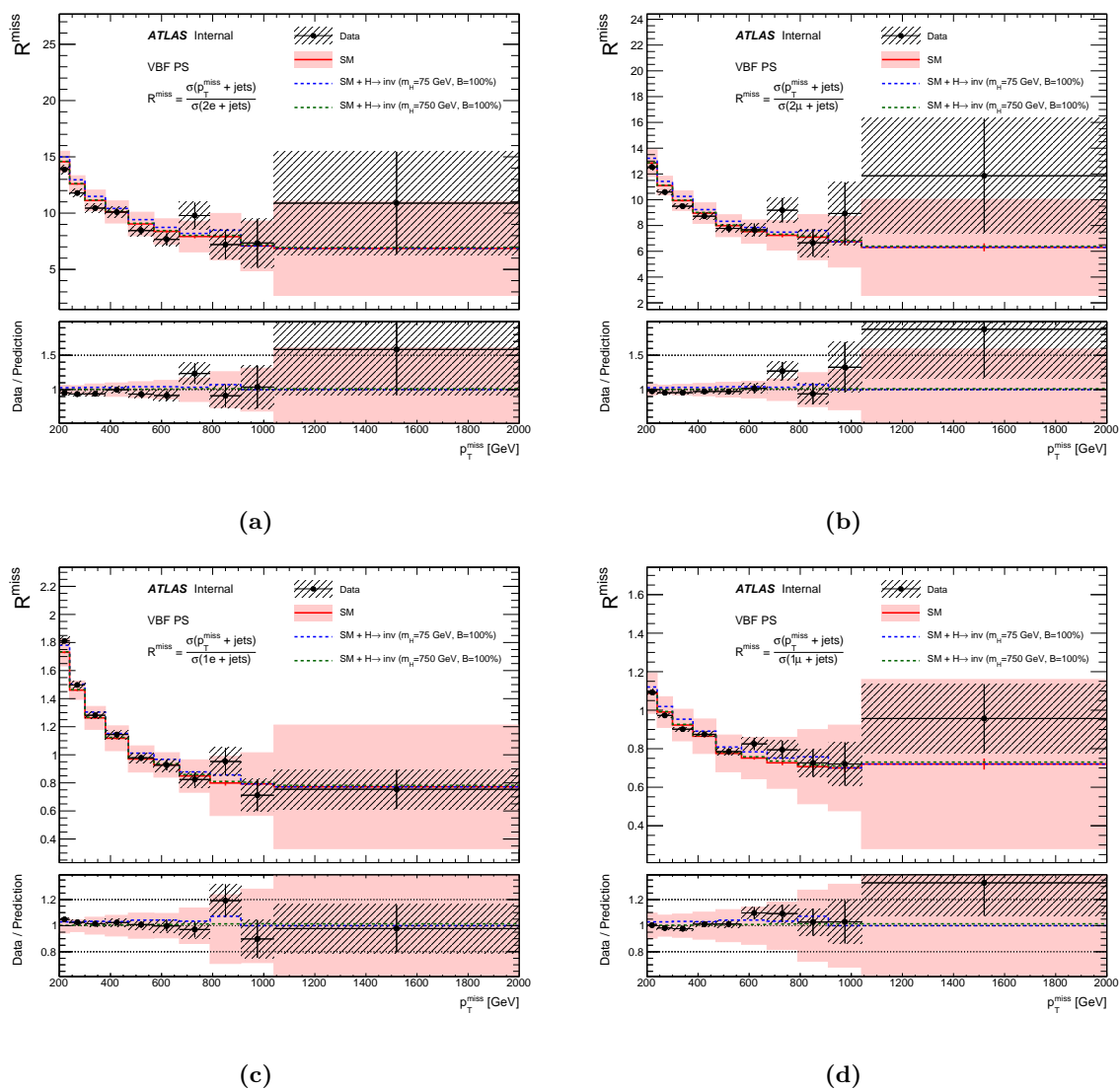


Figure 5.18 Particle-level data/MC comparisons for R^{miss} as a function of p_T^{miss} in the VBF phase-space. Statistical uncertainties are shown as error bars and the total statistical and experimental systematic uncertainty is shown as hatched lines. Theoretical systematic uncertainties are shown as a pink shaded band.

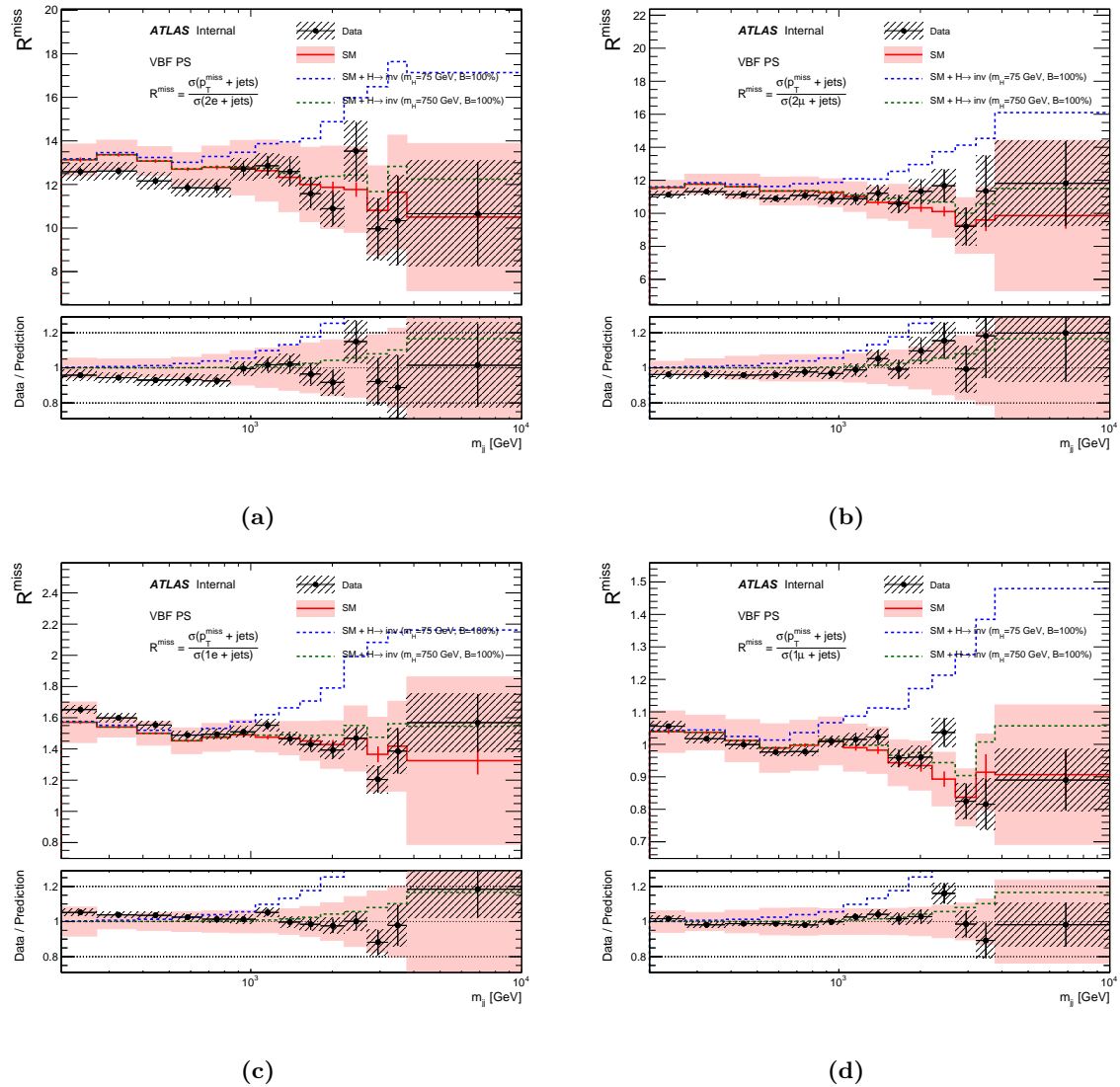


Figure 5.19 Particle-level data/MC comparisons for R^{miss} as a function of m_{jj} in the VBF phase-space. Statistical uncertainties are shown as error bars and the total statistical and experimental systematic uncertainty is shown as hatched lines. Theoretical systematic uncertainties are shown as a pink shaded band.

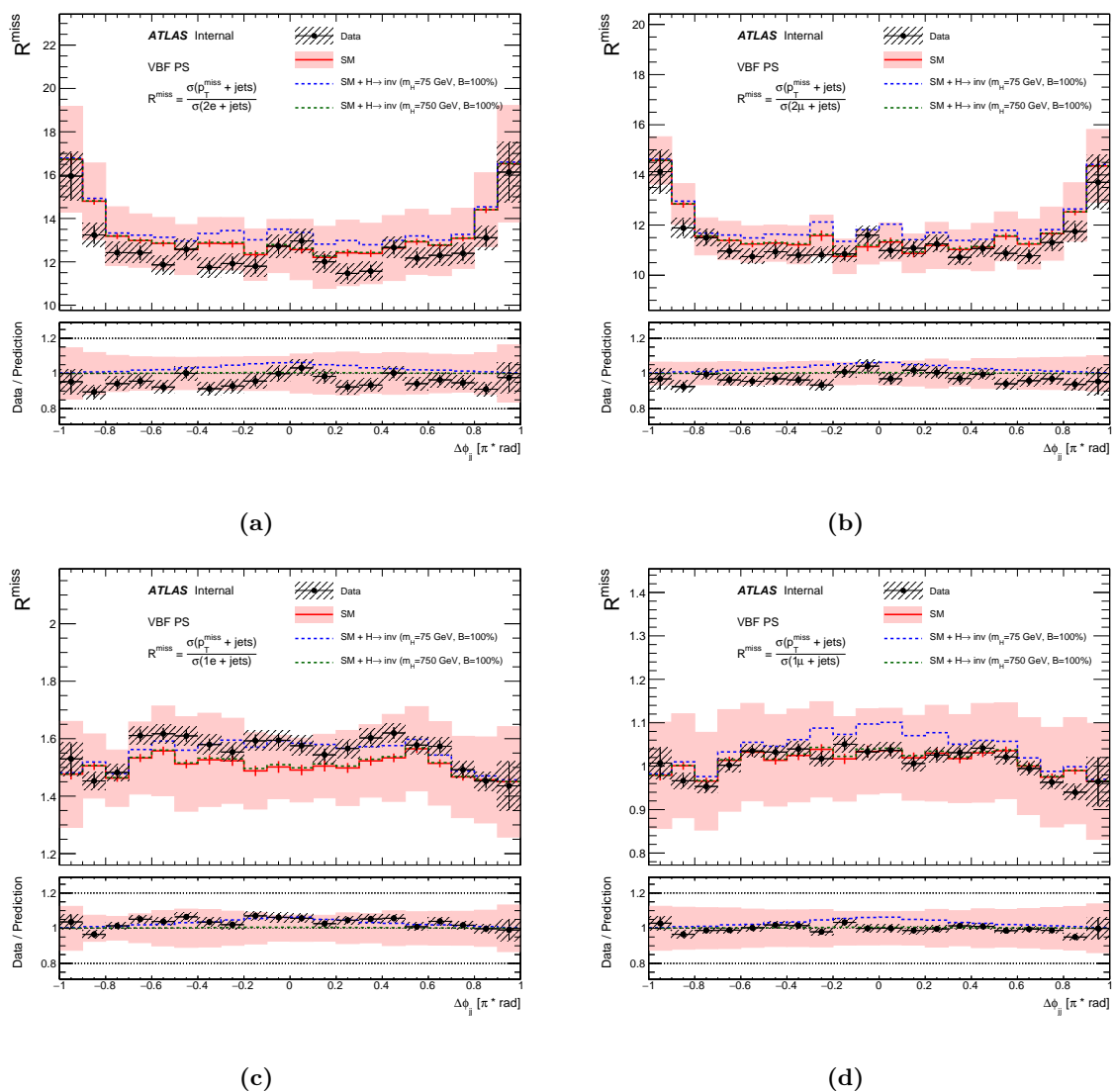


Figure 5.20 Particle-level data/MC comparisons for R^{miss} as a function of $\Delta\phi_{jj}$ in the VBF phase-space. Statistical uncertainties are shown as error bars and the total statistical and experimental systematic uncertainty is shown as hatched lines. Theoretical systematic uncertainties are shown as a pink shaded band.

Chapter 6

Conclusions

This thesis presents a measurement of differential cross-sections in regions of phase-space that are largely populated by well-known SM process but are also expected to be sensitive to the production of dark matter particles or other beyond the Standard Model physics. The differential cross-section of events with a $p_T^{\text{miss}} + \text{jets}$ final state is measured, along with the cross-sections of four regions containing charged leptons: $2e + \text{jets}$, $2\mu + \text{jets}$, $1e + \text{jets}$ and $1\mu + \text{jets}$. The lepton regions can be used to constrain the systematic uncertainties in the $p_T^{\text{miss}} + \text{jets}$ region coming from experimental inefficiencies and from theoretical modelling. Additionally, the lepton regions can be used to search for, and place limits on, new physics models with final states involving leptons. The measurements are performed in three different phase-spaces, defined by the jet kinematics of the events, aiming to be sensitive to different dark matter production mechanisms. Each region is measured differentially and double-differentially with respect to a number of observables, allowing for detailed structures in the data to be studied. A ratio of cross-sections is also presented as a function of numerous observables, allowing for structures in the data and in the modelling of these regions to be compared to each other. Experimental and theoretical systematic uncertainties are also significantly reduced in the ratio measurement. The measurements are corrected for detector effects and are presented at the particle-level, making them readily available to be compared to particle-level predictions without the need of a detector simulation.

6 Conclusions

The detector-corrected measured data are found to be consistent with the SM particle-level predictions within experimental and theoretical systematic uncertainties though discrepancies are observed in some of the regions. The MC samples used in the comparisons between the data and the SM prediction are known to suffer from inconsistencies between the V +jets processes and the production of a new set of particle-level predictions is currently under way. The unfolding method used to correct the data for detector effects has been shown to be robust against the exact knowledge of the process composition of the SM predictions and so inconsistencies in the MC samples do not affect the unfolded measurements.

A strong cancellation of experimental and theoretical systematic uncertainties is demonstrated in the construction of the R^{miss} ratio, leading to a much more precise measurement. The R^{miss} ratio is also shown to offer an increased sensitivity to BSM models, indicating that stronger limits can be set on BSM models using ratio measurements rather than individual differential cross-sections. Due to statistical fluctuations in poorly populated regions of the distributions, the theoretical systematic uncertainties don't exhibit as strong a cancellation as it is suggested from previous studies. This is expected to improve with future calculations of these uncertainties that use higher statistics.

Part III

Appendix

Appendix A

Monte Carlo samples description

The appendix describes the Monte Carlo samples used in this analysis using the standard description provided by the ATLAS collaboration.

A.1 MC samples for SM processes

V+jets

Events containing a single W or Z/γ^* bosons in association with jets are simulated with the SHERPA v2.2.1[64] parton shower Monte Carlo generator. In this setup, NLO-accurate matrix elements for up to two jets, and LO-accurate matrix elements for up to 4 jets are calculated with the COMIX [65] and OPENLOOPS [66, 67] libraries. The default SHERPA parton shower [68] based on Catani-Seymour dipoles and the cluster hadronisation model [69] are used. They employ the dedicated set of tuned parameters developed by the SHERPA authors for this version based on the NNPDF3.0NNLO set [70].

The NLO matrix elements of a given jet-multiplicity are matched to the parton shower using a colour-exact variant of the MC@NLO algorithm [71]. Different jet multiplicities are then merged into an inclusive sample using an improved CKKW matching procedure [72, 73] which is extended to NLO accuracy using the MEPS@NLO prescription [74]. The merging cut is set to $Q_{\text{cut}} = 20$ GeV.

The V +jets samples are normalised to a next-to-next-to-leading order (NNLO) prediction [75]. Details on the full process configuration for V +jets are given in the recent PUB note [76].

Matrix elements for the $\ell\ell jj$, $\ell\nu jj$ and $\nu\nu jj$ final states have been generated using SHERPA v2.2.1 with up to two additional parton emissions at LO accuracy beyond the first two jets. The matrix elements are merged with the SHERPA parton shower using the MEPS@LO prescription.

These samples were generated in the G_μ scheme using, ensuring an optimal description of pure electroweak interactions at the electroweak scale.

Dibosons

Fully leptonically decaying diboson samples are simulated with the SHERPA v2.2.2 [64] generator. In this setup multiple matrix elements are matched and merged with the SHERPA parton shower based on Catani-Seymour dipole [65, 68] using the MEPS@NLO prescription [71–74]. The virtual QCD correction for matrix elements at NLO accuracy are provided by the OPENLOOPS library [66, 67]. Samples are generated using the NNPDF3.0NNLO set [70], along with the dedicated set of tuned parton-shower parameters developed by the SHERPA authors.

Semileptonically decaying diboson samples are simulated with the SHERPA v2.2.1 [64] generator. In this setup multiple matrix elements are matched and merged with the SHERPA parton shower based on Catani-Seymour dipole [65, 68] using the MEPS@NLO prescription [71–74]. The virtual QCD correction for matrix elements at NLO accuracy are provided by the OPENLOOPS library [66, 67]. Samples are generated using the NNPDF3.0NNLO set [70], along with the dedicated set of tuned parton-shower parameters developed by the SHERPA authors.

Tribosons

Triboson production is simulated with the SHERPA v2.2.2 [64] generator. In this setup multiple matrix elements are matched and merged with the SHERPA parton shower based on Catani-Seymour dipole [65, 68] using the MEPS@NLO prescription [71–74]. The virtual QCD correction for matrix elements at NLO accuracy are provided by the OPENLOOPS library [66, 67]. Samples are generated using the NNPDF3.0NNLO set [70], along with the dedicated set of tuned parton-shower parameters developed by the SHERPA authors.

Details on the full process configuration for multi- V processes are given in the recent PUB note [77].

Top events

The production of $t\bar{t}$ events is modelled using the POWHEG-BOX [78–81] v2 generator at NLO with the NNPDF3.0NLO [70] parton distribution function (PDF) and the h_{damp} parameter¹ set to $1.5 m_t$ [82]. The events are interfaced with PYTHIA 8.230 [50] using the A14 tune [83] and the NNPDF2.3LO PDF set. The NLO $t\bar{t}$ inclusive production cross section is corrected

¹The h_{damp} parameter controls the transverse momentum p_T of the first additional emission beyond the leading-order Feynman diagram in the parton shower and therefore regulates the high- p_T emission against which the $t\bar{t}$ system recoils.

to the theory prediction at next-to-next-to-leading order (NNLO) in QCD including the resummation of next-to-next-to-leading logarithmic (NNLL) soft-gluon terms calculated using TOP++2.0 [84–90].

Single-top tW associated production is modelled using the POWHEG-BOX [79–81, 91] v2 generator at NLO in QCD in the five flavour scheme with the NNPDF3.0NLO [70] parton distribution function (PDF) set. The diagram subtraction scheme [92] was employed to handle the interference with $t\bar{t}$ production [82]. The events are interfaced with PYTHIA 8.230 [50] using the A14 tune [83] and the NNPDF2.3LO PDF set. The inclusive cross section is corrected to the theory prediction calculated at NLO in QCD with NNLL soft gluon corrections [93, 94].

Single-top t -channel production is modelled using the POWHEG-BOX [79–81, 95] v2 generator at NLO in QCD in the four flavour scheme with the NNPDF3.0NLOnf4 [70] parton distribution function (PDF) set. The events are interfaced with PYTHIA 8.230 [50] using the A14 tune [83] and the NNPDF2.3LO PDF set. The inclusive cross section is corrected to the theory prediction calculated at NLO in QCD with Hathor v2.1 [93, 94].

Single-top s -channel production is modelled using the POWHEG-BOX [79–81, 96] v2 generator at NLO in QCD in the five flavour scheme with the NNPDF3.0NLO [70] parton distribution function (PDF) set. The events are interfaced with PYTHIA 8.230 [50] using the A14 tune [83] and the NNPDF2.3LO PDF set. The inclusive cross section is corrected to the theory prediction calculated at NLO in QCD with Hathor v2.1 [93, 94].

A.2 MC samples for BSM processes

A number of BSM samples are generated for comparisons with the data and to test the robustness of the unfolding procedure in the presence of BSM physics. The following models are simulated:

Dark Matter s -channel interactions:

Weakly Interacting Massive Particle (WIMP) signals of type $\chi\bar{\chi} + \text{jet}$, where χ is the DM candidate. These are simulated with POWHEG-BOX using the following two implementations of simplified models:

1. $\chi\bar{\chi}$ production with spin-1 axial-vector mediator exchange, at NLO precision.
2. $\chi\bar{\chi}$ with spin-0 pseudo-scalar mediator exchange with a quark loop, at LO precision.

Renormalisation and factorisation scales are set to $H_T/2$ on an event-by-event basis, where $H_T = \sqrt{m_{\chi\chi}^2 + p_{T,j1}^2} + p_{T,j1}$. Events are generated using the NNPDF30 PDFs and interfaced to PYTHIA 8.205, with the ATLAS 14 tune. Couplings of the mediator to DM particles and

Standard Model quarks are set to $g_\chi = 1$ and $g_q = 1/4$ for the axial-vector mediator model. For the pseudo-scalar model, both couplings are set to 1. A grid of samples is produced for the DM masses ranging from 1 GeV to 1 TeV and the mediator masses between 10 GeV and 10 TeV.

Invisible decays of the Higgs:

Higgs samples are generated with the branching ratio of the decay to four neutrinos (via two Z bosons) set to 100% to provide simulations of Higgs bosons decaying invisibly. These are generated at different Higgs masses (75 GeV, 125 GeV and 750 GeV) for VBF production and 125 GeV for VH production. These samples are simulated using the Powheg-Box v2 generator interfaced with Pythia 8.212 for hadronization and parton shower modelling by using the AZNLO tune. The VH samples have the MinLO (Multiscale Improved NLO) procedure applied and the CT10 PDF set. The VBF samples use the NNPDF30 PDF set.

Appendix B

Top-enhanced control regions

In order to study the uncertainties associated with top event contributions in each phase-space, top enhanced control regions are defined for the $p_T^{\text{miss}} + \text{jets}$, $1e + \text{jets}$ and $1\mu + \text{jets}$ regions, where requirements on the presence of b-jets are made in addition to the base-line cuts. Top enhanced control regions requiring ≥ 1 or ≥ 2 b-jets were selected. A b-jet is defined as a jet with $p_T > 30$ GeV, $|\eta| < 2.5$ and with the MV2c10 tagger corresponding to the 60% efficiency working point.

B.1 $t\bar{t}$ contributions

The top row of figures in figure B.1 shows top enhanced control regions with ≥ 1 b-jets for p_T^{miss} in the VBF phase-space, in the $p_T^{\text{miss}} + \text{jets}$, $1e + \text{jets}$ and $1\mu + \text{jets}$ regions. The second panel of each Figure shows the fraction of $t\bar{t}$ and single-top events in the region where the nominal DS sample is used to simulate the Wt associated production. A first-order polynomial is used to fit the Data/MC agreement in each top enhanced control region, which is then used as a reweighting function for $t\bar{t}$ event contributions to each main region. Comparisons between nominal and top-reweighted curves for each region are shown in the bottom row of figures. The shift in the Data/MC agreement of each region after reweighting is shown in the fourth panel. The procedure is then repeated using top enhanced control regions with ≥ 2 b-jets (figure B.4). The systematic uncertainty associated with top event contributions and quantified in the shift in Data/MC agreement after reweighting is found to be well within the top contribution variation applied in the studies of Section 4.6.

The procedure is repeated for the following observables:

Figure B.2: Top enhanced control regions requiring ≥ 1 b-jets for m_{jj} in the VBF phase-space.

Figure B.3: Top enhanced control regions requiring ≥ 1 b-jets for $\Delta\phi_{jj}$ in the VBF phase-space.

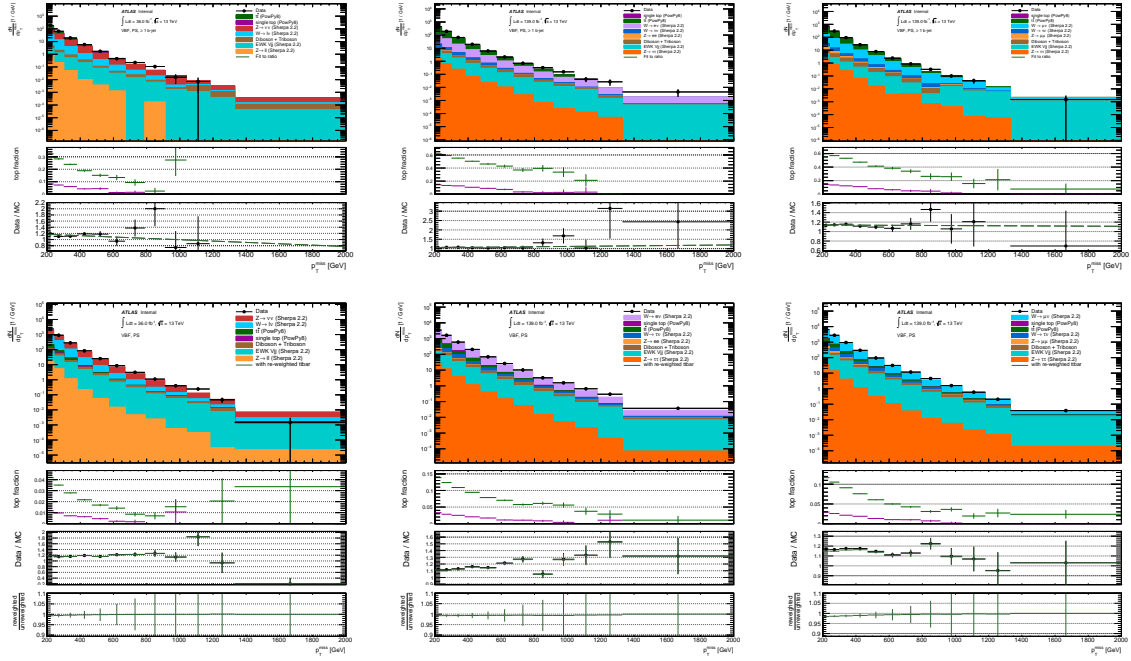


Figure B.1 Top row figures: $p_T^{\text{miss}} + \text{jets}$ (left), $1e + \text{jets}$ (middle) and $1\mu + \text{jets}$ (right) top enhanced control regions (requiring ≥ 1 b-jets) for p_T^{miss} in the VBF phase-space. Bottom row figures: Comparisons between nominal and reweighted $p_T^{\text{miss}} + \text{jets}$ (left), $1e + \text{jets}$ (middle) and $1\mu + \text{jets}$ (right) regions, where the top contributions are reweighted with the polynomial fit of the corresponding top enhanced control region.

Figure B.4: Top enhanced control regions requiring ≥ 2 b-jets for p_T^{miss} in the VBF phase-space.
 Figure B.5: Top enhanced control regions requiring ≥ 2 b-jets for m_{jj} in the VBF phase-space.
 Figure B.6: Top enhanced control regions requiring ≥ 2 b-jets for $\Delta\phi_{jj}$ in the VBF phase-space.

B.2 Single top uncertainties

Two distinct methods are used to simulate single top contributions: Diagram Subtraction (DS) and Diagram Removal (DR). Figure B.7 shows comparisons between detector-level distributions of p_T^{miss} in the ≥ 1 jet phase-space for ≥ 1 b-jet top-enhanced $p_T^{\text{miss}} + \text{jets}$, $1\mu + \text{jets}$ and $1e + \text{jets}$ control regions when using either of the two methods. The second panel of each Figure shows the fraction of single-top events in a region (using either DS or DR) and the third panel shows the Data/MC agreement (using either the DS or DR). Equivalent comparisons using ≥ 2 b-jet top-enhanced control regions are shown in Figure B.8. The DS subtraction scheme is found to provide better modelling of these regions and so it is chosen as the nominal.

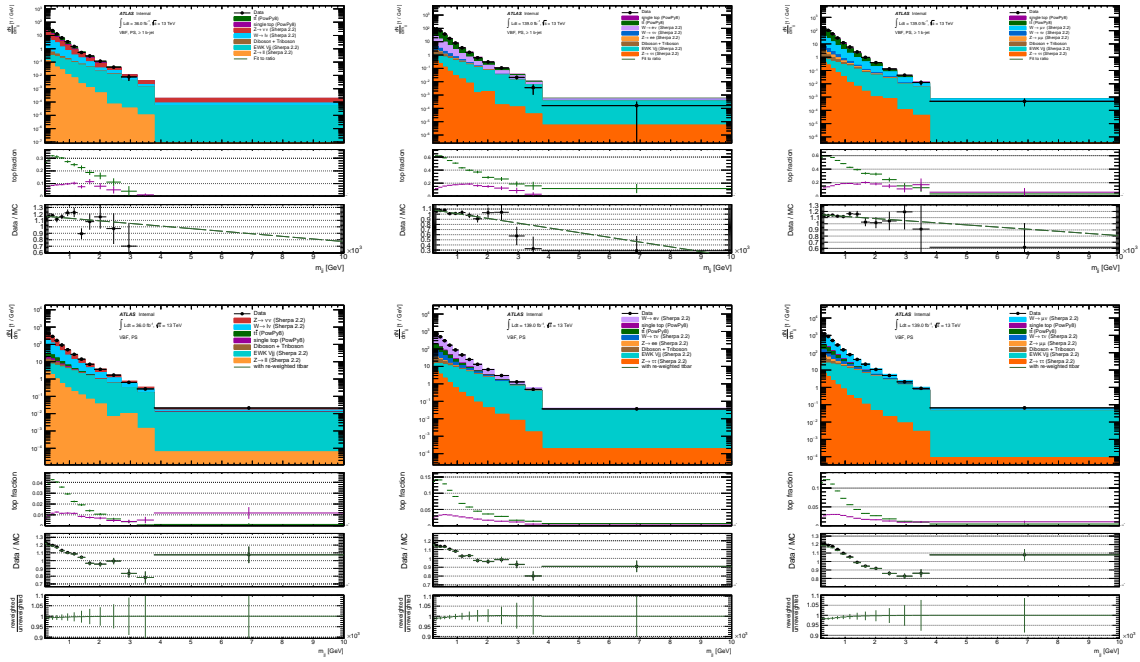


Figure B.2 Top row figures: $p_T^{\text{miss}} + \text{jets}$ (left), $1e + \text{jets}$ (middle) and $1\mu + \text{jets}$ (right) top enhanced control regions (requiring ≥ 1 b-jets) for m_{jj} in the VBF phase-space. Bottom row figures: Comparisons between nominal and reweighted $p_T^{\text{miss}} + \text{jets}$ (left), $1e + \text{jets}$ (middle) and $1\mu + \text{jets}$ (right) regions, where the top contributions are reweighted with the polynomial fit of the corresponding top enhanced control region.

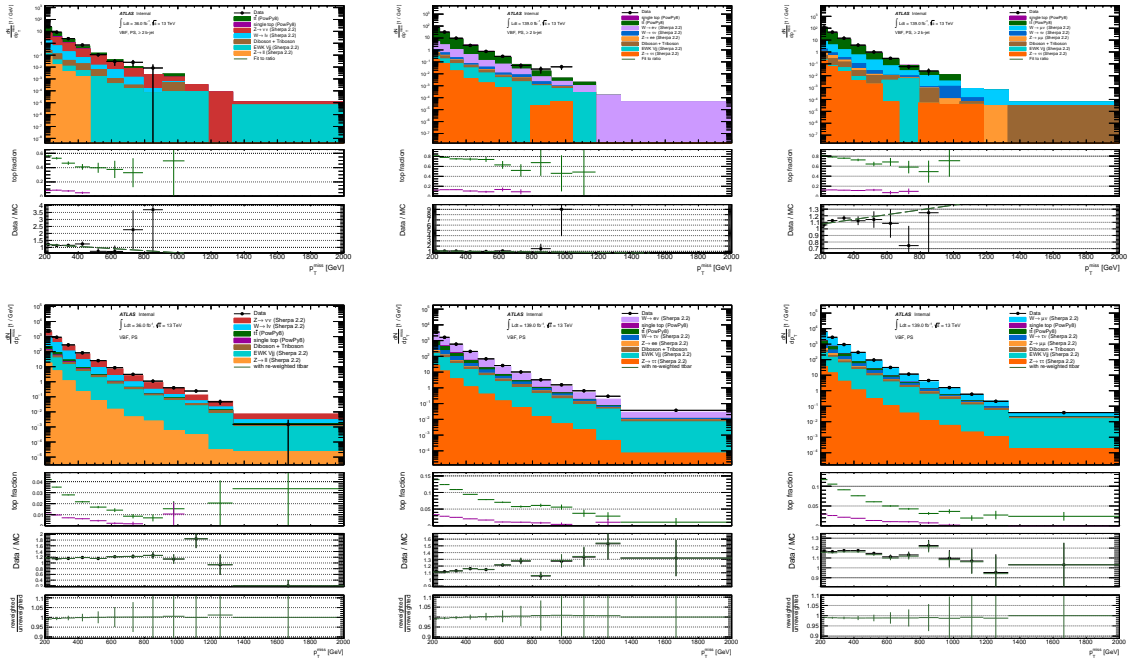


Figure B.4 Top row figures: $p_T^{\text{miss}} + \text{jets}$ (left), $1e + \text{jets}$ (middle) and $1\mu + \text{jets}$ (right) top enhanced control regions (requiring ≥ 2 b-jets) for p_T^{miss} in the VBF phase-space. Bottom row figures: Comparisons between nominal and reweighted $p_T^{\text{miss}} + \text{jets}$ (left), $1e + \text{jets}$ (middle) and $1\mu + \text{jets}$ (right) regions, where the top contributions are reweighted with the polynomial fit of the corresponding top enhanced control region.

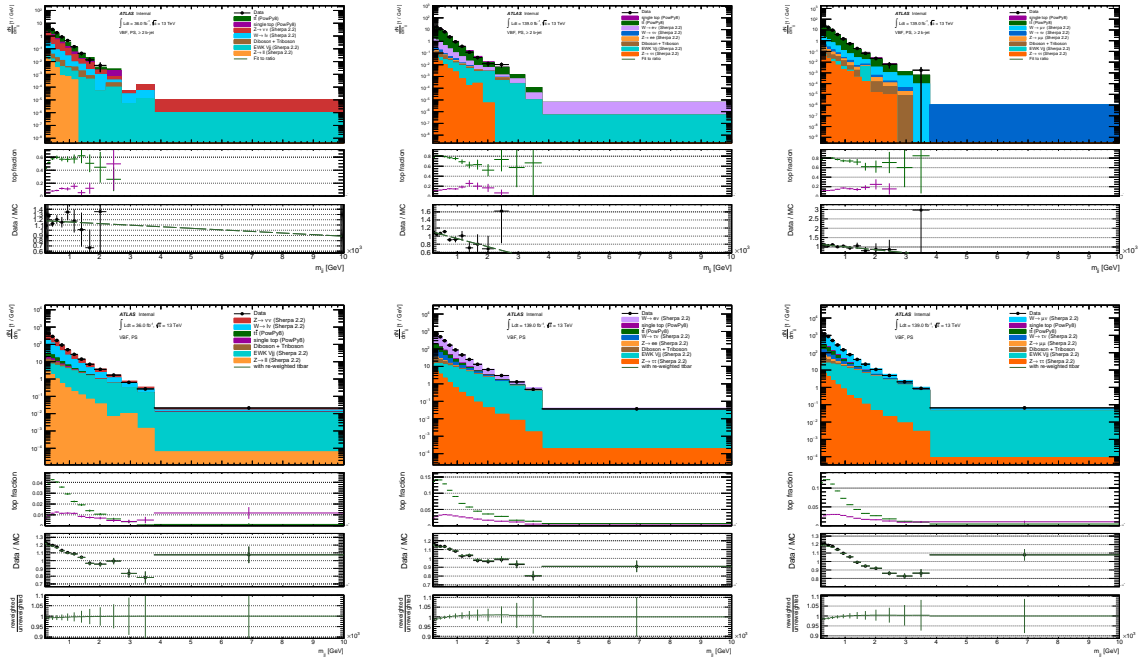


Figure B.5 Top row figures: $p_T^{\text{miss}} + \text{jets}$ (left), $1e + \text{jets}$ (middle) and $1\mu + \text{jets}$ (right) top enhanced control regions (requiring ≥ 2 b-jets) for m_{jj} in the VBF phase-space. Bottom row figures: Comparisons between nominal and reweighted $p_T^{\text{miss}} + \text{jets}$ (left), $1e + \text{jets}$ (middle) and $1\mu + \text{jets}$ (right) regions, where the top contributions are reweighted with the polynomial fit of the corresponding top enhanced control region.

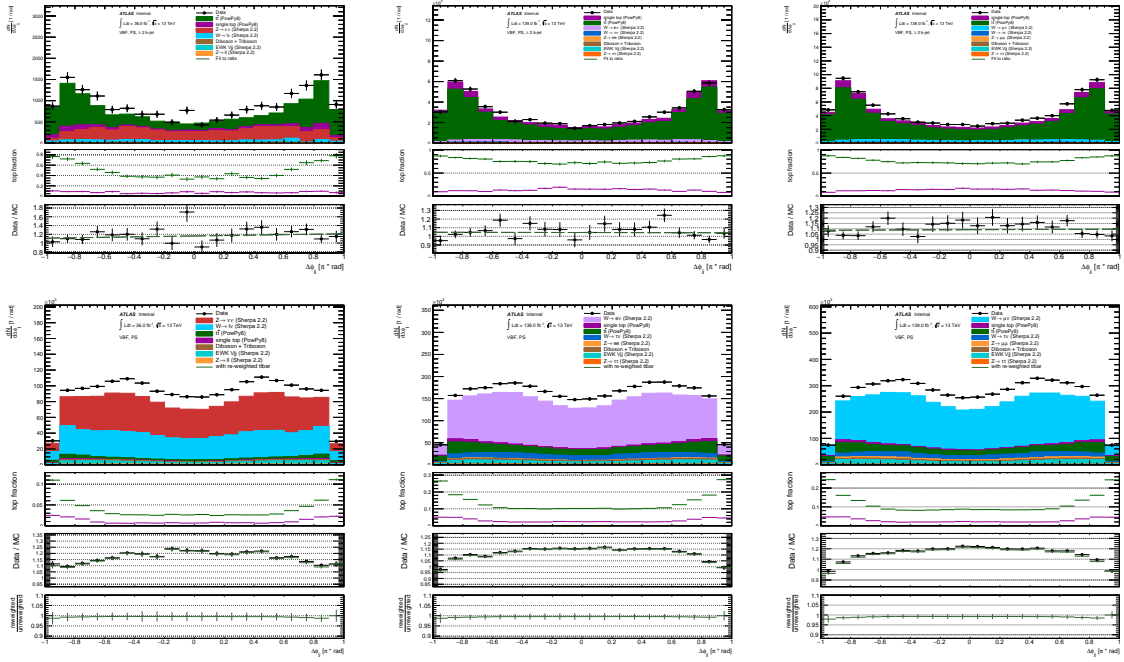


Figure B.6 Top row figures: $p_T^{\text{miss}} + \text{jets}$ (left), $1e + \text{jets}$ (middle) and $1\mu + \text{jets}$ (right) top enhanced control regions (requiring ≥ 2 b-jets) for $\Delta\phi_{jj}$ in the VBF phase-space. Bottom row figures: Comparisons between nominal and reweighted $p_T^{\text{miss}} + \text{jets}$ (left), $1e + \text{jets}$ (middle) and $1\mu + \text{jets}$ (right) regions, where the top contributions are reweighted with the polynomial fit of the corresponding top enhanced control region.

B Top-enhanced control regions

B.2 Single top uncertainties

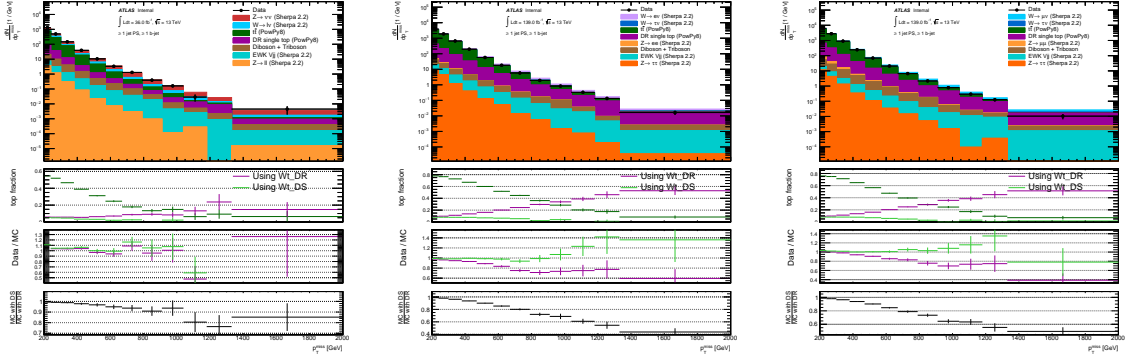


Figure B.7 Comparisons between detector-level distributions in the $p_T^{\text{miss}} + \text{jets}$ (left), $1e + \text{jets}$ (middle) and $1\mu + \text{jets}$ (right) top-enhanced control regions (≥ 1 b-jet) using either the DR or DS single-top subtraction scheme for p_T^{miss} in the ≥ 1 jet phase-space.

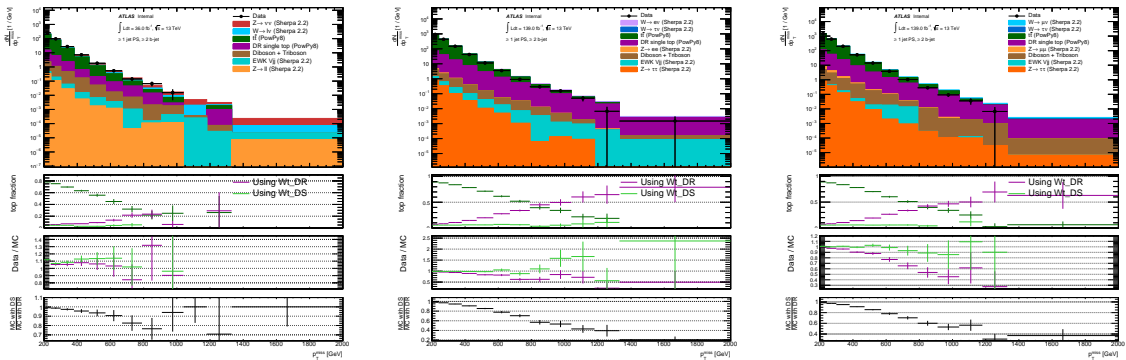


Figure B.8 Comparisons between detector-level distributions in the $p_T^{\text{miss}} + \text{jets}$ (left), $1e + \text{jets}$ (middle) and $1\mu + \text{jets}$ (right) top-enhanced control regions (≥ 2 b-jets) using either the DR or DS single-top subtraction scheme for p_T^{miss} in the ≥ 1 jet phase-space.

Appendix C

Detector response: migration matrices, reconstruction efficiencies, fiducial fractions and fiducial purity

Migration matrices as well as the reconstruction efficiency, fiducial fraction and fiducial purity of all regions in all phase-spaces are shown in this appendix.

Figure C.1 shows migration matrices for p_T^{miss} vs $p_T^{j_1}$ for all regions in the ≥ 1 jet phase-space.

Figure C.2 shows the fiducial purity, reconstruction efficiency and fiducial fraction for p_T^{miss} vs $p_T^{j_1}$ for all regions in the ≥ 1 jet phase-space.

Figure C.3 shows migration matrices for p_T^{miss} for all regions in the ≥ 2 jet phase-space.

Figure C.4 shows the fiducial purity, reconstruction efficiency and fiducial fraction for p_T^{miss} for all regions in the ≥ 2 jet phase-space.

Figure C.5 shows migration matrices for m_{jj} for all regions in the ≥ 2 jet phase-space.

Figure C.6 shows the fiducial purity, reconstruction efficiency and fiducial fraction for m_{jj} for all regions in the ≥ 2 jet phase-space.

Figure C.7 shows migration matrices for $\Delta\phi_{jj}$ for all regions in the ≥ 2 jet phase-space.

Figure C.8 shows the fiducial purity, reconstruction efficiency and fiducial fraction for $\Delta\phi_{jj}$ for all regions in the ≥ 2 jet phase-space.

Figure C.9 shows migration matrices for $\Delta\phi_{jj}$ versus m_{jj} for all regions in the ≥ 2 jet phase-space.

Figure C.10 shows the fiducial purity, reconstruction efficiency and fiducial fraction for $\Delta\phi_{jj}$ versus m_{jj} for all regions in the ≥ 2 jet phase-space.

Figure C.11 shows migration matrices for p_T^{miss} for all regions in the VBF phase-space.

Figure C.12 shows the fiducial purity, reconstruction efficiency and fiducial fraction for p_T^{miss} for all regions in the VBF phase-space.

C Detector response: migration matrices, reconstruction efficiencies, fiducial fractions and fiducial purity

Figure C.13 shows migration matrices for m_{jj} for all regions in the VBF phase-space.

Figure C.14 shows the fiducial purity, reconstruction efficiency and fiducial fraction for m_{jj} for all regions in the VBF phase-space.

Figure C.15 shows migration matrices for $\Delta\phi_{jj}$ for all regions in the VBF phase-space.

Figure C.16 shows the fiducial purity, reconstruction efficiency and fiducial fraction for $\Delta\phi_{jj}$ for all regions in the VBF phase-space.

Figure C.17 shows migration matrices for $\Delta\phi_{jj}$ versus m_{jj} for all regions in the VBF phase-space.

Figure C.18 shows the fiducial purity, reconstruction efficiency and fiducial fraction for $\Delta\phi_{jj}$ versus m_{jj} for all regions in the VBF phase-space.

C Detector response: migration matrices, reconstruction efficiencies, fiducial fractions and fiducial purity

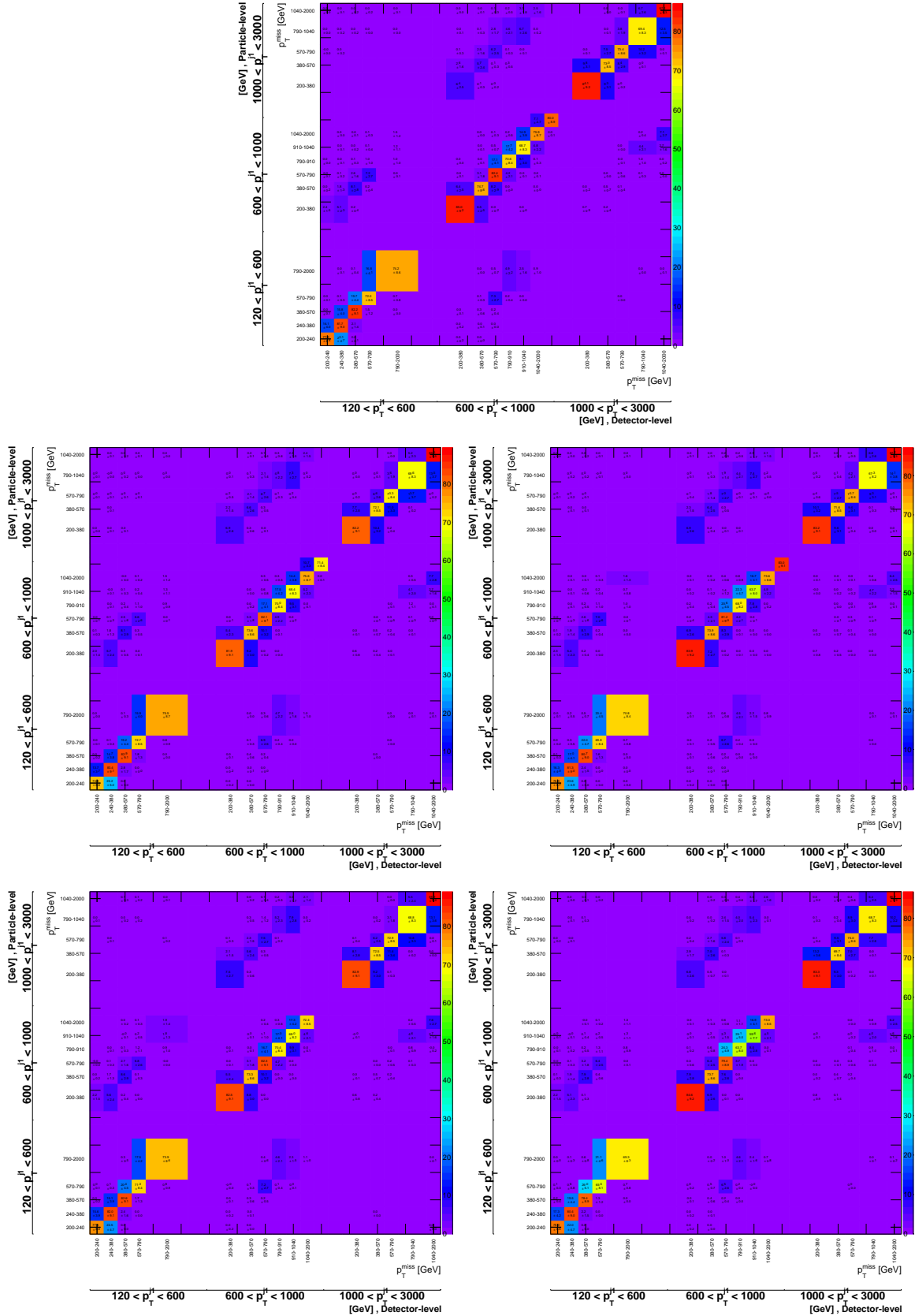


Figure C.1 Migration matrices for p_T^{miss} versus $p_T^{j_1}$ for $p_T^{\text{miss}} + \text{jets}$ (top), $1e + \text{jets}$ (middle left), $1\mu + \text{jets}$ (middle right), $2e + \text{jets}$ (bottom left), $2\mu + \text{jets}$ (bottom right) in the ≥ 1 jet phase-space.

C Detector response: migration matrices, reconstruction efficiencies, fiducial fractions and fiducial purity

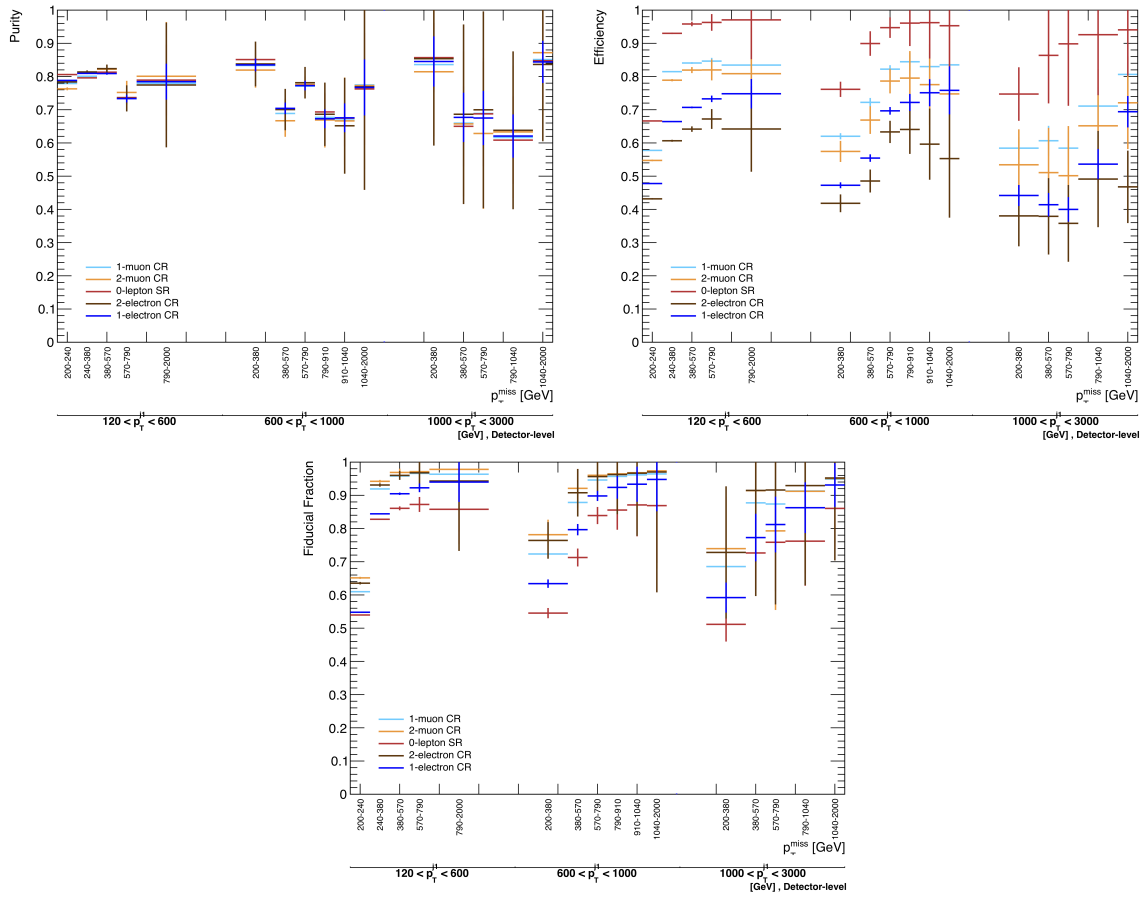


Figure C.2 Fiducial purity, reconstruction efficiency and fiducial fraction for p_T^{miss} versus $p_T^{j_1}$ for all regions in the ≥ 1 jet phase-space.

C Detector response: migration matrices, reconstruction efficiencies, fiducial fractions and fiducial purity

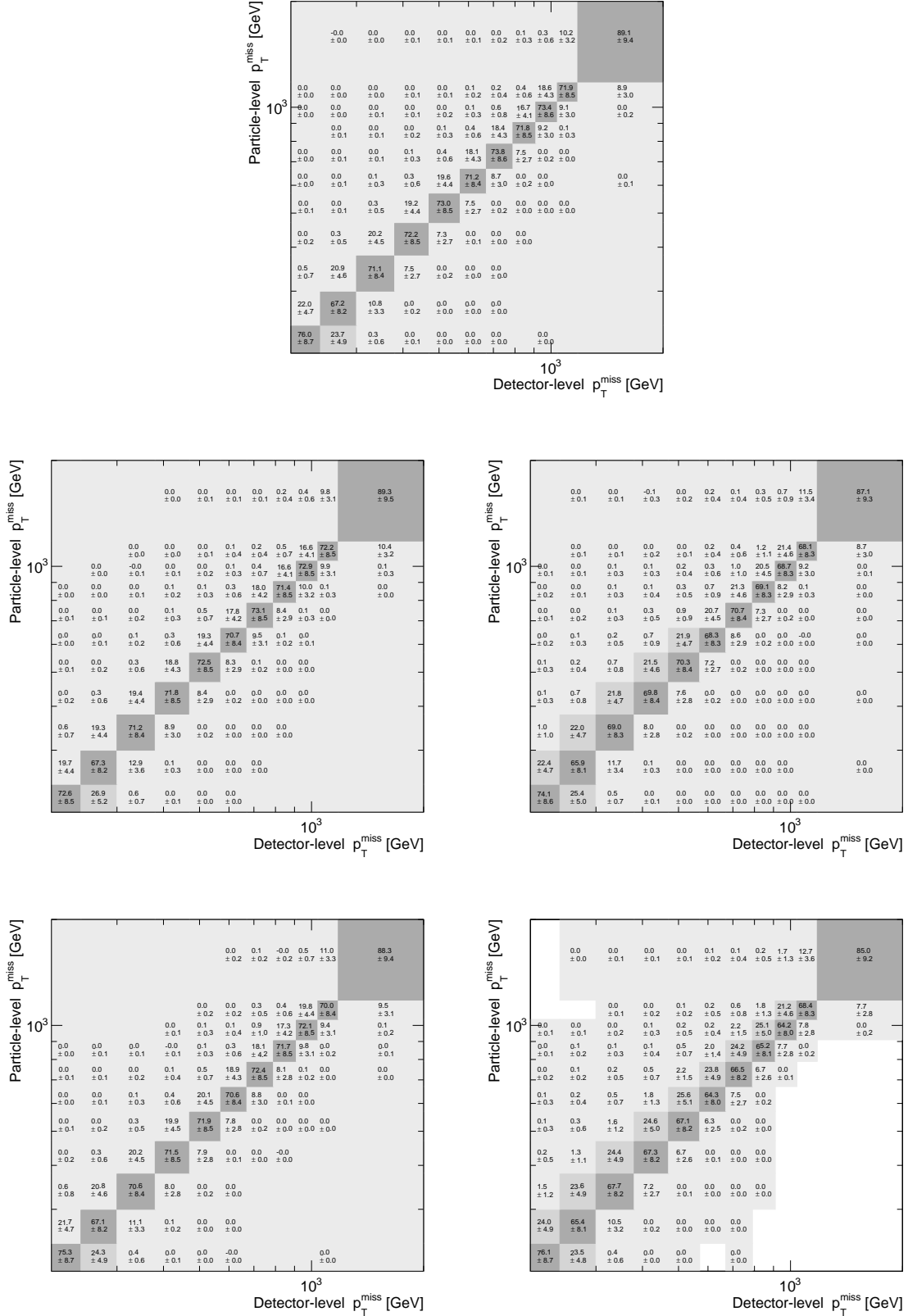


Figure C.3 Migration matrices for p_T^{miss} for p_T^{miss} + jets (top), 1e + jets (middle left), 1μ + jets (middle right), 2e + jets (bottom left), 2μ + jets (bottom right) in the ≥ 2 jet phase-space.

C Detector response: migration matrices, reconstruction efficiencies, fiducial fractions and fiducial purity

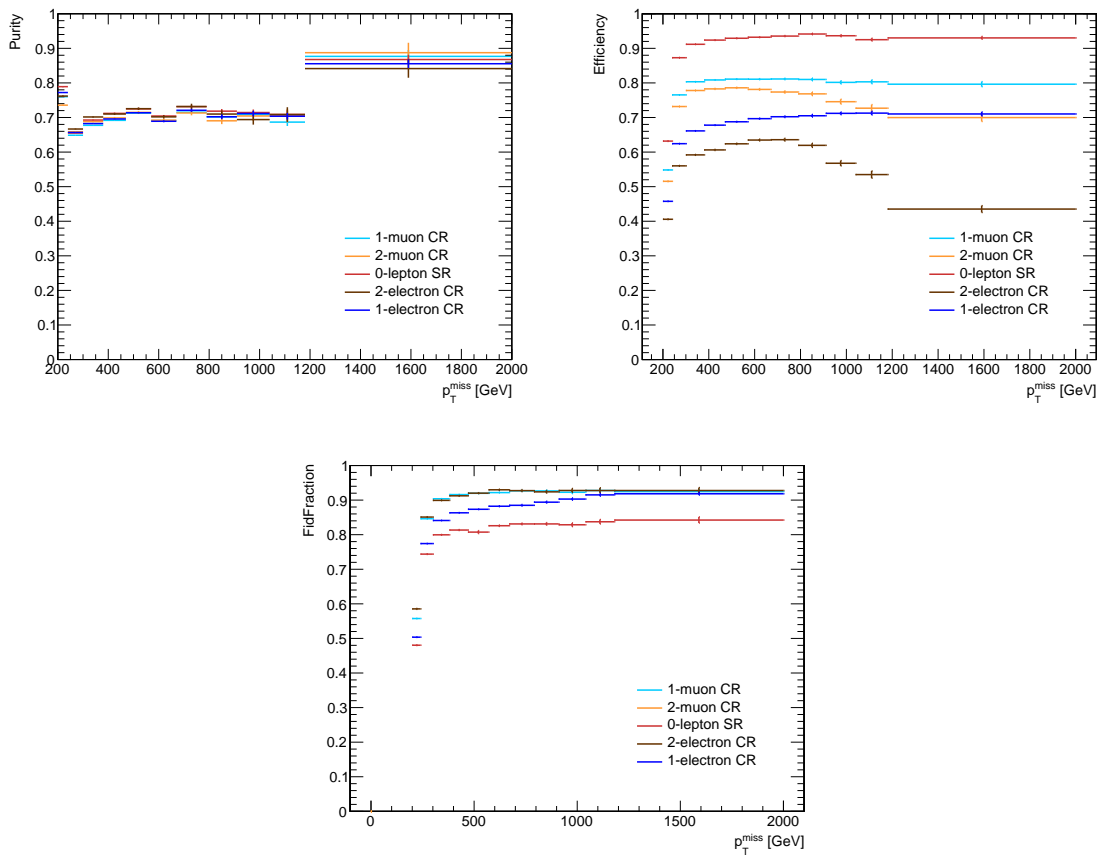


Figure C.4 Fiducial purity, reconstruction efficiency and fiducial fraction for p_T^{miss} for all regions in the ≥ 2 jet phase-space.

C Detector response: migration matrices, reconstruction efficiencies, fiducial fractions and fiducial purity

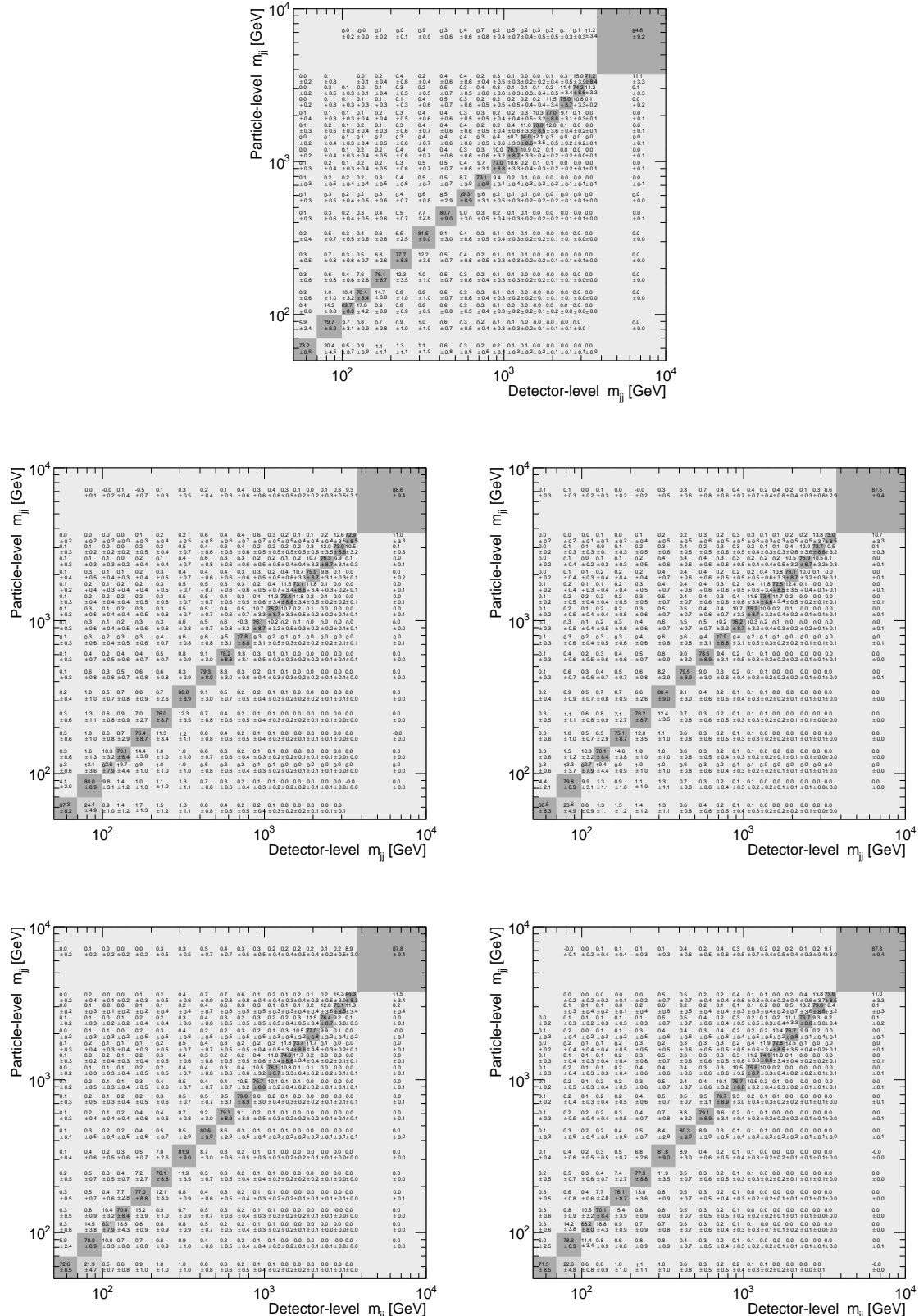


Figure C.5 Migration matrices for m_{jj} for $p_T^{\text{miss}} + \text{jets}$ (top), $1e + \text{jets}$ (middle left), $1\mu + \text{jets}$ (middle right), $2e + \text{jets}$ (bottom left), $2\mu + \text{jets}$ (bottom right) in the ≥ 2 jet phase-space.

C Detector response: migration matrices, reconstruction efficiencies, fiducial fractions and fiducial purity

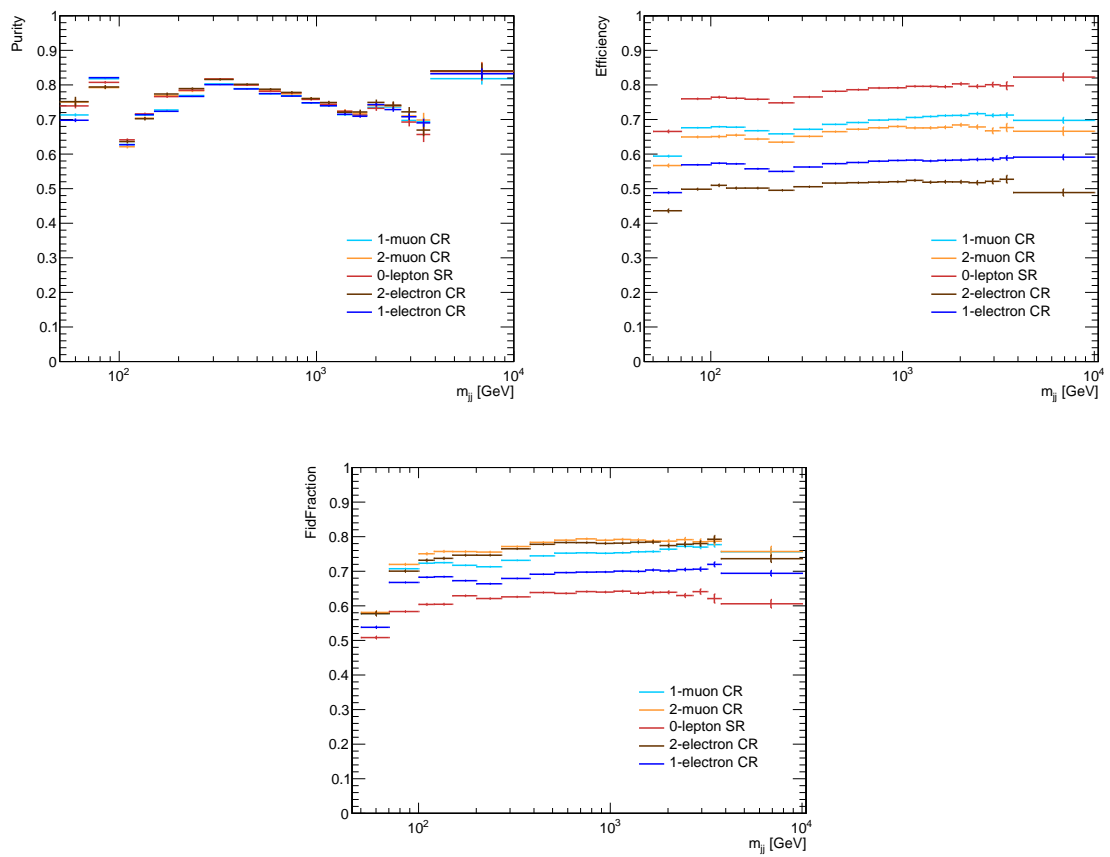


Figure C.6 Fiducial purity, reconstruction efficiency and fiducial fraction for m_{jj} for all regions in the ≥ 2 jet phase-space.

C Detector response: migration matrices, reconstruction efficiencies, fiducial fractions and fiducial purity

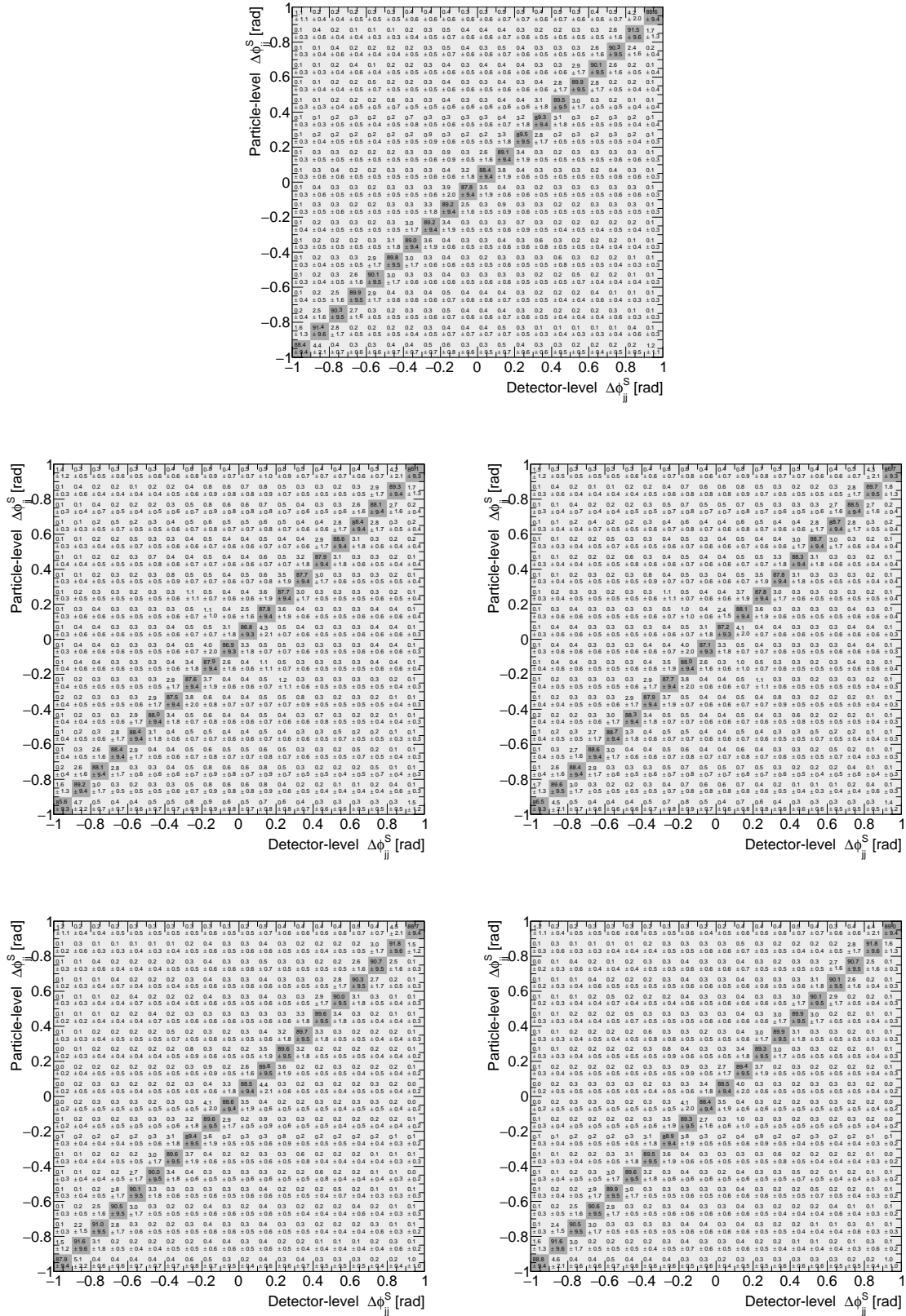


Figure C.7 Migration matrices for $\Delta\phi_{jj}^S$ for $p_T^{\text{miss}} + \text{jets}$ (top), $1e + \text{jets}$ (middle left), $1\mu + \text{jets}$ (middle right), $2e + \text{jets}$ (bottom left), $2\mu + \text{jets}$ (bottom right) in the ≥ 2 jet phase-space.

C Detector response: migration matrices, reconstruction efficiencies, fiducial fractions and fiducial purity

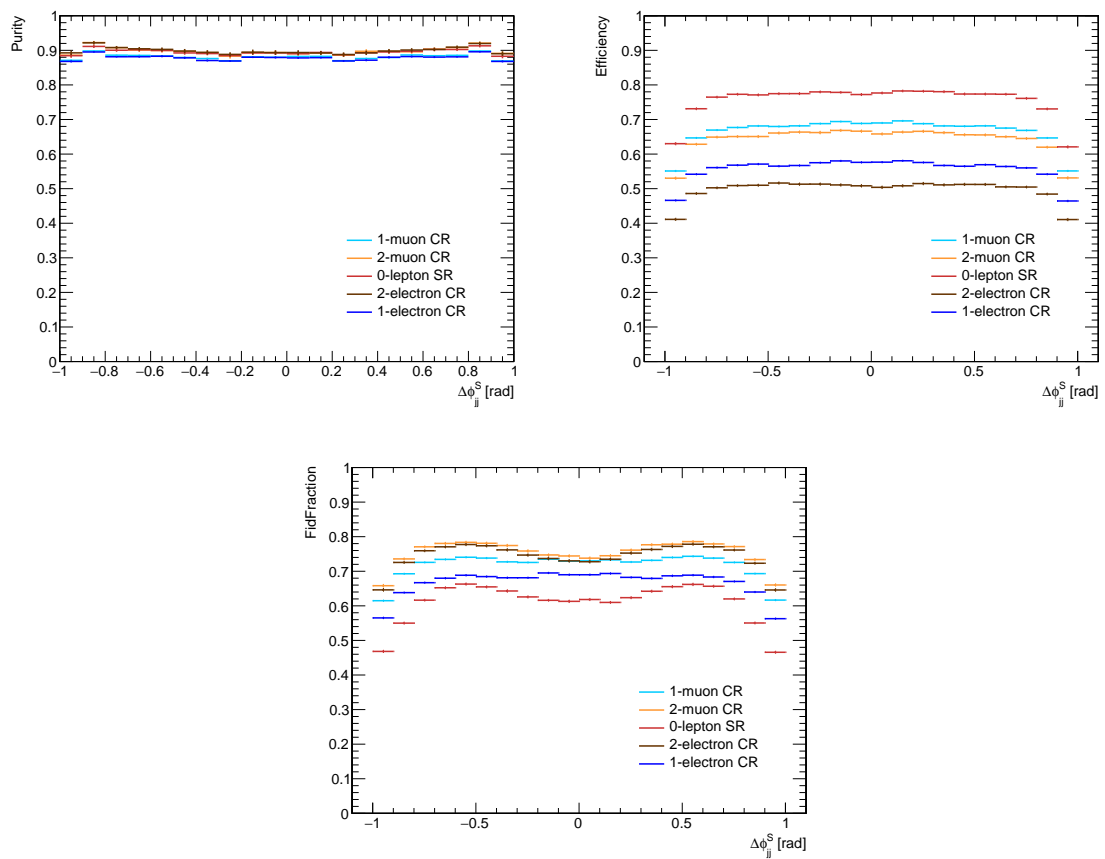


Figure C.8 Fiducial purity, reconstruction efficiency and fiducial fraction for $\Delta\phi_{jj}$ for all regions in the ≥ 2 jet phase-space.

C Detector response: migration matrices, reconstruction efficiencies, fiducial fractions and fiducial purity

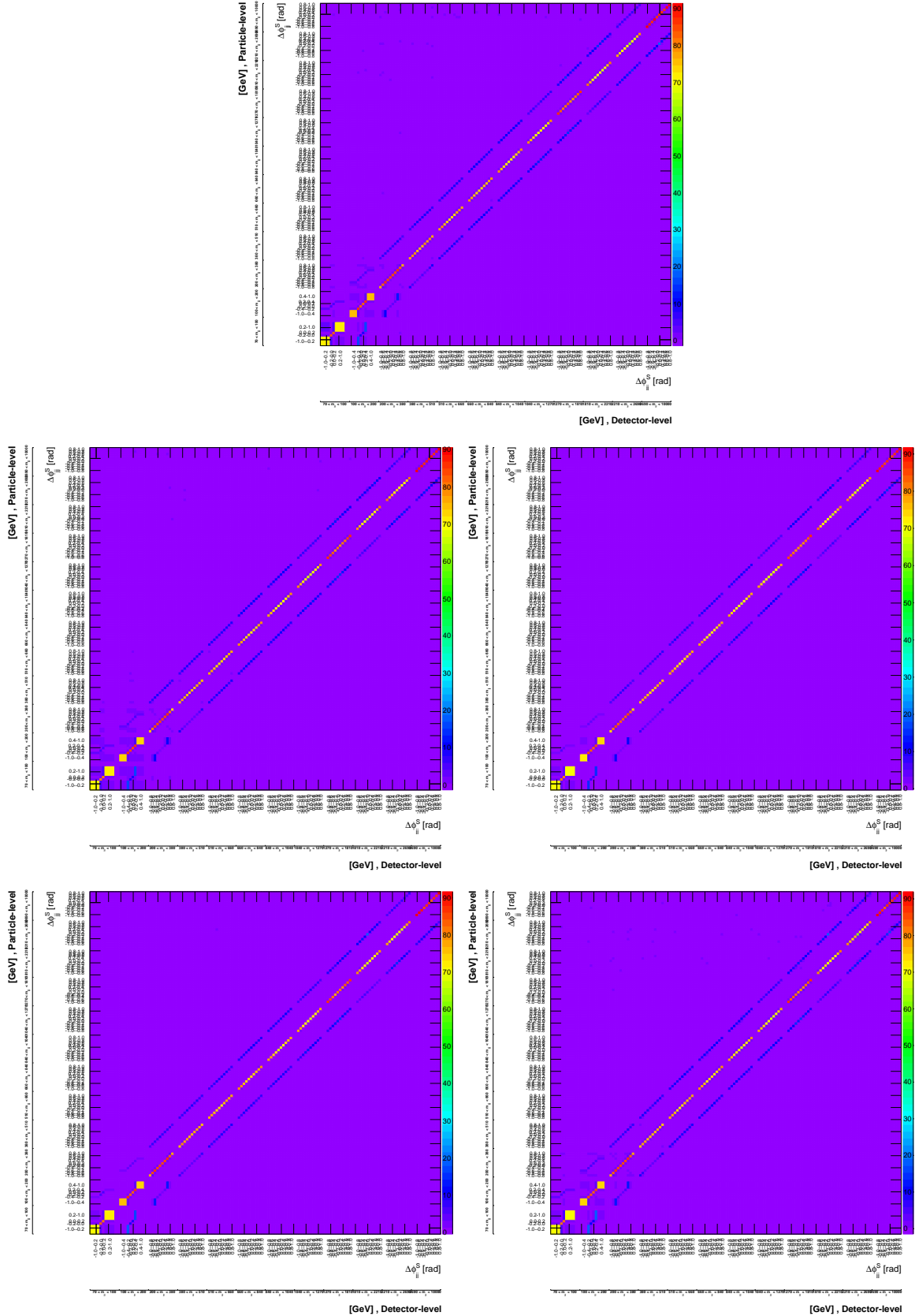


Figure C.9 Migration matrices for $\Delta\phi_{jj}$ versus m_{jj} for $p_T^{\text{miss}} + \text{jets}$ (top), $1e + \text{jets}$ (middle left), $1\mu + \text{jets}$ (middle right), $2e + \text{jets}$ (bottom left), $2\mu + \text{jets}$ (bottom right) in the ≥ 2 jet phase-space.

C Detector response: migration matrices, reconstruction efficiencies, fiducial fractions and fiducial purity

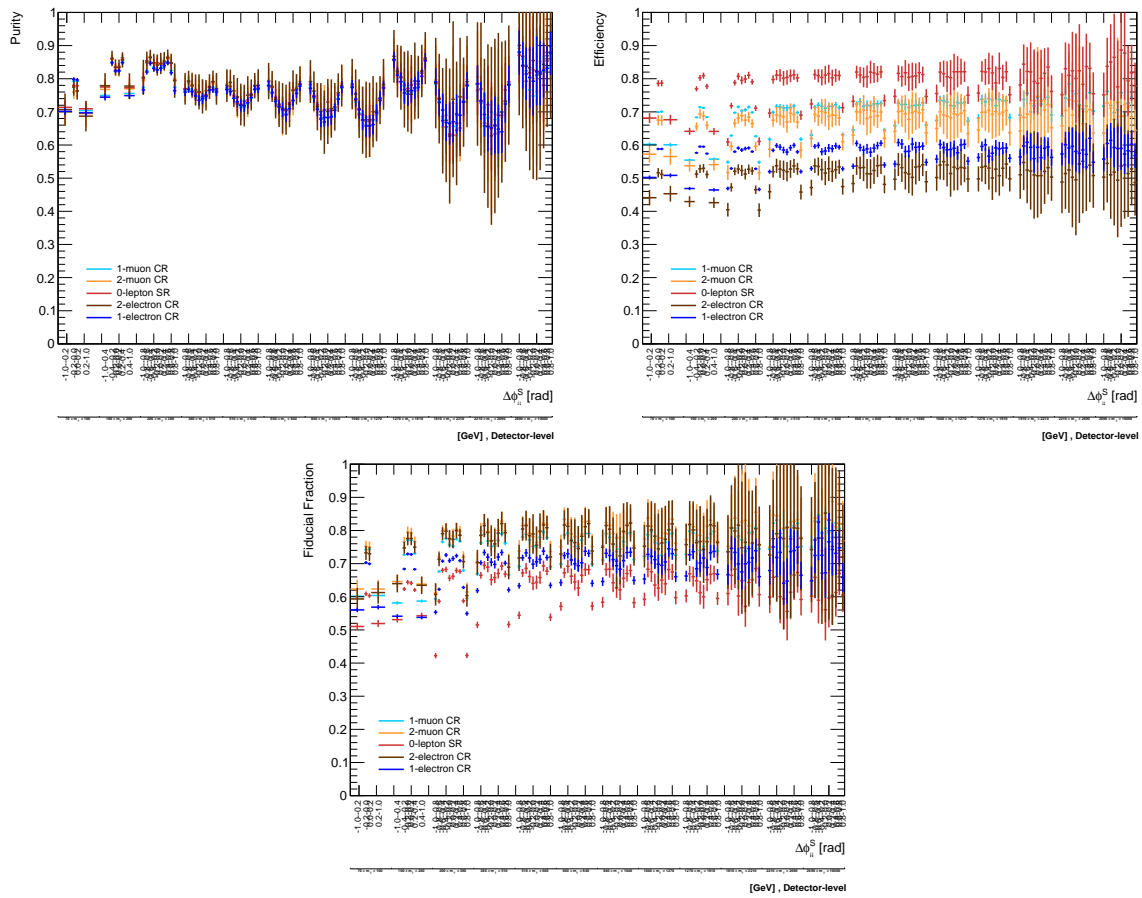


Figure C.10 Fiducial purity, reconstruction efficiency and fiducial fraction for $\Delta\phi_{jj}$ versus m_{jj} for all regions in the ≥ 2 jet phase-space.

C Detector response: migration matrices, reconstruction efficiencies, fiducial fractions and fiducial purity

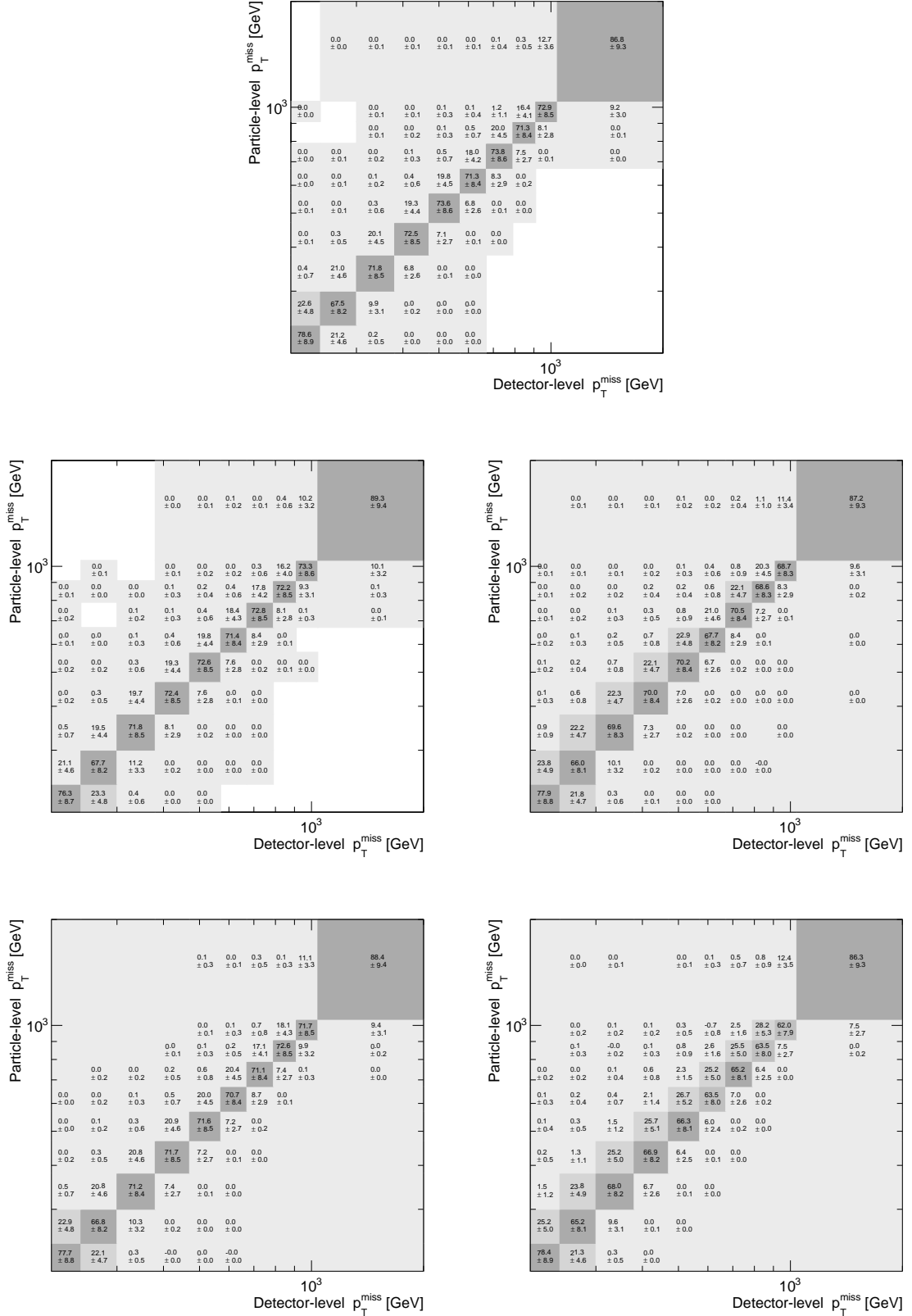


Figure C.11 Migration matrices for p_T^{miss} for $p_T^{\text{miss}} + \text{jets}$ (top), $1e + \text{jets}$ (middle left), $1\mu + \text{jets}$ (middle right), $2e + \text{jets}$ (bottom left), $2\mu + \text{jets}$ (bottom right) in the VBF phase-space.

C Detector response: migration matrices, reconstruction efficiencies, fiducial fractions and fiducial purity

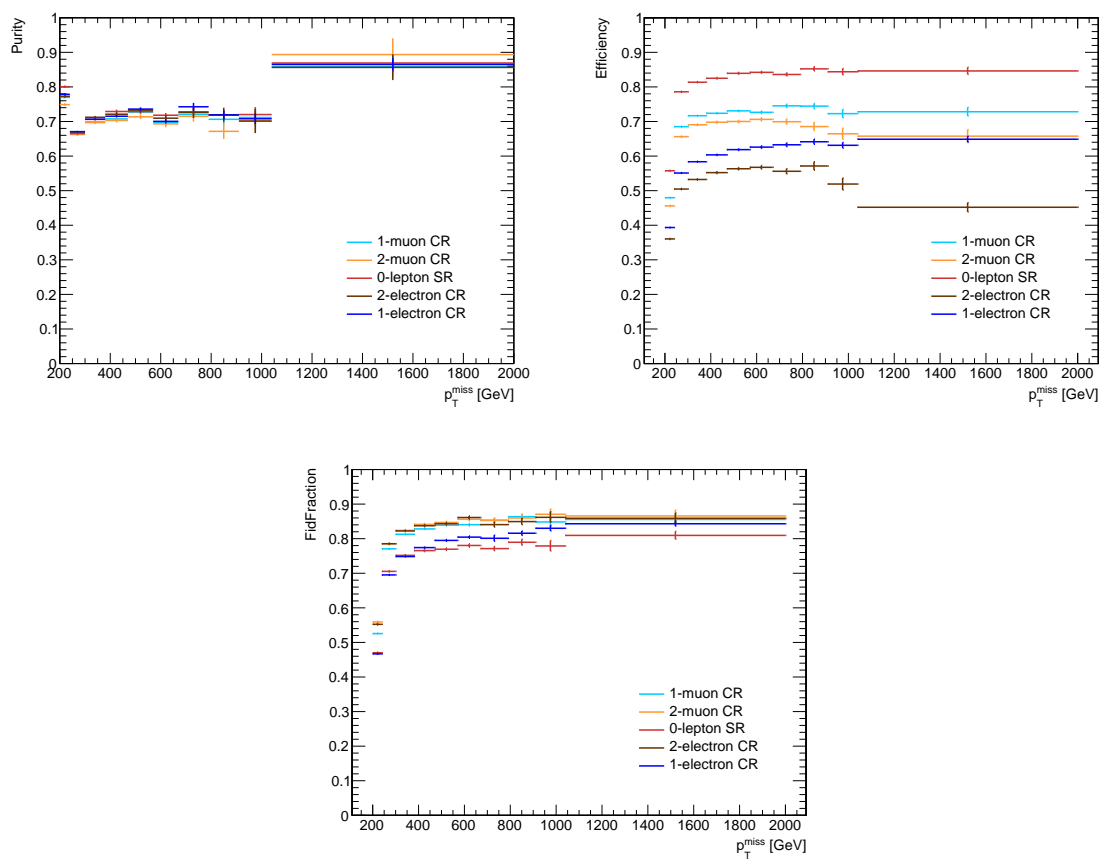


Figure C.12 Fiducial purity, reconstruction efficiency and fiducial fraction for p_T^{miss} for all regions in the VBF phase-space.

C Detector response: migration matrices, reconstruction efficiencies, fiducial fractions and fiducial purity

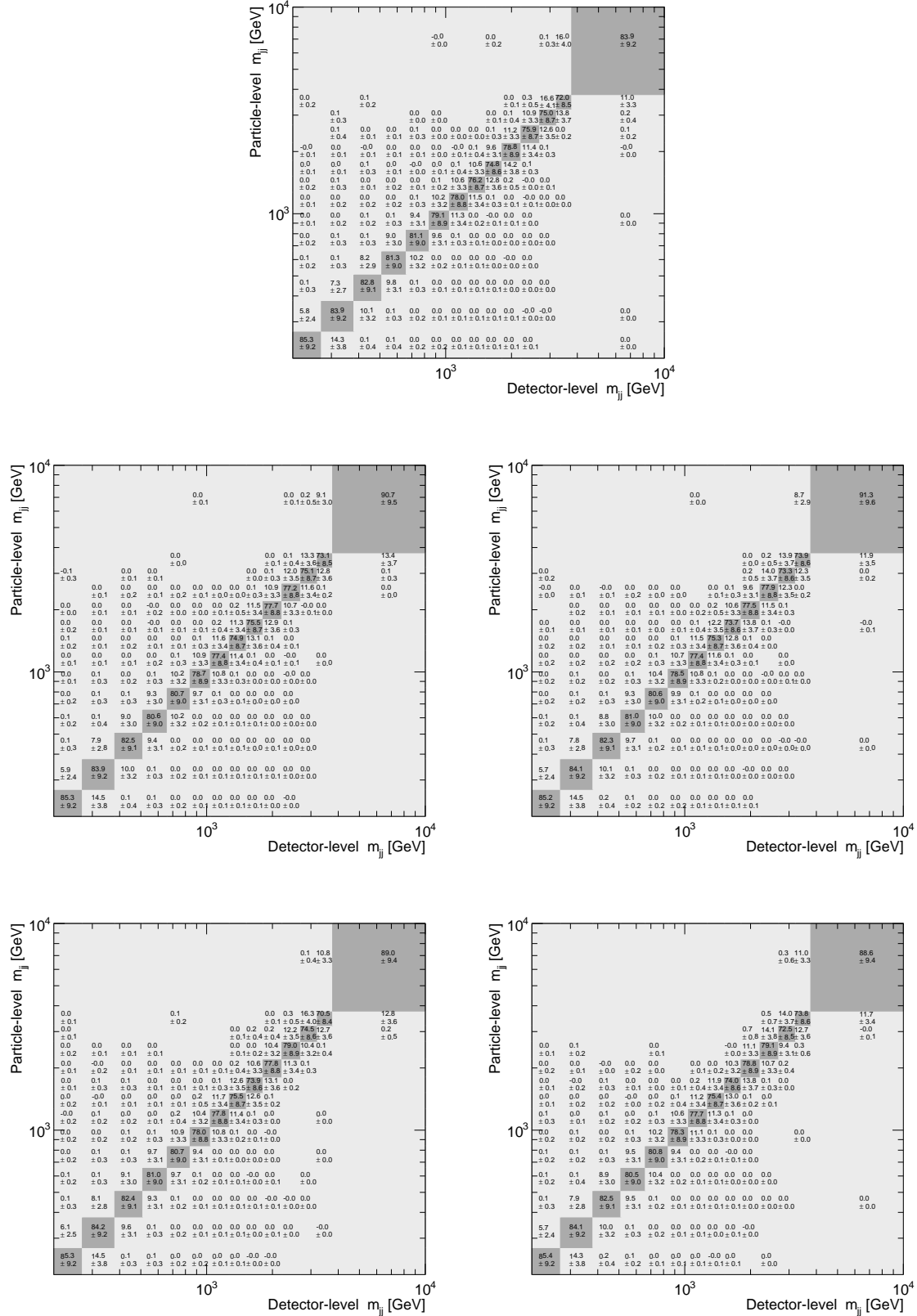


Figure C.13 Migration matrices for m_{jj} for $p_T^{\text{miss}} + \text{jets}$ (top), $1e + \text{jets}$ (middle left), $1\mu + \text{jets}$ (middle right), $2e + \text{jets}$ (bottom left), $2\mu + \text{jets}$ (bottom right) in the VBF phase-space.

C Detector response: migration matrices, reconstruction efficiencies, fiducial fractions and fiducial purity

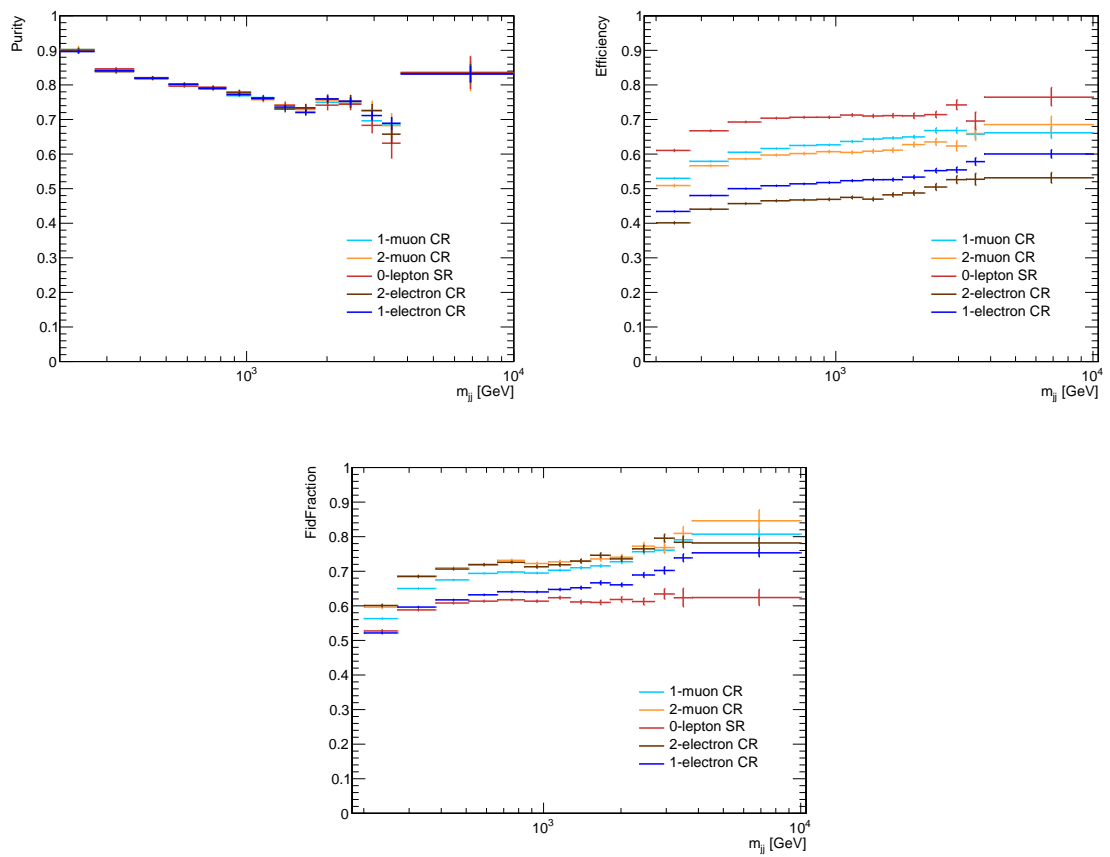


Figure C.14 Fiducial purity, reconstruction efficiency and fiducial fraction for m_{jj} for all regions in the VBF phase-space.

C Detector response: migration matrices, reconstruction efficiencies, fiducial fractions and fiducial purity

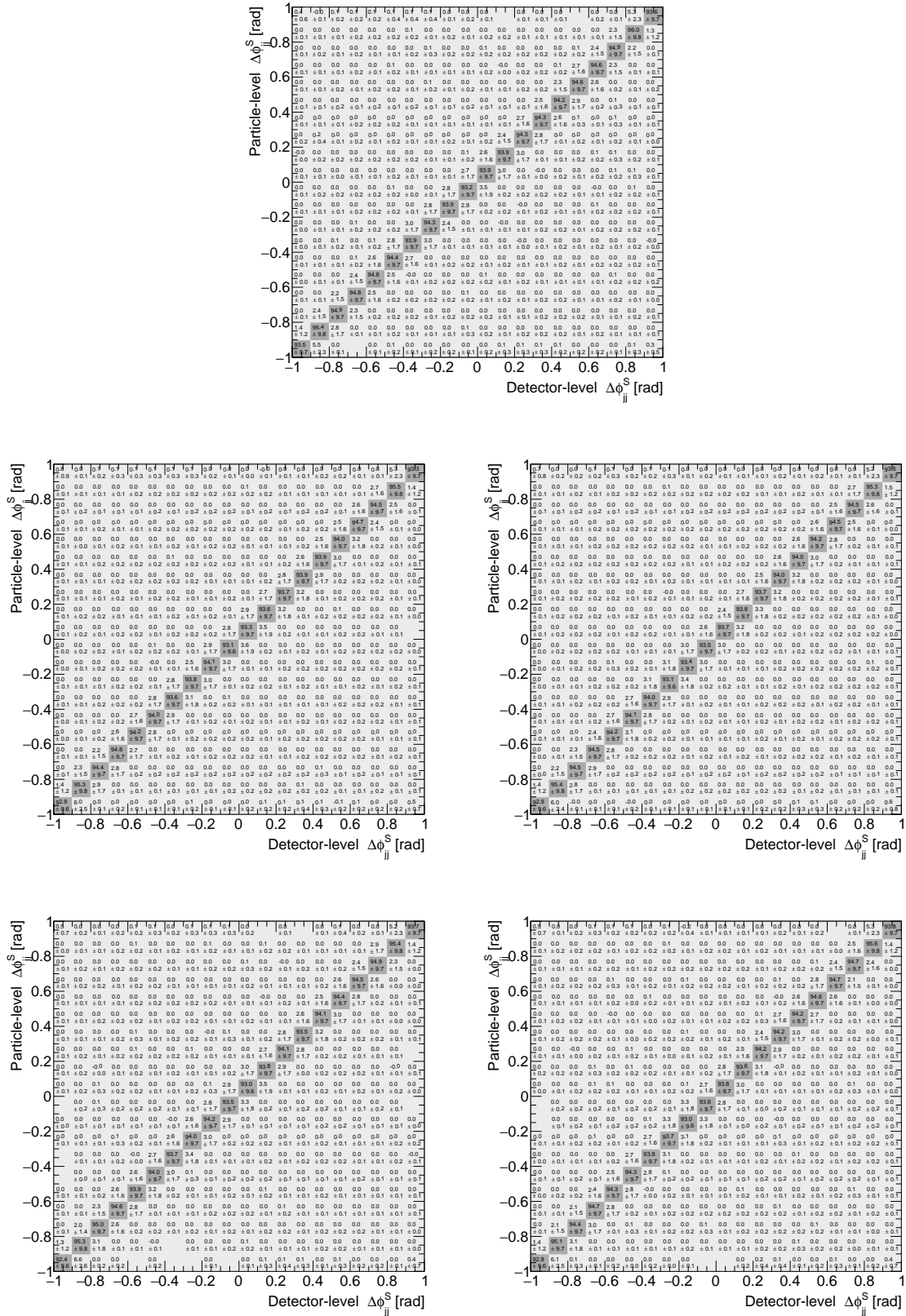


Figure C.15 Migration matrices for $\Delta\phi_{jj}$ for $p_T^{\text{miss}} + \text{jets}$ (top), $1e + \text{jets}$ (middle left), $1\mu + \text{jets}$ (middle right), $2e + \text{jets}$ (bottom left), $2\mu + \text{jets}$ (bottom right) in the VBF phase-space.

C Detector response: migration matrices, reconstruction efficiencies, fiducial fractions and fiducial purity

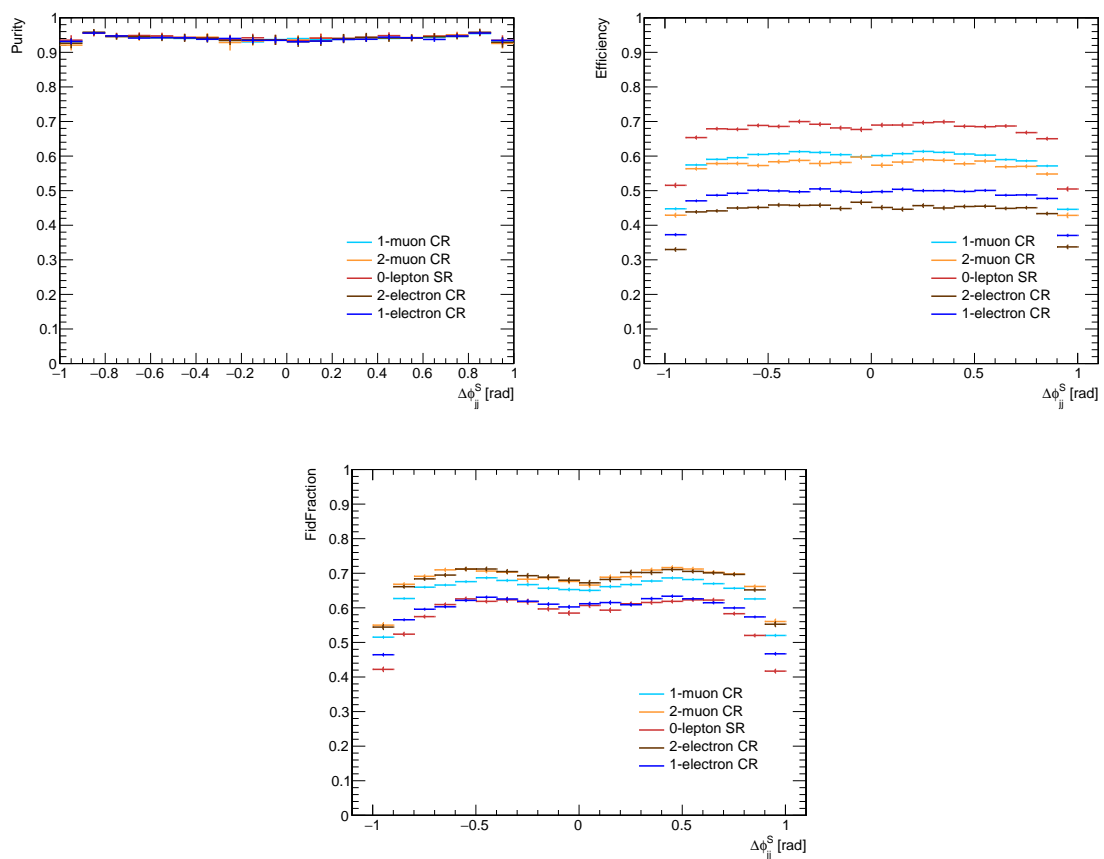


Figure C.16 Fiducial purity, reconstruction efficiency and fiducial fraction for $\Delta\phi_{jj}$ for all regions in the VBF phase-space.

C Detector response: migration matrices, reconstruction efficiencies, fiducial fractions and fiducial purity

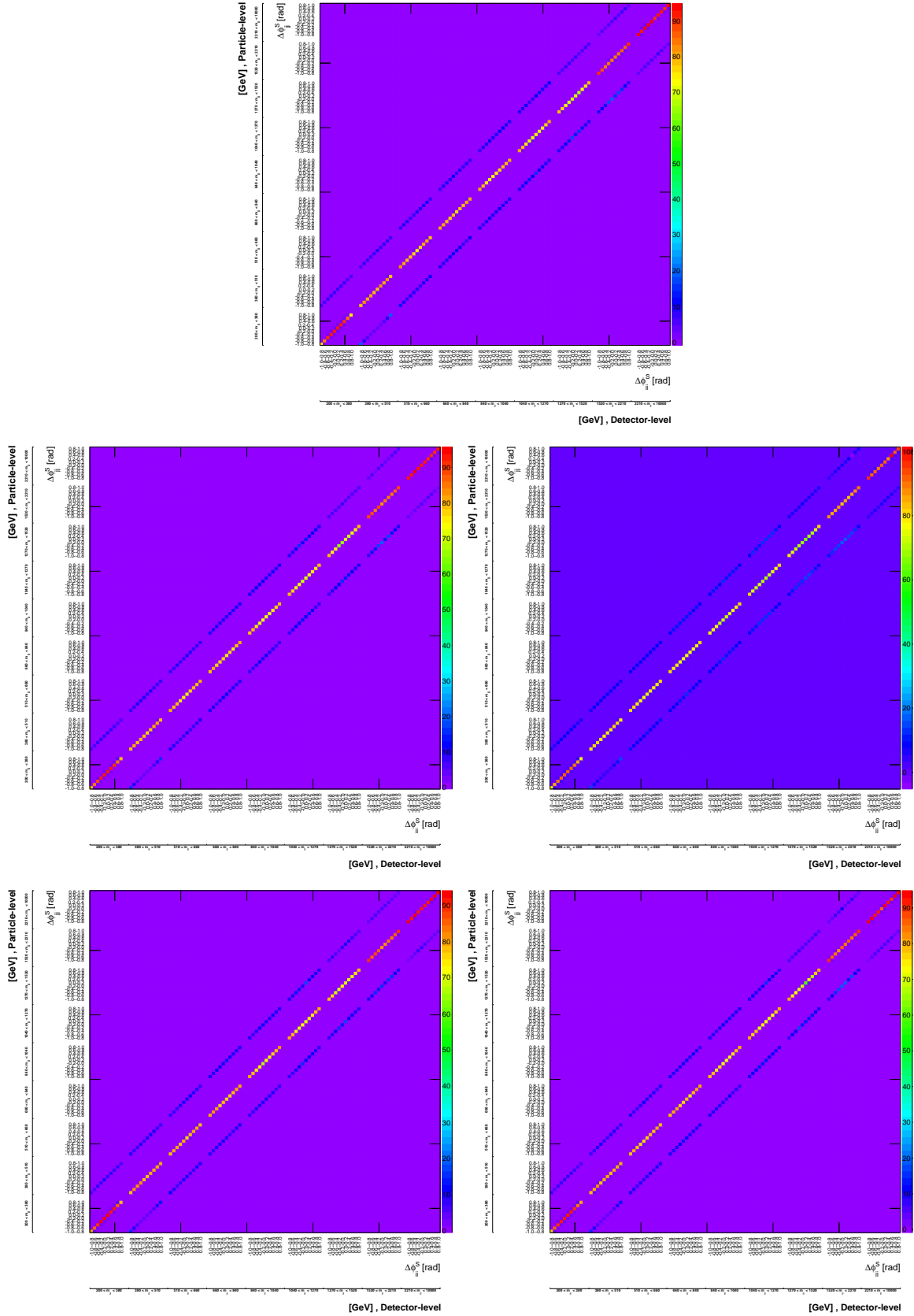


Figure C.17 Migration matrices for $\Delta\phi_{jj}$ versus m_{jj} for $1e + \text{jets}$ (top left), $1\mu + \text{jets}$ (top right), $2e + \text{jets}$ (bottom left) and $2\mu + \text{jets}$ (bottom right) in the VBF phase-space.

C Detector response: migration matrices, reconstruction efficiencies, fiducial fractions and fiducial purity

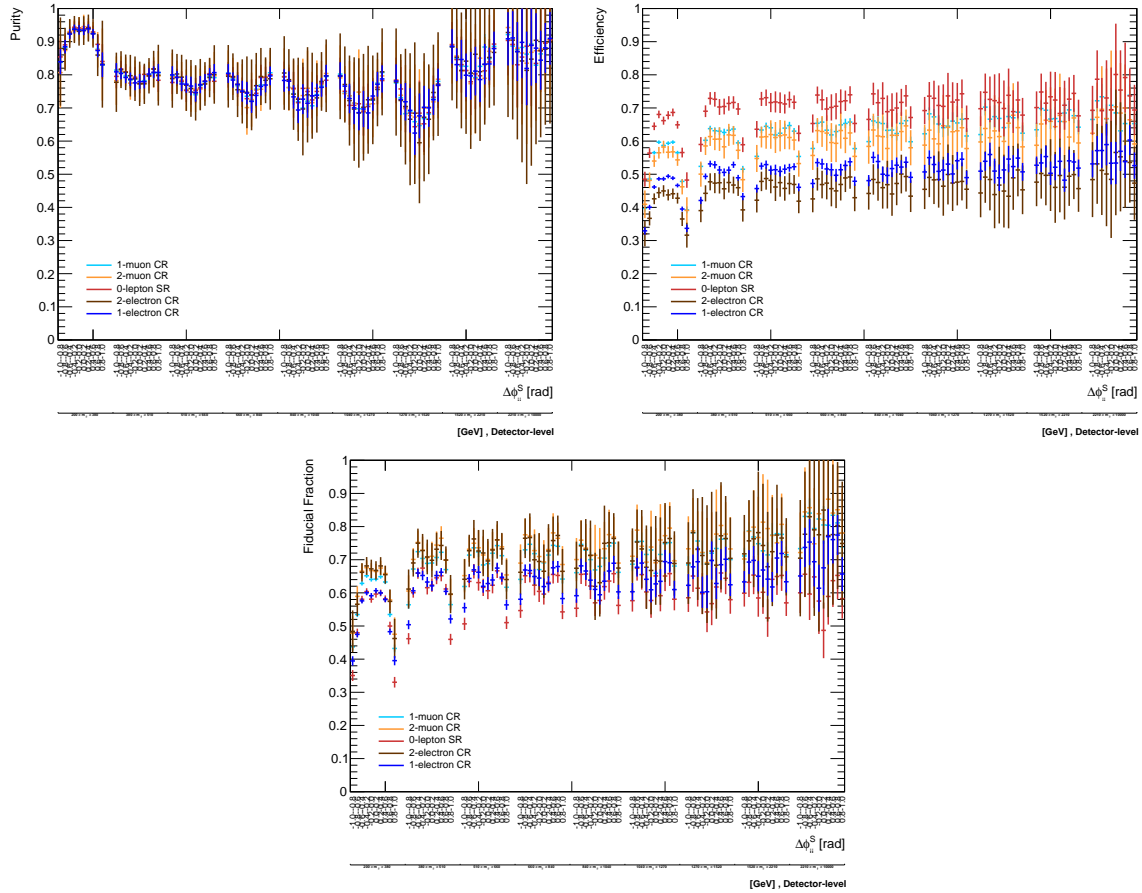


Figure C.18 Fiducial purity, reconstruction efficiency and fiducial fraction for $\Delta\phi_{jj}$ versus m_{jj} for $p_T^{\text{miss}} + \text{jets}$ (top), $1e + \text{jets}$ (middle left), $1\mu + \text{jets}$ (middle right), $2e + \text{jets}$ (bottom left), $2\mu + \text{jets}$ (bottom right) in the VBF phase-space.

Appendix D

Unfolded systematic uncertainties

The effect of the systematic uncertainties on the unfolded results are shown in this appendix for all observables. Systematics coming from the jet energy scale and resolution show significant fluctuations in bins with low statistics and so Friedman’s “super smoothing” technique [97] is used to smooth these systematics. Jet energy resolution systematics are only provided with an upward variation. The down variation for each one is estimated by mirroring the upward variation. For the $\Delta\phi_{jj}$ observable in both the ≥ 2 jet and VBF phase-spaces, the uncertainties for positive $\Delta\phi_{jj}$ are the same as those for negative $\Delta\phi_{jj}$, and so they are symmetrised along this dimension.

The grouped systematic uncertainties are shown in the following:

Figure D.1 shows the systematic breakdown for p_T^{miss} in the ≥ 1 jet phase-space.

Figure D.2 shows the systematic breakdown for p_T^{miss} vs $p_T^{j_1}$ in the ≥ 1 jet phase-space.

Figure D.3 shows the systematic breakdown for p_T^{miss} in the ≥ 2 jet phase-space.

Figure D.4 shows the systematic breakdown for m_{jj} in the ≥ 2 jet phase-space.

Figure D.5 shows the systematic breakdown for $\Delta\phi_{jj}$ in the ≥ 2 jet phase-space.

Figure D.6 shows the systematic breakdown for $\Delta\phi_{jj}$ vs m_{jj} in the ≥ 2 jet phase-space.

Figure D.7 shows the systematic breakdown for p_T^{miss} in the VBF phase-space.

Figure D.8 shows the systematic breakdown for m_{jj} in the VBF phase-space.

Figure D.9 shows the systematic breakdown for $\Delta\phi_{jj}$ in the VBF phase-space.

Figure D.10 shows the systematic breakdown for $\Delta\phi_{jj}$ vs m_{jj} in the VBF phase-space.

D Unfolded systematic uncertainties

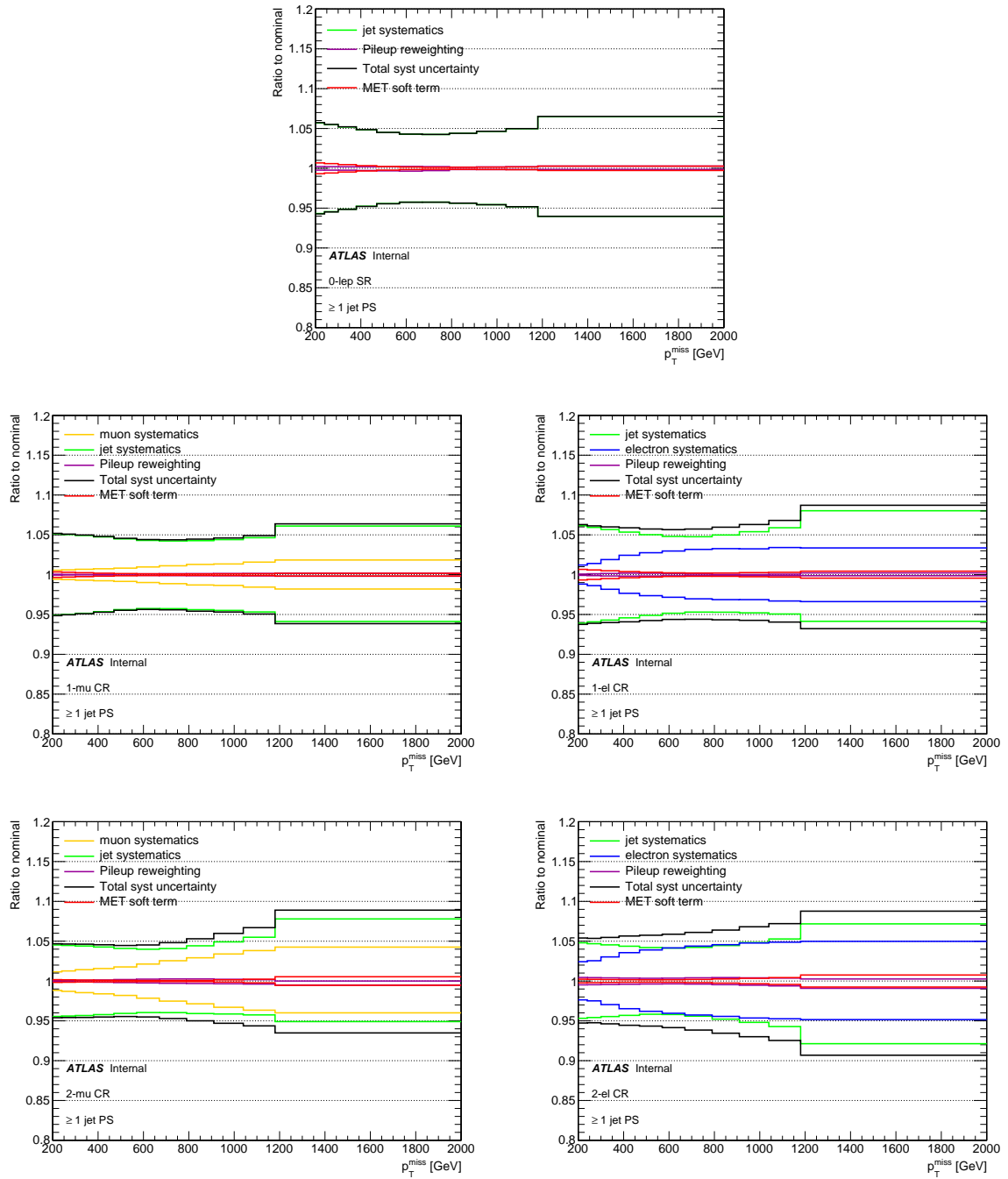


Figure D.1 Systematic breakdown for p_T^{miss} in the ≥ 1 jet phase-space for all regions.

D Unfolded systematic uncertainties

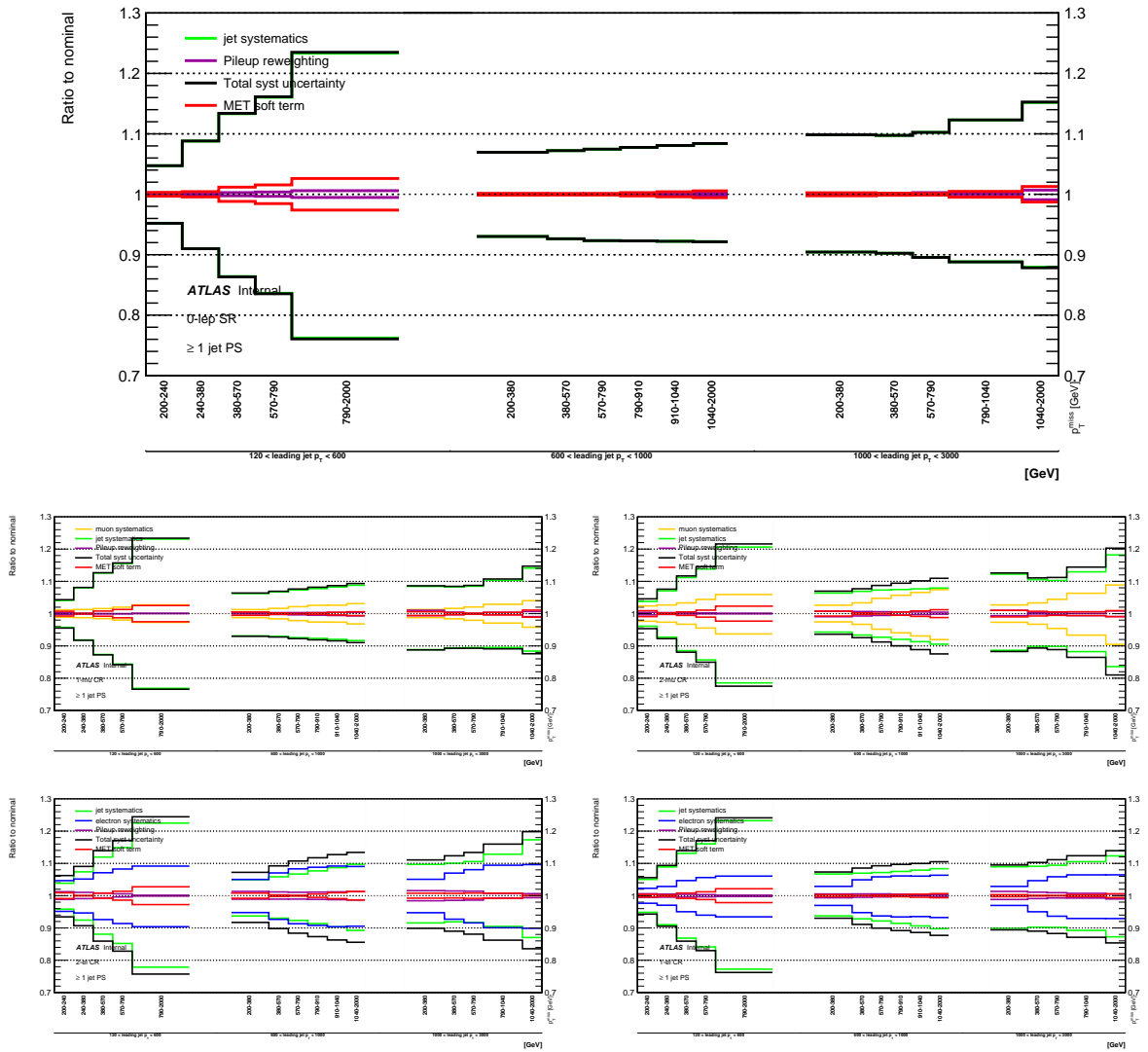


Figure D.2 Systematic breakdown for p_T^{miss} vs $p_T^{j_1}$ in the ≥ 1 jet phase-space for all regions.

D Unfolded systematic uncertainties

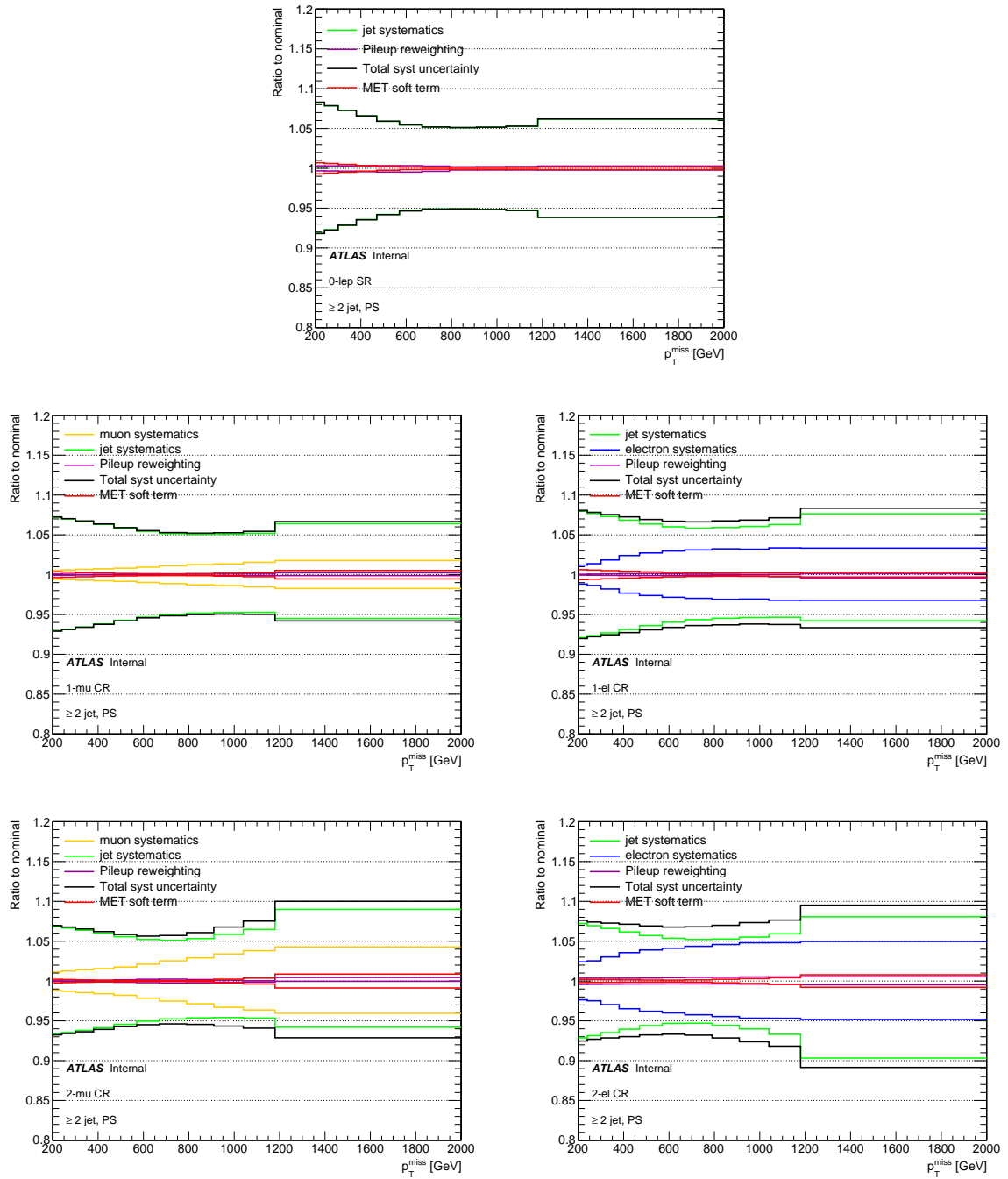


Figure D.3 Systematic breakdown for p_T^{miss} in the ≥ 2 jet phase-space for all regions.

D Unfolded systematic uncertainties

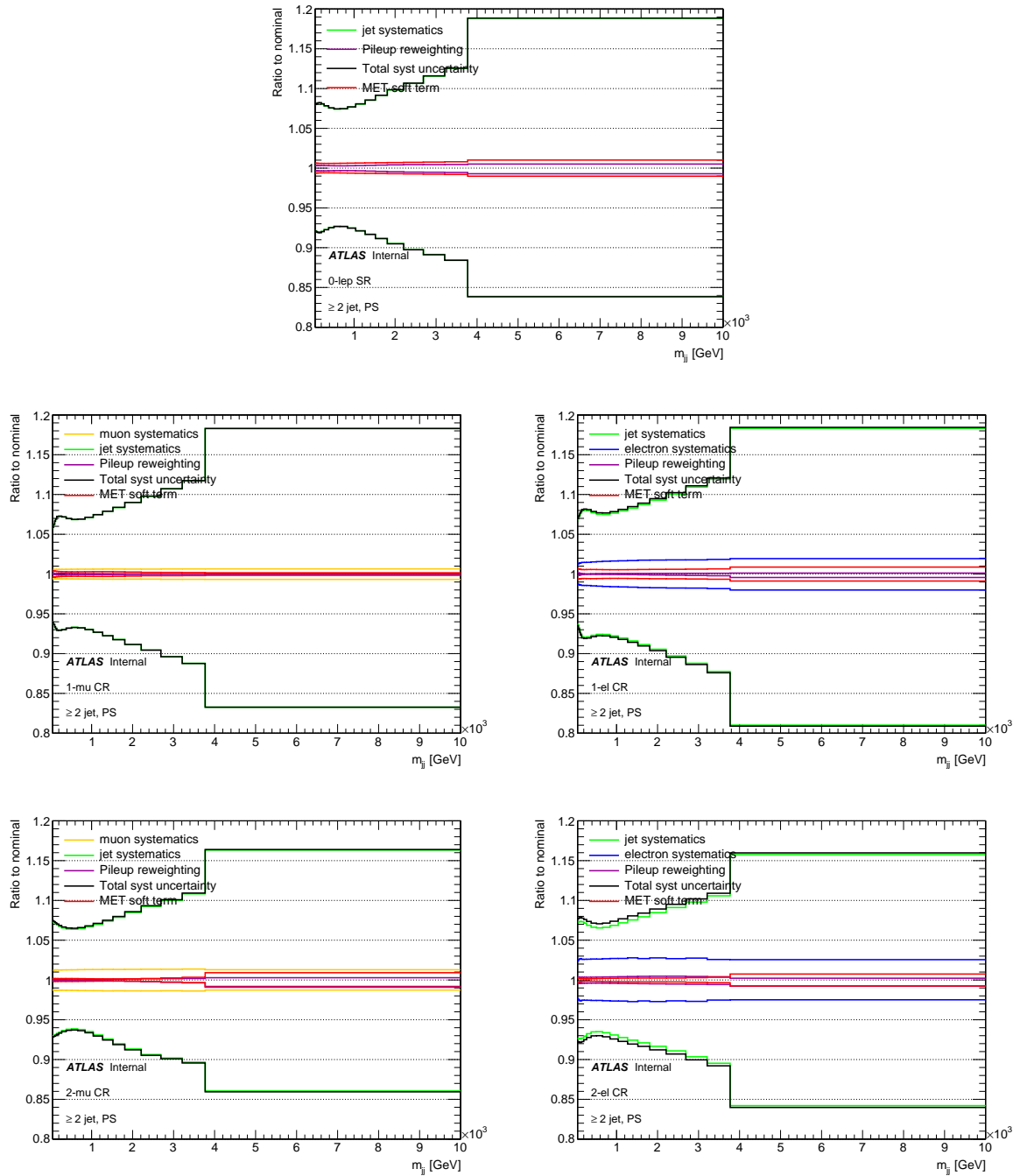


Figure D.4 Systematic breakdown for m_{jj} in the ≥ 2 jet phase-space for all regions.

D Unfolded systematic uncertainties

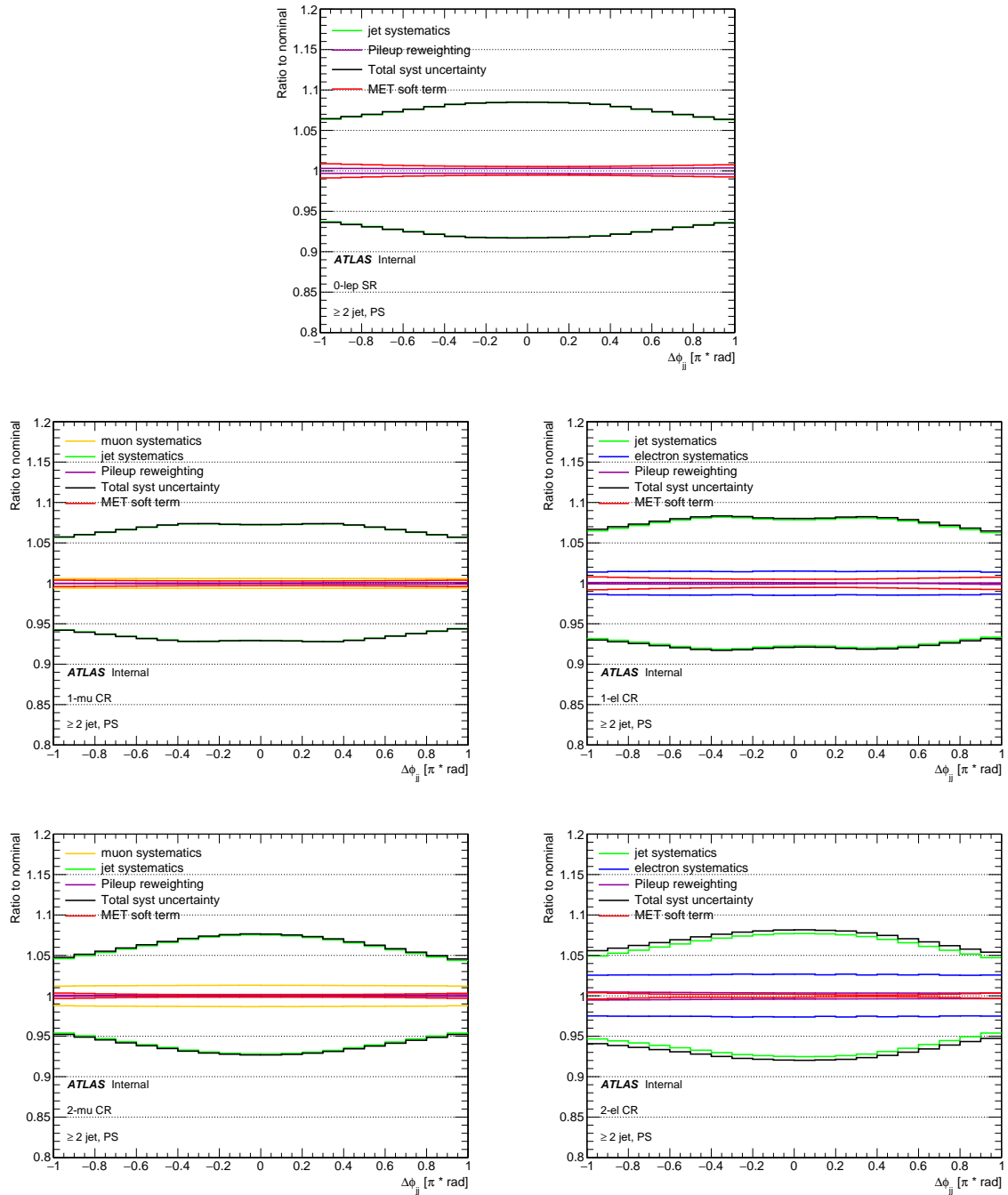


Figure D.5 Systematic breakdown for $\Delta\phi_{jj}$ in the ≥ 2 jet phase-space for all regions.

D Unfolded systematic uncertainties

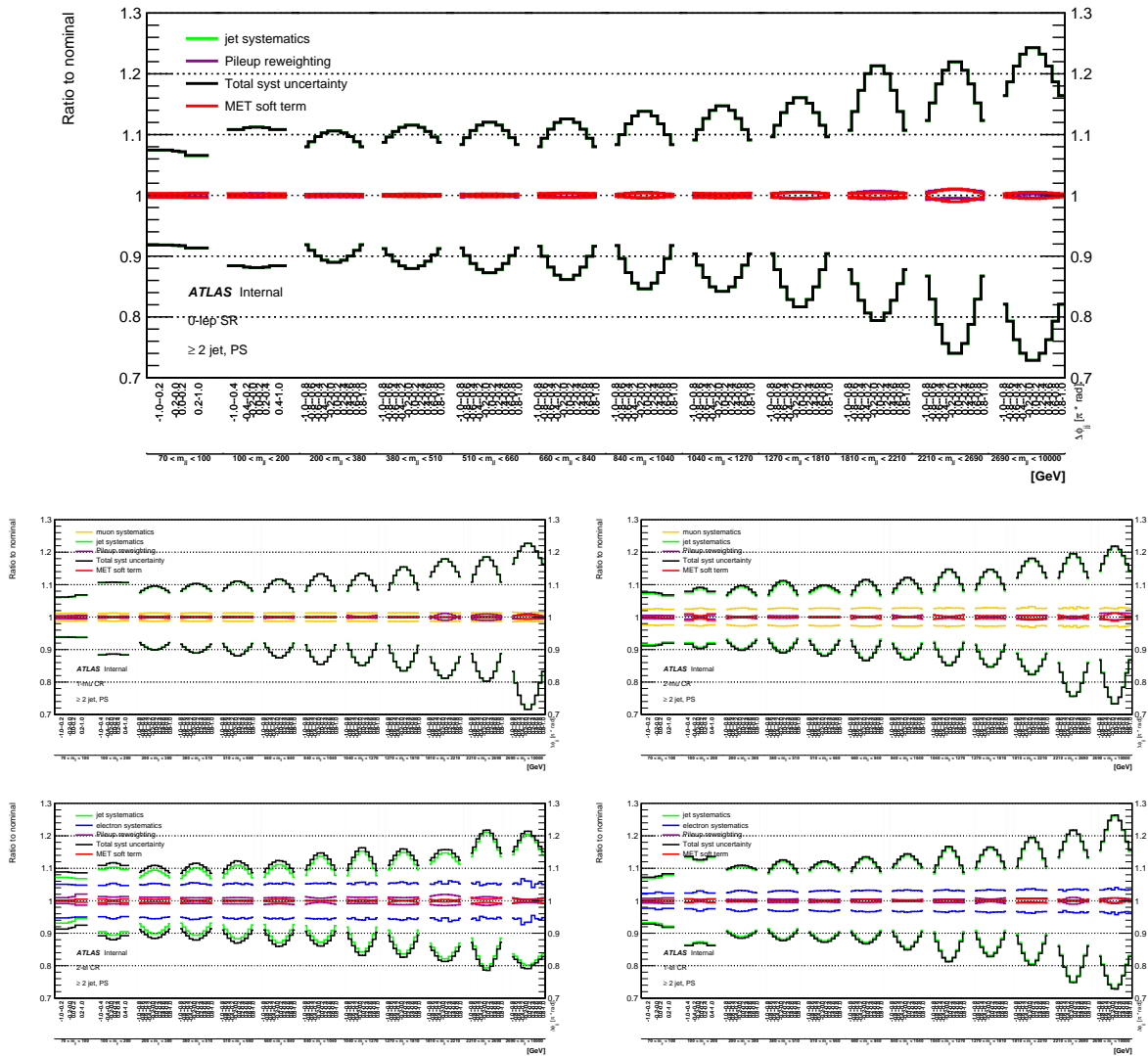


Figure D.6 Systematic breakdown for $\Delta\phi_{jj}$ vs m_{jj} in the ≥ 2 jet phase-space for all regions.

D Unfolded systematic uncertainties

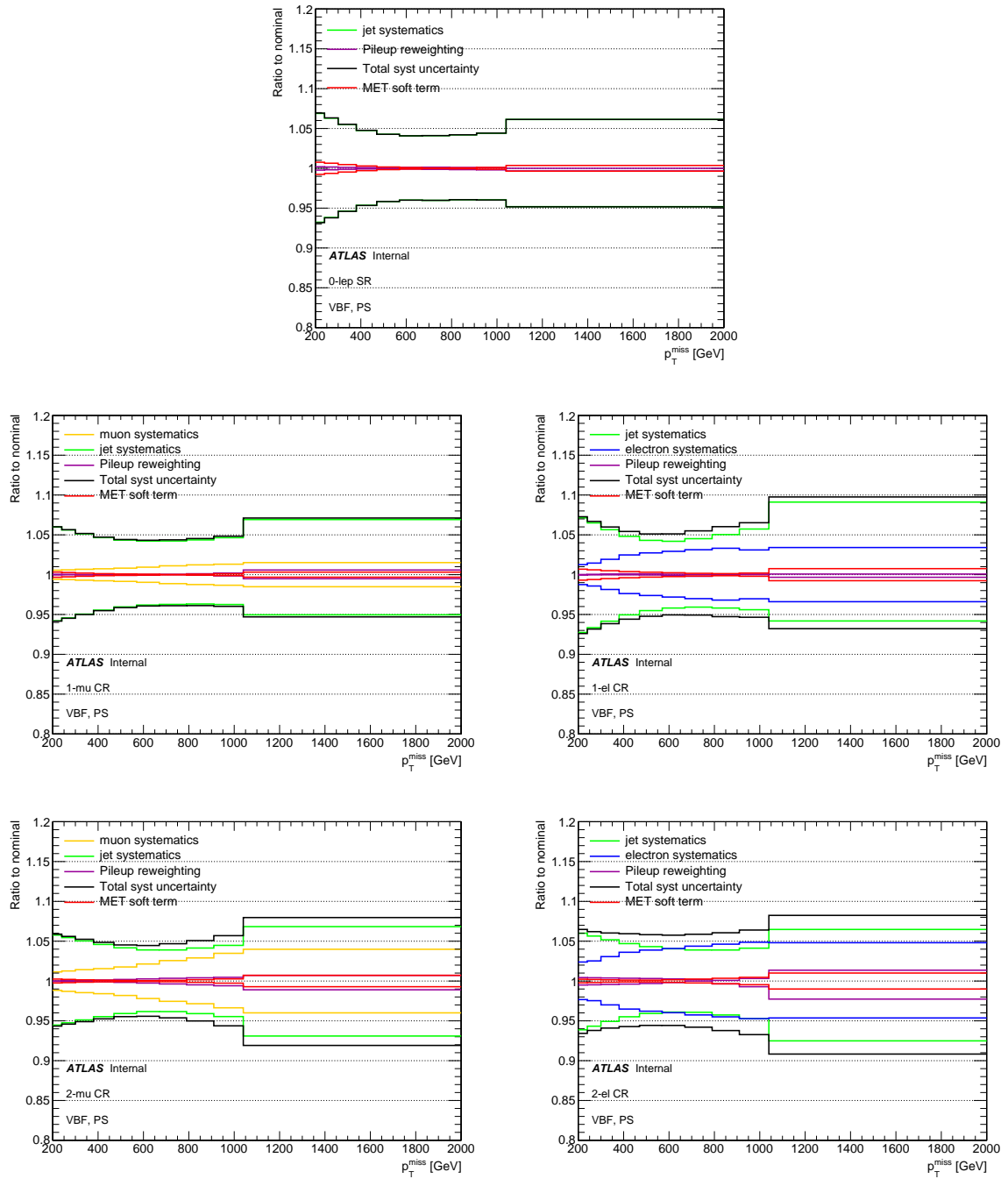


Figure D.7 Systematic breakdown for p_T^{miss} in the VBF phase-space for all regions.

D Unfolded systematic uncertainties

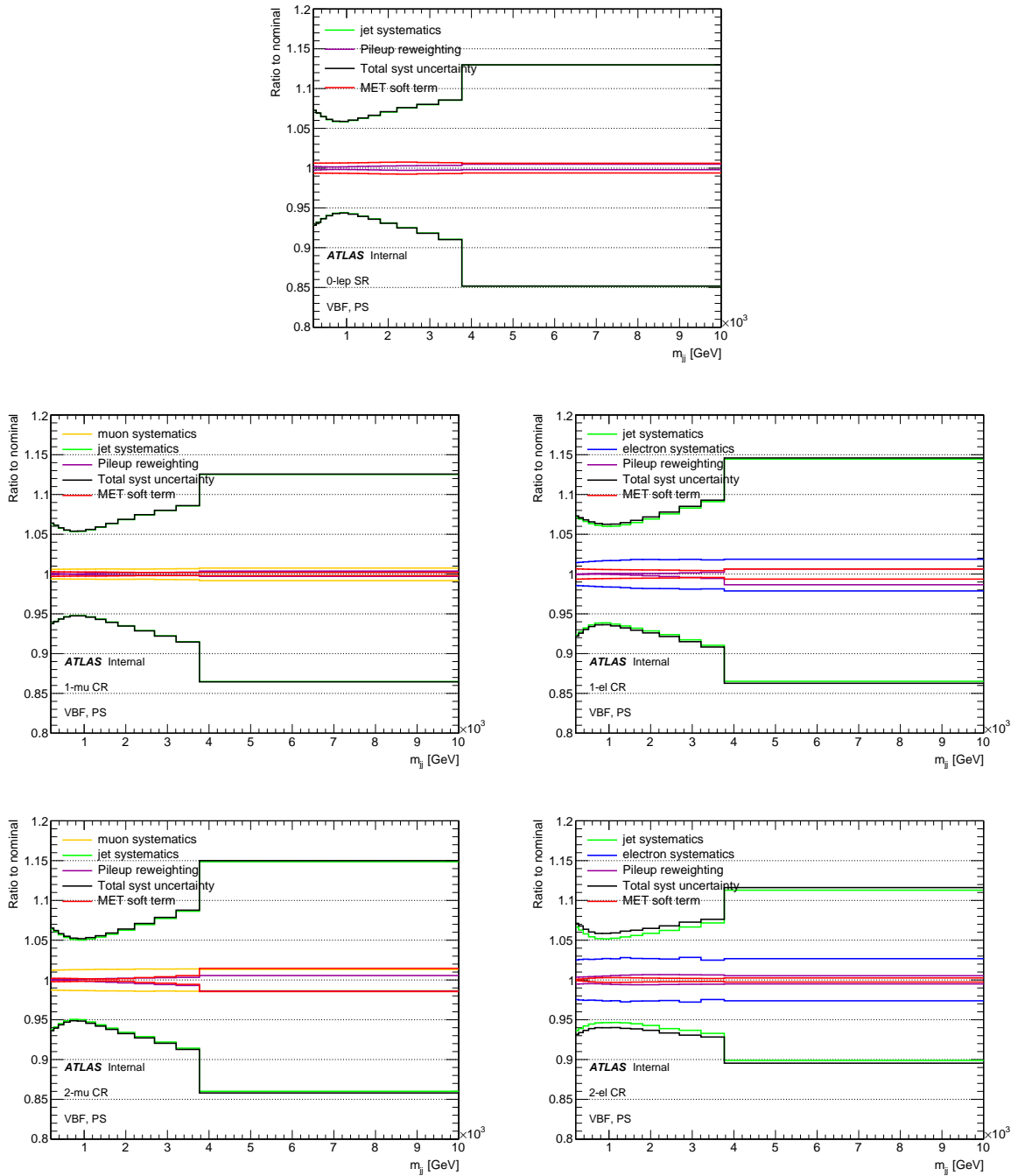


Figure D.8 Systematic breakdown for m_{jj} in the VBF phase-space for all regions.

D Unfolded systematic uncertainties

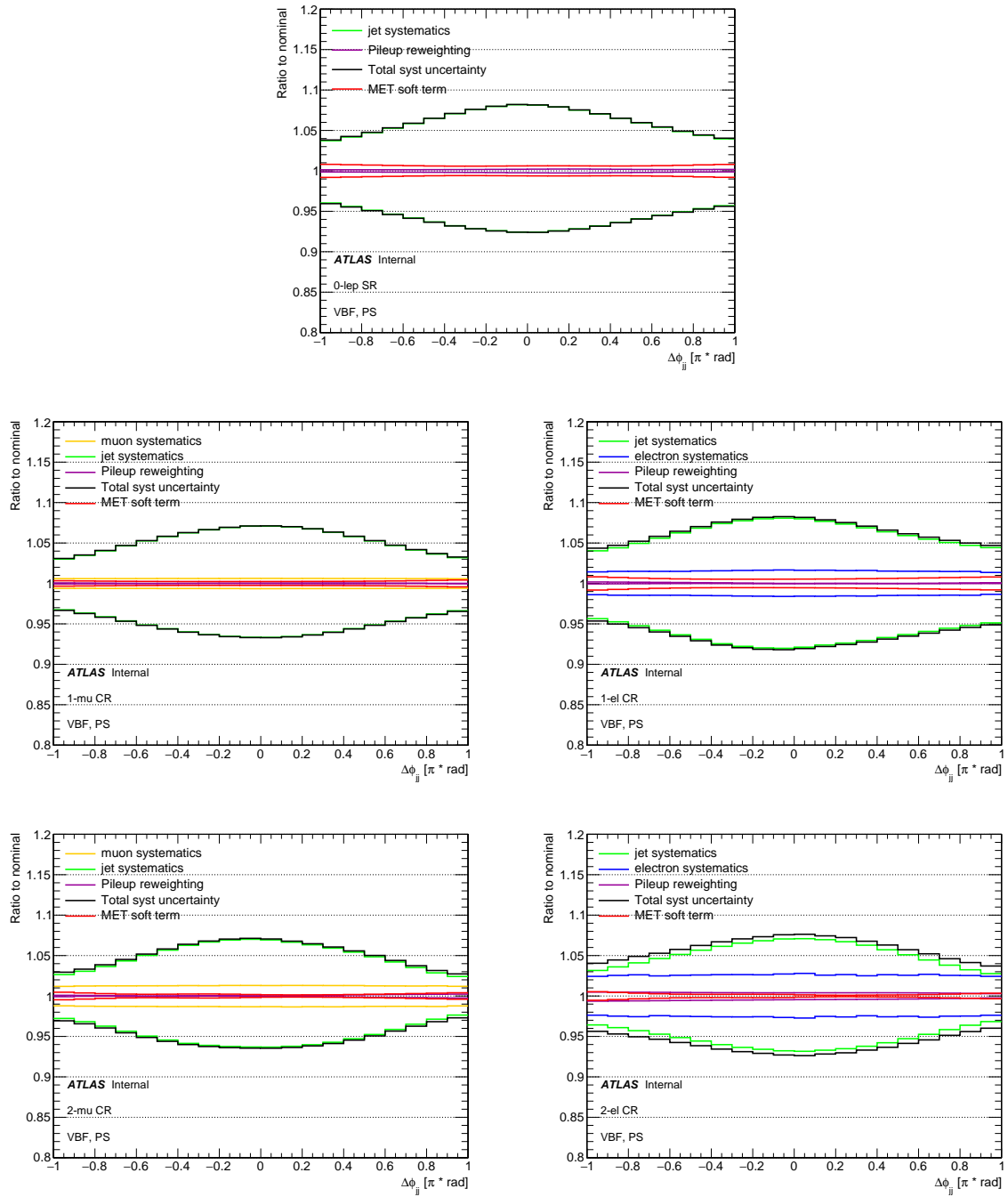


Figure D.9 Systematic breakdown for $\Delta\phi_{jj}$ in the VBF phase-space for all regions.

D Unfolded systematic uncertainties

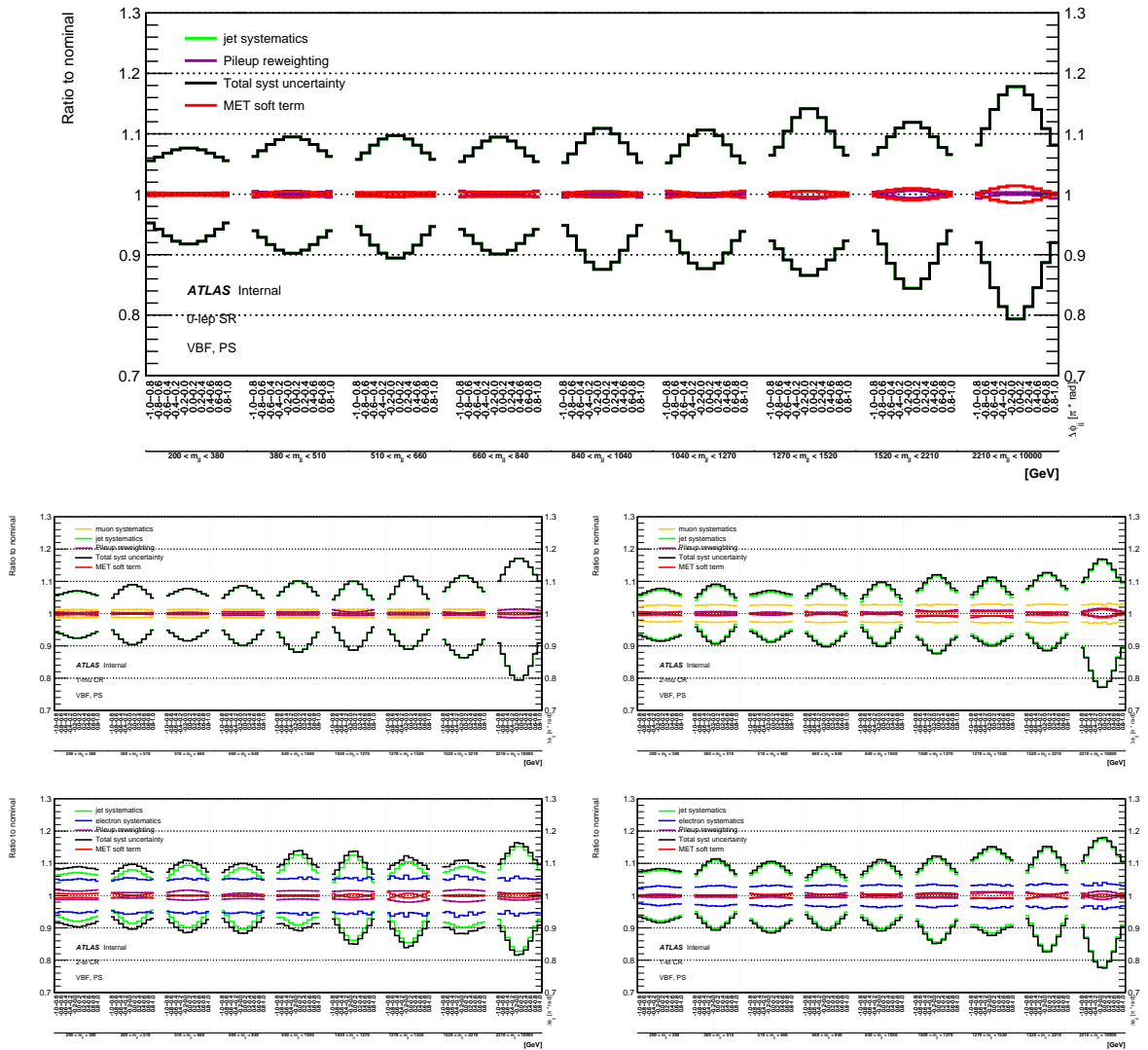


Figure D.10 Systematic breakdown for $\Delta\phi_{jj}$ vs m_{jj} in the VBF phase-space for all regions.

Appendix E

Systematic uncertainties on R^{miss}

The effect of the systematic uncertainties on the R^{miss} ratio are shown in this appendix for all observables. Experimental systematic uncertainties originating from the jet calibration procedure are significantly reduced in the ratio due to the similarity of the jet systems in the $p_{\text{T}}^{\text{miss}} + \text{jets}$ region in the numerator and the lepton regions in the denominator. The lepton efficiency systematics only affect the lepton regions in the denominator and are the dominant experimental systematic uncertainties on the R^{miss} ratio.

The systematic uncertainties on the R^{miss} ratio are shown as follows:

Figure E.1 shows the systematic breakdown for $p_{\text{T}}^{\text{miss}}$ in the ≥ 1 jet phase-space.

Figure E.2 shows the systematic breakdown for $p_{\text{T}}^{\text{miss}}$ in the ≥ 2 jet phase-space.

Figure E.3 shows the systematic breakdown for m_{jj} in the ≥ 2 jet phase-space.

Figure E.4 shows the systematic breakdown for $\Delta\phi_{jj}$ in the ≥ 2 jet phase-space.

Figure E.5 shows the systematic breakdown for $p_{\text{T}}^{\text{miss}}$ in the VBF phase-space.

Figure E.6 shows the systematic breakdown for m_{jj} in the VBF phase-space.

Figure E.7 shows the systematic breakdown for $\Delta\phi_{jj}$ in the VBF phase-space.

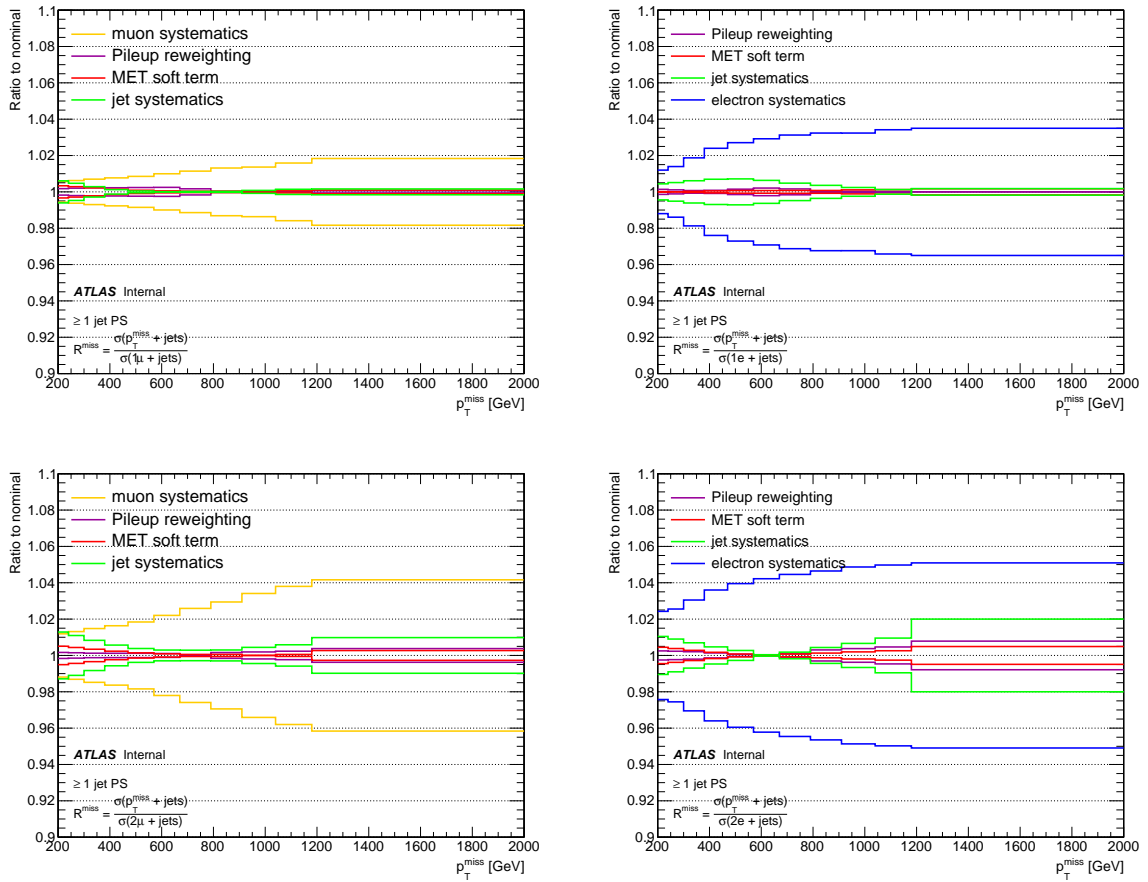


Figure E.1 Systematic breakdown for p_T^{miss} in the ≥ 1 jet phase-space for R^{miss} using any of the lepton regions in the denominator.

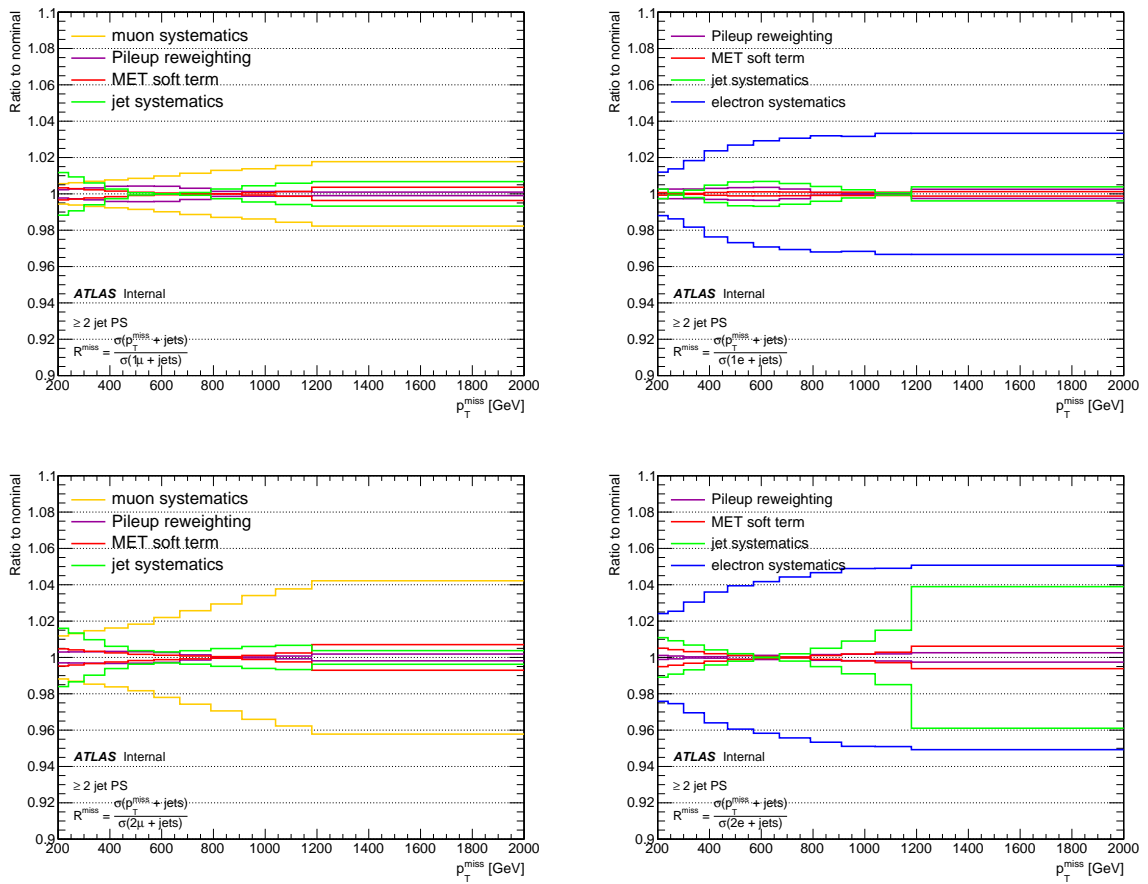


Figure E.2 Systematic breakdown for p_T^{miss} in the ≥ 2 jet phase-space for R^{miss} using any of the lepton regions in the denominator.

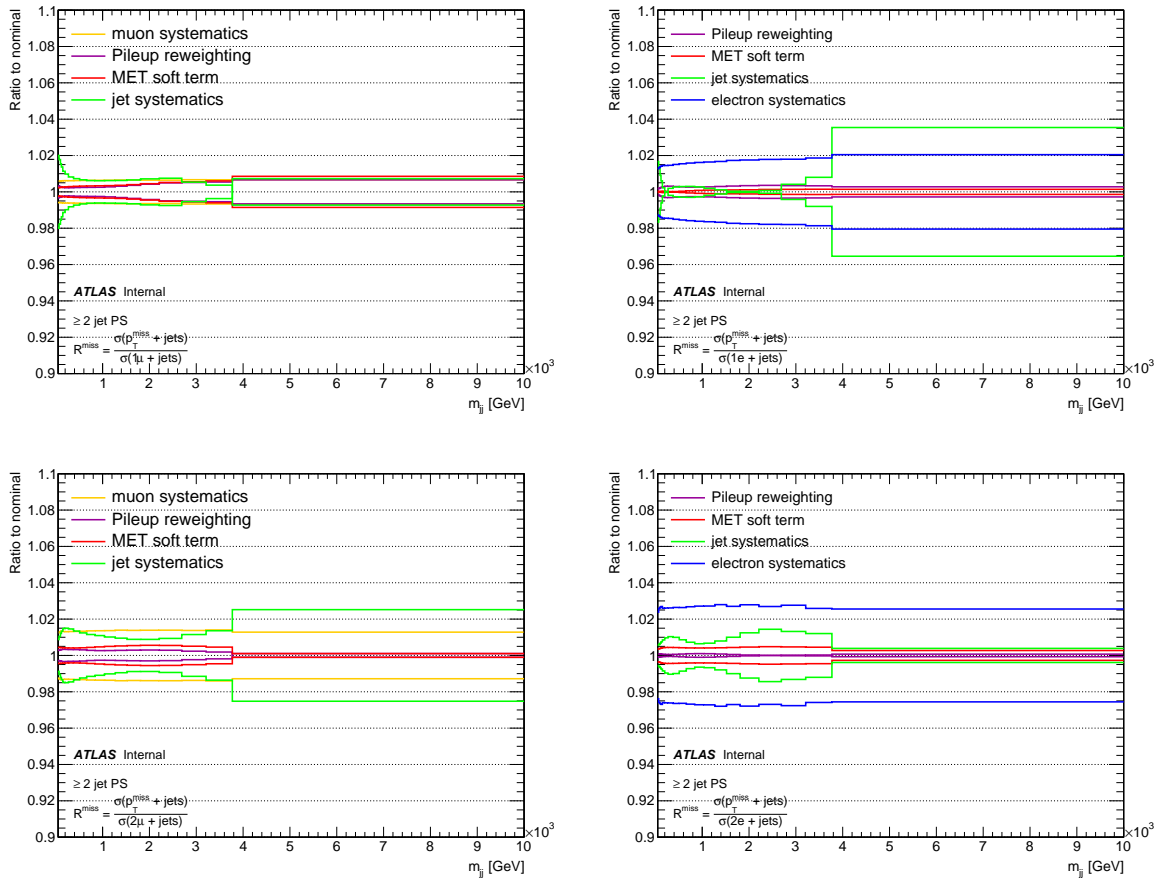


Figure E.3 Systematic breakdown for m_{jj} in the ≥ 2 jet phase-space for R^{miss} using any of the lepton regions in the denominator.

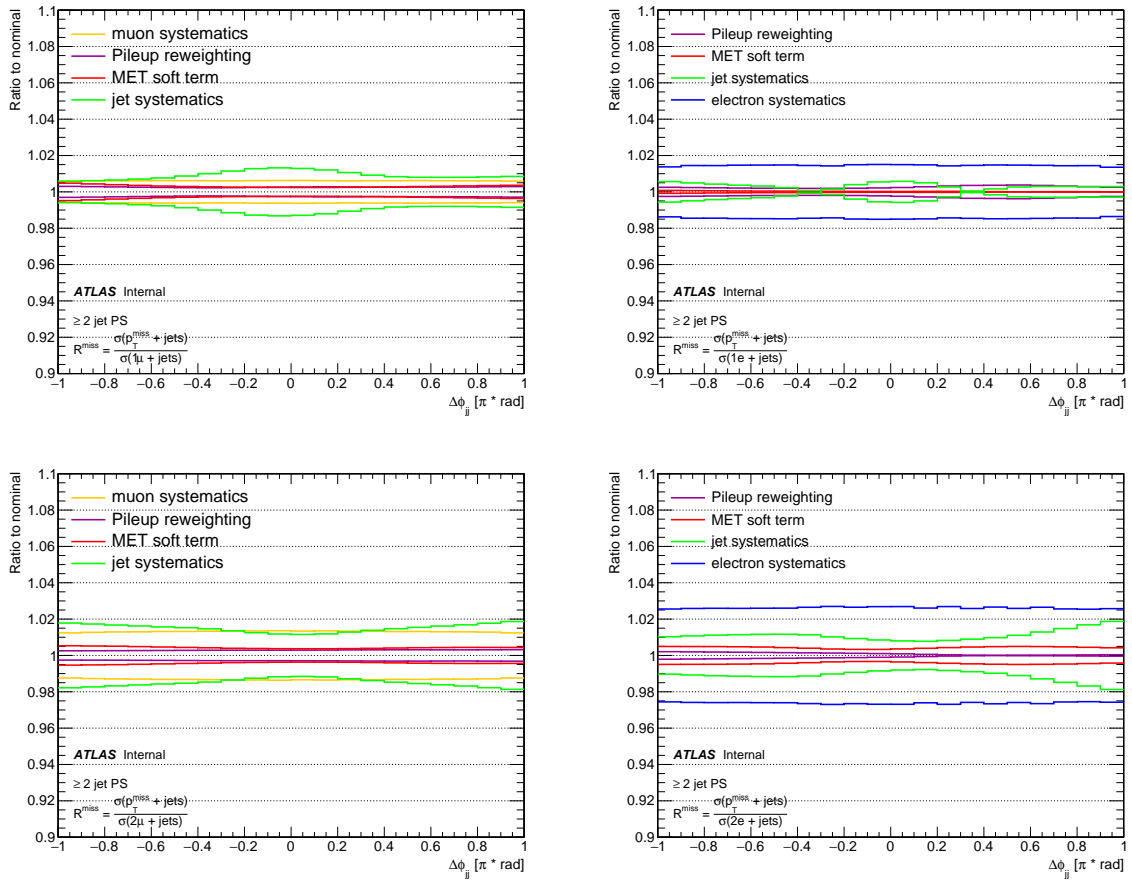


Figure E.4 Systematic breakdown for $\Delta\phi_{jj}$ in the ≥ 2 jet phase-space for R^{miss} using any of the lepton regions in the denominator.

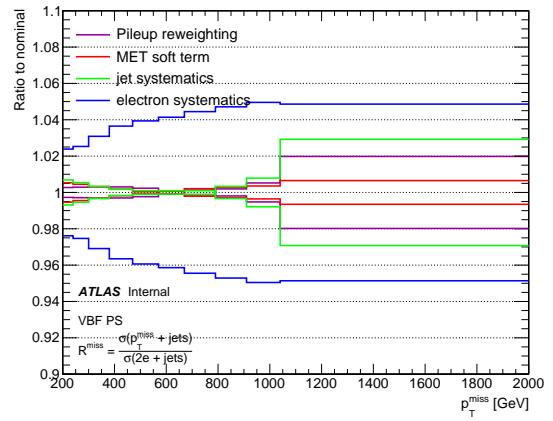
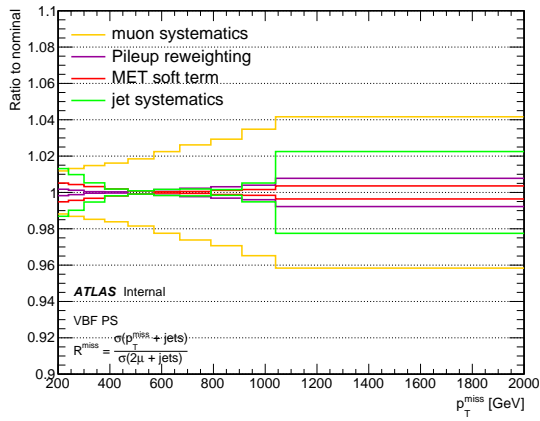
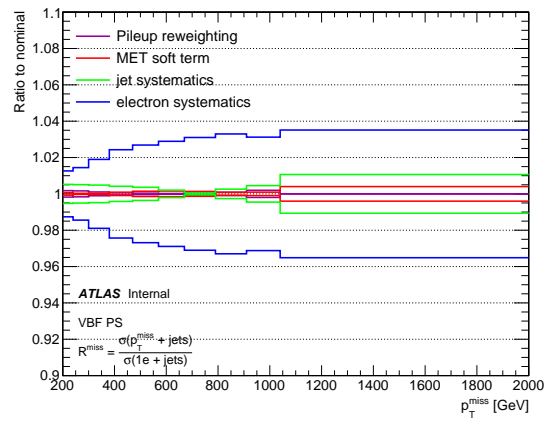
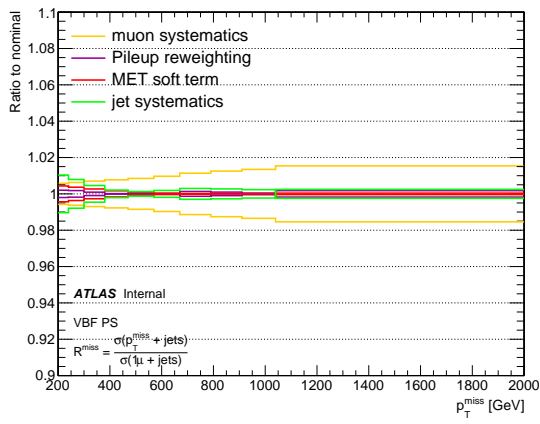


Figure E.5 Systematic breakdown for p_T^{miss} in the VBF phase-space for R^{miss} using any of the lepton regions in the denominator.

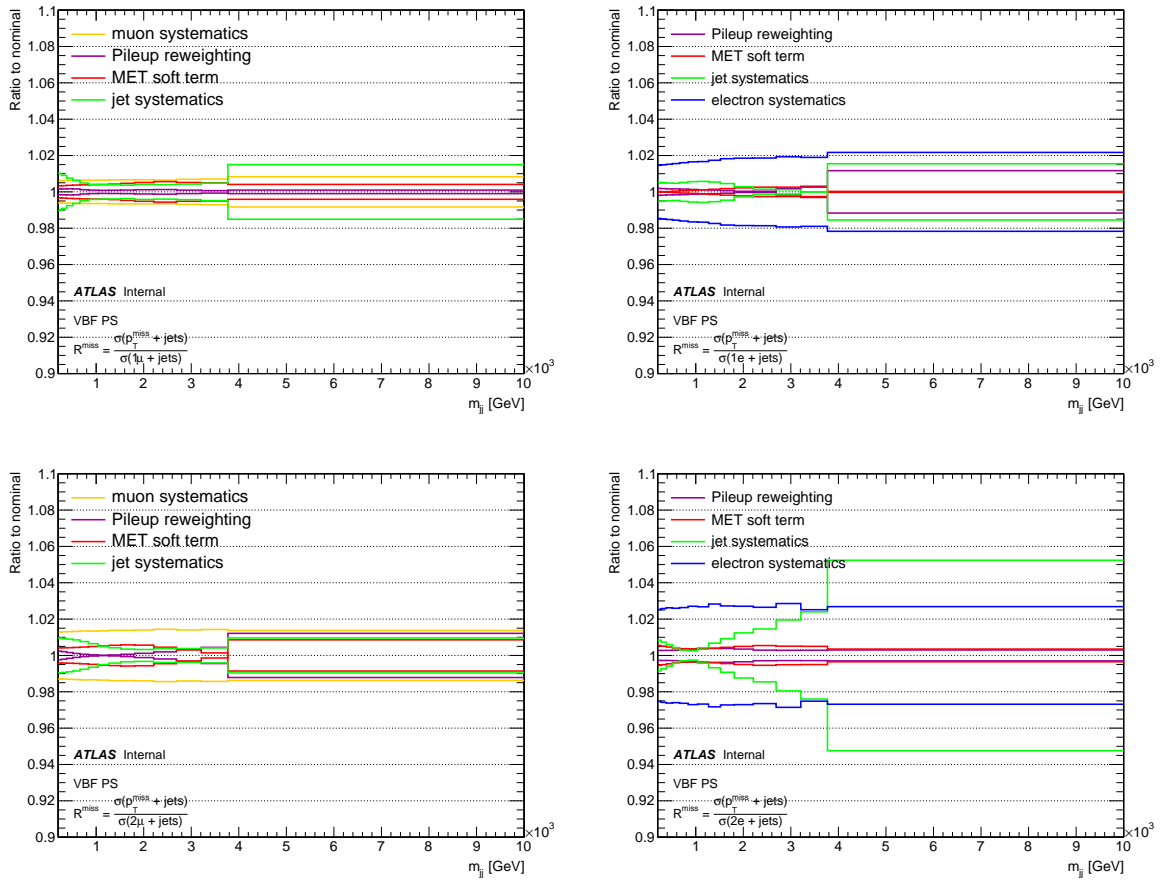


Figure E.6 Systematic breakdown for m_{jj} in the VBF phase-space for R^{miss} using any of the lepton regions in the denominator.

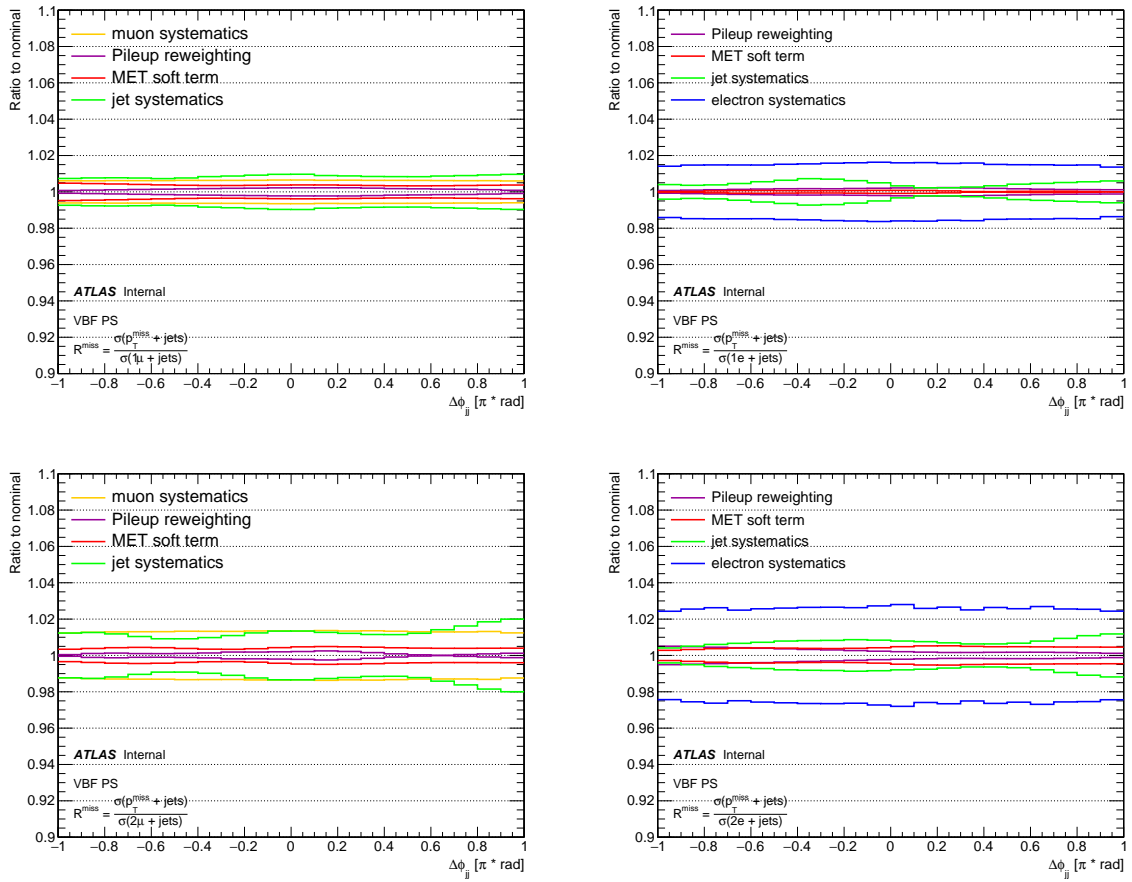


Figure E.7 Systematic breakdown for $\Delta\phi_{jj}$ in the VBF phase-space for R^{miss} using any of the lepton regions in the denominator.

Bibliography

- [1] A. Purcell, *Go on a particle quest at the first CERN webfest. Le premier webfest du CERN se lance à la conquête des particules.* <https://cds.cern.ch/record/1473657>.
- [2] A. S. Kronfeld and C. Quigg, *Resource Letter QCD-1: Quantum chromodynamics.* *American Journal of Physics* **78**(11) (Nov, 2010) p. 1081–1116.
<http://dx.doi.org/10.1119/1.3454865>.
- [3] S. L. Glashow, *Partial-symmetries of weak interactions.* *Nuclear Physics* **22**(4) (1961) pp. 579 – 588.
<http://www.sciencedirect.com/science/article/pii/0029558261904692>.
- [4] F. Englert and R. Brout, *Broken Symmetry and the Mass of Gauge Vector Mesons.* *Phys. Rev. Lett.* **13** (Aug, 1964) pp. 321–323.
<https://link.aps.org/doi/10.1103/PhysRevLett.13.321>.
- [5] P. Higgs, *Broken symmetries, massless particles and gauge fields.* *Physics Letters* **12**(2) (1964) pp. 132 – 133.
<http://www.sciencedirect.com/science/article/pii/0031916364911369>.
- [6] P. W. Higgs, *Broken Symmetries and the Masses of Gauge Bosons.* *Phys. Rev. Lett.* **13** (Oct, 1964) pp. 508–509. <https://link.aps.org/doi/10.1103/PhysRevLett.13.508>.
- [7] A. Buckley, J. Butterworth, S. Gieseke, D. Grellscheid, S. Höche, H. Hoeth, F. Krauss, L. Lönnblad, E. Nurse, P. Richardson, and et al., *General-purpose event generators for LHC physics.* *Physics Reports* **504**(5) (Jul, 2011) p. 145–233.
<http://dx.doi.org/10.1016/j.physrep.2011.03.005>.
- [8] S. Catani, F. Krauss, B. R. Webber, and R. Kuhn, *QCD Matrix Elements + Parton Showers.* *Journal of High Energy Physics* **2001**(11) (Nov, 2001) p. 063–063.
<http://dx.doi.org/10.1088/1126-6708/2001/11/063>.
- [9] B. Penning, *The pursuit of dark matter at colliders—an overview.* *Journal of Physics G: Nuclear and Particle Physics* **45**(6) (May, 2018) p. 063001.
<http://dx.doi.org/10.1088/1361-6471/aabea7>.

- [10] E. Aprile, J. Aalbers, F. Agostini, M. Alfonsi, F. Amaro, M. Anthony, F. Arneodo, P. Barrow, L. Baudis, B. Bauermeister, and et al., *XENON100 dark matter results from a combination of 477 live days*. *Physical Review D* **94**(12) (Dec, 2016) .
<http://dx.doi.org/10.1103/PhysRevD.94.122001>.
- [11] D. Akerib, S. Alsum, H. Araújo, X. Bai, A. Bailey, J. Balajthy, P. Beltrame, E. Bernard, A. Bernstein, T. Biesiadzinski, and et al., *Results from a Search for Dark Matter in the Complete LUX Exposure*. *Physical Review Letters* **118**(2) (Jan, 2017) .
<http://dx.doi.org/10.1103/PhysRevLett.118.021303>.
- [12] ATLAS Collaboration, *Search for new phenomena in the $Z(\rightarrow \ell\ell) + E_T^{\text{miss}}$ final state at $\sqrt{s} = 13$ TeV with the ATLAS detector*. ATLAS-CONF-2016-056, Aug, 2016.
<http://cds.cern.ch/record/2206138>.
- [13] M. Aaboud, G. Aad, B. Abbott, J. Abdallah, O. Abdinov, B. Abeloos, R. Aben, O. AbouZeid, N. Abraham, H. Abramowicz, and et al., *Search for dark matter produced in association with a hadronically decaying vector boson in pp collisions at $s=13$ TeV with the ATLAS detector*. *Physics Letters B* **763** (Dec, 2016) p. 251–268.
<http://dx.doi.org/10.1016/j.physletb.2016.10.042>.
- [14] A. M. Sirunyan, A. Tumasyan, W. Adam, E. Asilar, T. Bergauer, J. Brandstetter, E. Brondolin, M. Dragicevic, J. Erö, and et al., *Search for dark matter and unparticles in events with a Z boson and missing transverse momentum in proton-proton collisions at $\sqrt{s} = 13$ TeV*. *Journal of High Energy Physics* **2017**(3) (Mar, 2017) .
[http://dx.doi.org/10.1007/JHEP03\(2017\)061](http://dx.doi.org/10.1007/JHEP03(2017)061).
- [15] CMS Collaboration, V. Khachatryan, A. M. Sirunyan, and e. a. Tumasyan, *Search for physics beyond the standard model in final states with a lepton and missing transverse energy in proton-proton collisions at $\sqrt{s} = 8$ TeV*. *Phys. Rev. D* **91** (May, 2015) p. 092005. <https://link.aps.org/doi/10.1103/PhysRevD.91.092005>.
- [16] G. Aad, B. Abbott, J. Abdallah, S. A. Khalek, O. Abdinov, R. Aben, B. Abi, M. Abolins, O. S. AbouZeid, and et al., *Search for new particles in events with one lepton and missing transverse momentum in pp collisions at \sqrt{s}*

$$\sqrt{s}$$

= 8 TeV with the ATLAS detector. *Journal of High Energy Physics* **2014**(9) (Sep, 2014) .
[http://dx.doi.org/10.1007/JHEP09\(2014\)037](http://dx.doi.org/10.1007/JHEP09(2014)037).
- [17] M. Aaboud, G. Aad, B. Abbott, O. Abdinov, B. Abeloos, S. H. Abidi, O. S. AbouZeid, N. L. Abraham, H. Abramowicz, and et al., *Search for dark matter and other new phenomena in events with an energetic jet and large missing transverse momentum using*

- the ATLAS detector*. *Journal of High Energy Physics* **2018**(1) (Jan, 2018) .
[http://dx.doi.org/10.1007/JHEP01\(2018\)126](http://dx.doi.org/10.1007/JHEP01(2018)126).
- [18] V. Khachatryan, A. M. Sirunyan, A. Tumasyan, W. Adam, E. Asilar, T. Bergauer, J. Brandstetter, E. Brondolin, M. Dragicevic, and et al., *Searches for invisible decays of the Higgs boson in pp collisions at $\sqrt{s} = 7, 8, \text{ and } 13 \text{ TeV}$* . *Journal of High Energy Physics* **2017**(2) (Feb, 2017) .
[http://dx.doi.org/10.1007/JHEP02\(2017\)135](http://dx.doi.org/10.1007/JHEP02(2017)135).
- [19] ATLAS, M. Aaboud *et al.*, *Constraints on mediator-based dark matter and scalar dark energy models using $\sqrt{s} = 13 \text{ TeV}$ pp collision data collected by the ATLAS detector*. [arXiv:1903.01400](https://arxiv.org/abs/1903.01400) [hep-ex].
- [20] A. Sirunyan, A. Tumasyan, W. Adam, F. Ambroggi, E. Asilar, T. Bergauer, J. Brandstetter, M. Dragicevic, J. Erö, A. Escalante Del Valle, and et al., *Search for invisible decays of a Higgs boson produced through vector boson fusion in proton-proton collisions at $s=13\text{TeV}$* . *Physics Letters B* **793** (Jun, 2019) p. 520–551.
<http://dx.doi.org/10.1016/j.physletb.2019.04.025>.
- [21] L. Evans and P. Bryant, *LHC Machine*. *Journal of Instrumentation* **3**(S08001) (2008) .
- [22] CERN, *The CERN Accelerator Complex*. <https://cds.cern.ch/record/2636343> (accessed on 13/07/2019).
- [23] K. Schindl, *The Injector Chain for the LHC* in Proceedings of the 9th LEP-SPS Performance Workshop, Chamonix, France, 1999, pp. 47–52.
<https://cds.cern.ch/record/384396>.
- [24] CERN, *The Large Hadron Collider*.
<https://home.cern/science/accelerators/large-hadron-collider> (accessed on 13/07/2019).
- [25] ATLAS Collaboration, *The ATLAS Experiment at the CERN Large Hadron Collider*. *Journal of Instrumentation* **3**(S08003) (2008) .
- [26] CMS Collaboration, *The CMS experiment at the CERN LHC*. *Journal of Instrumentation* **3**(S08004) (2008) .
- [27] LHCb Collaboration, *The LHCb Detector at the LHC*. *Journal of Instrumentation* **3**(S08005) (2008) .
- [28] ALICE Collaboration, *The ALICE experiment at the CERN LHC*. *Journal of Instrumentation* **3**(S08002) (2008) .

- [29] ATLAS Collaboration, *Luminosity determination in pp collisions at $\sqrt{s} = 8$ TeV using the ATLAS detector at the LHC*. *The European Physics Journal C* **76**(653) (2016) .
- [30] *ATLAS Luminosity summary plots*, (Accessed March 30, 2020). <https://twiki.cern.ch/twiki/bin/view/AtlasPublic/LuminosityPublicResultsRun2>.
- [31] ATLAS Experiment, CERN, *Computer generated image of the whole ATLAS detector*. <https://cds.cern.ch/record/1095924> (accessed on 14/07/2019).
- [32] ATLAS Collaboration, *ATLAS Insertable B-Layer Technical Design Report*. CERN-LHCC-2010-013, ATLAS-TDR-19, 2010. <https://cdsweb.cern.ch/record/1291633>.
- [33] ATLAS Collaboration, *ATLAS inner detector: Technical Design Report*. CERN-LHCC-97-016, ATLAS-TDR-4, 1997. <https://cdsweb.cern.ch/record/331063>.
- [34] ATLAS Collaboration, *ATLAS high-level trigger, data-acquisition and controls: Technical Design Report*. CERN-LHCC-2003-022, ATLAS-TDR-16, 2003. <https://cdsweb.cern.ch/record/616089>.
- [35] B. Nachman, *Investigating the Quantum Properties of Jets and the Search for a Supersymmetric Top Quark Partner with the ATLAS Detector*, 2016.
- [36] M. Aaboud, G. Aad, B. Abbott, J. Abdallah, O. Abdinov, B. Abeloos, S. H. Abidi, O. S. AbouZeid, N. L. Abraham, and et al., *Performance of the ATLAS track reconstruction algorithms in dense environments in LHC Run 2*. *The European Physical Journal C* **77**(10) (Oct, 2017) . <http://dx.doi.org/10.1140/epjc/s10052-017-5225-7>.
- [37] M. Cacciari, G. P. Salam, and G. Soyez, *The anti- k_t jet clustering algorithm*. *Journal of High Energy Physics* **2008**(063) (2008) .
- [38] ATLAS Collaboration, *Jet Calibration and Systematic Uncertainties for Jets Reconstructed in the ATLAS Detector at $\sqrt{s} = 13$ TeV*. ATL-PHYS-PUB-2015-015, 2015. <https://cds.cern.ch/record/2037613>.
- [39] ATLAS Collaboration, *Jet energy scale measurements and their systematic uncertainties in proton-proton collisions at $\sqrt{s} = 13$ TeV with the ATLAS detector*. *Physical Review D* **96**(072002) (2017) .
- [40] G. Aad, T. Abajyan, B. Abbott, J. Abdallah, S. Abdel Khalek, A. A. Abdelalim, O. Abdinov, R. Aben, B. Abi, and et al., *Jet energy resolution in proton-proton collisions at $\sqrt{s} = 7$ TeV recorded in 2010 with the ATLAS detector*. *The European Physical Journal C* **73**(3) (Mar, 2013) . <http://dx.doi.org/10.1140/epjc/s10052-013-2306-0>.

- [41] ATLAS Collaboration, *Monte Carlo Calibration and Combination of In-situ Measurements of Jet Energy Scale, Jet Energy Resolution and Jet Mass in ATLAS*. ATLAS-CONF-2015-037, 2015. <https://cds.cern.ch/record/2044941>.
- [42] ATLAS Collaboration, “Selection of jets produced in 13 TeV proton–proton collisions with the ATLAS detector.” ATLAS-CONF-2015-029, 2015. <https://cds.cern.ch/record/2037702>.
- [43] ATLAS Collaboration, *Tagging and suppression of pileup jets with the ATLAS detector*. ATLAS-CONF-2014-018, 2014. <https://cds.cern.ch/record/1700870>.
- [44] ATLAS Collaboration, *Calorimeter Clustering Algorithms: Description and Performance*. ATL-LARG-PUB-2008-002, 2008. <https://cds.cern.ch/record/1099735>.
- [45] ATLAS Collaboration, *Electron efficiency measurements with the ATLAS detector using the 2015 LHC proton-proton collision data* in 51st Rencontres de Moriond on QCD and High Energy Interactions, 2016. <http://cds.cern.ch/record/2157687>.
- [46] ATLAS Collaboration, *Muon reconstruction performance of the ATLAS detector in proton–proton collision data at $\sqrt{s} = 13$ TeV*. *The European Physical Journal C* **76**(292) (2016) .
- [47] ATLAS Collaboration, *Topological cell clustering in the ATLAS calorimeters and its performance in LHC Run 1*. *The European Physical Journal C* **77**(490) (2017) .
- [48] ATLAS Collaboration, *Measurement of detector-corrected observables sensitive to the anomalous production of events with jets and large missing transverse momentum in pp collisions at $\sqrt{s} = 13$ TeV using the ATLAS detector*. *The European Physical Journal C* **77**(11) (Nov, 2017) . <http://dx.doi.org/10.1140/epjc/s10052-017-5315-6>.
- [49] F. U. Bernlochner, C. Englert, C. Hays, K. Lohwasser, H. Mildner, A. Pilkington, D. D. Price, and M. Spannowsky, *Angles on CP-violation in Higgs boson interactions*. *Physics Letters B* **790** (Mar, 2019) p. 372–379. <http://dx.doi.org/10.1016/j.physletb.2019.01.043>.
- [50] T. Sjöstrand, S. Ask, J. R. Christiansen, R. Corke, N. Desai, P. Ilten, S. Mrenna, S. Prestel, C. O. Rasmussen, and P. Z. Skands, *An Introduction to PYTHIA 8.2*. *Comput. Phys. Commun.* **191** (2015) pp. 159–177, [arXiv:1410.3012](https://arxiv.org/abs/1410.3012) [hep-ph].
- [51] R. D. Ball, V. Bertone, S. Carrazza, C. S. Deans, L. Del Debbio, *et al.*, *Parton distributions with LHC data*. *Nucl. Phys. B* **867** (2013) pp. 244–289, [arXiv:1207.1303](https://arxiv.org/abs/1207.1303) [hep-ph].
- [52] ATLAS Collaboration, “The Pythia 8 A3 tune description of ATLAS minimum bias and inelastic measurements incorporating the Donnachie–Landshoff diffractive model.”

- ATL-PHYS-PUB-2016-017, 2016. <https://cds.cern.ch/record/2206965>.
- [53] GEANT4, S. Agostinelli *et al.*, *GEANT4: A Simulation toolkit*. *Nucl. Instrum. Meth.* **A506** (2003) pp. 250–303.
- [54] J. Allison *et al.*, *Geant4 developments and applications*. *IEEE Trans. Nucl. Sci.* **53** (2006) p. 270.
- [55] J. M. Lindert *et al.*, *Precise predictions for $V + jets$ dark matter backgrounds*. *Eur. Phys. J.* **C77**(12) (2017) p. 829, [arXiv:1705.04664](https://arxiv.org/abs/1705.04664) [hep-ph].
- [56] S. Frixione, E. Laenen, P. Motylinski, C. White, and B. R. Webber, *Single-top hadroproduction in association with a W boson*. *Journal of High Energy Physics* **2008**(07) (Jul, 2008) p. 029–029. <http://dx.doi.org/10.1088/1126-6708/2008/07/029>.
- [57] S. Dulat, T.-J. Hou, J. Gao, M. Guzzi, J. Huston, P. Nadolsky, J. Pumplin, C. Schmidt, D. Stump, and C. P. Yuan, *New parton distribution functions from a global analysis of quantum chromodynamics*. *Phys. Rev. D* **93**(3) (2016) p. 033006, [arXiv:1506.07443](https://arxiv.org/abs/1506.07443) [hep-ph].
- [58] L. Harland-Lang, A. Martin, P. Motylinski, and R. Thorne, *Parton distributions in the LHC era: MMHT 2014 PDFs*. *Eur. Phys. J. C* **75**(5) (2015) p. 204, [arXiv:1412.3989](https://arxiv.org/abs/1412.3989) [hep-ph].
- [59] B. Malaescu, *An iterative, dynamically stabilized method of data unfolding*, 2009.
- [60] B. Efron, *Bootstrap Methods: Another Look at the Jackknife*. *Ann. Statist.* **7**(1) (01, 1979) pp. 1–26. <https://doi.org/10.1214/aos/1176344552>.
- [61] K. G. Hayes, M. L. Perl, and B. Efron, *Application of the bootstrap statistical method to the tau-decay-mode problem*. *Phys. Rev. D* **39** (Jan, 1989) pp. 274–279. <https://link.aps.org/doi/10.1103/PhysRevD.39.274>.
- [62] J. W. Monk and C. Oropeza-Barrera, *The HBOM Method for Unfolding Detector Effects*. *Nucl. Instrum. Meth.* **A701** (2013) pp. 17–24, [arXiv:1111.4896](https://arxiv.org/abs/1111.4896) [hep-ex].
- [63] E. Nurse, C. Gutsche, V. Konstantinides, A. S. Kelly, J. Butterworth, A. Pilkington, M. Vozak, D. Price, S. B. Menary, M. Dunford, P. Starovoitov, S. M. Weber, M. Klassen, T. M. Spieker, and D. P. Yallup, *Detector-corrected cross-sections in events with large missing transverse momentum in association with jets*. ATL-COM-PHYS-2019-1411, Nov, 2019. <https://cds.cern.ch/record/2702246>.
- [64] T. Gleisberg, S. Hoeche, F. Krauss, M. Schonherr, S. Schumann, F. Siegert, and J. Winter, *Event generation with SHERPA 1.1*. *JHEP* **02** (2009) p. 007, [arXiv:0811.4622](https://arxiv.org/abs/0811.4622) [hep-ph].

- [65] T. Gleisberg and S. Höche, *Comix, a new matrix element generator*. *JHEP* **12** (2008) p. 039, [arXiv:0808.3674 \[hep-ph\]](#).
- [66] F. Cascioli, P. Maierhofer, and S. Pozzorini, *Scattering Amplitudes with Open Loops*. *Phys. Rev. Lett.* **108** (2012) p. 111601, [arXiv:1111.5206 \[hep-ph\]](#).
- [67] A. Denner, S. Dittmaier, and L. Hofer, *Collier: a fortran-based Complex One-Loop Library in Extended Regularizations*. *Comput. Phys. Commun.* **212** (2017) pp. 220–238, [arXiv:1604.06792 \[hep-ph\]](#).
- [68] S. Schumann and F. Krauss, *A Parton shower algorithm based on Catani-Seymour dipole factorisation*. *JHEP* **03** (2008) p. 038, [arXiv:0709.1027 \[hep-ph\]](#).
- [69] J.-C. Winter, F. Krauss, and G. Soff, *A Modified cluster hadronization model*. *Eur. Phys. J.* **C36** (2004) pp. 381–395, [arXiv:hep-ph/0311085 \[hep-ph\]](#).
- [70] NNPDF, NNPDF Collaboration, R.D. Ball et al., *Parton distributions for the LHC Run II*. *JHEP* **04** (2015) p. 040, [arXiv:1410.8849 \[hep-ph\]](#).
- [71] S. Höche, F. Krauss, M. Schonherr, and F. Siegert, *A critical appraisal of NLO+PS matching methods*. *JHEP* **09** (2012) p. 049, [arXiv:1111.1220 \[hep-ph\]](#).
- [72] S. Catani, F. Krauss, R. Kuhn, and B. R. Webber, *QCD matrix elements + parton showers*. *JHEP* **11** (2001) p. 063, [arXiv:hep-ph/0109231](#).
- [73] S. Höche, F. Krauss, S. Schumann, and F. Siegert, *QCD matrix elements and truncated showers*. *JHEP* **05** (2009) p. 053, [arXiv:0903.1219 \[hep-ph\]](#).
- [74] S. Höche, F. Krauss, M. Schön herr, and F. Siegert, *QCD matrix elements + parton showers: The NLO case*. *JHEP* **04** (2013) p. 027, [arXiv:1207.5030 \[hep-ph\]](#).
- [75] C. Anastasiou, L. J. Dixon, K. Melnikov, and F. Petriello, *High precision QCD at hadron colliders: Electroweak gauge boson rapidity distributions at NNLO*. *Phys. Rev. D* **69** (2004) p. 094008, [arXiv:hep-ph/0312266](#).
- [76] ATLAS Collaboration, “ATLAS simulation of boson plus jets processes in Run 2.” ATL-PHYS-PUB-2017-006, 2017. <https://cds.cern.ch/record/2261937>.
- [77] ATLAS Collaboration, “Multi-Boson Simulation for 13 TeV ATLAS Analyses.” ATL-PHYS-PUB-2017-005, 2017. <https://cds.cern.ch/record/2261933>.
- [78] S. Frixione et al., *A positive-weight next-to-leading-order Monte Carlo for heavy flavour hadroproduction*. *JHEP* **09** (2007) p. 126, [arXiv:0707.3088 \[hep-ph\]](#).
- [79] P. Nason, *A New method for combining NLO QCD with shower Monte Carlo algorithms*. *JHEP* **0411** (2004) p. 040, [arXiv:hep-ph/0409146](#).

- [80] S. Frixione, P. Nason, and C. Oleari, *Matching NLO QCD computations with Parton Shower simulations: the POWHEG method*. *JHEP* **11** (2007) p. 070, [arXiv:0709.2092 \[hep-ph\]](#).
- [81] S. Alioli, P. Nason, C. Oleari, and E. Re, *A general framework for implementing NLO calculations in shower Monte Carlo programs: the POWHEG BOX*. *JHEP* **1006** (2010) p. 043, [arXiv:1002.2581 \[hep-ph\]](#).
- [82] ATLAS Collaboration, “Studies on top-quark Monte Carlo modelling for Top2016.” ATL-PHYS-PUB-2016-020, 2016. <https://cds.cern.ch/record/2216168>.
- [83] ATLAS Collaboration, “ATLAS Pythia 8 tunes to 7 TeV data.” ATL-PHYS-PUB-2014-021, 2014. <https://cds.cern.ch/record/1966419>.
- [84] M. Beneke, P. Falgari, S. Klein, and C. Schwinn, *Hadronic top-quark pair production with NNLL threshold resummation*. *Nucl. Phys. B* **855** (2012) pp. 695–741, [arXiv:1109.1536 \[hep-ph\]](#).
- [85] M. Cacciari, M. Czakon, M. Mangano, A. Mitov, and P. Nason, *Top-pair production at hadron colliders with next-to-next-to-leading logarithmic soft-gluon resummation*. *Phys. Lett. B* **710** (2012) pp. 612–622, [arXiv:1111.5869 \[hep-ph\]](#).
- [86] P. Bärnreuther, M. Czakon, and A. Mitov, *Percent Level Precision Physics at the Tevatron: First Genuine NNLO QCD Corrections to $q\bar{q} \rightarrow t\bar{t} + X$* . *Phys. Rev. Lett.* **109** (2012) p. 132001, [arXiv:1204.5201 \[hep-ph\]](#).
- [87] M. Czakon and A. Mitov, *NNLO corrections to top-pair production at hadron colliders: the all-fermionic scattering channels*. *JHEP* **12** (2012) p. 054, [arXiv:1207.0236 \[hep-ph\]](#).
- [88] M. Czakon and A. Mitov, *NNLO corrections to top pair production at hadron colliders: the quark-gluon reaction*. *JHEP* **1301** (2013) p. 080, [arXiv:1210.6832 \[hep-ph\]](#).
- [89] M. Czakon, P. Fiedler, and A. Mitov, *The total top quark pair production cross-section at hadron colliders through $O(\alpha_S^4)$* . *Phys. Rev. Lett.* **110** (2013) p. 252004, [arXiv:1303.6254 \[hep-ph\]](#).
- [90] M. Czakon and A. Mitov, *Top++: A Program for the Calculation of the Top-Pair Cross-Section at Hadron Colliders*. *Comput. Phys. Commun.* **185** (2014) p. 2930, [arXiv:1112.5675 \[hep-ph\]](#).
- [91] E. Re, *Single-top Wt -channel production matched with parton showers using the POWHEG method*. *Eur. Phys. J. C* **71** (2011) p. 1547, [arXiv:1009.2450 \[hep-ph\]](#).
- [92] S. Frixione, E. Laenen, P. Motylinski, B. R. Webber, and C. D. White, *Single-top hadroproduction in association with a W boson*. *JHEP* **0807** (2008) p. 029,

[arXiv:0805.3067](#) [[hep-ph](#)].

- [93] M. Aliev, H. Lacker, U. Langenfeld, S. Moch, P. Uwer, and M. Wiedermann, *HATHOR: HAdronic Top and Heavy quarks crOss section calculatoR*. [Comput. Phys. Commun.](#) **182** (2011) pp. 1034–1046, [arXiv:1007.1327](#) [[hep-ph](#)].
- [94] P. Kant, O. M. Kind, T. Kintscher, T. Lohse, T. Martini, S. Mölbitz, P. Rieck, and P. Uwer, *HatHor for single top-quark production: Updated predictions and uncertainty estimates for single top-quark production in hadronic collisions*. [Comput. Phys. Commun.](#) **191** (2015) pp. 74–89, [arXiv:1406.4403](#) [[hep-ph](#)].
- [95] R. Frederix, E. Re, and P. Torrielli, *Single-top t-channel hadroproduction in the four-flavour scheme with POWHEG and aMC@NLO*. [JHEP](#) **09** (2012) p. 130, [arXiv:1207.5391](#) [[hep-ph](#)].
- [96] S. Alioli, P. Nason, C. Oleari, and E. Re, *NLO single-top production matched with shower in POWHEG: s- and t-channel contributions*. [JHEP](#) **09** (2009) p. 111, [arXiv:0907.4076](#) [[hep-ph](#)]. [Erratum: [JHEP02,011\(2010\)](#)].
- [97] J. H. Friedman, *A VARIABLE SPAN SMOOTHER*.